Seismic Performance of GFRP-RC Beam-Column and Beam-Column-Slab Subassemblies

By

Shervin Khalili Ghomi

A Thesis Submitted to the Faculty of Graduate Studies of
The University of Manitoba
in partial fulfilment of the requirements for the degree of

Doctor of Philosophy

Department of Civil Engineering

University of Manitoba

Winnipeg

September 2019

ABSTRACT

In the past two decades, Fiber Reinforced Polymers (FRPs) have been introduced as an effective alternative for the conventional steel bars and stirrups in reinforced concrete (RC) structures mainly due to their superior performance in terms of corrosion resistance. However, despite the promising results of the studies on the behaviour of individual FRP-RC elements such as beams, columns and slabs under monotonic loading, studies on the integral behaviour of FRP-RC subassemblies where two or more structural elements interact with each other are scarce. The lack of research data is especially evident concerning one of the primary concerns about the performance of FRP-RC structures, the feasibility of using these materials in seismically active regions.

This study aims to enhance the understanding of the seismic performance of FRP-RC structures by conducting comprehensive investigations on the seismic behaviour of FRP-RC beam-column joints as key elements in framed structures. The program consists of an experimental phase, involving the construction and testing of twelve full-scale beam-column subassemblies, and an analytical phase, utilizing nonlinear finite element modelling (FEM) to simulate the seismic behaviour of FRP-RC connections in moment-resisting frames.

The effect of several primary parameters such as geometrical configuration (interior and exterior), joint shear stress, presence of lateral beams, type of reinforcement, and presence of cast-in situ slabs on the seismic performance of GFRP-RC beam-column connections was investigated. Additionally, an effective solution to address the lack of energy dissipation in FRP-RC structures as one of the concerns about their seismic performance was proposed.

As part of the analytical phase, a commercial FEM software (ATENA 3D) was used to perform a parametric study to further investigate the effect of various parameters on the performance of beam-column and beam-column-slab connections such as joint shear stress, size of lateral beams, reinforcement material, column axial load and geometrical configuration.

Results of the experimental and analytical investigations indicated that GFRP-RC subassemblies are capable of withstanding multiple cyclic loadings up to 8% drift ratio without exhibiting brittle failure. Moreover, it was found that the geometrical configuration significantly affects the level of concrete damage and energy dissipation of GFRP-RC beam-columns.

ACKNOWLEDEMENTS

My first and sincere appreciation goes to my supervisor Dr. Ehab El-Salakawy, PEng, FCSCE, Professor of Structural Engineering and former Canada Research Chair in Durability and Modernization of Civil Structures in the Department of Civil Engineering at the University of Manitoba, for his continuous guidance and support throughout the course of this research program. I am greatly thankful for his mentorship, patience and constant encouragement to take on new challenges.

I would like to express my deep gratitude to my friends and colleagues for their invaluable help and the technical staff of the McQuade Heavy Structural Laboratory at the University of Manitoba, especially Dr. Chad Klowak, PEng, for their technical assistance and valuable advice during the experimental program.

The financial support of the Natural Science and Engineering Research Council of Canada (NSERC) through Canada Research Chairs and Discovery programs as well as the University of Manitoba Graduate Fellowship (UMGF) is gratefully acknowledged.

Words will never be able to express my heartfelt gratitude to my dearest friend Diba, for her kindness, great patience, encouragement and continuous support.

Last, but not the least, I would like to thank my parents for believing in me and for their unconditional love, constant support and countless sacrifices. Without them, I could not make it here.

TABLE OF CONTENTS

LIST OF TABLES

LIST OF FIGURES

1 INTRODUCTION

1.1 Background

In the past two decades, Fiber Reinforced Polymers (FRPs) have been introduced as an effective alternative for conventional steel bars and stirrups in reinforced concrete (RC) structures due to their superior behaviour in terms of corrosion resistance, electrical and magnetic non-conductivity, and high strength-to-weight ratio. The promising characteristics of FRP materials have motivated many researchers to investigate different aspects of FRP-RC elements, mainly focusing on the performance of individual elements such as beams and columns under monotonic loading (Brown and Bartholimew 1993; Paramanantham 1993; Alsayed et al. 1999; Shehata et al. 2000; Choo et al. 2006; El-Sayed et al. 2007). Recently, the focus shifted to the integral behaviour of FRP-RC structures when two or more structural elements interact with each other such as beam-column joints and slab-column connections (Said and Nehdi 2004; Mady et al. 2011; Hasaballa et al. 2011; Sharbatdar et al. 2011; Dulude at al. 2013; Hassan et al. 2015; Hasaballa and El-Salakawy 2016; Ghomi and El-Salakawy 2016; El-Gendy and El-Salakawy 2016; Hassan at al. 2017).

The fundamental difference in the mechanical characteristics of FRP materials and steel necessitates the reinvestigation of structural performance of FRP-RC structures in various aspects. The inherent linear-elastic nature of FRP reinforcement results in lack of ductility, which is one of the key characteristics of steel reinforcement in the design methodology for RC elements. Moreover, the variation in mechanical properties of different FRP products in terms of ultimate strength, modulus of elasticity, bond-to-concrete characteristics and durability must be taken into account in the design of FRP-RC members.

Due to the lack of ductility, one of the aspects of the structural performance of FRP-RC structures, which needs a particular attention, is their performance under earthquake-induced loads. The seismic design methodology in the current building codes and guidelines has been developed based on the mechanical characteristics of ductile steel reinforcement and introduced seismic characteristics such as energy dissipation, deformability and redistribution of forces that needs to be addressed in the seismic design of non-ductile FRP-RC buildings.

In order to evaluate the seismic performance of FRP-RC buildings (frames), understanding the behaviour of beam-column joints, as key elements in stability of frames, under lateral loading is essential. Some pioneer studies (Fukuyama et al. 1995; Said and Nehdi 2004; Sharbatdar and Saatcioglou 2009; Mady et al. 2011; Hasaballa and El-Salakawy 2011; Sharbartdar et al. 2011; Tavassoli et al. 2015; Ghomi and El-Salakawy 2016) have investigated the feasibility of using FRP reinforcement in concrete frames prone to seismic loadings. The findings indicated that properly designed FRP-RC beam-columns are capable of withstanding significant lateral deformations under reversal lateral loadings. Researchers, especially, introduced Glass FRP (GFRP) as a suitable option among various FRP materials for seismic design (Hasaballa and El-Salakawy 2011; Ghomi and El-Salakawy 2016). The relatively high tensile strength of GFRP reinforcement (1,100 MPa) combined with its relatively low modulus of elasticity (60 GPa) allows GFRP-RC elements to withstand large deformations, defined as "deformability" of GFRP-RC elements.

Moreover, experiments on the performance of GFRP-RC beam-columns under reversal loadings, indicated that these elements are capable of withstanding significant lateral displacements as high as 5% inter-story drift ratios, while maintaining their linear nature to an acceptable degree without exhibiting a significant residual damage. This feature could potentially present GFRP materials as an effective solution to eliminate the drastic damage caused by plastic deformation of steel-RC

elements. Damage to steel-RC structures after an earthquake can cause costly rehabilitation or even, in some cases, the demolition of the whole structure. Therefore, using FRP-RC frames in seismic regions not only is feasible, but also can be a new approach toward earthquake-resistant structures since the frame can withstand several severe ground shakings without a significant residual damage.

However, to take advantage of this potential, the seismic behaviour of GFRP-RC elements in buildings and any influencing parameters must be fully understood. Up to date, only a few researchers studied the effect of various parameters such as joint shear stress, presence of lateral beams, concrete strength and column axial load on the seismic performance of GFRP-RC beam-columns (Mady et al. 2011; Hasaballa and El-Salakawy 2011; Ghomi and El-Salakawy 2016). However, the number of studies carried out in this area is still very few and many aspects of the seismic behaviour of FRP-RC elements are still uncovered.

Moreover, despite the satisfactory performance of FRP-RC beam-column joints in terms of linearity and residual damage, these elements still show low initial stiffness and lack of energy dissipation which are two of the key features in the design of earthquake-resistant structures. Although the deformability of GFRP-RC elements prevents their brittle failure during an earthquake and their linearity minimizes the cost of repair (after survival), the ability of GFRP-RC frames to solely withstand the lateral loads in a building needs to be enhanced. Without the necessary enhancements, GFRP-RC frames, may not be capable of withstanding high-demand lateral loads (moment-resisting frames) and should be used in conjunction with other lateral load-resisting systems (i.e. shear walls or steel-RC and GFRP-RC hybrid frames).

One of the ideas introduced in this program is to increase the initial stiffness and improve energy dissipation feature of GFRP-RC beam-column joints by externally attaching bolted steel side plates to GFRP-RC beams. The focus is to improve the seismic performance feature of the elements (energy dissipation and lateral stiffness) while maintaining the linear nature of FRP-RC joints.

1.2 Problem Definition

A solid understanding of seismic performance of FRP-RC frames can pave the way for more implementation of these materials in the construction industry. Despite the promising results of previous studies, there are still many parameters, which are known to affect the seismic performance of FRP-RC beam-column joints that have not been explored yet. One of these parameters is the geometrical configuration of the joints. All previous studies on FRP-RC beam-columns focused only on exterior joints (where, at least, one side of the column is not confined by beams). However, a proper design of FRP-RC moment-resisting frames to withstand lateral loads is not possible unless a solid understanding of the behaviour of all types of beam-column connections in the frame, including interior connections (having beams on all four sides of the column), is achieved. In an RC frame, interior beam-column joints are usually the most frequent type of connections. However, up to date, no research data is available on the seismic performance of this type of FRP-RC beam-column connections.

Moreover, although the Canadian code for design of FRP-RC structures (CSA 2012), in Chapter 12, provides the amount of transverse reinforcement required to confine an FRP-RC column subjected to seismic loading, it does not indicate the shear capacity of beam-column joints constructed according to this provision. Ghomi and El-Salakawy (2016) and Hasaballa and El-

Salakawy (2016) studied the shear capacity of various configurations of exterior beam-column joints; however, the capacity of interior joints has not been investigated yet.

Another gap in the available literature for the seismic behaviour of FRP-RC beam-columns is the effect of cast-in situ slabs. Test results from studies on steel-RC frames (Ehsani and Wight 1985-b; Pantazopoulou et al. 1988; Zerbe and Durrani 1990; Ning et al. 2014) have established that presence of slabs can affect stiffness and energy dissipation of RC frames. Moreover, contribution of the effective width of slabs as a flange for beams can change the column-to-beam flexural strength ratio. This issue must not be ignored since it can change structures' mode of failure from desirable "strong column-weak beam" mode to unstable "strong beam-weak column" mode. Up to date, none of the previous studies included slabs in testing of FRP-RC beam-column specimens. Therefore, it seems necessary to study the effect of monolithically cast slabs on the seismic behaviour of FRP-RC frames and determine the effective slab width that contributes to the moment resistance of main beams.

As mentioned, low energy dissipation is known as the main shortcoming of FRP-RC moment-resisting frames in seismic regions. To compensate for low energy dissipation, designers can use conjugated lateral load resisting systems in FRP-RC frames. Examples of that approach can be using shear walls or hybrid system frames (using FRP-RC elements only in exposed parts of the frame that have direct contact with harsh environment while the core of the frame is reinforced with steel). However, a solution to improve energy dissipation of FRP-RC elements, which seems the only reason for holding back FRP-RC moment-resisting frames from being eligible for solely resisting lateral seismic loads, hasn't been introduced yet. In this program, a mechanism for improving energy dissipation and initial stiffness of FRP-RC beam-column joint assemblies is proposed and evaluated through testing.

Although the linear nature of GFRP-RC elements could significantly lower the residual damage due to a seismic event the service and ultimate performance of a GFRP-RC moment-resisting frame, after an earthquake, has to be determined to assess the ability of the structure to remain in service. Therefore, the magnitude of damage and its effect on GFRP-RC moment frames, under reversed-cyclic loading must be investigated. However, up to date, no research data is available on the effect of reversal loadings on the magnitude of damage and deterioration of ultimate and service performance of FRP-RC beam-columns. This program aims to address this gap by investigating the effect of concrete damage on the performance of GFRP-RC beam-columns in terms of lateral stiffness and energy dissipation.

1.3 Research Objectives

The main objectives of this program are divided in three main groups as follows:

- Seismic behaviour of interior GFRP-RC beam-column joints:
    - To investigate a safe joint shear capacity of interior GFRP-RC beam-column joints;
    - To investigate the performance of interior GFRP-RC beam-column joints under seismic loading and compare with corresponding steel-RC connections in terms of lateral load carrying capacity, maximum lateral drift capacity, energy dissipation, cracking pattern and mode of failure;
    - To investigate the effect of reversal loadings on deterioration of service and ultimate performance of interior GFRP-RC beam-columns joints.
- Effect of slabs on the seismic behaviour of GFRP-RC beam-column joints:

  - To investigate the effect of cast-in situ slabs on the seismic performance of GFRP-RC beam-column joints and comparison with steel-RC counterparts;
  - To determine the effective width of GFRP-RC slabs contributing in beams moment resistance in interior and exterior joints with and without lateral beams;
  - To investigate the effect of multiple seismic events on the performance of GFRP-RC beam-column-slab subassemblies.

- Improving energy dissipation feature of GFRP-RC beam-column joints:
  - To investigate feasibility of using bolted steel side-plates to increase the initial stiffness and improve energy dissipation of GFRP-RC beam-column joints;
  - To propose a methodology for the seismic design of GFRP-RC beam-columns with steel side plates.

1.4 Scope of Work

Among various types of FRP reinforcing materials, GFRP is the most attractive for the construction industry because of its lower cost in comparison to the other main alternatives, carbon FRP and aramid FRP. Moreover, due to the relatively large strain at failure, deformability of GFRP-RC elements is especially favorable in the case of seismic performance. Consequently, in this program, GFRP bars and stirrups were used as the reinforcing materials.

Two types of beam-column joints were tested in this program, interior and exterior (edge). All interior beam-column joints were cast with lateral beams (with or without slabs) while two configurations of exterior joints, with and without lateral beams, were tested. Neither corner nor knee connections are in the scope of this program. All specimens had continuous columns and were tested while the columns were under constant axial load equal to approximately 15% of their

maximum concentric axial capacity. The specimens were isolated at the assumed points of contra-flexural, at mid-height of the columns and mid-span of the beams.

1.5 Work Methodology

This research program consists of both analytical and experimental phases. In the experimental phase, nine (9) full-scale beam-column assemblies (with or without slabs) and three (3) full-scale cantilever beams were constructed and tested under quasi-static cyclic loading. Properties of all test specimens are summarized in Appendix C.

To investigate the effect of concrete damage on the performance of GFRP-RC frames at ultimate and service states, the specimens were tested under two loading stages. In the first stage, a loading scheme that simulated a severe earthquake up to 5% drift ratio (defined as the ratio of the loading point displacement over the length of the element) was applied to the specimens. Then, the specimens were re-loaded up to failure following the same loading scheme in the second loading stage. The RC cantilever beams were tested to study the effectiveness of the proposed bolted steel side-plate system on enhancing energy dissipation and initial stiffness of beam-column joints.

In the experimental phase, the effect of various parameters on the seismic behaviour of GFRP-RC beam-column and beam-column-slab connections were investigated. These parameters included: reinforcement type (steel or GFRP), level of applied joint shear stress in interior beam-column joints with lateral beams, presence of slab in interior and exterior beam-column joints with and without lateral beams and presence of bolted steel side-plates to enhance energy dissipation of GFRP-RC beam-column joints.

In the analytical phase a specialized finite element modeling (FEM) program, ATEANA 3D (Cervenka et al. 2012), was used to simulate the seismic behaviour of FRP-RC beam-column

joints. Test results obtained from this program and those obtained from a previous study by the authors (Ghomi and El-Salakawy 2016), were integrated to validate and calibrate the models. The validated models were used to run parametric studies to investigate the effect of a wide range of various parameters including reinforcing materials, concrete strength, column axial load, slab width and size of lateral beams.

In addition, the nonlinear dynamic response of GFRP-RC moment resisting frames under an imposed ground acceleration was simulated using SAP2000 software. The effect of presence of cast-in situ slabs and type of reinforcement (steel and GFRP) was studied.

Moreover, a numerical method based on moment-curvature determination was used to investigate the maximum bending moment capacity of the GFRP-RC beams with bolted steel side-plates. The moment-curvature diagrams were generated by a computer program using the commercial software MATLAB.

1.6 Dissertation Layout

This thesis consists of nine (9) chapters as follows:

- Chapter 1: provides a brief introduction to the topic of the thesis and introduces the objectives of the research program, scope of the work and work methodology.
- Chapter 2: summarizes the available literature to identify the key influencing parameters on the seismic behaviour of beam-column connections and to establish an understanding of the load transfer mechanisms. Moreover, a brief summary of the main characteristics and properties of FRP materials, used as internal reinforcement in the construction industry, is provided.

The subsequent six (6) chapters correspond to six technical papers that have been either published or submitted for publication in scientific journals as described below. Each paper focusses on specific key parameter(s).

- Chapter 3 (1st article, published): Ghomi, S.K. and El-Salakawy, E. (2019). "Effect of Joint Shear Stress on Seismic Behaviour of Interior GFRP-Reinforced Concrete Beam-Column Joints". Journal of Engineering Structures, V.191, pp. 583-597.

  This chapter presents the results obtained from testing of four (4) full-scale interior beam-column joints under multiple reversed-cyclic loads. The main test parameters were joint shear stress ratio and type of reinforcement (steel or GFRP). The performance of the specimens was evaluated in terms of hysteresis diagrams, mode of failure, strains in the reinforcement and energy dissipations.

- Chapter 4 (2nd article, submitted): Ghomi, S.K. and El-Salakawy, E. "Effect of Geometrical Configuration on Seismic Behaviour of GFRP-Reinforced Concrete Beam-Column Joints." International Journal of Earthquake and Structures, Submitted in May 2019.

  This chapter provides a comparison between the seismic behaviour of GFRP-RC interior and exterior beam-column joints. The behaviour of three (3) full-scale beam-column joints are discussed. The specimens consist of two beam-columns constructed and tested in the current program and one extracted from a previous study by Ghomi and El-Salakawy (2016). The effect of joint shear stress on the performance of exterior beam-columns was investigated. The effect of concrete damage due to earthquake loading on the performance of beam-column joints under service and ultimate loading was studied and a modified

damage index was proposed to quantify the magnitude of damage in GFRP-RC beam-column joints under dynamic loading.

- Chapter 5 (3rd article, published): Ghomi, S.K. and El-Salakawy, E. (2018). "Seismic Behavior of Exterior GFRP-RC Beam-Column Connections: Analytical Study". ASCE, Journal of Composites for Construction, 22(4): 04018022, DOI: 10.1061/(ASCE)CC.1943-5614.0000858.

  This chapter presents an analytical study on the effect of various parameters on the seismic behaviour of beam-column joints. A specialized FEM software, ATENA 3D (Cervenka et al. 2012), was used to construct a nonlinear model, capable of simulating the hysteresis behaviour of RC beam-column joints under seismic loads. The nonlinear models were validated against the experimental results obtained by Ghomi and El-Salakawy (2016). The models were constructed by taking into account the effect of nonlinearity of concrete material, confinement provided by the internal reinforcement, cracks and bond-slip relationship between the reinforcing bars and surrounding concrete. The models were used to investigate the effect of joint shear stress, size of lateral beams, reinforcing material, column axial load and geometrical configuration on the performance of beam-column connections.

- Chapter 6 (4th article, published): Ghomi, S.K. and El-Salakawy, E. (2019). "Seismic Behaviour of GFRP-RC Interior Beam-Column-Slab Subassemblies." ASCE Journal of Composites for Construction, 23(6): 04019047, DOI: 10.1061/(ASCE)CC.1943-5614.0000980.

This chapter reports an experimental and analytical study on the seismic behaviour of GFRP-RC interior beam-column-slab connections. Three full-scale subassemblies, one beam-column and two beam-column-slabs, were constructed and tested to failure under reversal quasi-static cyclic loading. The main test parameters were the presence of slabs and type of reinforcement (steel and GFRP). Moreover, a series of FEMs were developed and used to investigate the effect of slab width and lateral beam size on the contribution of slabs.

- Chapter 7 (5^{th} article, submitted): Ghomi, S.K. and El-Salakawy, E. "Seismic Behavior of GFRP-RC Exterior Beam-Column-Slab Connections." ACI Structural Journal, Submitted in March 2019.

  This chapter presents a study on the seismic behaviour of GFRP-RC exterior beam-column-slab connections. Two full-scale GFRP-RC exterior beam-column-slabs were tested under reversed-cyclic loads to investigate their performance with a focus on the effect of lateral beams on the effective slab width. The results were compared with two previously tested beam-column specimens by Ghomi and El-Salakawy (2016), and Hasaballa and El-Salakawy (2016). Moreover, a series of FEMs were constructed to determine the influence of lateral beams size and slab thickness on the contribution of slabs.

- Chapter 8 (6^{th} article, published online): Ghomi, S.K. and El-Salakawy, E.F. (2019). "Seismic Performance Improvement of GFRP-RC Structures." Canadian Journal of Civil Engineering, DOI: 10.1139/cjce-2019-0274.

  This chapter presents a research study on seismic performance improvement of GFRP-RC moment-resisting frames. In this research, adding bolted steel side-plates at selected

locations in moment-resisting frames is proposed as a solution to improve seismic performance of FRP-RC structures. Three full-scale cantilever beams, one steel-RC, one FRP-RC and one FRP-RC with proposed steel plates were constructed and tested under reversed-cyclic loads. Moreover, a computer simulation, using moment-curvature determination process, was conducted to calculate bending moment capacity of FRP-RC beams with bolted steel side plates.

- Chapter 9: provides a summary of the research program and the main conclusions drawn from the experimental and analytical studies, as well as recommendations for future works on the topic.

2 LITERATURE REVIEW

2.1 Introduction

During past decades many studies have been conducted to investigate the behaviour of FRP-RC structural elements. The majority of these studies focused on the behaviour of individual elements under monolithic loads. However, recently, the seismic performance of FRP-RC structures has attracted some attentions (Fukuyama et al. 1995; Sharbatdar and Saatcioglu 2009; Mady 2011; Sharbatdar et al. 2011; Hasaballa and El-Salakawy 2011; Tavassoli et al. 2015; Mohamed et al. 2015; Hasaballa and El-Salakawy 2016; Ghomi and El-Salakawy 2016; Maranan et al. 2017).

One of the most influencing elements in the seismic behaviour of any RC frame is its beam-column connections. These elements are the path of load transitions from beams to columns; therefore, their performance in seismic events has significant effect on the stability of the whole frame. In seismic design, the main philosophy in proportioning beam-column joints is to ensure that the capacity of these elements remains higher than all the adjoining beams and columns. Up to date, the studies on seismic performance of FRP-RC beam-column joints are very few with many aspects still uncovered.

2.2 Key Influencing Parameters for Shear Behaviour of Steel-RC Joints

While the seismic behaviour of FRP-RC beam-column connections is a new subject, the performance of steel-RC joints in earthquakes has been studied extensively since 1960s. The significant amount of literature in this area provides essential understanding of the key parameters and the load transfer mechanisms in beam-column joints during an earthquake. This information helps to understand the effect of reinforcement type and layout on the performance of a beam-

column joint and any differences in the seismic behaviour that should be expected from FRP-RC joints. The following section provides a summary of the influencing parameters on the behaviour of steel-RC beam-column joints.

2.2.1 Effect of joint shear stress

Le-Trung et al. (2013) selected a total of 112 RC beam-column joint specimens of either special moment frame (SMF) or intermediate moment frame (IMF) available in the literature to investigate some of the seismic performance criteria. Among the selected specimens, 38 were qualified as SMF, which is the focus of this study, according to ACI 318-08 requirements (ACI Committee 318 2008). The effect of different parameters such as joint shear stress and column-to-beam flexural strength ratio on the performance of RC beam-column joints with various configurations (exterior or interior with or without lateral beams) has been investigated.

The authors defined the ratio of the resisting moment of the specimens at 3% lateral drift ratio to its nominal moment resistance ($M_{0.03}/M_n$) as a performance criterion. According to this criterion, performance of the specimens with the ratio of $M_{0.03}/M_n$ higher than 1 are considered as satisfactory. In other words, steel-RC beam-column joints in a special moment frame should be able to maintain their maximum capacity up to 3% lateral drift ratio.

Analyzing test results of the selected specimens showed that, in general, performance of the specimens deteriorates as the joint shear stress increases. High shear stresses accelerate the rate of damage in the joint which can cause early pullout of the longitudinal bars in beams and slippage of the reinforcement in columns. This significantly affects the load-carrying capacity of beam-column connections.

Test results indicated that the specimens with lateral beams exhibit better performance (higher $M_{0.03}/M_n$ ratio) in comparison to those without lateral beams. This was attributed to the joint confinement provided by lateral beams. The effect of lateral beams was more pronounced in the case of interior beam-column joints.

Ehsani and Wight (1985-a) tested six full-scale exterior beam-column joints under seismic loading to study the effect of various parameters on their behaviour. The test specimens had joint shear stresses ranging from $0.73\sqrt{f'_c}\,MPa$ to $1.27\sqrt{f'_c}\,MPa$. Based on the test results, the authors suggested limiting the maximum shear stress to $1.0\sqrt{f'_c}\,MPa$ to limit the pullout of the bars in the main beam and slippage of the bars in the column. However, it should be mentioned that the test results also showed that even the specimens with minor bar slippage at higher loading stages showed satisfactory behaviour. As a result, to some extent, the bar slippage and pullout can be tolerated.

2.2.2 Role of lateral beams and cast-in situ slabs

Ning et al. (2014) tested 2 two-third-scale spatial RC frames, one with (RC-1) and one without slabs (RC-2), under reversal cyclic loading to study the effect of cast-in situ slab on the seismic behaviour of RC frames. The performance of the two specimens was compared in terms of hysteresis diagram, energy dissipation, stiffness degradation, and lateral load-displacement envelop as follows.

The general shape of the hysteresis diagram was identical in both specimens as they showed linear behaviour prior to yielding of the reinforcement and, consequently, absorbed relatively small

amount of seismic energy. After yielding of the reinforcement, the amount of energy dissipation significantly increased in the specimens with the increase in the lateral displacement.

However, the hysteresis loops of the specimen with slabs enclosed larger areas, which indicates higher energy dissipation. The difference in the magnitude of energy dissipation of the specimens was small at the beginning, while it became more pronounced as the lateral displacement increased. At lateral drift ratio of 4.2%, RC-2 dissipated 30.4% more energy than RC-1.

Lateral stiffness degradation of the specimens was also compared. In both specimens the rate of degradation decreased as the lateral displacement increased. However, the rate of degradation was higher in the specimen with slabs. Although the presence of the slab provided significantly higher initial stiffness to RC-2, due to higher rate of stiffness degradation, both specimens reached approximately the same values of lateral stiffness at 2% lateral drift ratio. The stiffness of the specimens remained approximately the same after that point.

Lateral load-displacement envelops of the specimens had generally an identical shape. For both specimens, the graph consisted of three main parts: 1) linear elastic part, 2) flat elastic-plastic part, and 3) declined part after the peak load. Specimen RC-2 showed higher load capacity, which was expected due to presence of the slabs. Moreover, the load capacity degradation after reaching the peak load was more gradual in the specimen with slabs. However, due to the contribution of the slabs to the flexural capacity of the beams, the mode of failure in the frame with slabs (RC-2) changed to strong beam-weak column, which resulted in a brittle failure.

Measuring the tensile strain in the longitudinal bars of the slabs indicated that the geometrical configuration of joints (exterior or interior joint) can affect the strain distribution in slabs. According to the results, strains in the bars near exterior joints were higher than those adjacent to

interior joints at the ultimate stage. Moreover, occurrence of torsional cracks in lateral beams at exterior joints reduced the strains in the longitudinal reinforcement of slabs.

Based on 86 beam-column joints selected from available literature, Bonacci and Pantazopoulou (1993) performed a parametric study to investigate the influence of various parameters on the behaviour of beam-column joints. One of the studied parameters was the presence of lateral beams in interior beam-column joints. The effect of confinement provided by lateral beams on the mode of failure of interior beam-column connections was examined. Three possible geometrical configurations were considered: 1) no lateral beams, 2) one lateral beam on one side of the joint, and 3) two lateral beams on each side of the joint.

Failure due to excessive joint shear stress was observed widely in the specimens without lateral beams. In addition, joint shear failure was observed in only a few specimens with one lateral beam; however, to a smaller extent compared to those without lateral beams. In specimens with two lateral beams (having confinement on all four faces of the joint), there was no case of joint shear failure and all specimens failed due to development of plastic hinge in the beam.

The authors concluded that presence of lateral beams can improve the performance of beam-column connections by providing more confinement to the joint by their longitudinal reinforcement passing through the joint, as well as increasing the volume of concrete affecting the joint shear-resistance mechanism.

Ehsani and Wight (1985-b) performed an experimental program to study the effect of lateral beams and slabs on the behaviour of exterior beam-columns. Six full-scale beam-column assemblies were constructed with similar design parameters as the authors' earlier study (Ehsani and Wight 1985-a).

Comparing the hysteresis diagrams of the specimens with lateral beams and slabs with their counterparts (without lateral confinement), the most significant difference was the un-symmetric behaviour of the specimens with lateral beams and slab. When the columns in these specimens were loaded in the pushing direction the top bars in the main beam and the longitudinal reinforcement in the slab were in tension, while in the pulling direction only bars at the bottom of the main beam were in tension. This resulted in unequal stiffness (yield displacement) for each loading direction. Contrary to the test results of the study by Ning et al. (2014), in the study by Ehsani and Wight (1985-b) the specimens with lateral beams and slab showed lower stiffness degradation. The authors attributed this observation to the confinement provided by the lateral beams. Sufficient confinement of the joints with lateral beams led to fewer shear cracks, which, consequently, helped in reducing bar slippage or/and pullout.

Moreover, the test results indicated that the influence of various parameters can be affected due to presence of lateral beams. For example, although increasing transverse reinforcement in the specimens without lateral beams resulted in a significant improvement in the performance of the joint, the specimens with lateral beams and slabs did not show any significant strength improvement due to increasing transverse reinforcement. The authors argued that since the lateral beams already provide sufficient confinement, increasing the joint shear reinforcement has less pronounced influence on improvement of the behaviour.

Similarly, the effect of joint shear stress on the performance of beam-column joints was less pronounced in the joints with lateral beams and slabs. The authors' explanation for this observation was the increase in the effective concrete area resisting the shear stresses. For example, some of the longitudinal bars in the slab, included in calculating the joint shear stress, were actually anchored into the lateral beams. Therefore, a portion of the assumed joint shear stress demand was,

in fact, resisted by lateral beams, thus the actual shear stress resisted by the joint area was less than the initial estimations.

2.2.3 Effective slab width

Ning et al. (2014) used equivalent strain method to calculate the effective slab width contributing to the bending moment resistance of beams. Based on reinforcement stresses obtained from their test results, the effective slab width was calculated as:

$$b_{ef} = \frac{\sum_{i=1}^{n}\left[\frac{1}{2}\left(\sigma_{ssi-top} + \sigma_{ss(i+1)-top}\right)s + \frac{1}{2}\left(\sigma_{ssi-bot} + \sigma_{ss(i+1)-bot}\right)s\right]}{2f_{ys}} + b$$

where $\sigma_{ssi-top}$ and $\sigma_{ssi-bot}$ are the tensile stresses of the *i*th longitudinal bar in the slab at top and bottom, respectively; s is the spacing of the slab reinforcement; f_{ys} is the yield stress of the slab reinforcement.

The authors compared the calculated effective width with four other suggested formulas from the available literature as follows:

- For interior beam-column joints:

  $b_{ef} = b_{beam} + 4h_{beam}$ (Pantazopoulou et al. 1988 ; Zerbe and Durrani 1990)

  $b_{ef} = b_{beam} + 8h_{slab}$ (Paulay and Park 1984)

- For exterior beam-column joints:

  $b_{ef} = b_{beam} + 2h_{beam}$ (Zerbe and Durrani 1990; Ehsani and Wight 1985-b)

  $b_{ef} = b_{beam} + 4h_{slab}$ (Paulay and Park 1984)

The authors concluded that the equation proposed by Ehsani and Wight (1985-b), and Paulay and Park (1984) predict shorter effective widths than the observed values from the test results, while the width proposed by Pantazopolou et al. (1988) is longer than the measured effective widths. However, the test results were in good agreement with effective widths calculated based on the equation proposed by zerbe and Durrani (1990). Based on the test results, the authors suggested the following effective width for interior and exterior beam-column joints with transverse beams.

$$b_{ef} = b_{main\ beam} + 3.2h_{transvers\ beam}$$ at 2.0% drift ratio

$$b_{ef} = b_{main\ beam} + 3.4h_{transvers\ beam}$$ at 4.2% drift ratio

2.3 FRP Bars as Reinforcement for Concrete Structures

There are several applications for FRP composites in structural engineering. These materials can be employed either in the construction of new structures or in strengthening, repairing, and rehabilitating of existing structures. In this program, the focus is on new concrete structures reinforced with FRP reinforcement in the form of bars and stirrups.

FRP reinforcement has been introduced as an effective alternative for conventional steel reinforcement mainly because of its non-corrodible characteristics. Corrosion of steel reinforcement in concrete structures exposed to extremely harsh environment has been always a serious problem and designing, maintaining, and repairing of such structures has been a challenging and extremely costly procedure. In such cases replacing steel with FRP reinforcement has been a successful treatment proved by academic tests and real applications.

In addition to the corrosion resistance characteristics, FRP materials:

- have high strength-to-weight ratio;

- are not magnetic and electric conductors;
- have customizable properties;
- have low density; and
- have excellent long-term durability.

However, FRP materials possess different mechanical and chemical properties compared to those of conventional steel reinforcement, which could affect the structural performance of concrete elements reinforced with these materials. Therefore, a solid understanding of the characteristics of FRP materials is essential for their effective applications. The following section introduces the main mechanical and chemical features of the most common FRP materials in civil engineering.

2.3.1 FRP characteristics

FRPs are generally composite of two materials, fiber and resin. Although there are several types of fibers, in the construction industry the choice of fibers has been mainly limited to carbon, aramid, and glass. Fibre is the component that provides strength and stiffness of the composite while the resin binds the fibers together and protects them against ambient condition. Resin is a thermoset polymer which is mixed with fibers at a certain temperature and forms the final product after curing. Polyester, vinyl-ester, and epoxy are the most common resins in the construction filed (ISIS Canada 2007).

The choice of fibre and resin is based on their chemical and mechanical characteristics and desire properties of the final product. However, since the construction industry usually involves high amount of material consumption the need for maintaining a low cost is essential. On that base, glass fibres seem to be more attractive to this industry in comparison with carbon and aramid.

In the following sections some of the mechanical characteristics of Glass, Carbon, and Aramid FRP are provided.

2.3.2 Density

Density of FRP bars ranges from 1250 to 2100 kg/m^3 , which is 4- to 6-times lower than that of steel (ACI Committee 440 2015). Lower density of FRP bars reduces the transportation costs and makes them easier to handle at the job site. Since density of normal weight concrete is 2400 kg/m^3 it has been argued that lower density of FRP reinforcement compared to that of concrete can cause floating issues. Therefore, it is suggested to adequately tie down the FRP reinforcing cages to formwork to prevent any possible floating during concrete pouring and vibration (ISIS Canada 2007). However, no floating issue has been reported in any of the previous studies. Table 2.1 shows typical density of reinforcing bars.

Table 2.1 - Typical density of FRP reinforcement (ACI Committee 440 2015)

Type	Steel	GFRP	CFRP	AFRP
Density $\left({}^{kg}/_{m^3}\right)$	7900	1250 - 2100	1500 - 1600	1250 - 1400

2.3.3 Stress-strain relationship

FRP bars have a linear elastic behaviour up to failure due to the linear stress-strain relationship of the fibers. FRP bars generally offer higher tensile strength than that of steel while their ultimate strain capacity is typically lower (no yielding). Table 2.2 shows some typical values for modulus of elasticity of FRP bars (ACI Committee 440 2015; Pultrall Inc. 2019).

Since the fibers can carry loads only in their own direction, FRP bars have unidirectional behaviour. The behaviour of FRP bars in transverse direction is mostly influenced by the matrix,

therefore, FRP bars are generally weak in transverse direction (ACI Committee 440 2015). Moreover, FRP bars have lower strength in compression than tension due to micro buckling of fibers inside the matrix (Wu 1990). A typical decrease in compressive strength up to 55%, 78%, and 20% of the tensile strength is expected for Glass, Carbon, and Aramid FRPs, respectively (Wu 1990; Mallick 1988).

Table 2.2 - Typical properties of FRP reinforcement

Type	Typical Steel	GFRP	CFRP	AFRP
Modulus of Elasticity (GPa)	200	35-70	100-600	40-125
Tensile Strength (MPa)	400 to 500	450-1600	600-3700	1700-2500

2.3.4 Bond

Bonding-to-concrete behaviour of FRP bars is a function of the manufacturing process, mechanical properties, and environmental conditions (Al-Dulaijan 1996; Nanni et al. 1997; Bakis et al. 1998; Bank et al. 1998). The bond stress can be transferred between the bar and the surrounding concrete by (ISIS Canada 2007):

- chemical bond (adhesion resistance of the interface);
- friction resistance against slip;
- Mechanical bond interlock due to irregularity of the bar interface.

In FRP bars, bond shear stress is transferred to fibers by resin; consequently, the bond strength is limited by the matrix strength (ACI Committee 440 2015). Moreover, it has been reported that in FRP bars that do not rely on the bearing resistance of ribs (in deformed bars) the bond strength of FRP bars does not depend on the compressive strength of concrete (Benmokrane et al. 1996; Cosenza et al. 1997).

2.3.5 Bending FRP bars

Except for FRP bars with thermoplastic resins, FRPs cannot be bent or reshaped after manufacturing. The deformation required for producing stirrups or bent bars should be done during the manufacturing process; however, a strength reduction of 40% to 50%, relative to the tensile strength of a straight bar, is expected at the bent portion. Even the straight portion of a bent bar has lower strength than a straight bar without any bent (Pultrall Inc. 2019).

2.3.6 Durability of FRP reinforcing bars

Some concerns have been addressed regarding the long-term performance of GFRP reinforcement in high alkalinity environment such as concrete (Porter and Barnes 1998). The strength of both glass fibers and resin can decrease when exposed to such environments. Many researchers use accelerated aging process under simulated service condition to investigate the durability of GFRP reinforcement in RC structures. Damage to GFRP reinforcement embedded in concrete can be due to:

- Chemical attack to the glass fibers by the alkaline environment; and
- Growth of concrete hydration products between individual filaments.

However, later investigations (Robert et al. 2009; Debaiky et al. 2006) illustrated that laboratory tests under accelerated aging process may not properly represent the actual service life environment of GFRP bars. In many cases, simulated test environment was much more severe than the actual service environment. In order to investigate the performance of FRP reinforcing bars under service environment, ISIS Canada (ISIS Canada 2007) performed a field evaluation of existing GFRP-RC structures in Canada. The structures were aged between 5 to 8 years at the time of evaluation. The evaluations identified no visible degradation of reinforcement. This study

supports the main motivation for replacing steel reinforcement by FRP materials and concludes that FRP bars are non-corrosive, durable under harsh environment and highly compatible with concrete.

2.4 Feasibility of Using FRP-RC Beam-Column Joints in Seismic Regions

During the past decades, many experimental programs have been conducted to study various concrete elements reinforced with FRP materials. These programs mostly involved investigating the behaviour of individual FRP-RC members such as simply supported beams, slabs and columns, while the number of studies on the integral performance of FRP-RC framed structures, especially those subjected to seismic loadings, are still very few.

The lack of ductile behaviour of FRP-RC elements, because of the linear elastic nature of FRP reinforcement, causes a significantly different damping and energy dissipation characteristics for FRP-RC structures compared to their steel-RC counterparts.

The magnitude of energy dissipation is one of the main influencing parameters in a satisfactory seismic performance of an RC frame. The amount of energy consumption is represented by the area enclosed by the lateral load-displacement graph of a structural element. Steel-RC structures mainly show desirable ductility and energy dissipation due to yielding of the steel reinforcement. This phenomenon; however, is not applicable to FRP materials, which behave in a linear-elastic manner up to failure. However, the FRP materials with relatively low modulus of elasticity and high tensile strength (compared to those of steel), can undergo high tensile strains prior to failure. This feature verifies the feasibility of using FRP-RC structures in seismic regions by enabling them to withstand significant lateral deformations during an earthquake (Hasaballa and El-Salakawy 2016; Ghomi and El-Salakawy 2016).

The following section provides a brief review of the studies on feasibility of using FRP-RC beam-column joints in seismic regions.

Fukuyama et al. (1995) investigated the possibility of using Aramid FRP (AFRP) materials as longitudinal and transverse reinforcement in concrete structures that should resist significant lateral loads. An experimental study was conducted on the seismic behaviour of a half-scale three-storey concrete frame. Structural performance of the frame was compared with an analytically-modeled frame with the same dimensions but reinforced with conventional steel.

The beams in the frame were reinforced with a ratio of 0.64% and 0.48% for positive and negative moment, respectively. The columns had a constant ratio of 1.47% in all stories. To reduce the number of affecting parameters no hooks or lap splices were used for the main reinforcement.

According to the test results, the behaviour of the structure was divided into three stages:

- Drift ratios less than 0.5 %: elastic range before cracking;
- Drift ratios between 0.5 % and 2%: stable plastic behaviour due to growth of cracking in members;
- Drift ratios greater than 2%: unstable performance with major reduction in stiffness due to crushing of concrete.

Results of the experimental and the analytical study proved that it is possible to design FRP-RC members to resist high lateral loads. The frame remained elastic and showed small loop areas in lateral load-angle of rotation diagram until $1/50$ radian rotation, when crushing of the concrete began.

The authors concluded that it is easy to rehabilitate an FRP-RC frame that has undergone major displacements, since residual deformations of the frame remain small. This indicates that limitations for the ultimate deformation can be less stringent for FRP-RC structures compared to those for steel-RC ones.

Said and Nehdi (2004) compared the seismic performance of two full-scale, T-shape beam-column joints, one totally reinforced with GFRP and one totally reinforced with steel. The specimens were identical except for the reinforcement type and configurations. The area of the longitudinal reinforcement in the beam of the GFRP-RC specimen was proportioned to provide the same flexural capacity as the control steel-RC specimen, therefore, the same magnitude of shear stress was applied to the joints. The specimens were tested under reversal cyclic loadings.

As expected, the GFRP-RC beam-column joint showed very low plasticity. This resulted in lower energy dissipation of the GFRP-RC specimen compared to that of the steel-RC counterpart. Moreover, the GFRP-RC beam-column joint showed a lower lateral stiffness than the control specimen due to the lower stiffness of GFRP reinforcement compared to steel (30 GPa vs 200 GPa).

Despite of the lower ultimate drift capacity of the GFRP-RC specimen than that of the control steel-RC, the measured drift capacity of the GFRP-RC specimen was considered satisfactory, according to the minimum required deformability for a ductile frame building recommended by building codes and guidelines (mostly 3%).

Mady et al. (2011) studied the seismic behaviour of exterior beam-column joints reinforced with GFRP bars and stirrups. Several specimens have been tested among which test results of two specimens are discussed here. One prototype totally reinforced with conventional steel

reinforcement and another totally reinforced with GFRP bars and stirrups were tested under reversal lateral quasi-static loading to compare their performance.

The test results showed that GFRP bars and stirrups could be used as a reinforcing material for beam-column joints subjected to seismic loadings. The GFRP-RC specimen was able to reach 4% drift ratio without any significant permanent damage, which indicated that large elastic strain capacity of GFRP materials can compensate part of the deformability (ductile behaviour) of steel reinforcement in seismic regions.

2.5 Performance of FRP-RC Columns

Sharbatdar and Saatcioglu (2009) studied the seismic behaviour of square columns reinforced with CFRP longitudinal bars and CFRP transverse grids. Three specimens were constructed and tested to investigate the effect of column length (1,000 mm and 1,900 mm) and transverse grid spacing (175 mm and 88 mm).

All test specimens were able to reach 2% lateral drift ratio with little strength degradation. It was observed that the column with closely spaced transverse grids (88 mm) was able to ultimately reach 4% lateral drift ratio prior to failure. The failure occurred due to local buckling of fibres in the longitudinal bars under compression. The specimen with wider grid spacing (175 mm); however, exhibited a brittle failure shortly after 2% lateral drift ratio.

The maximum strain recorded in the transverse grids was reported as 0.5% and 0.31% for the specimen with 88 mm and 175 mm grid spacing, respectively. This indicated that the confinement mechanism was not fully developed in the column with widely spaced grids, and negatively influenced the performance of the column.

Tavassoli et al. (2015) studied the performance of circular columns with GFRP longitudinal and transverse (spirals) reinforcement under seismic loads. Nine large-scale specimens were tested under simultaneous axial (constant) and cyclic lateral loads. The performance of the specimens was evaluated in terms of lateral deformability, energy dissipation and strength.

Two levels of concrete axial load, $0.28P_o$ and $0.42P_o$ (where P_o is the nominal axial load capacity of the columns), were considered in the study. The authors reported that, similar to steel-RC columns, increase of axial load results in faster concrete deterioration in GFRP-RC columns, indicated by longer plastic hinge lengths. Moreover, it was stated that higher axial loads could decrease the ductility (deformability) of GFRP-RC columns.

The authors reported that decreasing the spiral pitch (increase in the lateral reinforcement ratio) improves the energy dissipation and deformability feature of the specimens. Closely spaced spirals provide better concrete core confinement, thus improving the performance. However, the effect of the increase in lateral reinforcement ratio was not as pronounced when the ratio was increased by changing the size of spirals instead of decreasing the spiral pitch.

Guerin et al. (2018) performed an experimental study to investigate the effect of longitudinal reinforcement ratio (1%, 1.4% and 2.5%) on the axial-flexural capacity of GFRP-RC columns. Twelve full-scale square columns were constructed and tested under four different levels of eccentricities, ranging from 10 to 80% of the column width.

The authors reported that increasing the longitudinal reinforcement ratio had relatively little effect on the axial capacity of the GFRP-RC columns. However, the effect of reinforcement ratio was more pronounced in specimens with large eccentricity. The authors attributed this behaviour to the different mode of failure of columns with different eccentricity. The columns with small

eccentricity failed due to concrete crushing, where the longitudinal reinforcement ratio had insignificant effect in the magnitude of damage. The columns with large eccentricity, on the other hand, failed due to wide cracks and excessive deformation. Increasing the reinforcement ratio in these cases improved the performance by eliminating the crack widening and reducing the tensile strain in the longitudinal bars.

2.6 Shear Capacity of GFRP-RC Beam-Column Joints

Following the verification of the feasibility of using FRP-RC structures in seismically active regions, more research was deemed necessary to investigate various parameters that can affect the seismic performance of such structures.

Hasaballa and El-Salakawy (2014) performed an experimental study to investigate the shear capacity of exterior T-shape GFRP-RC beam-column joints. The authors used headed-end bars to anchor the longitudinal reinforcement of the main beam inside the joint. As part of the study, three full-scale beam-column joints isolated from assumed points of contra-flexural at mid-height of the columns and mid-span of the beams were constructed and tested. None of the specimens had any out-of-plane members (slabs or lateral beams).

The behaviour of the beam-column joints under three levels of joint shear stress, $0.7\sqrt{f'_c}$ (Specimen II-30-0.7), $0.85\sqrt{f'_c}$ (Specimen II-30-0.85), and $1.0\sqrt{f'_c}$ (Specimen II-30-1.0) was studied by examining the lateral load-drift response, mode of failure, and ultimate capacity of the specimens.

Specimens II-30-0.7 and II-30-0.85 were able to reach their design capacity at 4% drift ratio. Majority of the concrete damage was concentrated at the main beam in Specimen II-30-0.7, while Specimen II-30-0.85 exhibited somewhat simultaneous failure at the beam and the joint.

Specimen II-30-1.0, on the other hand, was not able to reach its design capacity and failed prematurely due to shear failure of the joint. This indicates that $1.0\sqrt{f'_c}$ is beyond the shear capacity of exterior beam-column joints without lateral beams.

However, previous studies on steel-RC beam-columns, have established that existence of lateral beams can increase the shear capacity of beam-column joints. Ghomi and El-Salakawy (2016) studied the effect of presence of lateral beams on the seismic behaviour of exterior beam-column joints reinforced with headed-end GFRP bars. As part of the study, three full-scale beam-column joints with lateral beams were constructed and tested to failure under progressively increasing reversal cyclic loadings in term of lateral displacements (inter-story drift ratios). The specimens were proportioned for joint shear stresses of $0.85\sqrt{f'_c}$ (G-I-L), $1.0\sqrt{f'_c}$ (G-I-M), and $1.1\sqrt{f'_c}$ (G-I-H).

The lateral load-displacement response of the specimens was recorded during the testing procedure. All specimens reached the design capacity at 4% drift ratio. The lateral load carrying of the specimens continued to increase by further increasing the imposed displacements beyond 4% drift ratio.

The specimen with joint shear stress ratio of 0.85 (G-I-L) maintained its load carrying increase up to its failure at 7% drift ratio. The failure was brittle and occurred due to rupture of the longitudinal bars in the main beam. The ratio of the ultimate lateral load over the design capacity was recorded as 1.15 (the maximum-recorded lateral load was 15% higher than the design capacity).

The other two specimens, G-I-M and G-I-H continued the load carrying increase up to the maximum lateral load at 6% drift ratio, where they reached a lateral load equal to 1.2- and 1.15-times the design capacity, respectively. As the imposed lateral displacement increased beyond 6% drift ratio, the lateral load carrying capacity of the specimens gradually decreased. The test was stopped at 9% drift ratio due to significant lateral strength degradation (more than 30%) of the specimens.

Although Specimens G-I-M and G-I-H showed very similar lateral load-displacement response up to 6% drift ratio, because of the higher magnitude of joint shear stress, a higher rate of strength degradation was observed in the descending part of the response of Specimen G-I-H. However, since specimen G-I-H showed stable linear behaviour up to 6% drift ratio and was able to reach its designed capacity, $1.1\sqrt{f'_c}$ was still considered as a safe joint shear stress for exterior beam-column joints with lateral beams.

It should be mentioned that the ultimate drift capacity of the specimens (7% and 9% drift ratio) was significantly higher than the maximum allowable lateral drift suggested by the National Building Code of Canada (NRCC 2015), 2.5%. In all specimens the concrete damage at 3% (> 2.5%) drift ratio, was negligible and limited to minor concrete spalling at the beam-column interface.

3 EFFECT OF JOINT SHEAR STRESS ON SEISMIC BEHAVIOUR OF INTERIOR GFRP-REINFORCED CONCRETE BEAM-COLUMN JOINTS

Shervin K. Ghomi and Ehab El-Salakawy

Journal of Engineering Structures, 2019, V.191, pp. 583-597.

Abstract: Four full-scale specimens were constructed and tested under reversal cyclic loading to study the seismic performance of interior GFRP-RC beam-column joints. The main test parameters were joint shear stress ratio and type of reinforcement (steel or GFRP). The performance of the specimens was evaluated in terms of hysteresis diagrams, mode of failure, strains in the reinforcement and energy dissipations. Test results indicated that the linear nature of GFRP materials resulted in lower residual damage in GFRP-RC beam-column joints compared to the corresponding steel-RC counterparts. Moreover, GFRP-RC joints withstood multiple cyclic loadings up to 8% drift ratio without exhibiting brittle failure.

Keywords: GFRP-RC, Seismic performance, Interior beam-column joints, Glass fibre reinforced, Joint shear stress, Concrete moment-resisting frames, P-delta effect, Hysteresis response, column-to-beam flexural strength ratio.

3.1 Introduction

Fibre reinforced polymers (FRPs) have been established as an alternative for steel reinforcement in concrete structures mainly due to their superior performance in terms of corrosion resistance,

magnetic non-conductivity and higher strength-to-weight ratio. The FRP material possess different mechanical and chemical characteristics compared to conventional steel which can change the performance of reinforce concrete (RC) elements when the reinforcing steel is replaced with FRP. This necessitates to re-investigate various aspects of the behaviour FRP-RC elements.

Performance of various FRP-RC elements under predominately flexural (Brown and Bartholomew 1993; Vijay and GangaRao 2010; Yost and Gross 2002; Soric et al. 2002) and axial (Alsayed et al. 1999; Choo et al. 2006; Tobbi et al. 2012) monotonic loading has been studied over the last two decades. Although the study of individual FRP-RC elements under monotonic loading showed promising results, seismic performance of FRP-RC elements, in particular, still requires especial attention. The FRP materials in general exhibit linear elastic behaviour and brittle failure which significantly reduce ductility of FRP-RC structural elements compared to their counterparts reinforced with conventional steel. Ductility is a key feature required for structures in seismic regions. Lack of ductility can result in low energy dissipation and catastrophic collapse of structures during an earthquake.

To evaluate the seismic performance of FRP-RC structures, the behaviour of moment-resisting frames, as one of the main lateral load resisting systems used in the construction industry, under cyclic loading has been focused by few researchers. Fukuyama et al. (1995) conducted one of the early studies in investigating the seismic behaviour of FRP-RC frames by experimentally testing a half-scale three-story FRP-RC moment frame. It was concluded that FRP-RC moment-resisting frames can perform satisfactory under cyclic loadings, thus confirming the feasibility of using FRP-RC frames in seismic regions.

In contrary to steel, which possesses relatively consistent mechanical properties, FRP materials can be manufactured with significantly different mechanical properties by making changes in the choice of fibers used in the products. Carbon-FRP (CFRP), Aramid-FRP (AFRP), Glass-FRP (GFRP) and recently Basalt-FRP (BFRP) are mainly the most dominant types of FRP materials considered for the construction industry.

Among these FRP materials available for the construction industry, GFRP and BFRP possess a unique combination of low modulus of elasticity and high tensile strength that can prevent brittle failure of FRP-RC elements during an earthquake. Due to relatively high tensile strength and low modulus of elasticity of GFRP and BFRP, these materials can withstand high tensile strains prior to failure. This allows concrete elements reinforced with GFRP and BFRP to be able to undergo significantly large lateral displacements during an earthquake without exhibiting brittle failure.

Furthermore, the feasibility of using GFRP-RC frames in seismic regions has been investigated by Said and Nehdi (2004) and Mady and El-Salakawy (2011) by investigating the seismic behaviour of GFRP-RC beam-column joints, as the main elements in characterizing the seismic performance of moment-resisting frames. Results of these studies indicated that GFRP-RC beam-column joints can resist lateral displacements as high as 6% drift ratio without exhibiting brittle failure. This drift ratio is more than the maximum drift limit of 2.5% required by the National Building Code of Canada (NRCC 2015). Moreover, the linear characteristics of the GFRP bars resulted in significantly lower residual damage compared to conventional steel-RC elements. This will significantly reduce the repair costs after a seismic event. Moreover, to compensate for the lack of energy dissipation of GFRP-RC elements, using hybrid structures, where steel-RC elements provide lateral resistance, while GFRP-RC elements are used in the envelope of structures to eliminate corrosion and durability issues was suggested (Said and Nehdi 2004).

Although the behaviour of steel-RC beam-column joints under cyclic loadings has been studied since 1960s (Hanson and Conner 1967), investigating the effective parameters on the seismic performance of GFRP-RC beam-column joints is a relatively new field. After establishing the feasibility of using GFRP-RC frames in seismic regions, Ghomi and El-Salakawy (2016), and Hasaballa and El-Salakawy (2016) further investigated the effect of a number of parameters on the seismic performance of GFRP-RC beam-column joints such as joint shear stress, reinforcement anchorage type, concrete strength and joints configuration. However, the focus of these studies was only on exterior beam-column joints, while to be able to fully implement GFRP reinforcement in moment-resisting frames, a solid understanding of the seismic behaviour of all types of beam-column joints is necessary.

To date, no investigation has been done on seismic performance of interior beam-column joints, even though the majority of connections in a moment-resisting frame are mainly interior beam-column joints.

In this paper, the effect of joint shear capacity on the behaviour of interior beam-column joints is studied. Although the Canadian standards CSA/S806-12 (CSA 2012) allow using FRP reinforcement in columns in seismic regions and provide the amount of required transverse reinforcement for adequate confinement, they do not provide the shear capacity of the beam-column joints that have been reinforced according to these requirements.

3.2 Experimental Program

3.2.1 Test specimens

A total of four full-scale interior beam-column joints with lateral beams were constructed and tested; three reinforced with GFRP and one reinforced with steel as a control specimen. The specimens were isolated from assumed points of contra-flexure in an arbitrary moment-resisting frame at mid-height of the columns and mid-span of the beams. Figure 3.1 shows specimens' dimensions. Cross-sectional dimensions of the lateral beams are selected to cover approximately 60% of the joint area.

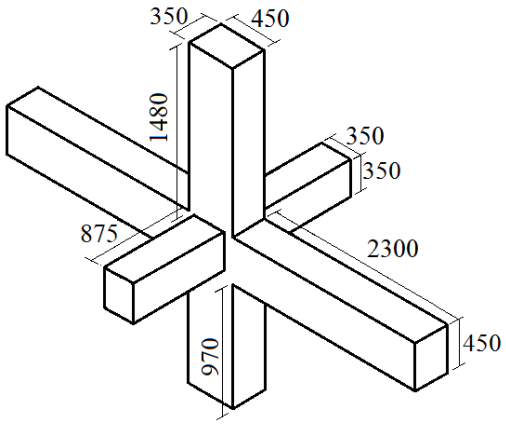

Figure 3.1 - Dimensions of test specimens (dimensions in mm)

One of the main objectives of the program was to investigate the shear capacity of GFRP-RC interior beam-column joints. Therefore, the GFRP-RC specimens were kept identical except for the number of main beam longitudinal reinforcement resulting in different shear stress applied to the joints.

The specimens are designated with a letter indicating the type of reinforcement ("G" for GFRP and "S" for steel) and a number indicating the applied joint shear stress (as a multiplier of $\sqrt{f'_c}$). The magnitude of joint shear stress ratio in the test specimens was calculated at the horizontal

cross-section located at the centre of the joint. Figure 3.2 shows the free-body diagram of the isolated upper half of the joint area, where V_j is the shear force at centre of the joint, T_r is the tensile force applied to the joint by the longitudinal bars of the main beam, C_c is the compressive force applied to joint by the concrete compression block in the main beam and V_c is the shear force applied to the joint by the column. The joint shear stress ratio is then calculated as:

$$\frac{V_j}{A_j\sqrt{f'_c}}$$

where A_j is the area of the horizontal cross-section of the joint and f'_c is the compressive concrete strength on the day of testing.

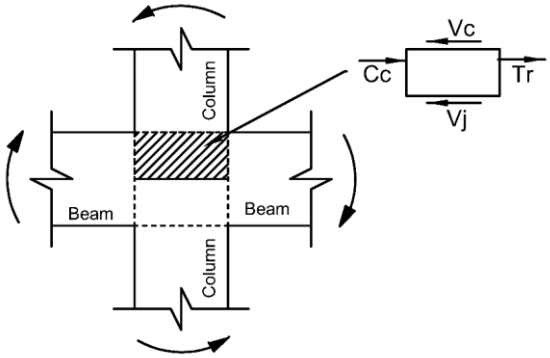

Figure 3.2 - Free-body diagram of joints

Figure 3.3 and Figure 3.4 show reinforcement detailing of the specimens and locations of the stirrups. It should be mentioned that the test specimens were designed according to the Canadian standards for design of steel-RC structures, CSA/A23.3-14 (CSA 2014-a), and FRP-RC structures, CSA/S806-12 (CSA 2012). The CSA/S806-12 (CSA 2012) requires the failure of FRP-RC sections to be initiated by concrete crushing in the compression zone, rather than rupture of the FRP bars. This is to prevent brittle failure of the section as the concrete exhibits more nonlinearity compared to the FRP. The CSA/A23.3 (CSA 2014-a), on the other hand, requires the failure of

steel-RC sections to be initiated by yielding of steel reinforcement as steel exhibits more nonlinearity than concrete.

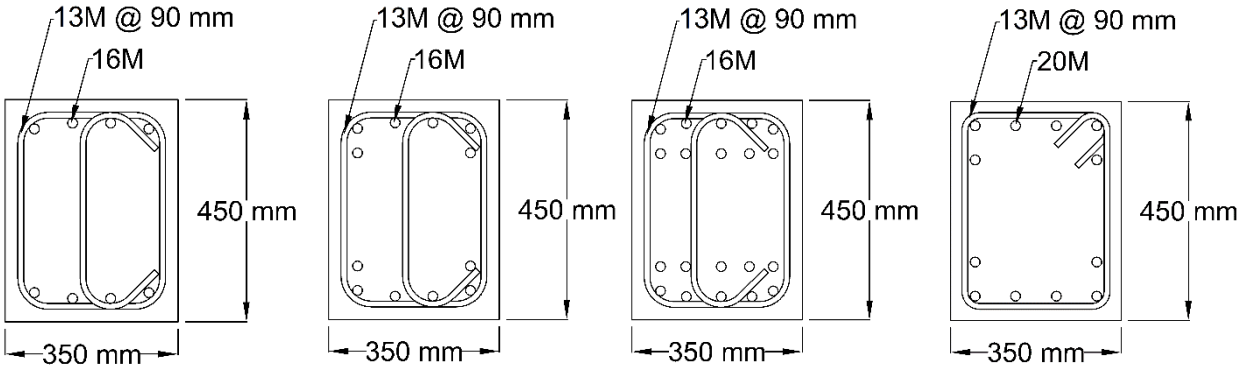

(a) Beam of G-1.3 (b) Beam of G-1.5 (c) Beam of G-1.8 (d) Beam of S-1.5

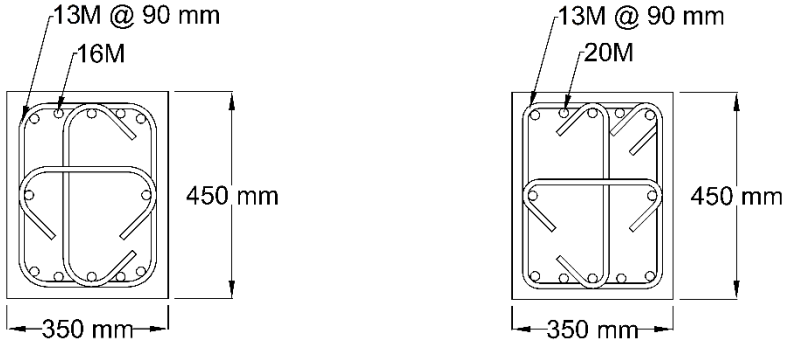

(e) Colum of GFRP-RC specimens (f) Colum of steel-RC specimen

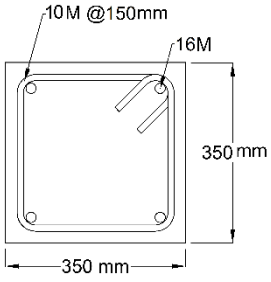

(g) Lateral beam of GFRP-RC specimens (h) Lateral beam of steel-RC specimen

Figure 3.3 - Reinforcement detailing of test specimens

Therefore, the approach in the current study is to compare the behaviour of a GFRP-RC beam-column, designed according to the current FRP-RC design codes, under cyclic loading with a

conventional steel-RC beam-column, designed based on the corresponding design standards, with the same magnitude of joint shear ratio. The properties of the test specimens are provided in Table 3.1.

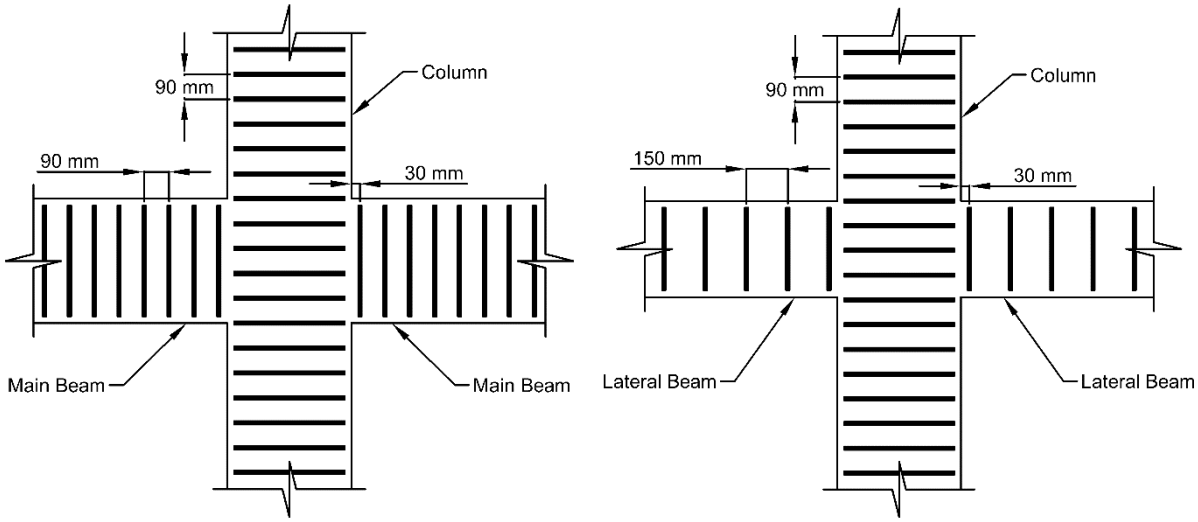

(a) Main beams and columns (b) Lateral beams

Figure 3.4 - Locations of stirrups

Table 3.1 - Properties of test specimens

Specimen	Beam Reinforcement (Top and Bottom)	Beam Reinforcement Ratio	Beam Flexural Capacity (kN.m)	Column Flexural Capacity[(a)] (kN.m)	Shear Ratio	Flexural Ratio	Concrete Strength (MPa)
G-1.3	4-16M	0.57%	264	280	1.30	1.06	38±0.4
G-1.5	6-16M	0.90%	330	325	1.49	0.98	49±3.0
G-1.8	10-16M	1.52%	422	352	1.85	0.83	58±1.2
S-1.5	6-20M	1.34%	361	420	1.56	1.16	56±1.1

[(a)] Includes the effect of column axial load

3.2.2 Material properties

Ready-mix concrete with target 28-day compressive strength of 40 MPa was used to cast the test specimens. Three standard concrete cylinders, 300-mm×150-mm, were tested on the day of testing to measure the actual compressive strength of the concrete as reported in Table 3.1.

Standard CSA grade G400 steel reinforcement was used in the construction of Specimen S-1.5 (steel-RC beam-column joint). The yield stress and strain of the steel reinforcement were obtained through a traction test and are provided in Table 3.2.

Table 3.2 - Properties of GFRP reinforcement

Reinforcement	Nominal Cross-Sectional Area (mm^2)	GFRP Tensile Strength, Steel Yield Strength (MPa)	Modulus of Elasticity (GPa)	GFRP Ultimate Strain, Steel Yield Strain (‰)
16M GFRP Bars	198	1184	62.6	18.9
13M GFRP Stirrups*	127	1312	65.6	20.0
20M Steel Bars	300	438	184.8	2.4

* Straight portion of the stirrup

Sand-coated GFRP bars and stirrups were used in the GFRP-RC specimens. Properties of the GFRP reinforcement was provided by the manufacturer (Pultrall Inc. 2019) and are presented in Table 3.2. The stress-strain relationships of the GFRP and steel longitudinal bars are compared in Figure 3.5.

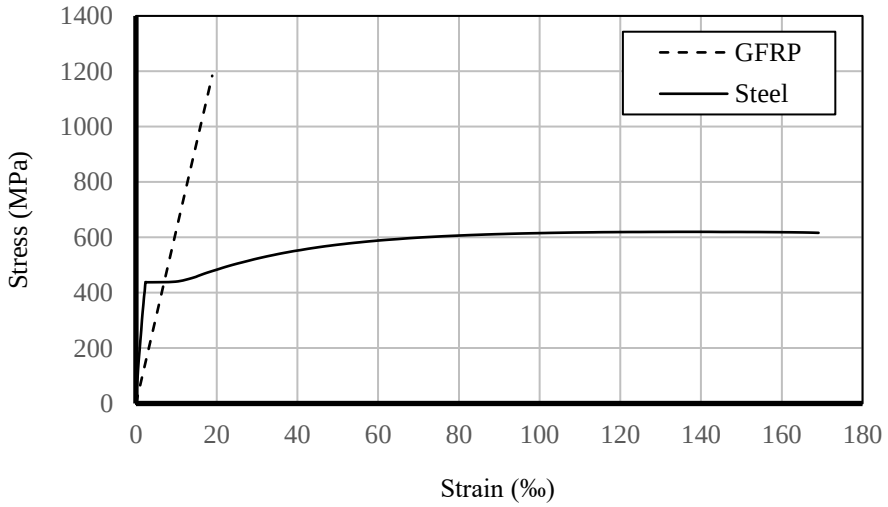

Figure 3.5 - Stress-strain relationship of steel and GFRP longitudinal bars

3.2.3 Test set-up

Figure 3.6 shows the set-up used to test the specimens with one specimen ready for testing. The column and the beams were in vertical and horizontal position, respectively. A fully dynamic 1000 kN-capacity actuator was attached to the tip of the column to apply reversal cyclic loading which simulated a seismic event. The actuator was mounted on a strong vertical concrete wall.

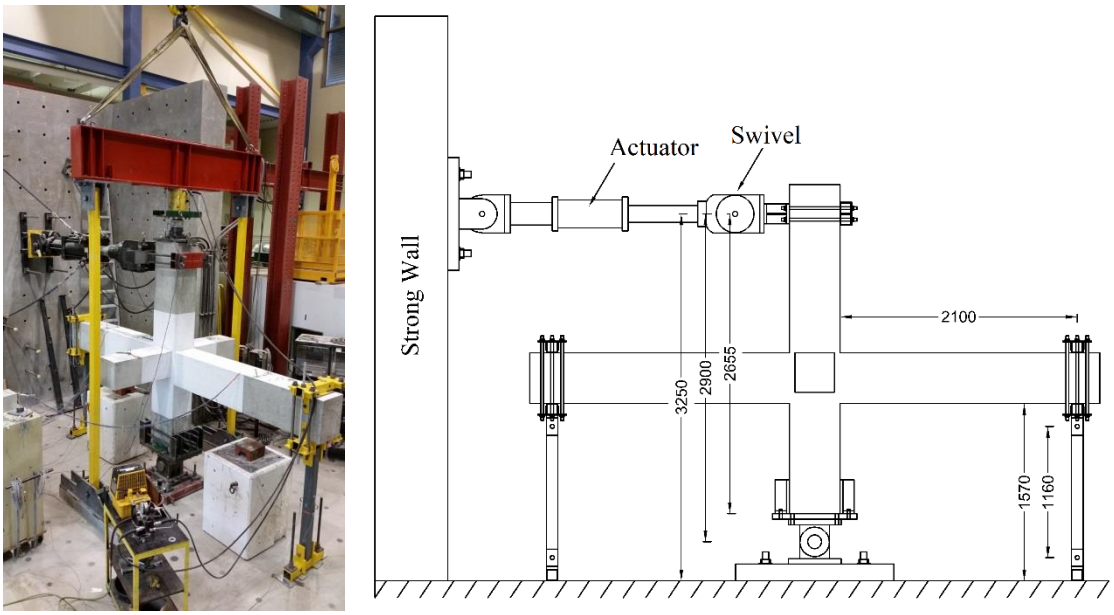

Figure 3.6 - Test set-up (dimensions in mm)

Tips of the main beams were attached to a strong floor by means of double-hinged elements (links) to simulate roller boundary condition at the ends of the beams. The links allowed free rotation and horizontal translation of the beam tips while restricting their vertical translation.

The column was attached to a hinge at its bottom to simulate a zero-moment location (contra-flexural point). The hinge was fixed on the strong floor by four pre-stressing dywidag bars, clamping the hinge to the strong floor, and was restrained against any lateral translation.

The column was under constant axial load during the test. The axial load was applied by a hydraulic jack located at the top of the column. The hydraulic jack was reacting against a stiff steel beam on top of the specimen. The beam was attached to the strong floor by means of two long double-hinged elements which allowed free lateral movement of the beam with the column while the actuator was applying reversal cyclic loading. Axis of the bottom pin of the long double-hinged elements (connecting the stiff steel beam to the floor) and the pin of the hinge at the bottom of the column were set on the same line. That was to eliminate any secondary moments by ensuring that the line of action of the column axial load passes through the centre of the bottom hinge at all time.

3.2.4 Loading scheme

As mentioned earlier, the columns were under constant axial load during the test while the actuator was applying reversal cyclic loading to simulate a seismic event. The magnitude of the axial load was set at approximately 15% of the maximum concentric axial capacity of the columns.

The main reversal cyclic loading was applied in a displacement-controlled mode. The ACI 374.1-05 (ACI Committee 374 2005) criteria were used as a guideline to proportion the cyclic loading scheme as shown in Figure 3.7. The cyclic loading procedure consisted of several loading steps gradually increasing in lateral drift ratio, which is defined as the ratio between the lateral displacement of tip of the column and the length of the column. The length of the column is measured from the centre of the pin at the bottom of the column to the point of load application on the column.

Each loading step consisted of three identical cycles to ensure stable crack propagation in each loading step. As shown in Figure 3.7, after 2% drift ratio, one load-controlled cycle with the amplitude equal to service load was applied after each loading step (three identical displacement-

controlled cycles with the same magnitude of lateral drift ratio) to measure the performance of the beam-column joints after different stages of cyclic loads under service condition. The service load was calculated as the horizontal load at the tip of the column (actuator load) causing a stress in the main beam reinforcement corresponding to 25% of the ultimate tensile strength of the GFRP bars, according to Canadian Highway Bridge Design Code (CSA 2014-b), and 60% of the yield strength of the steel bars (CSA 2014-a).

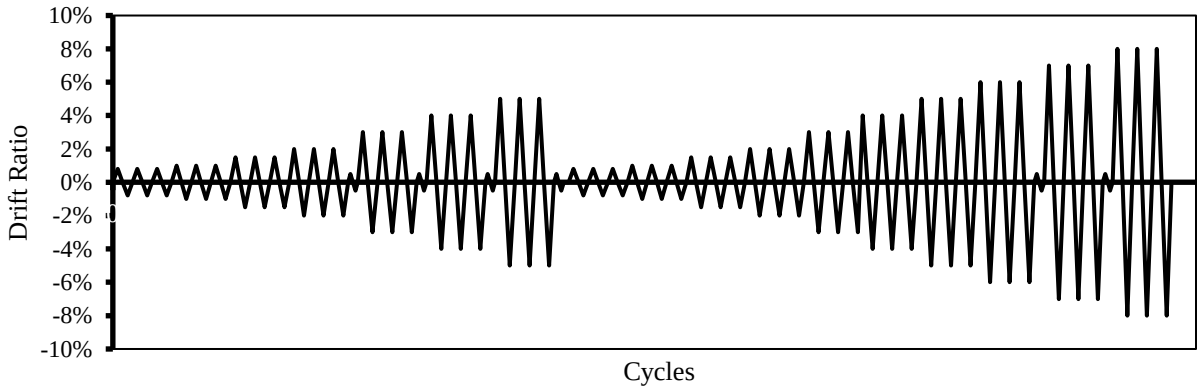

(a) Loading scheme for GFRP-RC specimens

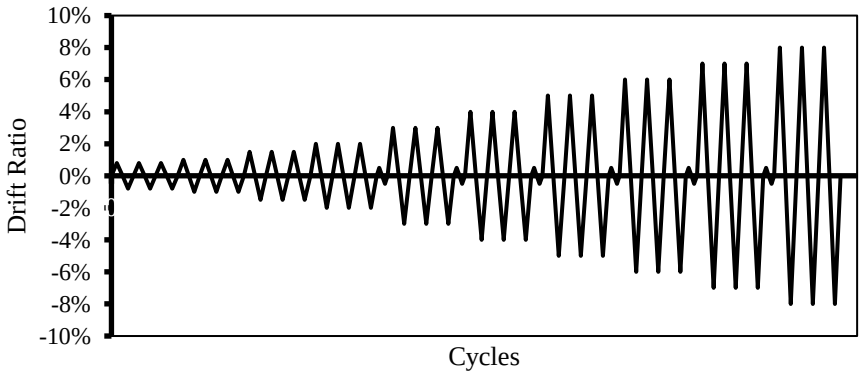

(b) Loading scheme for steel-RC specimen

Figure 3.7 - Loading Scheme

In this program, the GFRP-RC specimens were tested under two series of cyclic loadings, Phase I and Phase II. In Phase I, the specimens were tested from 0 to 5% lateral drift ratio. In phase II, the specimens were immediately re-tested by starting over the loading procedure from 0% lateral drift

ratio to failure. In the second loading phase the seismic performance of the GFRP-RC specimens was investigated while they had been already damaged to some extend in the first loading phase.

The 5% drift ratio was selected as the threshold for the first loading phase based on the following:

1. The authors attempt was to ensure that the specimens are loaded at least to their maximum design capacity (bending capacity of the main beams) during the first loading phase. Ghomi and El-Salakawy (2016) tested several GFRP-RC exterior beam-column joints under the same loading scheme as the first phase in this program and observed that the specimens reach their design capacity at 4% or 5% drift ratio. Using that observation as a baseline, 5% drift ratio was chosen as the threshold for the first loading phase in this program to ensure that the GFRP-RC specimens are loaded at least to their maximum design capacity.
2. Moreover, the objective was to satisfy the requirements of current building codes and guidelines for lateral displacements of moment-resisting frames in seismic regions in the first loading phase. The maximum allowable lateral drift ratios set by the National Building Code of Canada (NRCC 2015) is 2.5%. Moreover, the CSA/S806-12 (CSA 2012) requires a deformable moment-resisting frame to be able to withstand 4% drift ratio. The threshold of 5% drift ratio exceeds both requirements.

3.3 Test Results and Discussions

3.3.1 Hysteresis diagram and mode of failure

Lateral load-displacement relationship (hysteresis diagram) of the specimens are shown in Figure 3.8. The graphs corresponding to the GFRP-RC specimens are indicating the behaviour of the GFRP-RC specimens in the first loading phase (up to 5% drift ratio) while the graph corresponding

to the steel-RC specimen shows the response of the specimen till failure. As mentioned earlier, the steel-RC specimen, as oppose to the GFRP-RC specimens, was tested under one loading phase only (from 0% drift ratio till failure). Upon yielding of reinforcement in a steel-RC moment-resisting frame during a seismic event, the original condition of the frame cannot be restored and the building will not be able to stay in service. Therefore, re-testing the steel-RC specimen after yielding of its reinforcement is not valid.

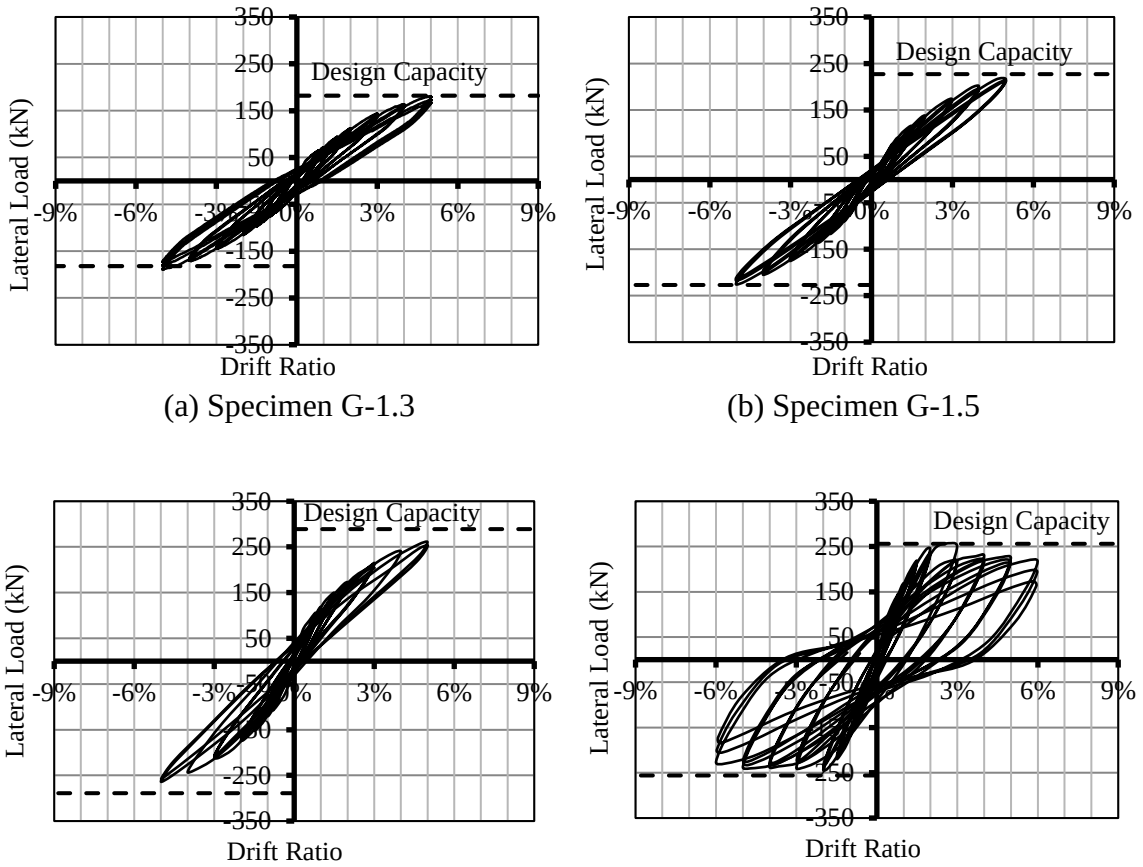

(a) Specimen G-1.3 (b) Specimen G-1.5

(c) Specimen G-1.8 (d) Specimen S-1.5

Figure 3.8 - Hysteresis diagram in the first loading phase

The dashed lines in the graphs indicate the design capacity of the specimens. The design capacity was defined as the magnitude of the lateral load at the tip of the column (applied by the horizontal actuator as shown in Figure 3.6) that results in the maximum design bending moment in the main

beams. It should be mentioned that 25% increase in the yield strength, as required by CSA/A23.3-14 (CSA 2014-a), was assumed in calculating moment capacity of Specimen S-1.5.

Comparing the hysteresis diagram of Specimen S-1.5 with Specimen G-1.5 (with identical joint shear stress and different reinforcement material) indicates lack of ductility in GFRP-RC beam-column joints. The steel reinforcement in Specimen S-1.5 yielded at 1.0% drift ratio which resulted in a plateau in lateral load-displacement response of the specimen. Specimen G-1.5, on the other hand, exhibited constant increase in lateral load carrying capacity due to the linear elastic nature of the GFRP reinforcement.

However, the ductile behaviour of Specimen S-1.5 comes with the cost of significant residual damage after yielding of the steel reinforcement. Figure 3.9 compares the column residual displacement at zero column load after each loading step. It is evident that the linear elastic behaviour of the GFRP reinforcement significantly reduced the magnitude of residual damage in the concrete at zero load condition in Specimen G-1.5 compared to Specimen S-1.5 after steel yielding.

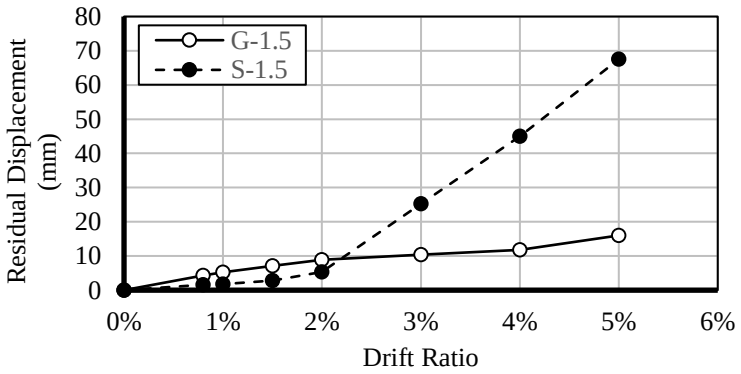

Figure 3.9 - Column residual displacement

The magnitude of residual displacement in beam-column joints can be interpreted as an indicator of the damage induced to their corresponding moment-resisting frame after an earthquake. Therefore, replacing steel reinforcement with GFRP bars and stirrups can significantly reduce the damage induced to concrete moment-resisting frames due to a seismic event and hence can reduce post-disaster costs due to reduced structural repair needs.

Moreover, a steel-RC moment-resisting frame might be able to survive a severe seismic event without total collapse; however, once yielding of the reinforcement occurs the structure can not restore its original condition. Therefore, in many cases the structure has to be demolished due to lack of serviceability.

The magnitude of equivalent stiffness of the specimens at different loading stages is compared in Figure 3.10, as another indicator of the level of damage after each drift ratio. The equivalent stiffness was defined as the slope of an imaginary straight line connecting the maximum positive and negative lateral load during each drift ratio in the graphs of Figure 3.8.

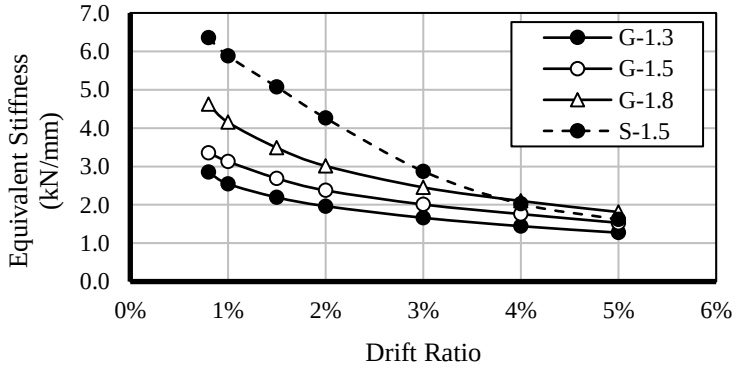

Figure 3.10 - Equivalent stiffness of test specimens

As expected, larger number of longitudinal bars in the main beams of the GFRP-RC specimens resulted in higher equivalent stiffness. Moreover, Specimen S-1.5 exhibited higher equivalent

stiffness at 0.8% drift ratio compared to Specimen G-1.5, due to higher modulus elasticity of steel than that of GFRP (184.8 GPa vs 62.6 GPa). However, the rate of stiffness deterioration was significantly higher in Specimen S-1.5 than G-1.5, which indicates the higher level of damage in Specimen S-1.5 due to yielding of the steel reinforcement.

Figure 3.11 shows condition of the GFRP-RC specimens after completion of the first loading phase (after 5% drift ratio). As expected, no significant concrete damage was observed in the GFRP-RC specimens after 5% drift ratio. However, comparing the condition of the specimens indicates that the increase in joint shear stress ratio increases the damage induced to the specimens in the vicinity of the joint area.

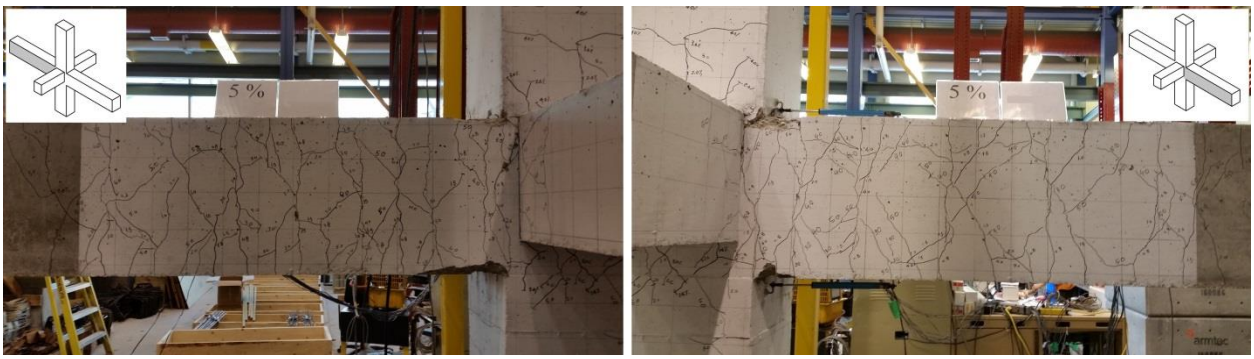

(a) Specimen G-1.3

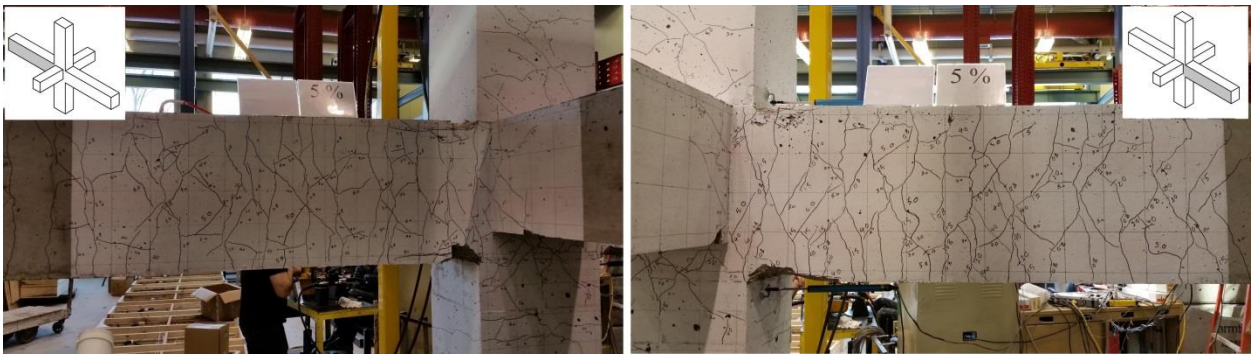

(b) Specimen G-1.5

(c) Specimen G-1.8

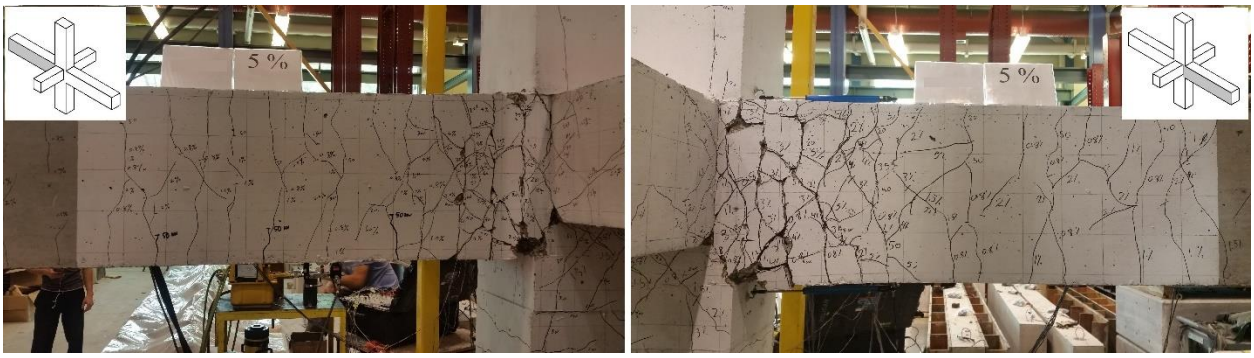

(d) Specimen S-1.5

Figure 3.11 - Condition of test specimens after 5% drift ratio (after the first loading phase for GFRP-RC specimens)

In addition, the effect of beam longitudinal reinforcement on the concrete damage of the GFRP-RC specimens has to be considered. Increasing the number of beam longitudinal reinforcement increases bending moment capacity of the beams hence the column-to-beam flexural strength ratio decreases. The column-to-beam flexural strength ratio is commonly used as an indicator of the location of the damage concentricity in beam-column joints. The lower the ratio, the closer the centre of the damage to the column (joint area). As shown in Table 3.1, column-to-beam flexural strength ratio of the GFRP-RC specimens decreases as their joint shear ratio increases.

As shown in Figure 3.8, in contrary to Specimens G-1.3 and G-1.5, Specimen G-1.8 was not able to reach its design capacity during the first loading phase. The reason can be explained by the

lower column-to-beam flexural strength ratio in Specimen G-1.8 compared to the other GFRP-RC specimens. Building codes and design guidelines commonly suggest column-to-beam flexural strength ratios more than unity to prevent failure of the columns prior to failure of the beams (strong column-weak beam concept). However, this ratio in Specimen G-1.8 was calculated as 0.83. Therefore, the column reached its design capacity prior to the beam as shown in Figure 3.11 in forms of concrete cover spalling in the column adjacent to the main beams. This resulted in a decrease in lateral stiffness of the specimen, therefore the design capacity was not reached during the first loading phase.

Figure 3.12 compares the normalized lateral load envelop (ratio of the maximum lateral load to the design capacity) of the test specimens up to the first 5% drift ratio. As shown in the graph, the steel-RC specimen exhibited significantly higher initial stiffness compared to the GFRP-RC specimens. This is due to the higher modulus of elasticity of steel (200 GPa) compared to that of the GFRP reinforcement used in this program (62.5 GPa).

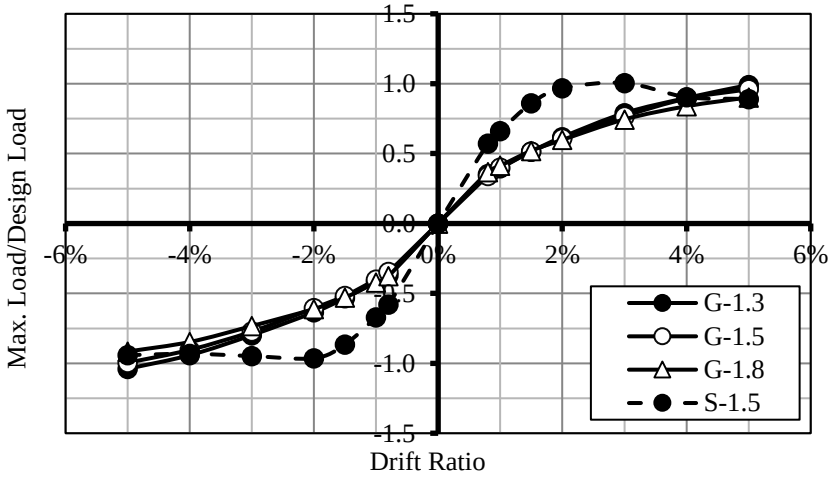

Figure 3.12 - Normalized lateral load envelops

The lower initial stiffness of GFRP-RC beam-column joints can significantly affect seismic behaviour of GFRP-RC moment-resisting frames by increasing lateral displacement of the

structure during an earthquake. Excessive lateral deformation of the structure increases the secondary moments induced to the column due to significant gaps between centre of gravity and centre of geometry of the structure (P-delta effect) as will be explained in later sections.

Figure 3.13 shows lateral load-drift response of the GFRP-RC specimens during the second loading phase. Specimen G-1.5 was able to reach the design capacity again during the second loading phase. This indicates that it is possible to design GFRP-RC frames to withstand the ultimate state loading multiple times. However, due to the damage induced to the specimen during the first loading phase, the lateral stiffness of the specimen decreases which resulted in reaching the design capacity at a higher lateral drift ratio (6%) compared to the first loading phase (5%). As mentioned before, the GFRP-RC specimens were not repaired after the first loading phase and the second loading phase was applied to the specimens immediately after the completion of the first loading phase.

Followed by achieving the maximum lateral load carrying capacity at 6% drift ratio, gradual decrease in lateral load was observed in Specimen G-1.5 during the consecutive drift ratios. The test was stopped after 8% drift ratio due to failure of the specimen. As suggested by ACI 374.1-05 (ACI Committee 374 2005), failure was defined as the point with more than 25% decrease in lateral load compared to the maximum lateral load exhibited by the specimens.

In contrary to Specimen G-1.5, Specimen G-1.3 was not able to reach the maximum design capacity in the second loading phase. This observation contradicted the expected behaviour of the specimens. Compared to Specimen G-1.5, Specimen G-1.3 with lower joint shear stress was expected to exhibit less concrete damage in the joint area hence behaving in a more stable manner in the second loading phase. However, the authors believe that the lack of strength of Specimen

G-1.3 in the second loading phase (compared to Specimen G-1.5) was because of the damage occurred in the main beams and not the joint.

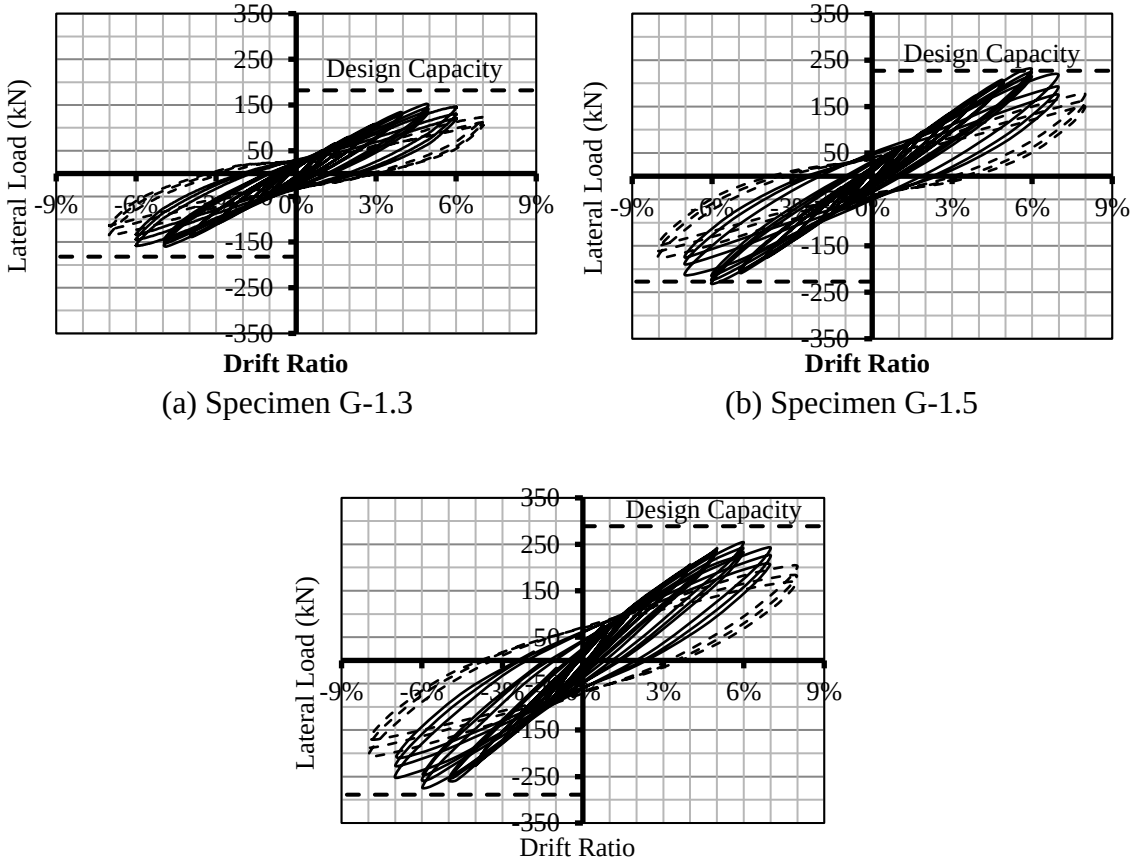

(a) Specimen G-1.3 (b) Specimen G-1.5

(c) Specimen G-1.8

Figure 3.13 - Hysteresis diagram of GFRP-RC specimens in the second loading phase

As shown in Figure 3.3, the beams in Specimen G-1.3 were reinforced with one layer of bars while the beams in Specimen G-1.5 were reinforced with two layers of bars. The higher number of reinforcement layers resulted in more confinement of the concrete core in the main beams in Specimen G-1.5. Therefore, less damage was induced to the main beams of Specimen G-1.5 compared to the beams of Specimen G-1.3 hence less reduction in its lateral strength was observed.

Although early concrete spalling in the column prevented Specimen G-1.8 from gaining the design capacity during the first loading phase, the specimen was able to reach the design capacity in the second loading phase at 6% drift ratio. As shown in Table 3.1, the joint shear stress ratio applied to the joint area of Specimen G-1.8 when the main beams are loaded to their design bending capacity was calculated as $1.8\sqrt{f'_c}$. Based on this observation, it was concluded that the interior GFRP-RC beam-column joints tested in this program are able to withstand joint shear stress ratio of $1.8\sqrt{f'_c}$.

The maximum lateral load observed during testing of the GFRP-RC specimens in each drift ratio is shown in Figure 3.14. The solid lines and the dashed lines in the graphs indicate the response in the first and the second loading phase, respectively. As expected, all specimens showed linear behaviour up to 5% drift ratio during the second loading phase. This is indicated in the figure by the straight portion of the graphs connecting the origin to the point corresponding to the maximum lateral load during the third cycle of loading at 5% drift ratio in the first loading phase.

Figure 3.15 shows the condition of the specimens after the final loading step (failure). Comparing the condition of the GFRP-RC specimens indicates that the increase in the joint shear stress ratio increases the damage induced to the joint area. As explained earlier, lower column-to-beam flexural strength ratio of the specimens with higher joint shear stress also results in penetration of the damage further into the joint. In all specimens, the damage is more severe at the lower part of the column (below lateral beams) due to the lack of confinement by lateral beams. As shown in Figure 3.1, the top surface of lateral beams was flush with the top surface of the main beams leaving the bottom 100-mm of the joint area unconfined.

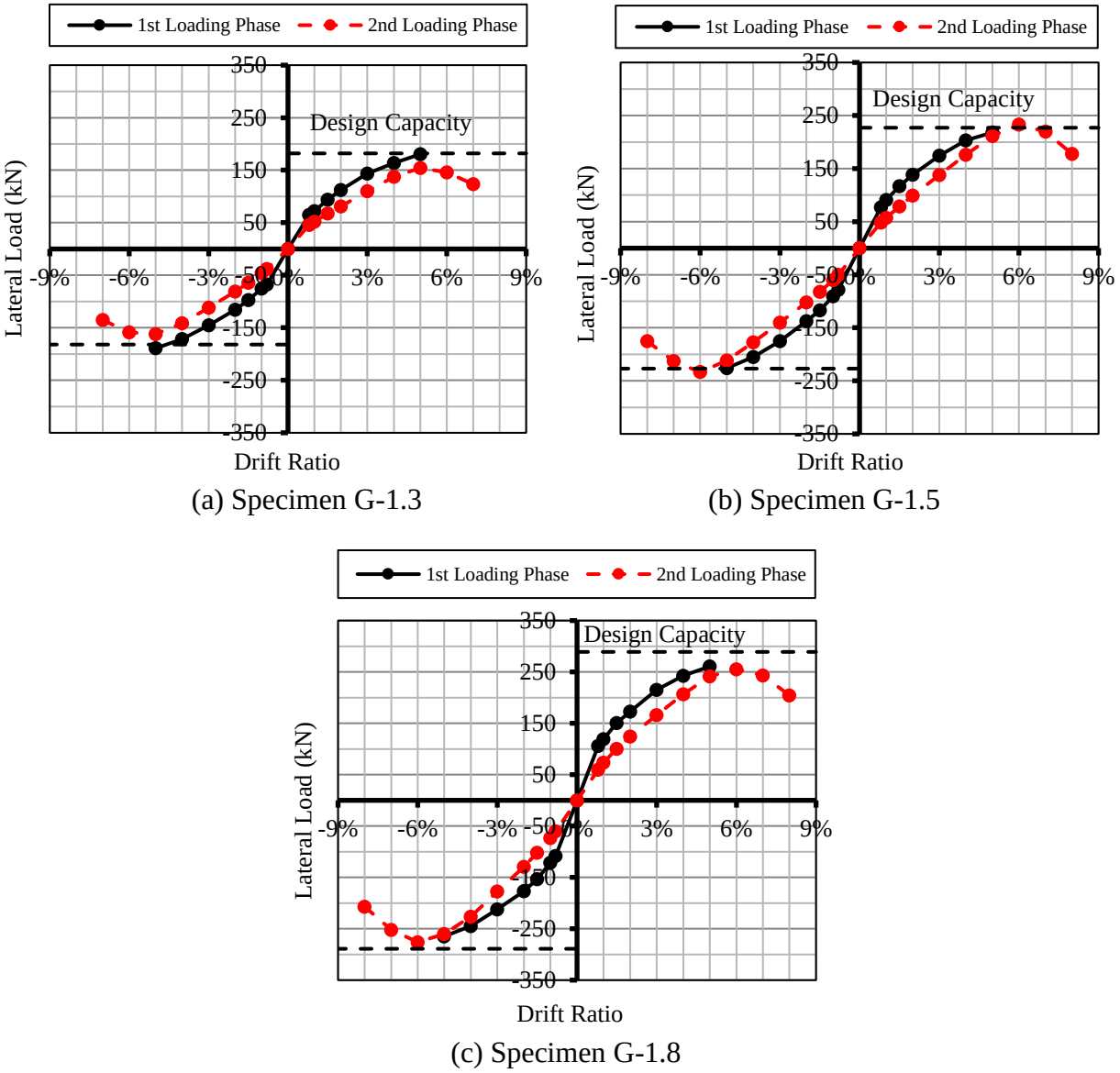

(a) Specimen G-1.3

(b) Specimen G-1.5

(c) Specimen G-1.8

Figure 3.14 - Lateral load envelops of GFRP-RC specimens

The GFRP-RC were designed as over-reinforced sections causing the mode of failure to be concrete crushing prior to rupture of the reinforcing bars. Therefore, the failure in the GFRP-RC specimens was initiated by crushing of concrete at the outermost fibre of the beam or column sections. This was observed by losing concrete cover in the beams or columns near the joint area. However, at that point, the damage remained limited to the unconfined concrete cover. The concrete core, due to the confinement provided by the stirrups and the longitudinal bars, exhibited

higher compressive strength and the specimens continued to maintain their maximum lateral load carrying capacity after losing the concrete cover. However, as the lateral drift ratio was further increased, the concrete damage gradually increased in both the joint and the beams resulting in gradual softening of the beam-column joints and decrease in the maximum lateral load.

(a) Specimen G-1.3

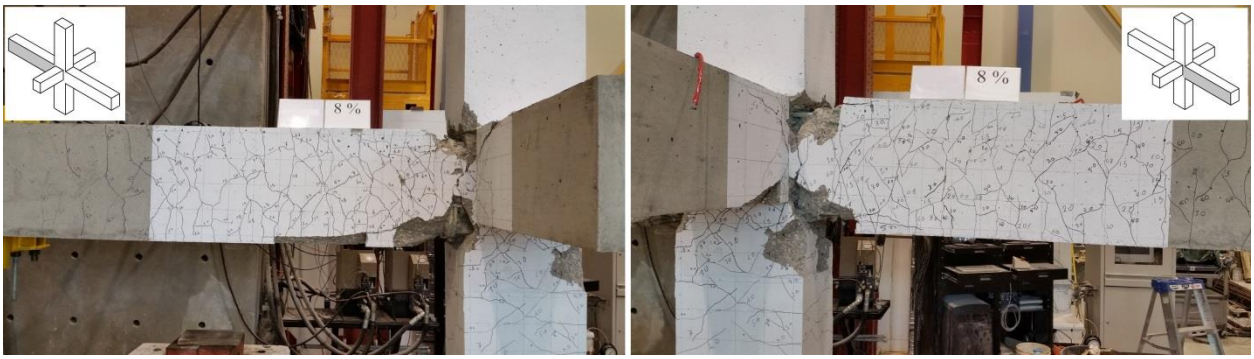

(b) Specimen G-1.5

(c) Specimen G-1.8

(d) Specimen S-1.5

Figure 3.15 - Condition of test specimens at failure

This gradual failure, as oppose to sudden rupture of the longitudinal bars, is opposite of what is generally expected from GFRP-RC elements. Sudden and brittle failure of GFRP-RC elements was one of the main concerns regarding constructing these types of structures in seismic regions. However, this observation indicates that GFRP-RC beam-column joints can be proportioned in a way that prevents brittle failure of moment-resisting frames.

This behaviour was very similar to the behaviour observed from the steel-RC specimen, even though the steel-RC beams were designed as under-reinforced sections (yielding of the reinforcement occurring prior to concrete crushing). Followed by yielding of the reinforcement, elongation of the reinforcement continued until the outer most fibre of the concrete section reached the compressive strength of the concrete and the same sequence as described for the GFRP-RC specimen until failure occurred.

3.3.2 Effect of secondary moments

As mentioned earlier, the test set-up used in this program was designed to prevent the effect of secondary moments (P-delta) on the specimens during the loading procedure. However, due to lower lateral stiffness of GFRP-RC beam-column joints compared to conventional steel-RC

counterparts, higher lateral displacements should be expected for GFRP-RC moment-resisting frames during an earthquake. Large lateral deformation of structures can result in significant secondary moments in the columns. Therefore, it seems necessary to include the effect of probable secondary moments into the lateral load-drift response of the test specimens.

The Canadian standards CSA/A23.3-14 (CSA 2014-a) require to magnify column end moments due to secondary moments for sway frames. The maximum bending moment in the columns adjacent to the joint area corresponding to each lateral drift ratio was calculated based on test results of the specimens. In order to follow the same approach as the CSA/A23.3-14 (CSA 2014-a), the secondary moments due to P-delta effect are also added to the bending moments of the columns.

Since the column axial load was kept constant during the test, the component corresponding to the P-delta effect can be calculated by multiplying the column axial load (approximately 650 kN) by the column tip displacement.

Figure 3.16 compares the magnitude of bending moment in the columns above the joint area with and without the effect of secondary moments during the first loading phase (up to 5% drift ratio). The horizontal dashed lines in the graphs indicate bending moment capacity of the columns. As shown in the graphs, in Specimens G-1.3 and G-1.5 the maximum bending moment capacity (design capacity) of the columns was reached at 5% drift ratio, which is the drift ratio that the specimens reached the lateral design capacity corresponding to the bending moment capacity of the main beams. This was due to the column-to-beam flexural strength ratios close to unity in Specimens G-1.3 and G-1.5. In Specimen G-1.8, on the other hand, the design capacity of the

column was reached prematurely at 4% drift ratio due to column-to-beam flexural strength ratio less than unity (0.83), as explained earlier.

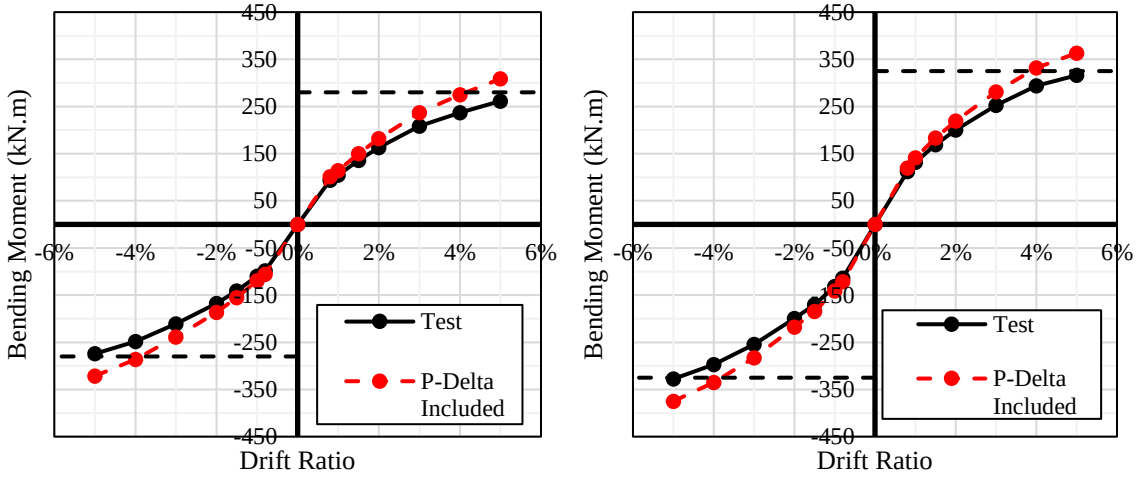

(a) Specimen G-1.3 (b) Specimen G-1.5

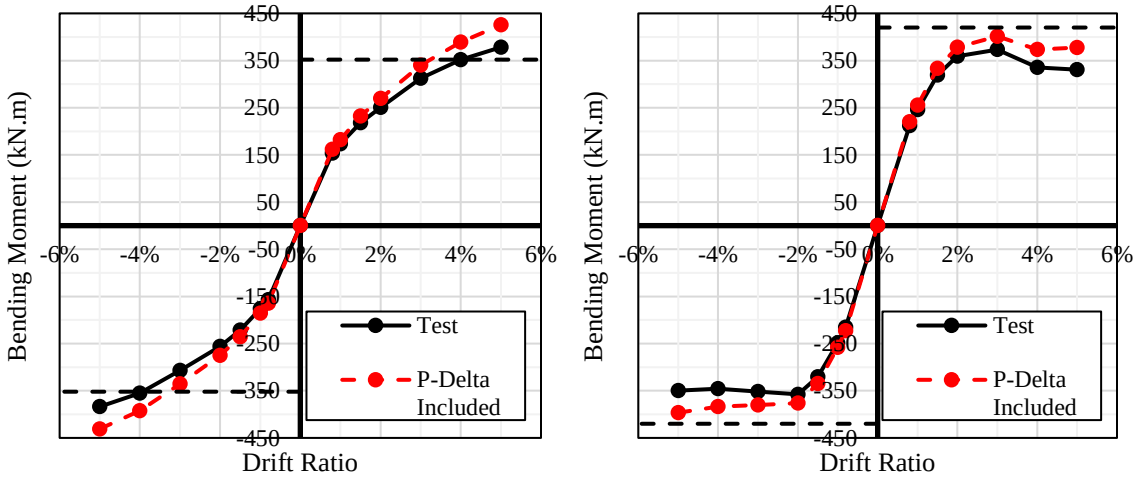

(c) Specimen G-1.8 (d) Specimen S-1.5

Figure 3.16 - P-delta effect on bending moments of columns

Since secondary moments increase the magnitude of bending moments at the columns, failure of columns could occur prior to the beams. As shown in the graphs of Figure 3.16, including the effect of secondary moments results in reaching the maximum design capacity of the columns at

4% drift ratio in Specimens G-1.3 and G-1.5, which is less than 5%, the drift ratio that the flexural capacity of the main beams of the specimens were reached.

In Specimen S-1.5 with column-to-beam flexural strength ratio of 1.16; however, adding the effect of secondary moments did not result in exceeding the bending moment design capacity in the column. Therefore, it is suggested to limit the minimum column-to-beam flexural strength ratio to 1.2 in the design of GFRP-RC beam-column joints. The ratio of 1.2 is conservatively obtained by rounding up the column-to-beam flexural strength ratio of Specimen S-1.5, 1.16.

However, it should be mentioned that reaching the bending moment capacity of the columns does not necessarily result in total collapse of the beam-column joints. As explained earlier, reaching the design capacity is corresponding to compressive failure of unconfined concrete of the cover, while the confined concrete core will continue to resist further loadings.

It should be mentioned that the graphs of Figure 3.16 and the suggested limit of column-to-beam flexural strength ratio, 1.2, are based on the column axial load applied to the test specimens in this program (650 kN). However, columns in a real structure may be under various magnitude of axial load depending on the ultimate load and their location in the structure. The magnitude of column axial load affects the amount of secondary moments. However, the same procedure as describe earlier may be used to set appropriate column-to-beam flexural strength ratio based on the applicable axial loads.

3.3.3 Strain-drift relationship

For each specimen, a total of six strain gauges were installed on the stirrups located in the joint area. Figure 3.17 shows the maximum strain obtained from these strain gauges at different drift

ratios. The CSA/S806-12 (CSA 2012) limits the maximum strain in FRP stirrups to 5000 micro-strain. This limit is indicated in the graph of Figure 3.17 by a solid line.

As expected, the increase in the joint shear stress ratio of the specimens increased the maximum strain observed in the joint stirrups. However, as shown in the graphs, in none of the specimens the maximum strain limit was exceeded prior to 5% drift ratio (in either first or second loading phase).

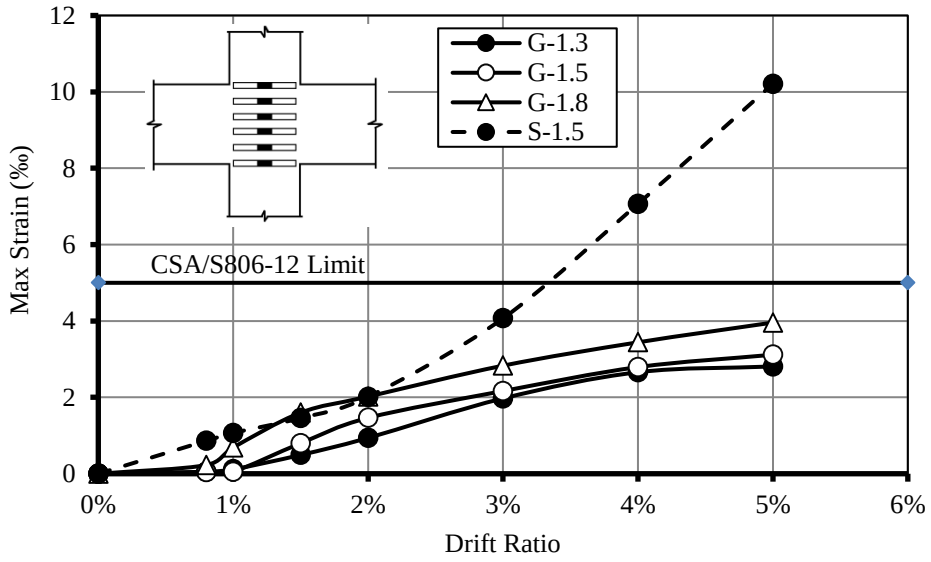

Figure 3.17 - Maximum strain in joint stirrups

This observation along with the satisfactory performance of the GFRP-RC specimens up to 5% drift ratio (no concrete damage in the joint area) indicates the adequacy of the transverse reinforcement used in the joint area. The joint reinforcement of the GFRP-RC specimens tested in this program was designed according to the requirements for confinement of the columns in seismic regions suggested by the CSA/S806-12 (CSA 2012).

In Specimen S-1.5, on the other hand, the maximum strain captured in the joint stirrups exceeded 2000 micro-strain, yielding strain of steel, at 2% drift ratio. As explained earlier, once the yielding

of the internal reinforcement occurs the building has to be demolished even if it does not totally collapse during an earthquake event.

Figure 3.18 shows the maximum strain captured on the longitudinal bars of the main beams in the vicinity of the columns (maximum moment location). Comparing the maximum strain observed in the bars of the beams with the ultimate strain capacity of the GFRP bars (rupture strain), 18,900 micro-strain, indicates a significant margin. This is in agreement with what was observed as the mode of failure of the tested GFRP-RC beam-column joints in forms of gradual softening without brittle failure due to rupture of the bars. Therefore, designers can calculate the maximum strain at the point of failure (concrete crushing) in the GFRP-RC beams and ensure that a safe margin between the maximum probable and the rupture point exists.

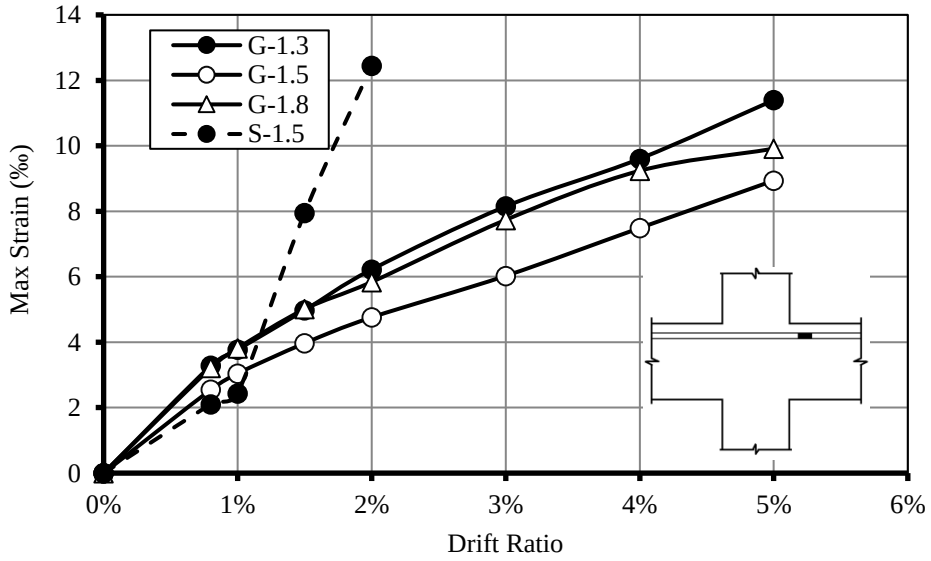

Figure 3.18 - Maximum strain in beam longitudinal bar

In the design process of the test specimens, the maximum expected strains in the outermost layer of the longitudinal bars of the beams at the point of concrete crushing were calculated as 14,400, 13,250 and 10,850 micro-strain for Specimens G-1.3, G-1.5 and G-1.8, respectively. However, it is very important to take into account the effect of concrete damage on increasing the strains in the

bars compared to the theoretically calculated values. For example, even though the maximum strain in bars of Specimen G-1.8 was calculated as 10,850 micro-strain, the maximum observed value during the test was 11,550 micro-strain. This difference was due to significant damage in the concrete that increase the stress applied to the beam longitudinal bars.

In Specimen S-1.5, the steel bars reached the yielding strain (2000 micro-strain) at 1.0%. Therefore, to prevent yielding of the reinforcement during an earthquake, the lateral displacement of the arbitrary moment-resisting frame that the test beam-column joint has been extracted from should be limited to 1.0% drift ratio. However, the extra cost associated with that purpose may make the structure economically unreasonable to construct.

The maximum strains in the longitudinal bars of the main beams were also monitored during the second loading phase. The maximum strains corresponding to the GFRP-RC specimens during the second loading phase up to 5% drift ratio were very close to the values captured during the first loading phase. This confirms the ability of GFRP-RC beam-column joints to maintain their functionality after being loaded to their maximum design capacity.

3.3.4 Energy dissipation

Low energy dissipation of GFRP-RC structures compared to steel-RC counterparts is one of the main concerns regarding using FRP reinforcement in seismic regions. Ductile behaviour of steel reinforcement provides significant energy absorption at higher drift ratios. Although the linear elastic nature of GFRP bars limits the residual damage after an earthquake (as discussed earlier) it comes with the cost of compromising energy dissipation of GFRP-RC frames.

Energy dissipation can be related to damping feature of structures which, if increased, can decrease the lateral deformation of structures during an earthquake. This, in turn, can reduce damage induced to the structure and secondary moments (due to P-delta) effect. Therefore, lower energy dissipation of GFRP-RC beam-column joints compared to steel-RC counterparts increases their vulnerability to high deformations. It should be mentioned that the effect of low energy dissipation on lateral deformation will be added to the effect of low initial stiffness of GFRP-RC beam-column joints, as mentioned earlier.

Figure 3.19 compares cumulative energy dissipation of the test specimens during the first loading phase (first cycle of each loading step). The energy dissipation was calculated as the area enclosed by the hysteresis diagram loops during each loading cycle.

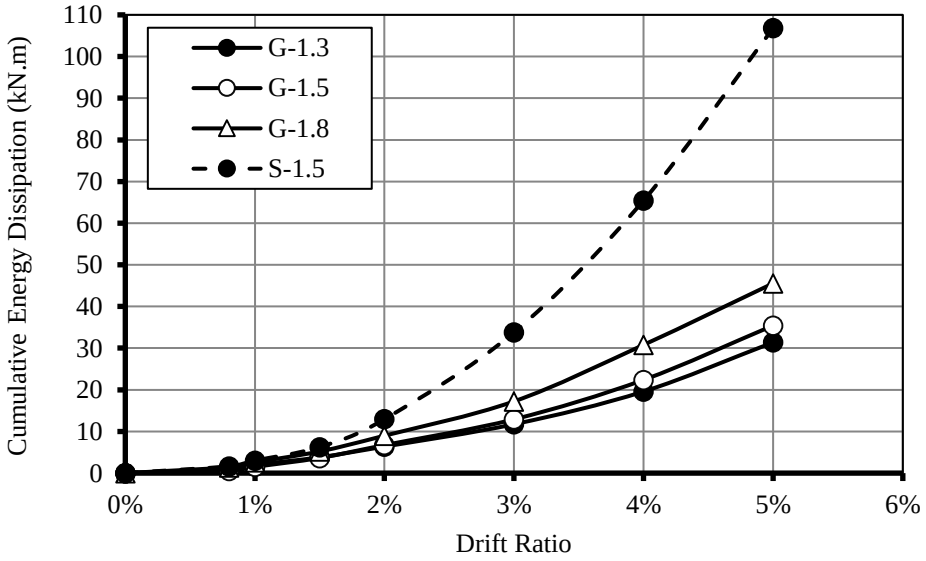

Figure 3.19 - Cumulative energy dissipation

Comparing the behaviour of the GFRP-RC beam-column joints indicates that the increase in joint shear stress increases the magnitude of dissipated energy. This is attributed to more concrete damage induced to the joint area due to higher shear stresses.

As expected, the steel-RC beam-column joint (S-1.5) exhibited significantly more energy dissipation compared to its corresponding GFRP-RC specimen with the same magnitude of joint shear stress (G-1.5). Yielding of the steel reinforcement, as opposed to the linear behaviour of GFRP bars, resulted in 1.44- and 3.06-times more energy dissipation in Specimen S-1.5 compared to Specimen G-1.5 at 2% and 5% drift ratio, respectively.

In conclusion, the seismic performance of GFRP-RC is double-sided. On one hand, the linear elastic nature of GFRP-RC elements significantly reduces the residual damage in a structure after an earthquake and increases its adequacy for service after surviving an earthquake event. On the other hand, such linear elastic nature along with the low modulus of elasticity of GFRP materials reduce the initial stiffness and energy dissipation of GFRP-RC moment-resisting frames which can lead to large lateral deformations that can increase the damage and likelihood of failure due to secondary moments. However, in the authors' opinion, this issue can be resolved by implementing a supplementary lateral load resisting system in addition to the lateral resistance provided by GFRP-RC beam-column joints, such as shear walls. This combination could potentially result in structures with superior performance in seismic events compared to conventional steel-RC moment resisting frames.

3.3.5 Effect of reinforcement ratio and concrete compressive strength on joint shear stress ratio

As shown earlier, the joint shear stress is calculated at the horizontal centre-line of the joint area as the algebraic sum of the tensile force applied to the joint by the longitudinal bars, the compressive force applied to joint by the concrete compression block and the shear force applied to the joint by the column. Therefore, by maintaining the dimensions of beams and columns, the

joint shear stress ratio will be a function of longitudinal reinforcement ratio of the main beams and the concrete compressive strength. However, as mentioned earlier, GFRP-RC and steel-RC beams are designed with different philosophies. The GFRP-RC beams are designed as over-reinforced sections (concrete crushing prior to rupture of the reinforcement), while steel-RC beams are designed as under-reinforced sections (yielding of the reinforcement prior to concrete crushing). This difference in design philosophy results in different relationship between reinforcement ratio of the beams and concrete compressive strength and joint shear stress ratio in GFRP-RC and steel-RC beam-column joints.

In order to investigate the effect of reinforcement ratio of the main beams and concrete compressive strength on joint shear stress ratio in the joints, the magnitude of joint shear stress ratio in Specimen G-1.3 was recalculated with various arbitrary values of reinforcement ratio and concrete compressive strength. The same analysis was also repeated with the assumption of having steel reinforcement. For simplicity, the longitudinal reinforcement in the main beams was assumed to be only in one layer and in 400-mm depth from top of the main beam in the analysis. Concrete compressive values ranging from 20 MPa to 80 MPa and reinforcement ratios ranging from 0% to 3.2% were considered. Figure 3.20 shows a three-dimensional graph indicating the relationship between the variables (joint shear stress ratio, concrete strength and reinforcement ratio) for GFRP-RC and steel-RC beam-column joints.

As shown in the graphs of Figure 3.20, a significantly different relationship was observed from the analysis of the two types of joints. To better compare the response of steel-RC and GFRP-RC beam-column joints, the relationship between reinforcement ratio of the main beam and the joint shear stress ratio at 40 MPa concrete strength and the relationship between the concrete strength

and the joint shear stress ratio at reinforcement ratio of 1.5% are shown in Figure 3.21-a and Figure 3.21-b, respectively.

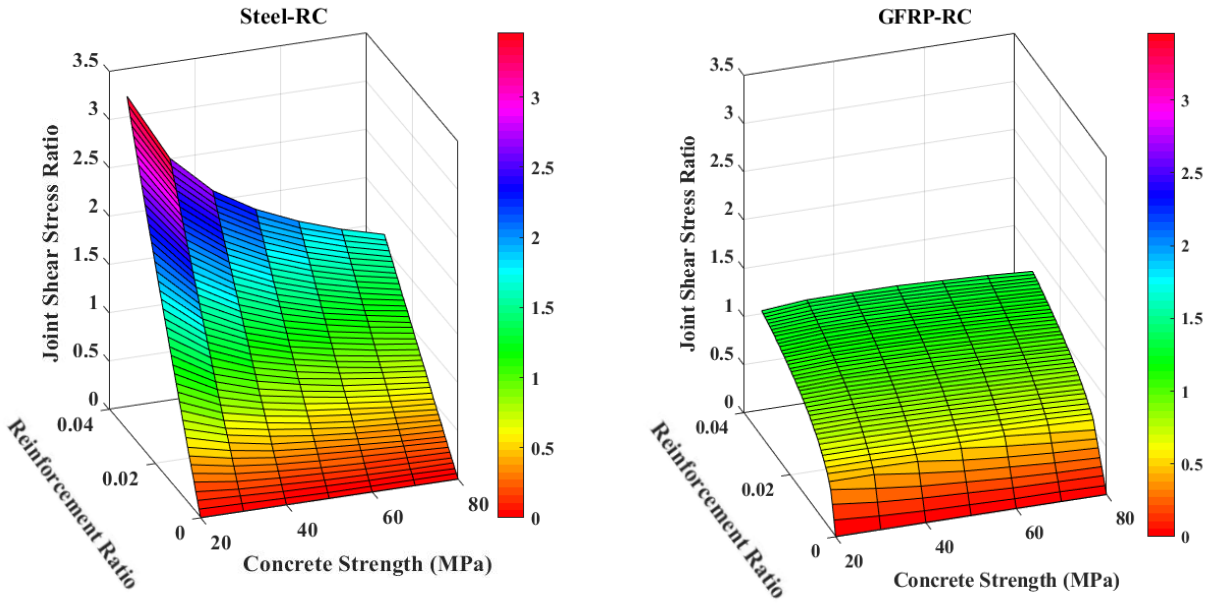

Figure 3.20 - Relationship between joint shear stress ratio, concrete strength and reinforcement ratio of main beams

As shown in the graphs of Figure 3.21, the joint shear stress in steel-RC joints show higher sensitivity to reinforcement ratio of the main beams and concrete strength. Figure 3.21-a indicates that although at lower reinforcement ratios, GFRP-RC joints exhibit higher joint shear stresses compared to their steel-RC counterparts, steel-RC beam-column joints surpass the GFRP-RC beam-column joints in terms of joint shear stress at higher reinforcement ratios.

Moreover, as shown in Figure 3.21-b, with the increase in concrete compressive strength the joint shear stress ratio in a GFRP-RC beam-column joint remains approximately constant while the joint shear stress ratio drops significantly in a steel-RC beam-column joint.

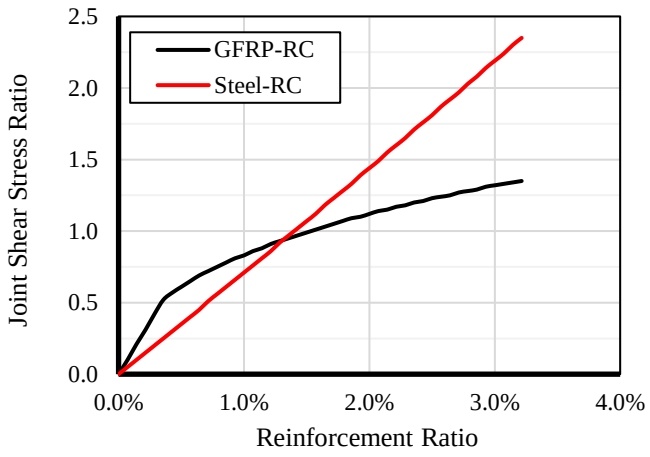

(a) Joint shear stress ratio-reinforcement ratio of beam at 40 MPa concrete strength

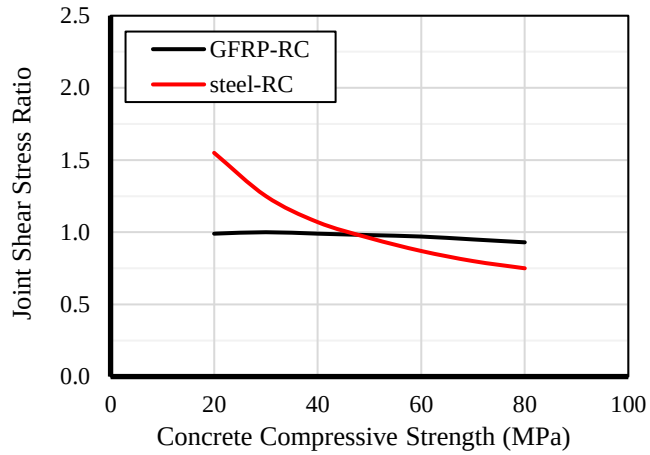

(b) Joint shear stress ratio-concrete compressive strength at 1.5% reinforcement ratio

Figure 3.21 - Relationship between joint shear stress ratio and longitudinal reinforcement ratio of main beams and concrete compressive strength

3.4 Conclusions

Based on the results obtained from testing of 4 full-scale interior beam-column joints, the following conclusions can be made:

- All GFRP-RC specimens tested in this program were able to achieve their design capacity. This indicates that interior GFRP-RC beam-column joints with lateral beams covering 60% of the joint area are able to withstand joint shear stress ratio of $1.8\sqrt{f'_c}$.
- After reaching the design capacity, all tested GFRP-RC beam-column joints exhibited a gradual decrease in lateral load carrying capacity without rupture of reinforcement up to 7% or 8% drift ratio. This indicates that GFRP-RC beam-column joint can be designed in a manner that allows them to reach significantly high lateral drift ratios without exhibiting brittle failure.
- The maximum strain measured in the joint lateral reinforcement (stirrups) remained lower than the limit suggested by the CSA/S806-12 (CSA 2012) up to 5% drift ratio during both first and second loading phases. This observation along with insignificant concrete damage in the joint area up to 5% drift ratio indicated that the requirements of the CSA/S806-12 (CSA 2012) for confinement of columns in seismic regions are adequate.
- Including the effect of secondary moments due to P-delta effect resulted in reaching the design capacity of the columns prior to design capacity of the beams in the GFRP-RC beam-column joints. This behaviour does not agree with the strong-column-weak-beam concept suggested by CSA/S806-12 (CSA 2012). Based on the results obtained from the steel-RC specimen with an axial load of 650 kN, a value of 1.2 for the minimum column-to-beam flexural strength ratio is suggested.
- Unlike the ductile performance of steel reinforcement, the linear nature of the GFRP reinforcement resulted in lower energy dissipation of the GFRP-RC specimen (G-1.5) compared to its steel-RC counterpart specimen (S-1.5) with the same magnitude of joint shear stress. Specimen S-1.5 showed 1.44- and 3.06-times higher energy dissipation than

Specimen G-1.5 at 2% and 5% drift ratio, respectively. Moreover, test results indicated that the increase in the joint shear stress increases the magnitude of energy dissipation in GFRP-RC beam-column joints.

- Investigating the tri-relationship between joint shear stress ratio, longitudinal reinforcement ratio and concrete compressive strength in the joints indicated that the joint shear stress ratio in GFRP-RC beam-column joints are less sensitive to the reinforcement ratio and concrete compressive strength compared to their steel-RC counterparts.

4 EFFECT OF GEOMETRICAL CONFIGURATION ON SEISMIC BEHAVIOUR OF GFRP-REINFORCED CONCRETE BEAM-COLUMN JOINTS

Shervin K. Ghomi and Ehab El-Salakawy

Submitted to the International Journal of Earthquake and Structures, May 2019.

Abstract: Glass fiber reinforced polymer (GFRP) bars have been introduced as an effective alternative for the conventional steel reinforcement in concrete structures to mitigate the costly consequences of steel corrosion. However, despite the superior performance of these composite materials in terms of corrosion, the effect of replacing steel reinforcement with GFRP on the seismic performance of concrete structures is not fully covered yet. To address some of the key parameters in the seismic behaviour of GFRP-reinforced concrete (RC) structures, two full-scale beam-column joints reinforced with GFRP bars and stirrups were constructed and tested under two phases of loading, each simulating a severe ground motion. The objective was to investigate the effect of damage due to earthquakes on the service and ultimate behaviour of GFRP-RC moment-resisting frames. The main parameters under investigation were geometrical configuration (interior or exterior beam-column joint) and joint shear stress. The performance of the specimens was measured in terms of lateral load-drift response, energy dissipation, mode of failure and stress distribution. Moreover, the effect of concrete damage due to earthquake loading on the performance of beam-column joints under service loading was investigated and a modified damage

index was proposed to quantify the magnitude of damage in GFRP-RC beam-column joints under dynamic loading. Test results indicated that the geometrical configuration significantly affects the level of concrete damage and energy dissipation. Moreover, the level of residual damage in GFRP-RC beam-column joints after undergoing lateral displacements was related to reinforcement ratio of the main beams.

Keywords: GFRP-RC, Seismic performance, Cyclic loading, Beam-column joints, Reinforcement ratio, Latera load-drift response, Interior beam-column joints, Exterior beam-columns, Damage index.

4.1 Introduction

Beam-column joints are key elements in defining seismic behaviour of moment-resisting frames in terms of lateral stiffness and energy dissipation. Moreover, failure of these elements during an earthquake can lead to partial or even total failure of the structure. Steel-reinforced concrete (RC) moment-resisting frames are considered as one of the main lateral load resisting systems in buildings. Therefore, various parameters affecting the seismic behaviour of steel-RC beam-column joints have been extensively studied (Hanson and Connor 1967; Paulay et al. 1978; Ehsani and Wight 1985-a; Ehsani and Wight 1985-b; Kim and LaFave 2007; Le-Trung et al. 2013).

However, replacing the steel reinforcement with alternative materials may be undertaken by structural designers to achieve superior performance in specific aspects, which can affect the seismic behaviour of moment-resisting frames. For example, fiber reinforced polymers (FRP) are used as an effective alternative reinforcement to improve the performance of RC structures in terms of corrosion resistance, especially in harsh environments. However, the possible effects that

this replacement can have on seismic performance of beam-column joints, which in turn affect the seismic behaviour of moment-resisting frames, is not fully understood yet.

Among various types of FRP materials commonly available in the construction industry, Glass-FRP (GFRP) is considered the most suitable option for seismic design (Ghomi and El-Salakawy 2016; Hasaballa and El-Salakawy 2016). This is due to the relatively high tensile strength and low modulus of elasticity of GFRP materials that allows them to withstand significantly large deformations prior to rupture. This characteristic, so-called "deformability", compensates for the lack of ductility in FRP-RC beam-column joints caused by the linear elastic stress-strain relationship of FRP material without any yielding (as oppose to conventional steel reinforcement).

Ghomi and El-Salakawy (2016) and Hasaballa and El-Salakawy (2016) studied the seismic behaviour of various exterior GFRP-RC beam-column joints and observed that well-designed GFRP-RC beam-column joints can withstand lateral drift ratios as high as 9% without exhibiting brittle failure. Since 9% lateral drift ratio is much more than what is generally expected from a beam-column joint in a regular moment-resisting frame, it was concluded that GFRP-RC elements can be used in seismic regions.

Moreover, the authors concluded that, due to the linear elastic nature of GFRP materials, exterior GFRP-RC beam-column joints exhibit significantly lower residual damage after a seismic event compared to steel-RC counterparts. This feature can significantly reduce the cost of repair or eliminate the need for demolishing the structure after an earthquake event.

However, following an earthquake, the service and ultimate performance of a GFRP-RC moment-resisting frame has to be determined to assess the ability of the structure to remain in service.

Therefore, the magnitude of damage and its effect on GFRP-RC moment frames, under reversed-cyclic loading must be investigated.

To address this gap, two full-scale GFRP-RC beam-columns joints were constructed and tested under multiple reversal loading schemes. The magnitude of damage, energy dissipation, mode of failure and stress distribution at various loading stages are investigated. Moreover, the performance of the specimens under service loading after surviving various intensity of earthquake loadings was studied.

Although several quantitative measures of deterioration of steel-RC structures under reversal loadings have been proposed in the literature, up to date, no model has been developed to quantify the magnitude of damage in GFRP-RC elements. Therefore, in the current program a modified damage index based on the model proposed by Park and Ang (1985) is proposed as a tool to measure the magnitude of damage in GFRP-RC beam-column joints under dynamic loadings.

Recently, several studies have investigated the seismic performance of FRP-RC beam-column joints and various key parameters such as type of reinforcement, joint shear stress, presence of lateral beams, reinforcement detailing and concrete strength (Fukuyama et al. 1995; Said and Nehdi 2004; Mady et al. 2011; Ghomi and El-Salakawy 2016; Hasaballa and El-Salakawy 2016). However, there are still many parameters affecting the behaviour of GFRP-RC beam-column joints that are not fully explored.

Although the effect of joints' geometrical configuration (interior and exterior connections) has been established for steel-RC (ACI, 2002), up to date, no clear comparison between the seismic behaviour of interior and exterior GFRP-RC beam-column joints has been performed. Therefore,

in the current program, the effect of geometrical configuration on the seismic performance of GFRP-RC beam-column joints is investigated.

4.2 Experimental Program

4.2.1 Test specimens

Two full-scale GFRP-RC beam-column joints were constructed and tested under quasi-static reversal cyclic loading. Figure 4.1 shows dimension of the specimens. Height of the columns and length of the beams were 2,655 and 2,100 mm, respectively. Dimensions of the lateral beams were proportioned to cover approximately 60% of the joint area. Both specimens were designed to have a maximum joint shear stress of $1.3\sqrt{f'_c}$.

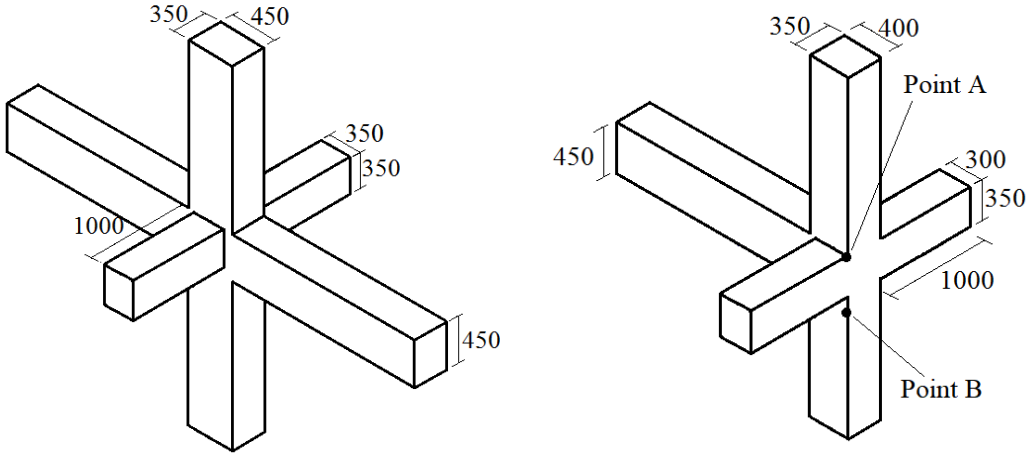

(a) Interior beam-column joint (b) Exterior beam-column joint

Figure 4.1 - Dimensions of test specimens (dimensions in mm)

The maximum joint shear stress in the specimens was calculated at middle-height of the joint area according to the free-body diagrams (hatched areas) shown in Figure 4.2. In Figure 4.2, V_j indicates the shear force at mid-height of the joint, T_r indicates tensile force applied to the joint by the longitudinal reinforcement in the main beam, C_c indicates compressive force applied to the joint

by the concrete compressive block and V_c indicates the shear force applied to the joint by the column.

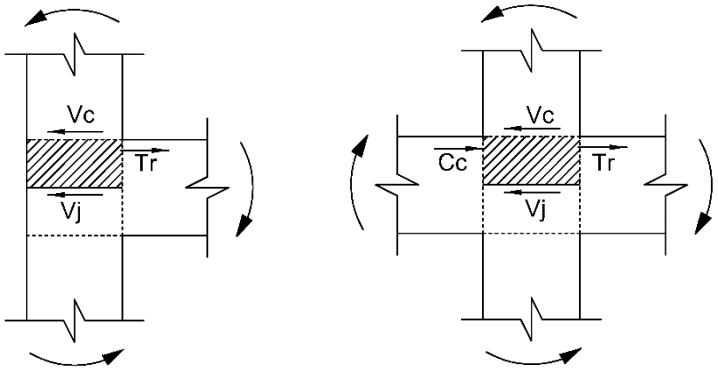

Figure 4.2 - Free-body diagrams to calculate shear force at mid-height of joints

One of the main parameters previously studied by the authors (Ghomi and El-Salakawy 2016) was joint shear stress in exterior beam-column joints. The authors attempted to introduce a joint shear stress limit as the allowable stress in exterior GFRP-RC beam-column joints. The authors tested three full-scale exterior beam-column joints with joint shear stresses of $0.85\sqrt{f'_c}$, $1.0\sqrt{f'_c}$and$1.1\sqrt{f'_c}$. Test results indicated that GFRP-RC exterior beam-column joints can withstand all three levels of joint shear stress tested. Therefore, it still remains unknown that whether such beam-column joints can withstand higher levels of joint shear stresses or not. Therefore, in this program, the joint shear stress of $1.3\sqrt{f'_c}$ was selected as the baseline for the design of test specimens.

The results obtained from testing the exterior specimen (with joint shear stress of $1.3\sqrt{f'_c}$ is compared to the findings of Ghomi and El-Salakawy (2016) from testing an exterior GFRP-RC beam-column joint with the same dimensions but different number of longitudinal bars in the main beam, which resulted in a different level of joint shear stress $1.0\sqrt{f'_c}$.

The specimens presented in this document are designated with a two-part name, the first part indicating the type of connection ("Ex" for exterior beam-column joints and "In" for interior beam-column joint) and the second part indicating the level of joint shear stress ("1.0" for joint shear stress of $1.0\sqrt{f'_c}$ and "1.3" for joint shear stress of $1.3\sqrt{f'_c}$. Reinforcement detailing of the test specimens, In-1.3 and Ex-1.3, and the beam-column joint previously tested by Ghomi and El-Salakawy (2016), Ex-1.0, are shown in Figure 4.3.

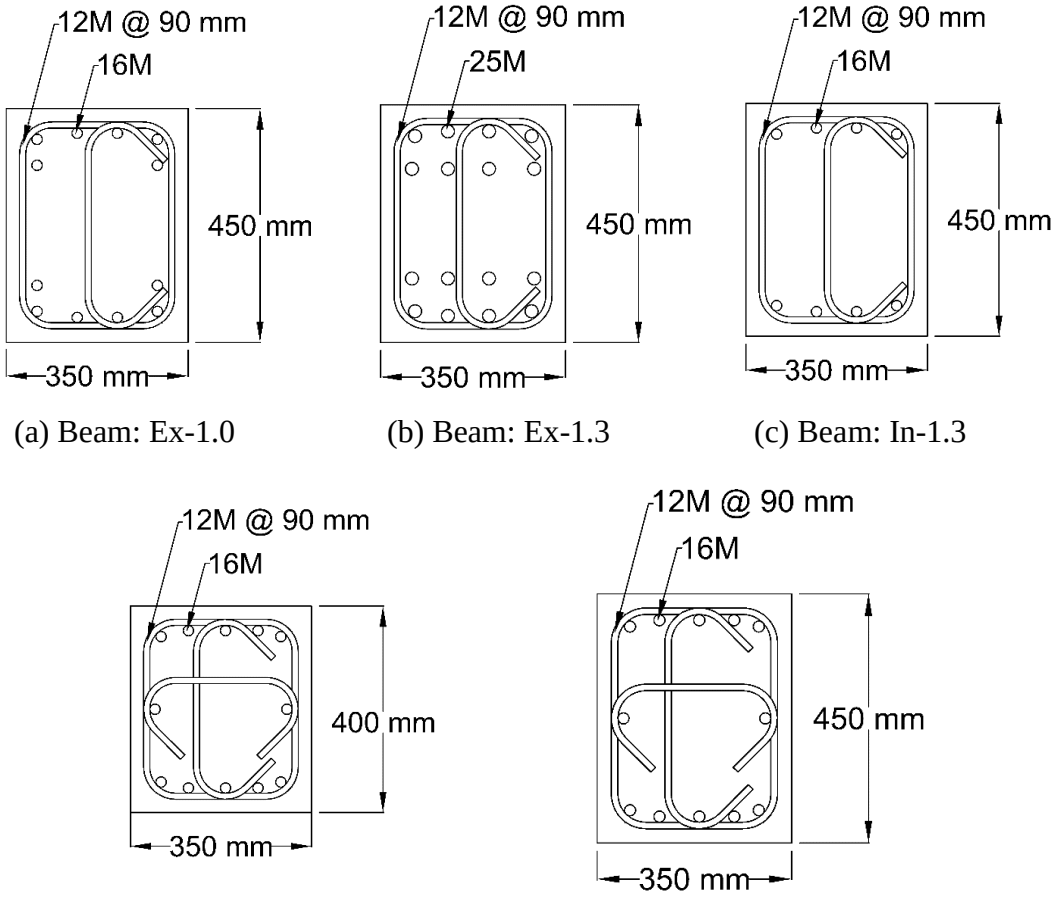

(a) Beam: Ex-1.0 (b) Beam: Ex-1.3 (c) Beam: In-1.3

(d) Column: exterior joint (e) Column: interior joint

Figure 4.3 - Reinforcement detailing of test specimens

Table 4.1 shows the properties of test specimens based on the compressive strength of concrete on the day of testing. In the exterior specimens, the longitudinal reinforcement of the beam was bent into the column to provide sufficient anchorage.

Table 4.1 - Specimens' properties

Specimen	Beam Reinforcement (Top and Bottom)	Beam Flexural Capacity (kN.m)	Column Flexural Capacity[(a)] (kN.m)	Flexural Ratio	Shear Ratio	Concrete Strength f'_c (MPa)	Reinforcement Ratio of Beam
Ex-1.0	6-20M	352	254	1.45	0.96	47	1.34%
Ex-1.3	8-25M	454	262	1.15	1.29	49	3.05%
In-1.3	4-16M	264	280	1.06	1.30	38	0.57%

[(a)] Includes the effect of column axial load

4.2.2 Material

Ready-mix concrete with target 28-day compressive strength of 40 MPa were used to cast the test specimens. The actual concrete compressive strength was measured through standard compressive test of 150 × 300 mm cylinders. The concrete compressive strength of each specimen on the day of testing is presented in Table 4.1.

Sand-coated GFRP bars and stirrups were used to reinforce the test specimens in the current program (Ex-1.3 and In.1.3). The mechanical properties of the reinforcement, as provided by the manufacturer (Pultrall Inc. 2019), are presented in Table 4.2. As mentioned earlier, bent bars were used to anchor longitudinal bars of the main beam into the joint area of Specimen Ex-1.3. The ultimate tensile strength and modulus of elasticity of the longitudinal bars in the main beam of Specimen Ex-1.0 were reported by the manufacturer (Schoeck Canada Inc. 2019) as 850 MPa and 50 GPa, respectively. Details of the mechanical properties of the reinforcement of Specimen Ex-1.0 are provided elsewhere (Ghomi and El-Salakawy 2016).

Table 4.2 - Reinforcement properties

Reinforcement Type	Tensile Strength (MPa)	Modulus of Elasticity (GPa)	Ultimate Tensile Strain (micro-strain)	Area (mm^2)
Straight Bars	1,184	62.6	18,900	198
Bent Bars*	992	50.0	19,850	507
Stirrups and Ties*	1,022	50.0	20,450	71

*Properties provided in the table are corresponding to the straight portion of the bar

4.2.3 Test set-up

The specimens were tested while the columns and the beams were in vertical and horizontal position, respectively (Figure 4.4). The specimens were isolated from the assumed points of zero-moments in an arbitrary moment-resisting frame. Therefore, a roller and a pin boundary condition were simulated in the test set-up at tips of the beams and bottom of the columns, respectively.

Figure 4.4 - Test set-up

The roller boundary condition was simulated by means of a link (double-hinged element). The links were connecting the tips of the beams to the laboratory strong floor. The pin boundary

condition was simulated by means of a hinge at the bottom of the column. Similar to the links, the hinge was also attached to the strong floor by the pre-stressing force of four dywidag bars.

A fully dynamic 1000-kN capacity actuator was mounted on a strong concrete wall and was attached to upper tip of the column to apply reversal cyclic loading to simulate a seismic event. the columns were also under constant axial load during the test by means of a hydraulic jack reacting against a stiff steel beam on top of the specimens. The stiff steel beam was connected to the strong floor by means of two double-hinged elements to allow for its free movement while the actuator applies reversal loadings to the column by pivoting about the axis of the pin in the bottom hinge.

Therefore, the line of action of the column axial load always passed through the center of the pin of the hinge at the bottom of the column. This was done to eliminate secondary moments in the column due to the distance between center of gravity of the column and the line of action of the axial load.

4.2.4 Loading scheme

Figure 4.5 shows the loading scheme that was used to test the specimens in this program. The general scheme of the loading procedure was in displacement-controlled mode and was obtained from the ACI 374.1-05 report (ACI Committee 374 2005).

In this program, the specimens were tested under two loading phases. In the first phase, the specimen was tested according to a loading scheme that simulated a severe earthquake up to 5% drift ratio. Then the specimen was re-loaded up to failure following the same loading scheme in

the second loading phase to study their performance in ultimate loading state after surviving an earthquake.

Based on orientation of the specimens in the test set-up that was used in this program, the lateral drift ratio was defined as the ratio of column tip displacement to column height.

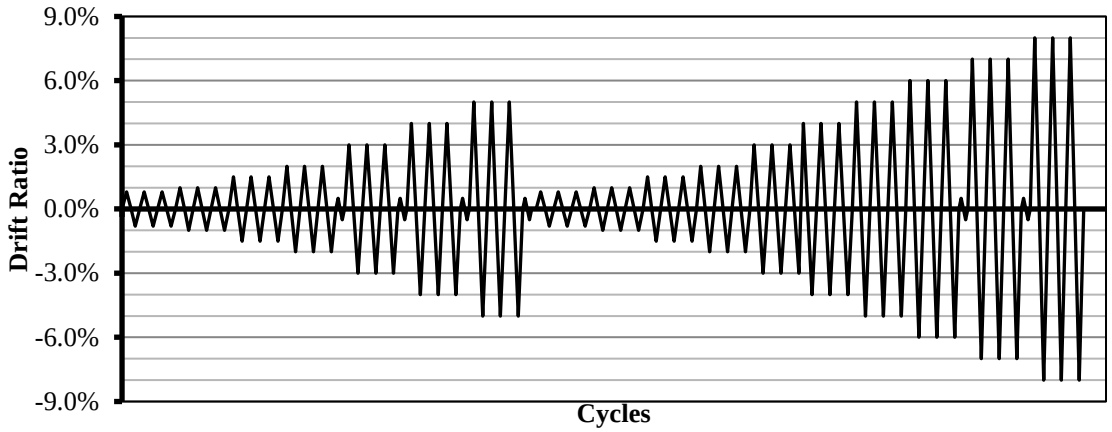

Figure 4.5 - Loading scheme

The loading scheme consisted of several loading steps gradually increasing in lateral drift ratio. Each loading step included three identical loading cycles. After 2% drift ratio, one load-controlled cycle with an amplitude equal to service load was applied after each loading step. the service load condition was defined as the state corresponding to 25% of the ultimate strain capacity of the longitudinal GFRP bars in the beams.

4.3 Test Results and Discussions

4.3.1 Lateral load-drift response

The relationship between the load at tip of the column (actuator load) and the lateral drift ratio (hysteresis diagram) of the test specimens are shown in Figure 4.6-a and Figure 4.6-b. Moreover, the column lateral load-drift response corresponding to the exterior beam-column joint with joint

shear ratio of $1.0\sqrt{f'_c}$, previously tested by the authors (Ghomi and El-Salakawy 2016) is shown in Figure 4.6-c for comparison. The dashed lines in the hysteresis diagrams show the design capacity of the specimens, defined as the column lateral load that results in the maximum design bending moment in the main beams.

It should be mentioned that, the test set-up used to test Specimen Ex-1.0 was different from the set-up used to test the specimens in the present program (Specimen Ex-1.3 and Specimen In-1.3). Details of the test set-up used for testing Specimen Ex-1.0 are presented elsewhere (Ghomi and El-Salakawy 2016). However, it should be mentioned that despite the different test set-ups, the same loading configuration was applied to all specimens included in this paper; therefore, the results are comparable.

Comparing the hysteresis diagram of interior and exterior specimens indicates asymmetric behaviour of the exterior beam-column joints compared to the interior one. Specimen In-1.3 showed very similar behaviour in both negative and positive direction. This is evident by the fact that the specimen reached its design capacity at 5% drift ratio in both positive and negative direction.

The exterior specimens (Ex-1.0 and Ex-1.3), on the other hand, showed slightly higher stiffness during loading in the positive direction than the negative direction. The specimens reached their design capacity at 4% and 5% drift ratios in positive and negative directions, respectively. This could be due to asymmetric geometry of the exterior beam-column joints.

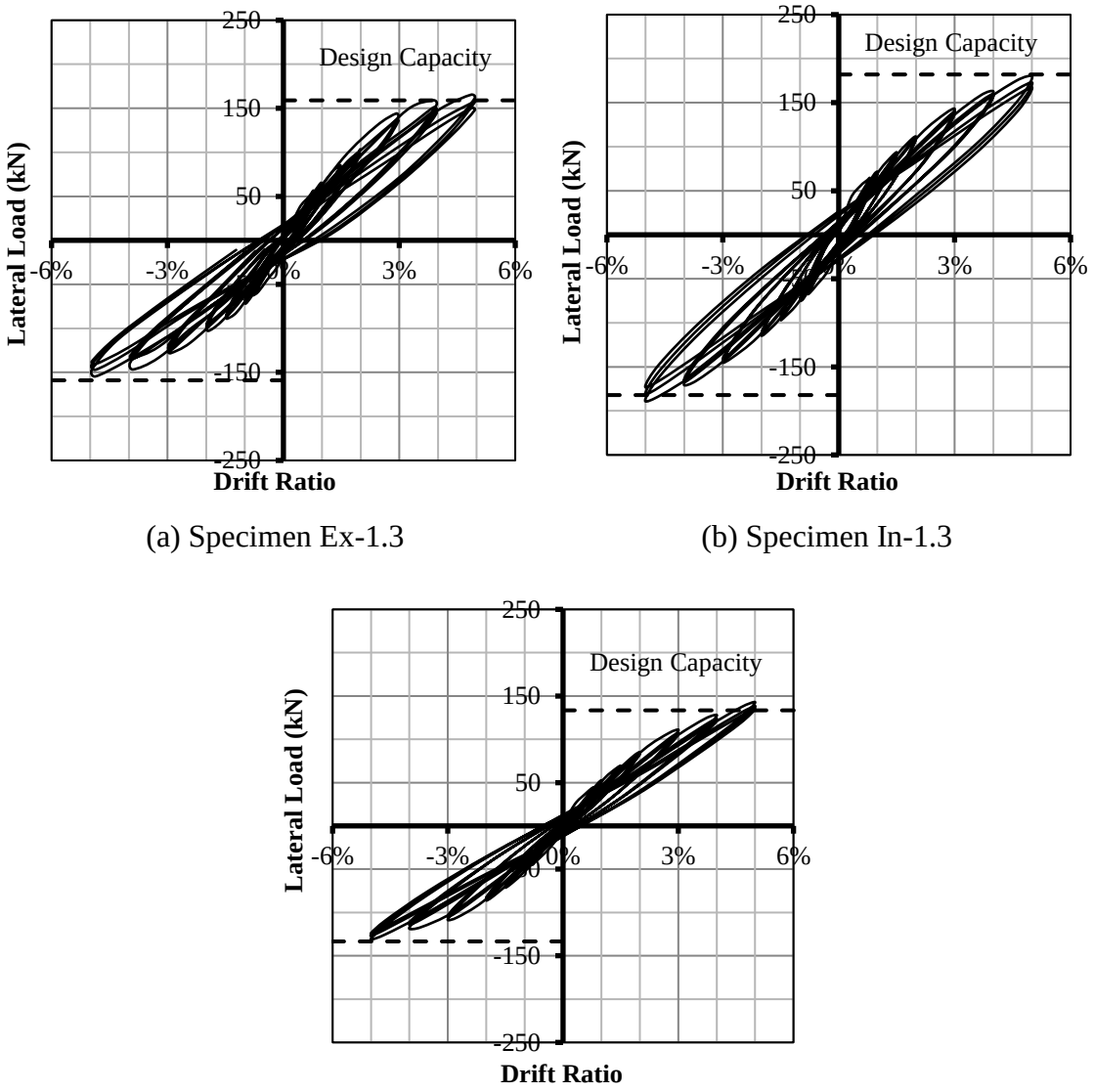

(a) Specimen Ex-1.3

(b) Specimen In-1.3

(c) Specimen Ex-1.0

Figure 4.6 - Lateral load-drift response of test specimens during the first loading phase

As shown in Figure 4.1, centerline of the lateral beams in the exterior beam-column joints does not coincide with center point of the joints as the lateral beams are flush with the backside of the column and topside of the main beam. With this configuration, Point A is confined by the lateral beams while there was no confinement at Point B (Figure 4.1). Therefore, the concrete in the vicinity of Point A provided higher compressive resistance compared to the concrete in the vicinity

of Point B. Consequently, the test specimens showed higher lateral load carrying capacity when the columns were pushed toward the positive direction (Point A in compression) and lower capacity when the columns were pulled toward the negative direction (Point B in compression). The interior specimen; however, due to symmetrical geometry with respect to centerline of the column, exhibited similar behaviour in both positive and negative direction.

By reaching its maximum bending capacity, the main beam in Specimen Ex-1.3 exerted a joint shear stress of $1.3\sqrt{f'_c}$ (as shown in Table 4.1). Therefore, it can be concluded that GFRP-RC exterior beam-column joints with the geometrical configuration tested in this program are able to withstand joint shear stress of $1.3\sqrt{f'_c}$.

All specimens were able to reach their design capacity prior to 5% drift ratio without exhibiting significant concrete damage. However, the magnitude of observed residual displacement varied among the specimens. Figure 4.7 shows residual displacement of the specimens at tip of the columns after each loading step during the first loading phase. The residual displacements were measured at the point of zero lateral load.

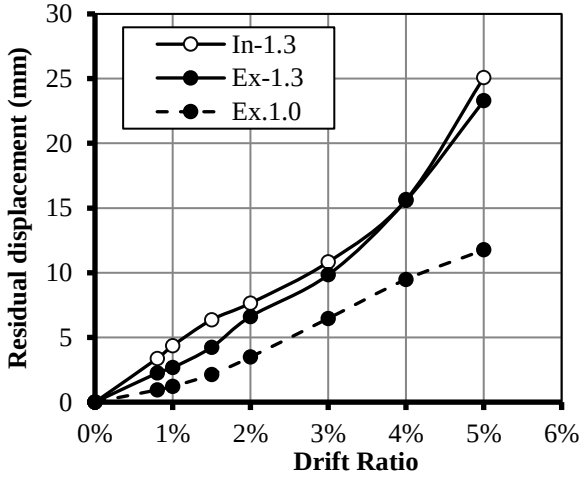

Figure 4.7 - Residual displacement of tip of columns during the first loading phase

As indicated in Figure 4.7, the increase in joint shear stress of exterior beam-column joints increased the magnitude of residual damage. This is due to higher concrete damage induced to the joint area because of higher joint shear stresses. This can be also observed in the hysteresis diagrams by wider loops in response of Specimen Ex-1.3 compared to that of Specimen Ex-1.0.

In general, Specimen In-1.3 showed slightly more residual deformation compared to Specimen Ex-1.3, with the same level of joint shear stress. That could be attributed to the fact that Specimen In-1.3 contained more concrete volume compared to Specimen Ex-1.3, which resulted in more areas that inelastic deformation due to concrete damage (cracks) occurred.

As mentioned earlier, the beam-column joints in the current program were tested under a two-phase loading scheme. Figure 4.8 shows hysteresis diagram of Specimens In-1.3 and Ex-1.3 during the second loading phase. The hysteresis loops of the last loading step (failure) is shown with dashed lines in Figure 4.8.

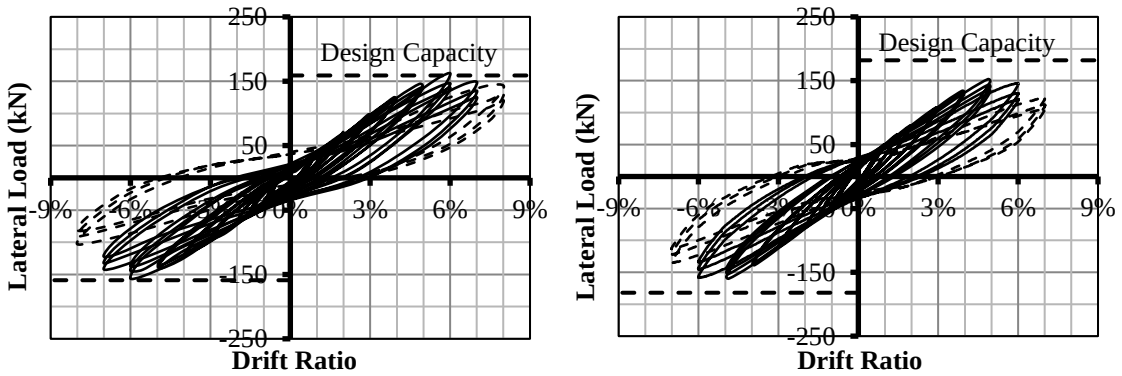

(a) Specimen Ex-1.3 (b) Specimen In-1.3

Figure 4.8 - Lateral load-drift response of test specimens during the second loading phase

As expected, the specimens showed linear behaviour up to 5% drift ratio during the second loading phase. Specimen Ex-1.3 and In-1.3 reached their maximum lateral load during the second loading phase at 6% and 5% lateral drift ratio, respectively. Both specimens exhibited gradual decrease in

lateral load carrying capacity after reaching the maximum lateral load during the second loading phase until the failure was observed in the specimens (8% and 7% in Specimen Ex-1.3 and In-1.3, respectively).

According to ACI 374.1-05 (ACI Committee 374 2005), the failure was defined as the stage at which the lateral load carrying capacity of the specimens decreased less than 75% of the maximum lateral load.

Figure 4.9 compares lateral load envelopes of Specimens In-1.3 and Ex-1.3 during the first and the second loading phase. The linear behaviour of the specimens during the second loading phase up to 5% drift ratio is indicated by a straight line connecting the origin to the maximum lateral load that the specimens obtained during the third cycle of the 5% drift ratio-loading step in the first loading phase.

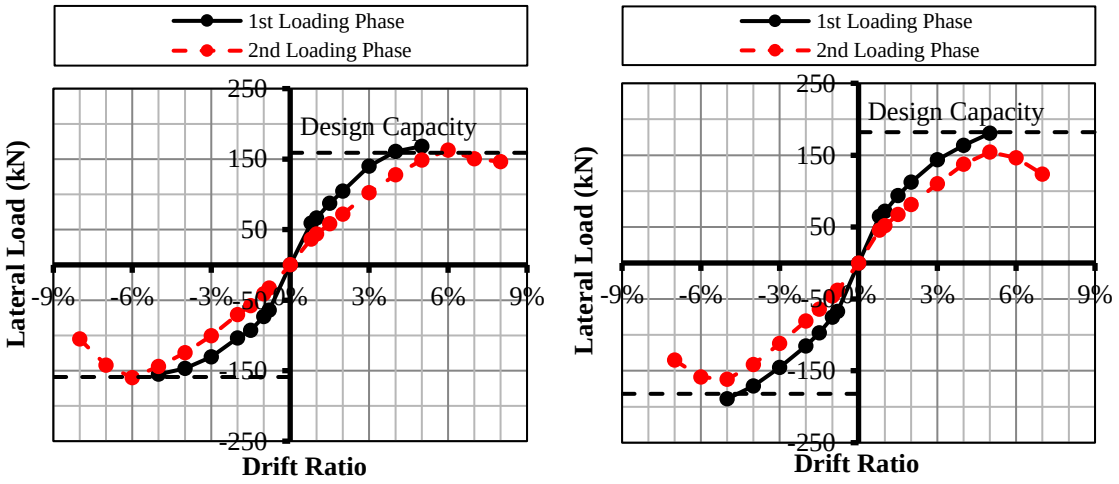

(a) Specimen Ex-1.3 (b) Specimen In-1.3

Figure 4.9 - Lateral load envelope of test specimens during the first and the second loading phase

Specimen Ex-1.3 was able to reach its design capacity during the second loading phase while Specimen In-1.3 with the same magnitude of joint shear stress only reached 85% and 89% of the

design capacity in positive and negative direction during the second loading phase, respectively. However, this observation was opposite to what was expected. In general, the interior beam-column joint was expected to exhibit less loss in lateral load carrying capacity compared to the exterior beam-column joint because of more confinement provided to the joint area from the main beams on each side of the joint.

However, the authors believe the main reason for the better performance of Specimen Ex-1.3 compared to Specimen In-1.3 during the second loading phase is the more confinement in the main beams provided by the longitudinal reinforcement. As shown in Figure 4.3, the main beam in Specimen Ex-1.3 are heavily reinforced with two layers of 25M bars, while the beams in Specimen In-1.3 are only reinforced with one layer of reinforcement. Thus, less confinement is provided to the concrete core in the main beams of Specimen In-1.3. This resulted in more concrete damage in the main beams which led to more loss in the lateral load carrying capacity in Specimen In-1.3 compared to Specimen Ex-1.3.

4.3.2 Mode of failure

Figure 4.10 shows the condition of the test specimens at the end of the first loading phase (5% drift ratio). As shown in the figure, in both specimens, concrete damage is only limited to concrete cover spalling in the main beam adjacent to the column. Since the GFRP-RC beam-column joints were designed as over-reinforced sections (failure occurs due to crushing of concrete), the concrete cover spalling observed in the beams was indicating that maximum bending moment capacity of the beam section was reached.

(a) Specimen Ex-1.3

(b) Specimen In-1.3

Figure 4.10 - Condition of test specimens at the end of the first loading phase

Figure 4.11 shows condition of Specimens In-1.3 and Ex-1.3 at failure during the second loading phase. As shown in the pictures, Specimen Ex-1.3 exhibited severe concrete damage in the joint area, while the joint in Specimen In-1.3 with the same amount of joint shear stress remained intact. This was due to the additional confinement provided to the joint area by the main beams on the opposite sides of the joint in the interior specimen, which increased concrete strength in the joint area and reduced the damage.

However, as shown in the hysteresis diagrams of specimens, both specimens failed due to gradual decrease in lateral load carrying capacity without exhibiting any brittle failure or sudden rupture

of the GFRP reinforcement. This was due to the significant reserve of strain in the longitudinal bars of the main beams (difference between measured strain and strain capacity). The authors concluded that providing this methodology in designing GFRP-RC sections can prevent brittle failure of GFRP-RC moment-resisting frames during an earthquake.

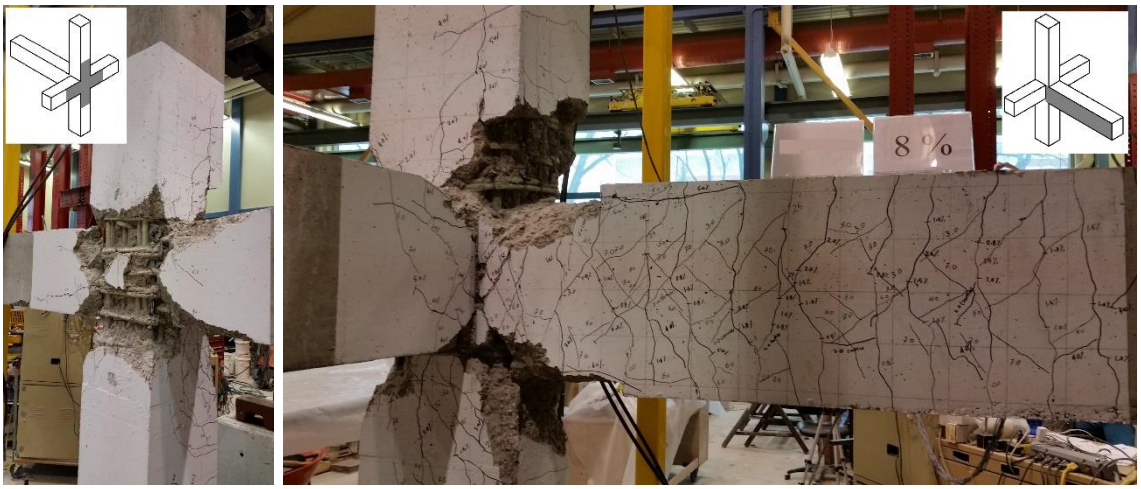

(a) Specimen Ex-1.3

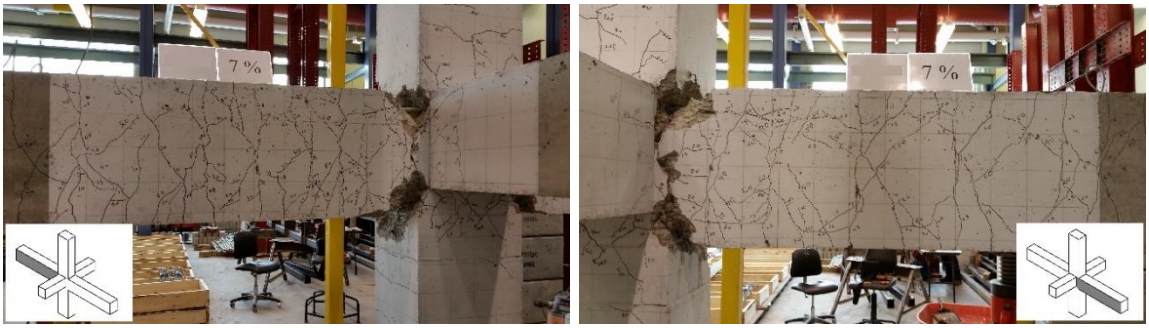

(b) Specimen In-1.3

Figure 4.11 - Condition of test specimens at failure

4.3.3 Strain-drift response

The specimens were well instrumented with electrical strain gauges installed on the internal GFRP reinforcement in various locations including 6 gauges on transverse reinforcement (stirrups) in the

joint area. Figure 4.12 shows the maximum strain obtained from those strain gauges at each drift ratio.

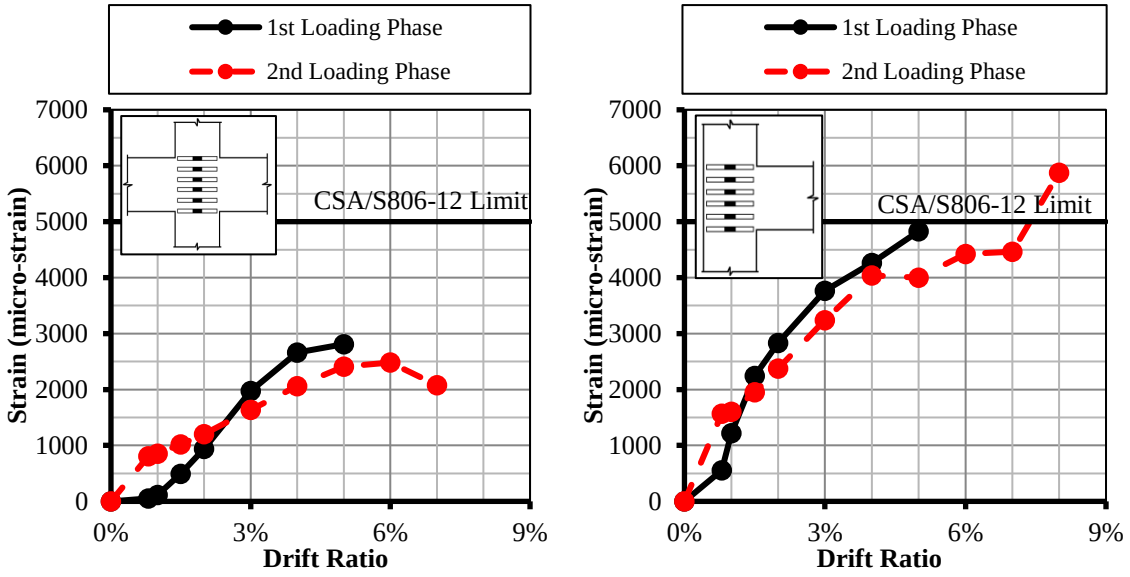

(a) Specimen In-1.3 (b) Specimen Ex-1.3

Figure 4.12 - The maximum strains in joint stirrups

Although both Specimens Ex-1.3 and In-1.3 were designed with the same maximum joint shear stress, it can be seen from the graphs in Figure 4.12 that the maximum measured strain in the joint stirrups of Specimen In-1.3 were significantly lower than those in Specimen Ex-1.3. This indicates more concrete damage in the joint of Specimen Ex-1.3 due to less confinement (as explained earlier), which increased shear stresses in the joint stirrups.

The solid horizontal lines in the graphs of Figure 4.12 indicate the maximum allowable strain in FRP stirrups according to CSA/S806-12 (CSA 2012). As shown in the graphs, this limit was not exceeded in any of the specimens except at 7% drift ratio (failure) in Specimen Ex-1.3. As shown in Figure 4.11, Specimen Ex-1.3 exhibited significant concrete damage in the joint area, which resulted in excessive stresses in the joint stirrups. However, it should be mentioned that 7% drift

ratio is beyond the expected drift ratios of buildings during an earthquake. National Building Code of Canada (NRCC 2015) requires limiting the maximum lateral drift ratio of buildings to 2.5%. Therefore, it can be assumed that the maximum strain in joint stirrups will not exceed the limit set by CSA/S806-12 (CSA 2012) during the expected response range of GFRP-RC buildings to earthquakes.

Figure 4.13 shows the maximum strain observed in the longitudinal bars of the main beams at the column face. Strains recorded from Specimen In-1.3 were significantly higher than those recorded from Specimen Ex-1.3. This was due to the higher reinforcement ratio in Specimen Ex-1.3 than Specimen In-1.3. The effect of reinforcement ratio on the maximum expected strain in the longitudinal bars of the main beams will be discussed in the following section. As shown in Table 4.1, the reinforcement ratio of Specimens In-1.3 was lower than that of Specimen Ex-1.3 (0.57% and 3.05%, respectively).

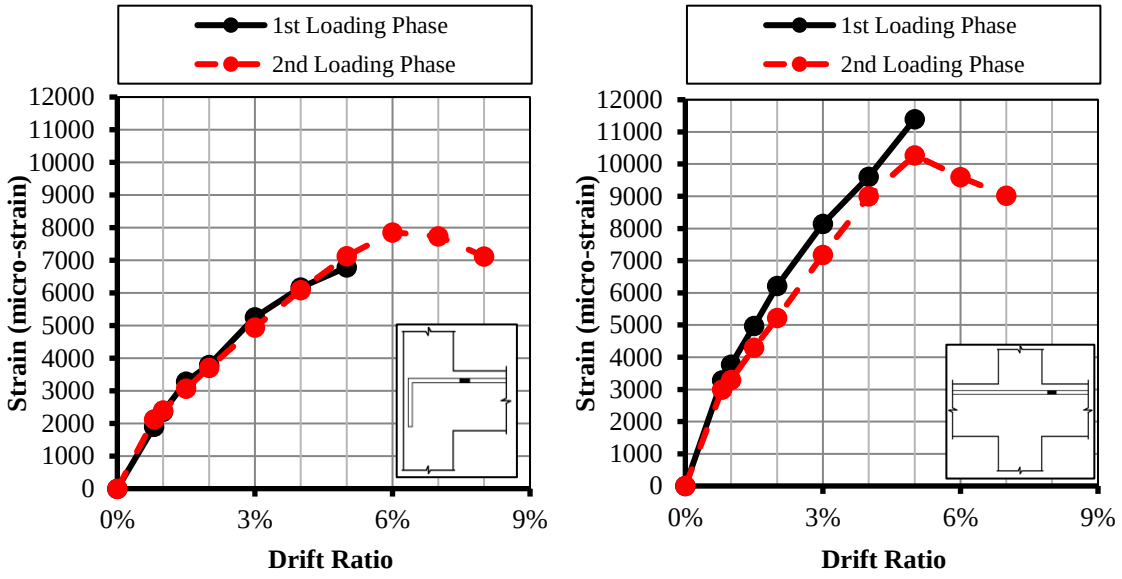

(a) Specimen Ex-1.3 (b) Specimen In-1.3

Figure 4.13 - The maximum strains in longitudinal bars of beams

4.3.4 Effect of reinforcement ratio on maximum tensile strain in longitudinal bars

The maximum expected strain in longitudinal bars of a given GFRP-RC section has direct relationship with the reinforcement ratio. As explained earlier, it is desirable to maintain a margin between the maximum expected tensile strain in GFRP longitudinal reinforcement and their maximum tensile strain capacity.

The effect of reinforcement ratio on the maximum bar strain in an arbitrary section (shown as a thumbnail) is illustrated in Figure 4.14. In the schematic drawing of the arbitrary section, A_s is the area of tensile reinforcement. The same reinforcement properties as those of Specimen Ex-1.3 and In-1.3 were used in producing Figure 4.14. According to CSA/S806-12 (CSA 2012), GFRP-RC beams should be design as over-reinforced sections with provided reinforcement ratios more than the balanced ones (the reinforcement ratio corresponding to simultaneous compressive failure of outer most concrete fiber and tensile failure of outer most reinforcement layer).

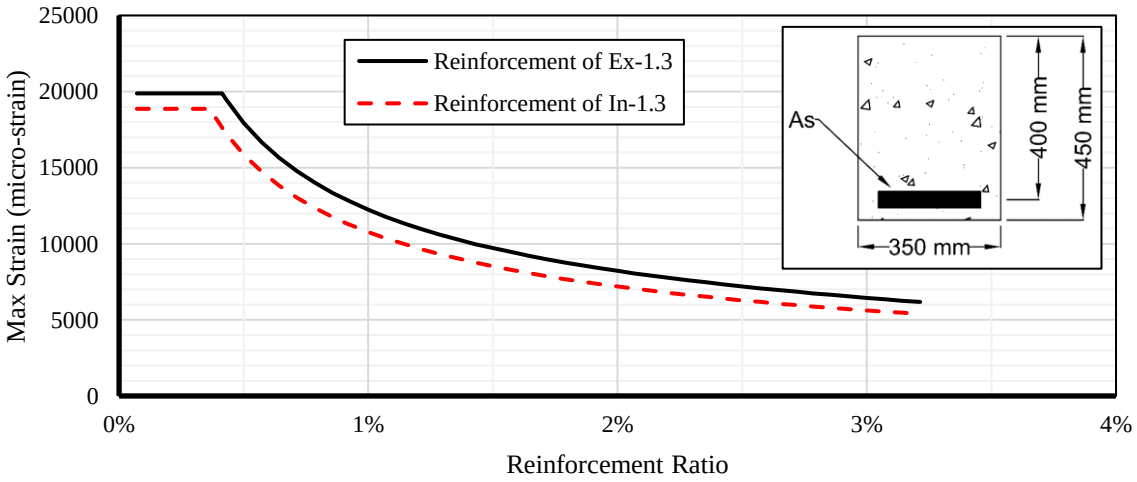

Figure 4.14 - Effect of reinforcement ratio on maximum strain in longitudinal bars

It should be mentioned that the values in Figure 4.14 were calculated as strains in longitudinal bars when the strain at the outermost fiber of the concrete reaches 3,500 micro-strain, the ultimate

compressive strain of concrete according to CSA/A.23-14 (CSA 2014-a). However, as discussed earlier, the concrete section may continue its lateral load carrying further after this stage and exhibit higher strains in the longitudinal reinforcement due to confinement of the concrete core. The effect of such over-strength is not included in Figure 4.14.

The balanced reinforcement ratio for the cross-section under consideration (Figure 4.14) was calculated as 0.41% and 0.36% for reinforcement properties corresponding to Specimens Ex-1.3 and In-1.3, respectively. Therefore, reinforcement ratios lower than that limit resulted in failure of the section due to bar rupture. This is shown in Figure 4.14 as a straight line with value of 19,850 micro-strain and 18,900 micro-strain for Specimen Ex-1.3 and In-1.3, respectively.

As shown earlier in Figure 4.13, Specimen Ex-1.3 and In-1.3 had a reserve of 60% and 40% of their ultimate tensile strain capacity compared to the maximum measured tensile strain in the bars and no bar rupture was observed. Therefore, it was concluded that a margin of 40% of the ultimate tensile strain capacity between the maximum expected tensile strain of the longitudinal bars and their ultimate strain capacity may be sufficient to prevent brittle failure of GFRP bars in beams. Therefore, a threshold of 60% of the ultimate tensile strain capacity for GFRP bars is suggested to be maintained when designing GFRP-RC beam-column joints in seismic regions.

To provide 60% threshold in the arbitrary section under consideration (Figure 4.14), reinforcement ratios more than 1.05% and 0.91% should be provided in the section with the reinforcement properties of Specimen Ex-1.3 and In-1.3, respectively. These reinforcement ratios are approximately 2.5 times more than the balanced reinforcement ratio that is required by CSA/S806-12 (CSA 2012) (0.41% and 0.36% for Specimen Ex-1.3 and In-1.3, respectively). The same

methodology can be used by designers to reduce the risk of brittle failure of GFRP-RC elements during an earthquake event.

4.3.5 Effect of secondary moments

As mentioned earlier, the test set-up used in this program eliminated the effect of secondary moments on the behaviour of the specimens. However, secondary moments induced to columns due to lateral movement of frames can significantly increase the magnitude of moments applied to the columns. This can result in premature failure of the columns and collapse of the moment-resisting frames during an earthquake.

To take into account the effect of secondary moments on the test specimens, the additional moment applied to the columns due to lateral displacements were calculated based on the free-body diagram shown in Figure 4.15. Total bending moment applied to the columns at Point 1, if the line of action of the axial load applied to the columns were kept vertical during the test (which is the case in a real structure during an earthquake), is calculated as:

$$F_L \times l_c + F_A \times \Delta \qquad (4.1)$$

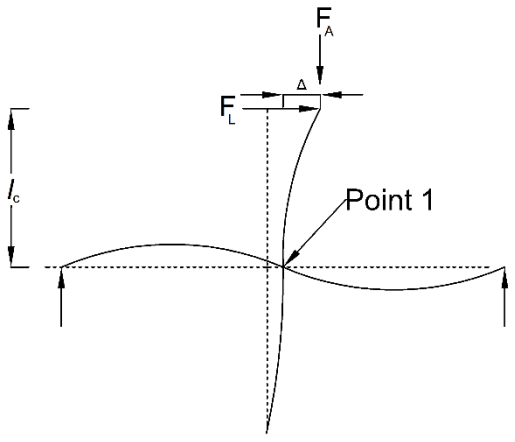

Figure 4.15 - Effect of reinforcement ratio on maximum strain in longitudinal bars

where F_L is the lateral load applied by the actuator to the upper tip of the column, l_c is the distance between the upper face of the main beams and the centre-line of the actuator, F_A is the axial load applied to the column and Δ is the lateral displacement of the column with respect to the joint.

Figure 4.16 compares the maximum bending moments in columns (at top of the joint area, Point 1) of the specimens at each drift ratio with and without considering the secondary bending moments.

As shown in the graphs, including the effect of secondary moments significantly increases the moment applied to the columns at higher drift ratios (19 and 18% at 5% drift ratio in Specimen Ex-1.3 and In-1.3, respectively). Even though none of the test specimens exceeded the bending moment capacity of the columns up to 5% drift ratio (the first loading phase) in the experiment, the graphs indicate that including the effect of secondary moments would result in the column capacities to be exceeded at 4% drift ratio. This could result in premature failure of the moment-resisting frames during an earthquake. Therefore, in this case, the lateral drift ratio of the frame should be limited to 4% drift ratio.

It should be mentioned that the graphs in Figure 4.16 were developed based on the axial load applied to the specimen during testing. The magnitude of axial loads on columns could vary based on their location in the building and level of service load. However, the same procedure can be followed to obtain an appropriate limit for the lateral drift ratio of a moment-resisting frame.

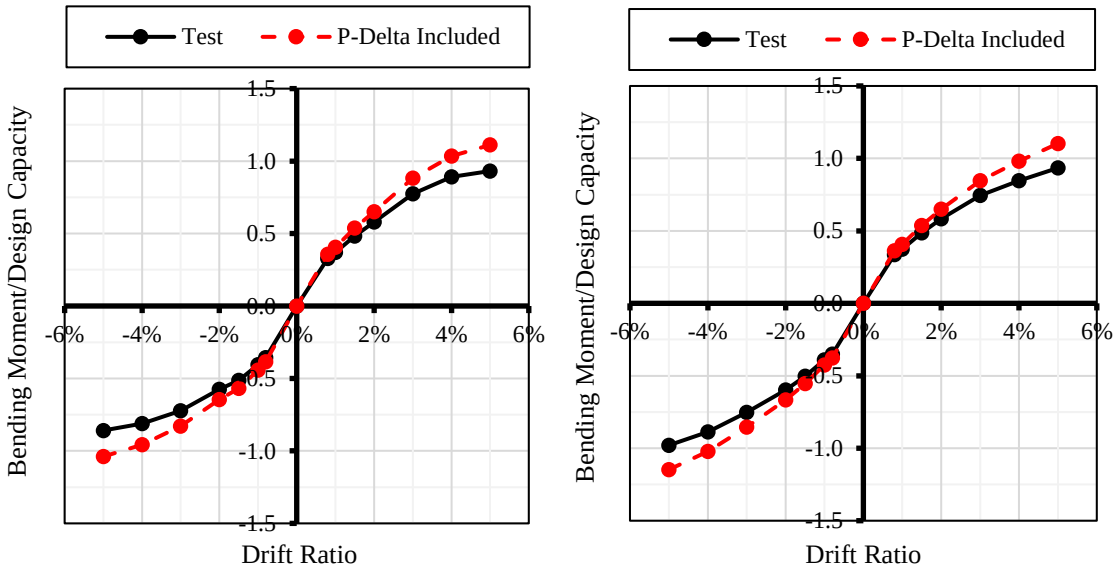

(a) Specimen Ex-1.3 (b) Specimen In-1.3

Figure 4.16 - Effect of secondary moments on bending moments of columns

4.3.6 Energy dissipation and magnitude of damage

The amount of energy dissipated by the specimen during a specific loading cycle was calculated as the area enclosed by loops corresponding to that loading cycle in the lateral load-displacement diagram Figure 4.17 compares the cumulative energy dissipation of the test specimens.

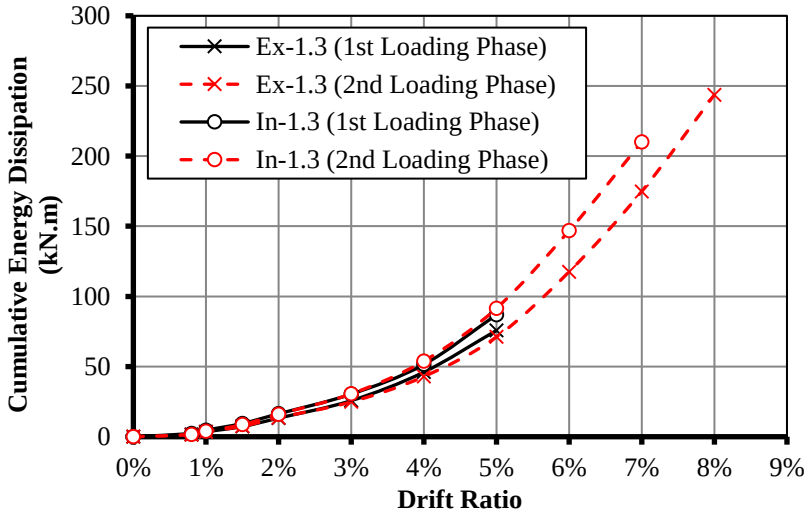

Figure 4.17 - Cumulative energy dissipation of test specimens

As shown in Figure 4.17, both specimens showed very similar behaviour in terms of energy dissipation during the first and the second loading phases. Comparing the graphs indicates that the interior specimen (In-1.3) showed higher energy dissipation compared to the exterior one (Ex-1.3). This was expected due to the more residual damage in the interior specimen compared to the exterior one, as discussed earlier. The larger amount of concrete in Specimen In-1.3 increases the area of damaged concrete (crushed or cracked). Since GFRP bars do not yield, the main source of energy dissipation in GFRP-RC frames is limited to concrete damage and slippage of the reinforcement.

Previously, the magnitude of residual deformation was introduced as an indication of the damage level in the test specimens. However, it seems appropriate to also adapt a quantitative measurement in terms of damage index to better compare the performance of GFRP-RC beam-column joints in terms of magnitude of damage. Park and Ang (1985) have introduced a damage index defined as the linear summation of the damage caused by excessive deformation and the damage caused by repeated cyclic loading effect:

$$D = \frac{\delta_{Mx}}{\delta_u} + \frac{\beta}{Q_y . \delta_u} \int dE \qquad (4.2)$$

where, δ_{Mx} is the maximum deformation under earthquake loading; δ_u is the ultimate deflection under monotonic loading; Q_y is calculated yield strength; dE is incremental absorbed hysteric energy and β is a model parameter.

However, due to the linear-elastic nature of GFRP materials, the ductility factor (defined as the ratio of the ultimate deflection over the deflection at design capacity) for GFRP-RC elements is generally lower than their steel-RC counterparts. Therefore, the expression in the damage index

corresponding to the excessive damage may not properly reflect the behaviour of GFRP-RC beam-column joints.

Since the energy dissipation of GFRP-RC beam-columns are dominantly governed by the magnitude of concrete damage, the authors propose a modified damage index only related to the cumulative energy dissipation of GFRP-RC beam-column joints as follows:

$$D_m = \frac{\beta_m}{Q_d . \delta_{us}} \int dE \qquad (4.3)$$

where, δ_{us} is the ultimate deflection from reversal cyclic loading tests; Q_d is calculated design strength; dE is incremental absorbed hysteric energy and β_m is a model parameter. The corresponding value of β_m for each specimen is calculated by setting D_m equal to 1.0 at failure (0.151 and 0.175 for Specimen EX-1.3 and In-13, respectively).

Figure 4.18 compares the calculated damage index for test specimens during the first loading phase. As expected, Specimen In-1.3 constantly exhibited higher damage index compared to Specimen Ex-1.3.

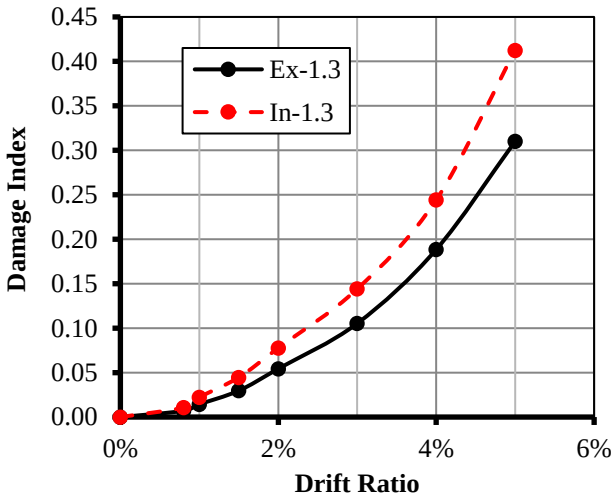

Figure 4.18 - Damage index-drift ratio

4.3.7 Performance under service loading

To measure performance of the specimens under service loading after withstanding severe lateral displacements, one load-controlled cycle with an amplitude equal to service load was applied after each loading step passed the 2% drift ratio. Generally, service loads in the beams are applied in gravity direction in real structures while the test set-up used in this program only allowed the application of lateral displacements to the upper tip of the column. Therefore, in order to apply service bending moments to the main beams in the test specimens, service loading condition was calculated as the corresponding lateral load at the tip of the column that exerts bending moments equal to service condition into the main beams.

Figure 4.19-a shows the maximum column tip displacement at each of the service loading cycles as a ratio of the column tip displacement when the service load condition was reached for the first time (2% and 0.8% drift ratios in Specimens Ex-1.3 and In-1.3, respectively). The performance of Specimen Ex-1.0 is also included in the graphs for comparison. According to the graph (Figure 4.19-a), the performance of the specimens under service loadings shows direct relationship to the reinforcement ratio of the main beams. The higher the reinforcement ratio, the lower the increase in the lateral displacement ratio during service loading cycles.

The lateral stiffness of the specimens during each service loading cycle is illustrated in Figure 4.19-b as a ratio of the lateral stiffness of the specimens during the first cyclic loading step (0.8% drift ratio). The lateral stiffness was calculated as the slope of the straight line connecting the maximum positive and negative points in the hysteresis diagram during the service loading cycles. Comparing the behaviour of Specimens Ex-1.0 and Ex-1.3 illustrates that the increase in shear stress ratio increases the stiffness degradation of beam-column joints. This is due to the higher concrete damage in the joint area as a result of higher joint shear stresses.

Moreover, comparing the interior and the exterior specimens with equal joint shear stress ratios (Ex-1.3 and In-1.3) indicates that the interior beam-column joints exhibit lower stiffness degradation compared to their exterior counterparts. This is attributed to the better confinement provided to the joint area by the main beams in interior beam-column joints compared to the exterior ones.

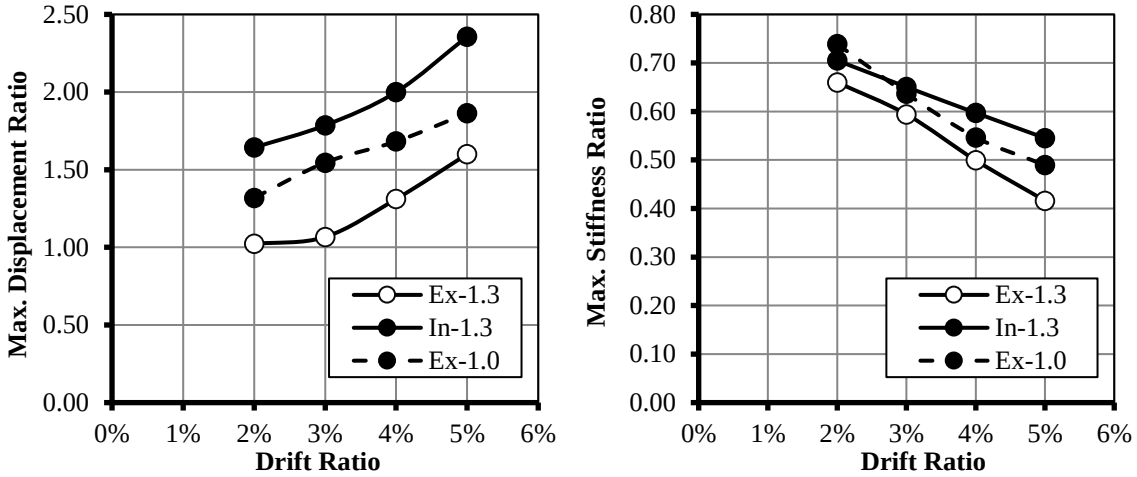

(a) Maximum displacement ratio (b) Lateral stiffness ratio

Figure 4.19 - Performance of test specimens during service load stage

4.4 Summary and Conclusions

Based on the results obtained from the test specimens, the following conclusions can be made:

- The exterior beam-column joint (Ex-1.3) was able to reach its maximum design lateral load capacity resulting in joint shear stress of $1.3\sqrt{f'_c}$. Therefore, it is concluded that exterior GFRP-RC beam-column joints with lateral beams can withstand joint shear stress ratios of 1.3.

- Both test specimens (In-1.3 and Ex-1.3) were able to reach their design capacity during the first loading phase (up to 5% drift ratio) without exhibiting significant concrete

damage. Therefore, it is concluded that GFRP-RC moment-resisting frames can withstand significant lateral deformations and still maintain their original condition up to an acceptable level. This characteristic can significantly reduce the repair costs of moment-resisting frames after an earthquake event.

- During the second loading phase, both test specimens showed linear behaviour up to 5% lateral drift ratios. The exterior beam-column joint (Ex-1.3) was able to reach the design capacity for the second time during the second loading phase while the interior specimen with the same magnitude of joint shear stress (In-1.3) was not able to reach its design capacity. This was attributed to the effect of longitudinal reinforcement in the main beams on the confinement of concrete core, which improved the performance of Specimen Ex-1.3.

- Both test specimens failed due to gradual decrease in lateral load carrying capacity (more than 25%) without brittle failure or sudden rapture of the GFRP bars. Therefore, it is concluded that GFRP-RC beam-column joints can be designed to prevent sudden and catastrophic failure.

- At failure, significant damage was observed in the joint area of the exterior specimen (Ex-1.3), while the concrete damage in the interior specimen (In-1.3) was concentrated in the beam area in the vicinity of the joint. This was attributed to the better confinement provided to the joint area in the interior specimen by the main beams, which increased the shear capacity of the joint.

- The maximum strain measured in the joint stirrups did not exceed the limit suggested by the CSA/S806-12 (CSA 2012) up to 5% drift ratio during both loading phases. This

indicates that the amount of lateral reinforcement suggested by CSA/S806-12 (CSA 2012) for confinement of columns in seismic regions is sufficient to withstand a joint shear stress of $1.3\sqrt{f'_c}$ in exterior and interior GFRP-RC beam-column joints.

- Test results showed that the longitudinal reinforcement ratio of the main beams had a significant effect on the maximum strain observed in the longitudinal bars during an earthquake. This should be taken into account to prevent rupture of the longitudinal bars by providing sufficient margin between the maximum expected strain in the bars and their tensile strain capacity.

- Test results indicated that the secondary moments, calculated considering the column load remains vertical, resulted in a 19 and 18% increase in the bending moment in columns of Specimens Ex-1.3 and In-1.3, respectively, at 5% drift ratio.

- Measured cumulative energy dissipation of the test specimens indicated that interior beam-column joints dissipate more energy than their exterior beam-column counterparts with equal magnitude of joint shear stress. This is attributed to the fact that, compared to exterior ones, interior beam-column joints have more concrete which increases the area of damage concrete (cracked or crushed) that represents the main source of energy dissipation in GFRP-RC beam-column joints.

- Investigating the performance of the test specimens under service loading condition indicated that the reinforcement ratio of the main beams have significant effect on the performance of the specimens in terms of deformations under service loads. Higher reinforcement ratios resulted in less deformation increase under service loads after undertaking seismic loading cycles.

5 SEISMIC BEHAVIOUR OF EXTERIOR GFRP-REINFORCED CONCRETE BEAM-COLUMN CONNECTIONS: ANALYTICAL STUDY

Shervin K. Ghomi and Ehab El-Salakawy

American Society of Civil Engineers (ASCE), Journal of Composites for Construction, 2018, Vol. 22, No. 4: 04018022, DOI: 10.1061/(ASCE)CC.1943-5614.0000858.

Abstract: Four full-scale specimens were constructed and tested under reversal cyclic loading to study the seismic behaviour of exterior glass fiber-reinforced polymer (GFRP)-reinforced concrete (RC) beam-column joints with lateral beams. The test variables were joint shear stresses (0.85, 1.0 and 1.1 times the square root of the concrete compressive strength) and type of reinforcement (steel or GFRP). Test results indicated that well-designed exterior GFRP-RC beam-column joints confined with lateral beams exhibit linear behaviour with minimum residual damage up to 5% drift ratio. A specialized software was used to construct a finite elements model, capable of simulating hysteresis behaviour of reinforced concrete beam-column joints under seismic loading by taking into account the nonlinear behaviour of concrete, confinement provided by the internal reinforcement, the effect of cracks and bond-slip relationship between reinforcing bars and surrounding concrete. The model was used to investigate the effect of joint shear stress, size of lateral beams, reinforcement material, column axial load and geometrical configuration on the joints behaviour.

Keywords: Beam-column joints, glass fiber reinforced, seismic behaviour, joint shear stress, lateral beams, column axial load, joint configuration, nonlinear finite element analysis.

5.1 Introduction

In the past two decades, fiber-reinforced polymers (FRPs), due to their non-corrodible nature, have been introduced as a promising alternative for conventional steel reinforcement in concrete structures to eliminate the costly damages caused by corrosion of steel. Up to date, many researchers have been involved in investigating the behaviour of various FRP-reinforced concrete (RC) elements. However, the majority of the studies in this area focused on the behaviour of individual FRP-RC members under monotonic loadings. In contrary, studies to investigate the performance of FRP-RC structures under reversal cyclic loading (e.g. earthquake) are very limited (Fukuyama et al. 1995; Said and Nehdi 2004; Mady et al. 2011).

The conventional approach to design an earthquake-resistant RC structure is based on members' plastic deformation ("ductility"), mainly due to yielding of reinforcing steel. The FRP materials; however, exhibit linear-elastic stress-strain relationship up to failure (no yielding), which raised some concerns about feasibility of using these materials in structures located in seismically active regions. Pioneer studies in this area (Said and Nehdi 2004; Mady et al. 2011); however, indicated that concrete frames reinforced with glass fiber-reinforced polymer (GFRP) are able to withstand significant lateral displacements without exhibiting brittle failure. This was attributed to the high tensile strength and low modulus of elasticity of GFRP reinforcement which allows the frames to undergo large deformations before reaching their ultimate capacity. This feature is called "deformability".

Followed by the promising results of the early studies on feasibility of using GFRP reinforcement in seismic regions, more studies are required to investigate the parameters affecting the performance of GFRP-RC moment-resisting frames. In order to achieve this goal, understanding the behaviour of beam-column joints, as a key element in stability of frames under lateral loading, is essential. Ghomi and El-Salakawy (2016) and Hasaballa and El-Salakawy (2016) investigated the seismic performance of exterior GFRP-RC beam-column joints with focus on variables such as joint shear stress, reinforcement detailing, presence of lateral beams and concrete compressive strength. However, still, there are many parameters, which are known to affect the seismic performance of FRP-RC beam-column joints that have not been investigated yet. Due to this lack of research and data, current codes and design guidelines for FRP-RC structures do not have comprehensive provisions for seismic design (CSA 2012). Implementation of GFRP-RC frames in seismic regions is not possible unless solid understanding of different parameters affecting the behaviour of such beam-column joints is achieved.

In this study, a series of finite element models (FEMs) were built using a specialized software (ATENA 3D version 5.3.1, Cervenka et al. 2012) to simulate the seismic behaviour of GFRP-RC exterior beam-column joints. The models were validated based on results of the specimens previously tested by the authors (Ghomi and El-Salakawy 2016) and were used to perform an extensive analytical study on some of the possible affecting parameters, including joint shear stress, size of lateral beams, reinforcement material, column axial load and geometrical configuration. The accuracy of the FEM was improved by taking into account the nonlinear behaviour of concrete, the reduction in concrete compressive strength due to crack propagations, the confinement provided to the concrete by the internal reinforcement and bond-slip relationship

between the reinforcement and concrete. These parameters have significant effect on the seismic performance of RC beam-column joints.

5.2 Summary of Experimental Program

5.2.1 Test specimens

As part of the study conducted by the authors (Ghomi and El-Salakawy 2016), four full-scale exterior beam-column joints with lateral beams were constructed and tested under reversal cyclic loadings to evaluate their seismic performance. The specimens were extracted from an arbitrary RC moment-resisting frame at assumed points of contra-flexure, at mid-height of the columns and mid-span of the beams. All specimens had the same dimensions as shown in Figure 5.1-a.

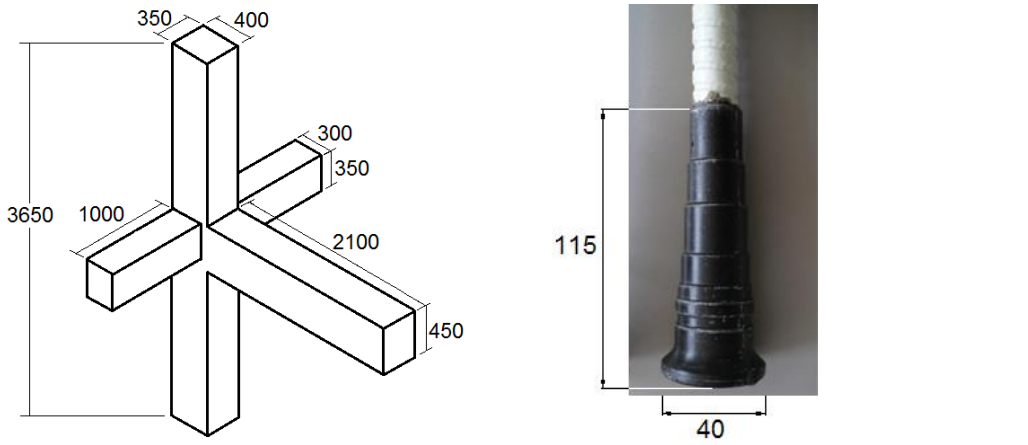

(a) Specimens dimensions (b) Beam longitudinal GFRP bars anchorage

Figure 5.1 - Specimens dimensions and GFRP bars anchorage type (dimensions in mm)

One of the specimens was reinforced with conventional steel as the control, while three specimens were reinforced with GFRP bars and stirrups. The GFRP-RC specimens were identical except for the number of beam longitudinal bars, which resulted in different shear stress applied to the joint, $0.85\sqrt{f'_c}$, $1.0\sqrt{f'_c}$ and $1.1\sqrt{f'_c}$, where f'_c is the concrete compressive strength.

In this paper, the experimental specimens are designated with three parts as follows. The first part, "E" indicates that the specimens are from the experimental part of the study, the second part, indicates the reinforcing material, "G" for GFRP and "S" for steel and the third part indicates the level of joint shear stress as a coefficient of $\sqrt{f'_c}$. The control specimen, E-S-1.0, was designed to have the same moment capacity as Specimen E-G-1.0. Table 5.1 shows the properties of the test specimens.

Table 5.1 - Design characteristics of test specimens

Specimen ID	ρ / ρbal*	Beam Flexural Capacity (kN.m)	Column-to-Beam Flexural Strength Ratio**	Joint shear Stress (MPa)	Concrete Strength (MPa)
E-G-0.85	1.64	307	1.61	0.82√f'c	44
E-G-1.0	2.65	350	1.47	0.96√f'c	48
E-G-1.1	3.62	356	1.35	1.07√f'c	42
E-S-1.0	0.32	304	1.73	1.00√f'c	41

* ρ / ρ_{bal} is the ratio between the provided reinforcement ratio to the balanced reinforcement ratio of the beam section
** Effect of column axial load is included in the flexural capacity of columns

The specimens were cast using normal-weight, ready-mix concrete with maximum aggregate size of 20 mm and target strength of 35 MPa. The actual compressive strength for each specimen was obtained on the day of testing (Table 5.1). Table 5.2 shows the mechanical properties of the ribbed-deformed GFRP bars and stirrups (Schoeck Canada Inc. 2012) used in the experiment. It should be mentioned that a mechanical anchorage (headed-end bar) was used to anchored GFRP beam longitudinal bars inside the joint (Figure 5.1-b), while a standard hook according to CSA/A23.3-14 (CSA 2014-a) was used to anchor steel longitudinal bars.

Table 5.2 - Properties of FRP bars and stirrups used in the experiment

Bar Configuration	Tensile Elastic Modulus (GPa)	Ultimate Tensile Strength (MPa)
GFRP Stirrups*	50	1000
GFRP Bars	60	1100
CFRP Stirrups*	120	950
CFRP Bars	140	1650

*Properties of the straight portion of the bent bar/stirrup as given by the manufacturer

5.2.2 Test set-up and loading procedure

Figure 5.2 shows the test set-up. In order to facilitate the testing procedure, the specimens were rotated 90-degree from the original orientation in a moment-resisting frame. The column was in a horizontal position and was subjected to constant axial load by means of a hydraulic jack. For the whole duration of the test, the axial load was kept equal to approximately 15% of the columns maximum nominal concentric capacity. Moreover, lateral beams were under a constant load, with direction and magnitude equal to service load, in order to include the effect of out-of-plane moments on the behaviour of the joint.

It should be mentioned that, in the experimental program, it was intended to prevent failure of columns prior to failure of beams. Thus, by maintaining the column axis aligned with the applied axial load during testing, the effect of secondary moments due to relative movement of the column ends was eliminated. Moreover, as shown in Table 5.1, the specimens were designed to have column-to-beam flexural strength ratios higher than 1.0. However, it is also possible to experimentally-test reinforced concrete beam-column joints by maintaining the horizontal axis of the main beam while applying reversal cyclic loading to the tip of the column. In the later setup, while applying constant vertical load to the column during testing, the effect of secondary moments can be included (Yu et. al. 2016). Such effect of secondary moments could be significant and may result in premature failure of columns especially with the increase in the axial load.

However, several researchers have employed the approach that was used in this program (Hanson and Conner 1967; Ospina and Alexander 1998) for testing beam-column joints since it is less complex and more convenient for particular objectives. In the experimental part of the present study (Ghomi and El-Salakawy 2016), the focus was to investigate the shear capacity of GFRP-RC beam-column joints. As such, the approach was to prevent flexural failure of columns prior to

either flexural failure of beams or shear failure of joints. Therefore, eliminating secondary moments as well as designing the specimens with high column-to-beam flexural capacity ratio were the measures taken to prevent the premature failure of columns.

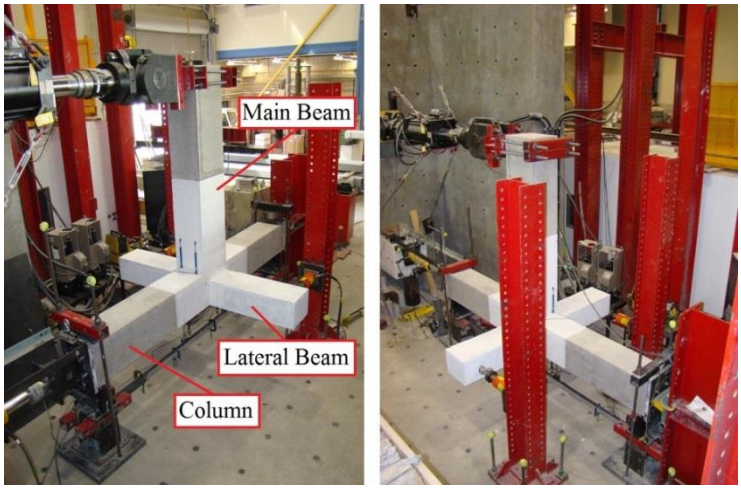

Figure 5.2 - Test set-up

A quasi-static reversed-cyclic load, based on ACI 374.1-05 (ACI Committee 374 2005), was applied to the tip of the main beam by means of a fully dynamic 1000-kN capacity actuator. The displacement-controlled cyclic loading was applied in several loading steps, gradually increasing in lateral drift ratio. Lateral drift ratio is defined as the ratio of beam tip displacement over the beam length. Each loading step consisted of three identical loading cycles to ensure stable crack propagation. Figure 5.3 shows the loading scheme. As shown in the graph, after 2% drift ratio, one load-controlled cycle with an amplitude equal to service loading was applied after each loading step to evaluate the stiffness degradation of the specimens, if any.

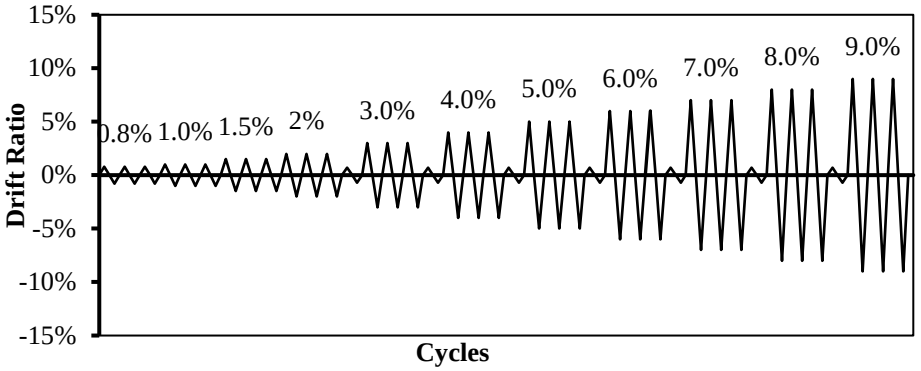

Figure 5.3 - Cyclic loading scheme

5.3 Finite Element Modelling

To extend the investigation of the key parameters affecting the seismic performance of FRP-RC beam-column joints, a series of FEMs were constructed using a specialized finite-element software ATENA-3D version 5.3.1 (Cervenka et al. 2012). The FE models simulated the response of various beam-column joints at the same loading scheme and boundary conditions, as described in the above experimental program.

ATENA-3D provides useful features in modeling reinforced concrete elements such as: 1) comprehensive non-linear constitutive model of concrete; 2) implementing the effect of cracks on behaviour of reinforced concrete; 3) including the effect of concrete compressive strength reduction due to cracks and tension stiffening; and 4) implementing user-defined bond-stress relationship between reinforcement and concrete.

The authors in the experimental part of this program (Ghomi and El-Salakawy 2016) reported that all GFRP-RC specimens not only achieved their design capacity but also exceeded that limit. Moreover, the lateral drift capacity of the specimens was significantly higher than the maximum lateral drift expected from a properly designed frame (7, 9 and 9% for E-G-0.85, E-G-1.0 and E-G-1.1, respectively). The National Building Code of Canada (NRCC 2015) limits lateral drift of

stories to 2.5% to eliminate the possibility of structural failure due to excessive P-Δ moments. In addition, the maximum expected lateral drift ratio of a story in CSA/S806-12 (CSA 2012) is 4%. Thus, although the behaviour of beam-column joints at high drift ratios is achievable in laboratories, it may not be applicable in real structures. Therefore, in order to more realistically evaluate the performance of GFRP-RC beam-column joints, the FEMs simulated the behaviour of the beam-column joints up to 5% drift ratio, since any drift ratios higher than that limit are unlikely to occur.

5.3.1 Concrete material

Eight-node brick elements, "CCIsoBrick", were used in modeling concrete geometry. To model the concrete material, Fracture-Plastic Constitutive Model (CC3D Non-Linear Cementitious 2) was used. In this model, the software combines two different constitutive models for tensile (fracture) and compressive (plastic) behaviour of concrete. The classical orthotropic smeared crack formulation and crack band model is used for the fracture model. This model employs Rankine failure criterion and exponential softening. For compressive behaviour of concrete, the program uses a softening/hardening plasticity model based on Menétrey-Willam failure surface. The model adopts elliptical hardening and linear softening relationship based on the experimental work by Van Mier (1986). This model can be used to simulate concrete cracking and crushing under high confinement.

To include the effect of confinement provided by internal reinforcement to the concrete, the stress-strain model for confined concrete suggested by Mander et al. (1988) and Saatcioglu & Razvi (1992) was used. However, these models were developed for steel-RC elements, while GFRP bars and stirrups have lower modulus of elasticity compared to steel reinforcement, which can affect

the behaviour of confined concrete. Therefore, an equivalent area of GFRP bars and stirrups were used. The equivalent area was defined as the area of a steel bar, which produces the same stiffness as the actual GFRP bar. For example, for GFRP bars with a modulus of elasticity of 60 MPa, the equivalent area of each GFRP bar is equal to the actual area of the bar multiplied by 60/200 (ratio of modulus of elasticity of the GFRP bar to that of a steel bar).

In addition, it should be mentioned that very few studies on the strength of confined concrete in GFRP-RC rectangular columns are available in the literature. One of the latest and most comprehensive studies investigating GFRP-RC rectangular columns has been conducted by Tobbi et al. (2014) proposing a revised version of the equation introduced by Mander et al. (1988).

Both models proposed by Tobbi et al. (2014) and used by the authors yielded very similar results in the case of columns considered in this study, which essentially resulted in the same finite element models.

The effect of cracked concrete on the tensile stiffness of reinforcement (tension stiffening) is accounted for in ATENA-3D. The program specifies a tension-stiffening factor, c_{ts}, which represents a relative limiting value of tensile strength in the tension softening of concrete. This value was set as 0.3 in this study. More details on the materials modeling in ATENA-3D can be found in the user manual of the software (Cervenka et al. 2012).

5.3.2 Reinforcement material

Discrete model was used for both longitudinal and transverse reinforcement embedded inside the concrete. The GFRP bars and stirrups were modelled with linear stress-strain relationship while

bilinear behaviour with strain hardening was used to model steel reinforcement. The same properties for the FRP reinforcement as shown in Table 5.2 were used in the FEMs.

ATENA-3D provides the option of defining bond-slip relationship between reinforcing bars and surrounding concrete. The bond-slip relationship, provided by the manufacturer, for ribbed-deformed FRP bars was used to simulate the behaviour of FRP-RC beam-column joints under seismic loading (Figure 5.4). For steel reinforcement, a pre-defined bond-slip model in the software, according to slip law by Bigaj, was used (Cervenka et al. 2012). This bond-slip model is generated based on concrete compressive strength and reinforcing bar diameter.

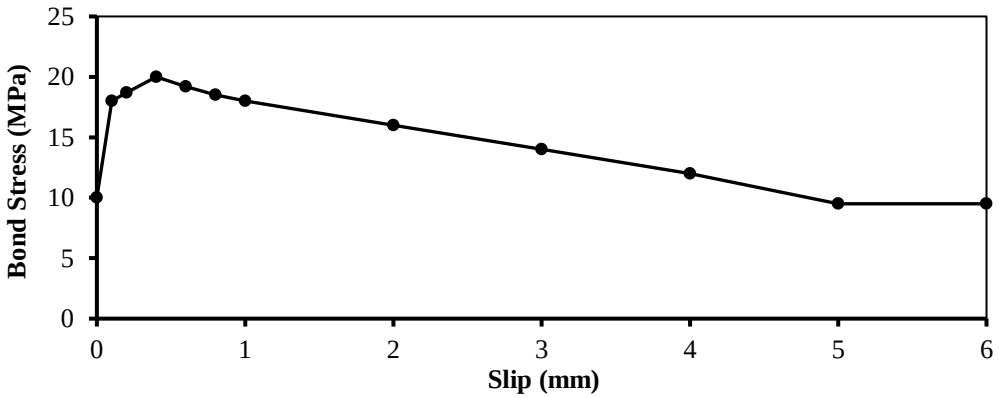

Figure 5.4 - Bond-slip relationship of GFRP bars

5.3.3 Model geometry and boundary conditions

Figure 5.5 shows the FEM of Specimen E-G-0.85. The FEM of the beam-column joint was constructed with the same orientation as the test set-up (column and main beam were in horizontal and vertical positions, respectively). As shown in Figure 5.2, the hydraulic actuator was clamped to tip of the main beam by a series of hollow square steel (HSS) sections. In order to simulate the same loading configuration, a rigid steel sleeve was created around the beam tip. The displacement-controlled reversal loading, as described earlier, was applied to the sleeve.

Moreover, thick steel plates were added at location of supports and load applications to prevent stress concentrations.

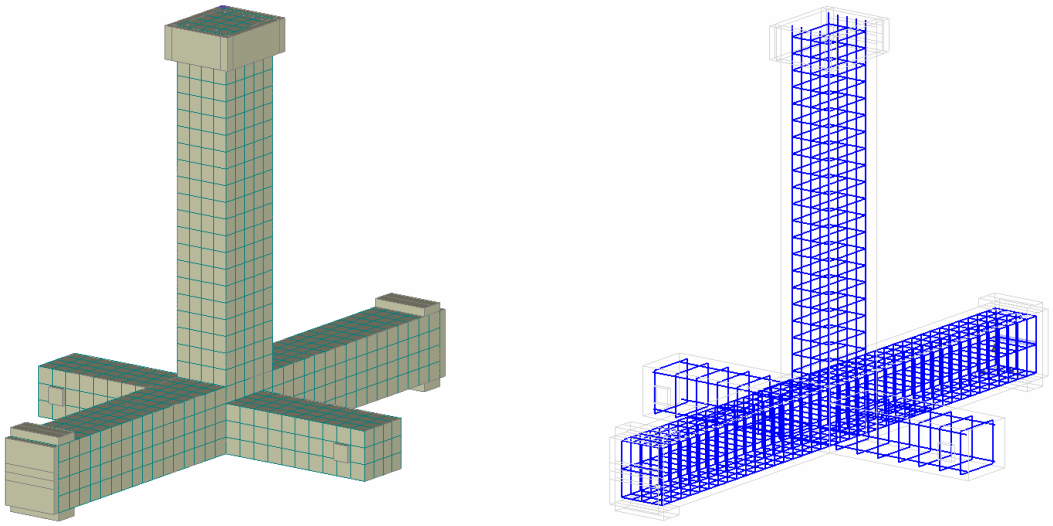

Figure 5.5 - FEM geometry and reinforcing configuration

In order to simulate the mechanical anchorage used for the beam longitudinal bars (headed-end bars) the reinforcement ends were restricted against slippage in the FEM. Brick meshing system with a maximum size of 0.1 m was used in the model. Based on several trials, this meshing size was found to provide an acceptable balance between accuracy of the results and running time.

5.3.4 Model validation

In order to validate the constructed FEM, the results of the model were compared with results of the experiment. Figure 5.6 compares lateral load-drift response of the experimental and FEM specimens in the first cycle of loading in each loading step up to 5% drift ratio (as described earlier). According to the figure, results are in reasonable agreement (within 10% error).

The dashed lines in the figures indicate design capacity of the specimens based on concrete strength on the day of testing. The design capacity of the GFRP-RC specimens was defined as the moment causing concrete compressive failure in the beams. In order to account for steel strain hardening in the steel-RC specimen, the capacity was calculated by assuming a tensile stress of $1.25f_y$, where f_y is the yield strength of steel, in the longitudinal reinforcement at failure.

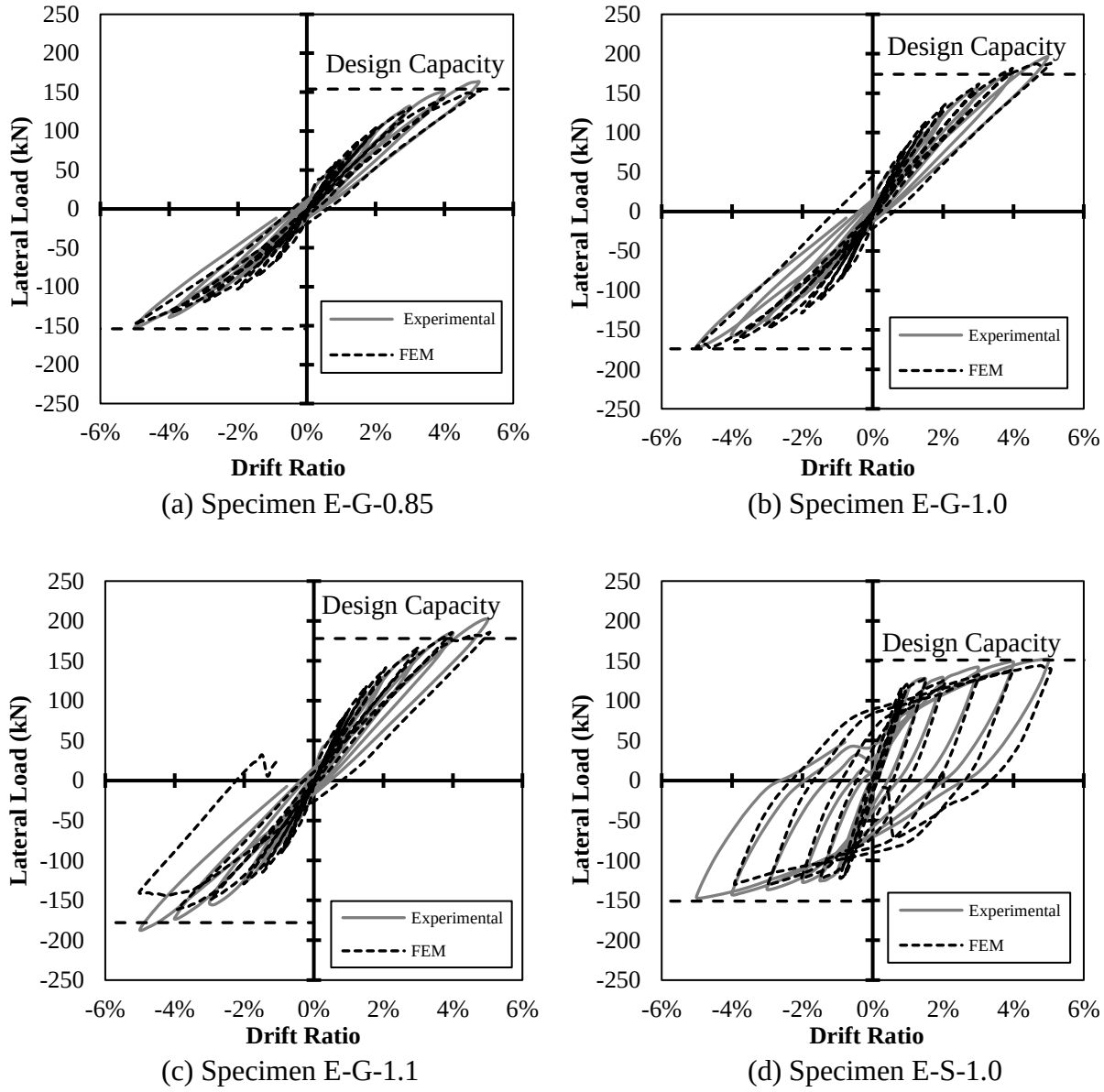

(a) Specimen E-G-0.85

(b) Specimen E-G-1.0

(c) Specimen E-G-1.1

(d) Specimen E-S-1.0

Figure 5.6 - Hysteresis diagrams of test specimens and corresponding modelled specimens

According to Figure 5.6, all tested GFRP-RC specimens reached their design capacity at 4% and 5% drift ratio in pushing and pulling directions, respectively. As shown in Figure 5.3, reversal loadings in this program always started with pushing the beams to the positive direction followed by pulling it back to the negative direction. This loading scheme resulted in a lower lateral load-carrying capacity in the negative direction due to the effect of cracks that were generated in the specimens while the beam was pushed to the positive direction. Consequently, the specimens reached the design capacity at higher drift ratios in negative direction compared to the positive one. The same behaviour was obtained by the FEMs.

In contrary to the GFRP-RC specimens, the control steel-RC specimen showed ductile behaviour. The longitudinal steel bars yielded at 1.5% drift ratio, resulting in significant energy dissipation, indicated by wide hysteresis loops. As part (d) of Figure 5.6 shows, the software was not able to model the behaviour of Specimen E-S-1.0 completely in the 5% drift ratio cycle. As in the laboratory testing of Specimen E-S-1.0, during the 5% drift ratio cycle the concrete cover of the beam was lost and the yielded longitudinal reinforcement became completely exposed and un-confined (Figure 5.7). Due to this mass loss, the behaviour of the specimen could not be accurately simulated with the analytical modeling.

The analytical specimens were designated in the same manner as the experimental ones, except for the first letter (“A” instead of “E”) which indicates that the specimen belongs to the “Analytical” part of the study. Figure 5.8 shows the cracking pattern obtained from the FEMs of Specimens A-G-0.85, A-G-1.1 and A-S-1.0 at the maximum positive displacement (5% drift ratio). The lines indicate the major cracks with a width wider than 0.1 mm. As expected, increasing beam longitudinal reinforcement ratio resulted in a lower column-to-beam flexural strength ratio. It is common to use this ratio as an indicator for the location of the inelasticity centre (damage centre);

the lower the ratio the closer the inelasticity centre to the joint area. This phenomenon can be observed in Figure 5.8-a and Figure 5.8-b, which is in agreement with the experimental observations.

Figure 5.7 - Concrete loss in Specimen E-S-1.0 at 5% drift ratio

Comparing the behaviour of GFRP-RC with steel-RC specimens (Figure 5.8-b and Figure 5.8-c) indicates that bi-linear behaviour of steel reinforcement results in concentration of the flexural and shear cracks near the joint area, at the location of the plastic hinge. In GFRP-RC beam-column joints, on the other hand, due to the linear behaviour of GFRP reinforcement, the flexural cracks are distributed over a longer length of the beam. Moreover, due to high column-to-beam flexural strength ratio (1.7) in Specimen A-S-1.0, there was no sign of damage penetration into the joint area.

Readings of the strain gauges attached on the beam longitudinal reinforcement of the experimental specimens were compared with those obtained from the FEMs. Figure 5.9 compares the maximum strain observed in beam bars at a distance of 30 mm from the column face for specimens E-G-0.85 and E-G-1.1 and their FEM counterparts.

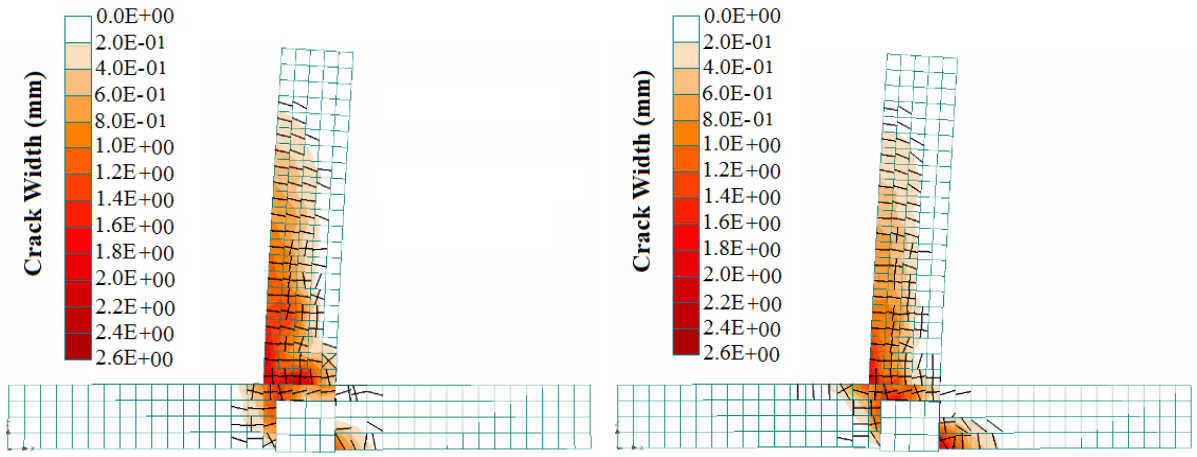

(a) Specimen E-G-0.85 (b) Specimen E-G-1.1

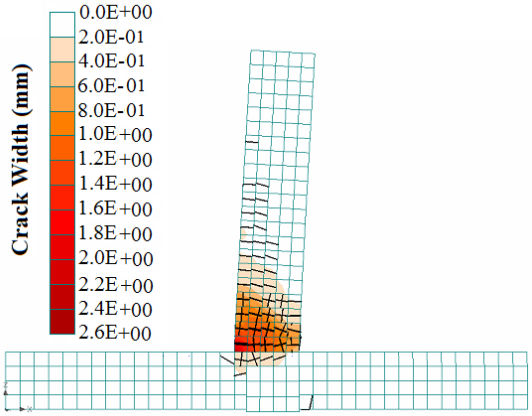

(c) Specimen E-S-1.0

Figure 5.8 - Cracking pattern obtained from FEMs

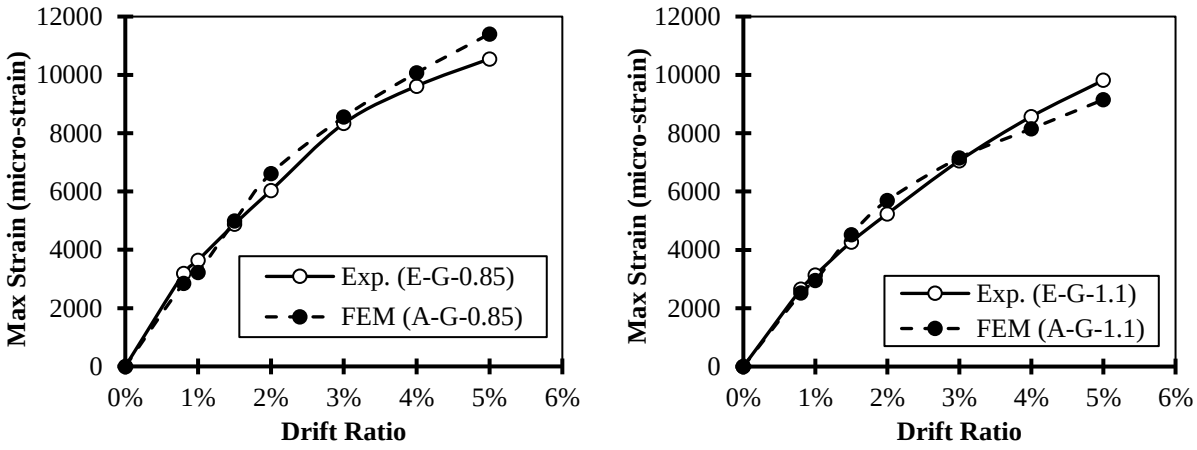

Figure 5.9 - Strains at beam longitudinal bars

Following the validation of the FEMs, the models were used to study the effect of five parameters on the seismic behaviour of exterior beam-column joints: 1) joint shear stress, 2) lateral beam size, 3) column axial load, 4) type of reinforcement, and 5) geometrical configuration.

5.4 Results and Discussion of the Parametric Study

5.4.1 Joint shear stress

Since Specimen E-G-1.1 was able to reach its design capacity without any significant damage at the joint area, it was concluded that GFRP-RC exterior beam-column joints with lateral beams can withstand joint shear stress of $1.1\sqrt{f'_c}$. However, yet it was not clear whether such joints can withstand higher joint shear stresses or not. In order to answer this question, a series of beam-column joints, identical to Specimen E-G-1.0 except for the magnitude of joint shear stress, were numerically modelled in this paper. In these models, beam longitudinal bar diameter in Specimen A-G-1.0 was increased to induce higher shear stress in the joint while the axial load was maintained at 15% of the nominal capacity of the column. Table 5.3 shows properties of the modelled specimens.

Table 5.3 - Analytical test matrix for the effect of joint shear stress

Parameter under Study	Specimen ID	Joint Shear Stress × $\sqrt{f'_c}$	Lateral Beam Size*	Concrete Compressive Strength (MPa)	Column Axial Load**
Joint Shear Stress	A-G-1.0	1.0	58%	48	15%
	A-G-1.2	1.2			
	A-G-1.4	1.4			
	A-G-1.6	1.6			

*Percentage of joint's area
**Percentage of the maximum axial capacity of columns

Figure 5.10-a shows the ratio of the maximum lateral load to the design capacity at each lateral drift ratio for the modelled specimens until failure (due to concrete crushing). According to the

graph, as the joint shear stress increases, the performance of the beam-column connection degrades. Specimen A-G-1.0, with joint shear stress of $1.0\sqrt{f'_c}$, was able to reach its design capacity in both positive and negative direction (as shown earlier in Figure 5.6-b).

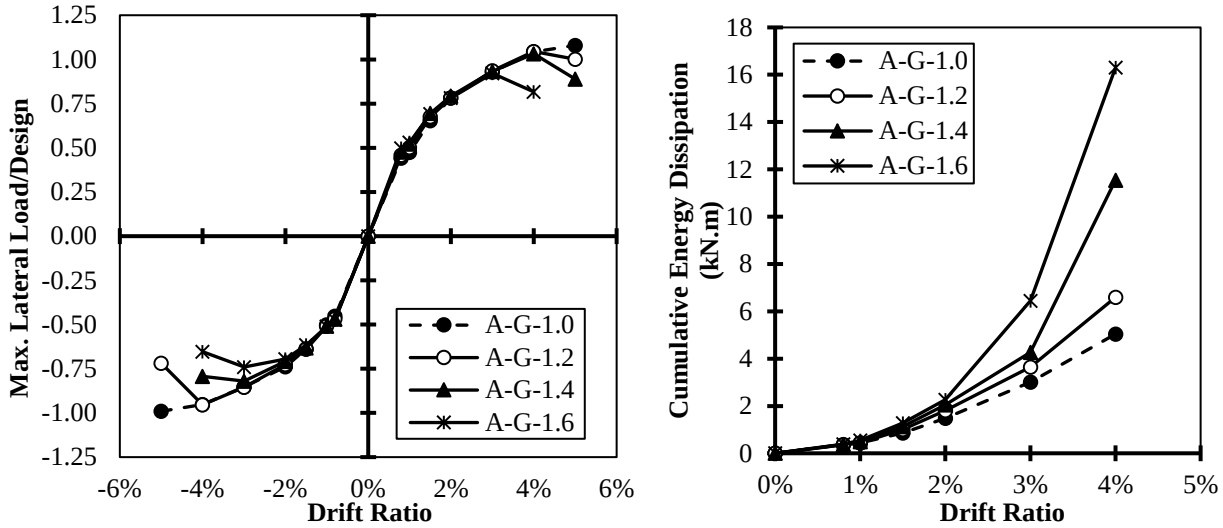

(a) Normalized lateral load-drift ratio (b) Cumulative energy dissipation

Figure 5.10 - Beam-column joints with various joint shear stresses (15% nominal column capacity)

Specimens A-G-1.2 and A-G-1.4 with $1.2\sqrt{f'_c}$ and $1.4\sqrt{f'_c}$ joint shear stress, respectively, also were able to reach the design capacity in the positive direction. In the negative direction, Specimen A-G-1.2 was able to reach 95% of its design capacity while Specimen A-G-1.4 was not able to achieve more than 82% of the capacity. This lower load-carrying capacity in the negative direction was expected due to the effect of loading sequence, as describe earlier.

Specimen A-G-1.2 was able to reach -5% drift ratio, while increasing the joint shear stress to $1.4\sqrt{f'_c}$ in Specimen A-G-1.4 resulted in a premature failure of the specimen prior to reaching -5% drift ratio. With further increasing the joint shear stress to $1.6\sqrt{f'_c}$, Specimen A-G-1.6 failed to reach its design capacity in either positive or negative direction.

Figure 5.10-b shows cumulative energy dissipation of the specimens considering the first loading cycle in each drift ratio. The energy dissipation is defined as the area enclosed by loops in lateral load-drift graphs of the beam-column joints. Since Specimens A-G-1.4 and A-G-1.6 failed prior to completing the 5% drift ratio cycle, the graph only includes the energy dissipation up to 4% drift ratio.

Since GFRP reinforcement behaves linearly, energy dissipation in the beam-column joints is mainly due to concrete cracking. Therefore, energy dissipation can also be interpreted as an indicator of the concrete damage severity. According to the graph, both specimens A-G-1.0 and A-G-1.2 showed stable behaviour (constant gradual increase in the energy dissipation value) while specimens A-G-1.4 and A-G-1.6 showed a sudden increase in the energy dissipation graph at 3% and 2% drift ratio, respectively. This sudden jump was due to significant concrete damage occurred due to high joint shear stresses, which resulted in wider loops in the hysteresis diagrams of the specimens.

It should be mentioned that CSA/A23.3-14 (CSA 2014-a) suggests a joint shear limit of $1.6\sqrt{f'_c}$ for steel-RC exterior beam-column joints. The lower capacity for GFRP-RC joints compared to steel-RC joints is due to the lower stiffness of GFRP reinforcement that results in wider cracks in the joint area. Wider cracks significantly reduce the concrete integrity and confinement and can reduce the bond quality between the reinforcement and the concrete.

To investigate the effect of joint shear stress on beam-column joints with higher magnitudes of column axial loads (representing beam-column joints at lower stories in a multi-story building), the analyses with the column axial load equal to 75% of the nominal concentric column capacity were performed. The same designations as those in Table 5.3 were used for these models with the

addition of "75%" in parentheses at the end of each specimen's ID, indicating the magnitude of column axial load. Figure 5.11 shows the ratio of maximum lateral load to the design capacity for these specimens. As shown in the graph, the increase in the column load significantly deteriorates the performance of the beam-column joints. None of the modeled specimens reached the design capacity in either loading directions.

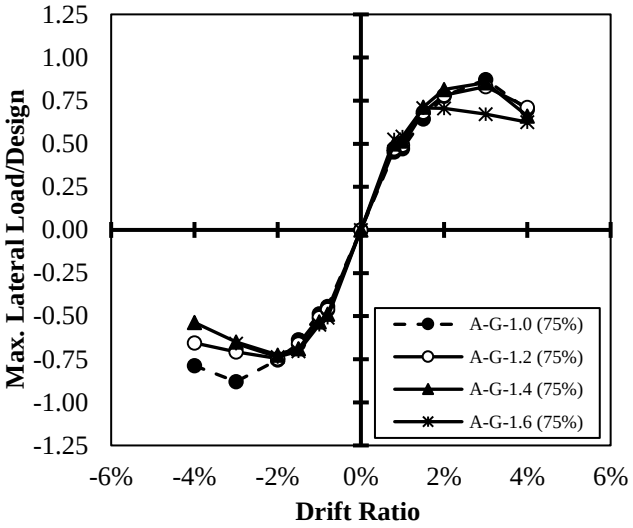

Figure 5.11 - Beam-column joints with various joint shear stresses (75% nominal column capacity)

Moreover, Figure 5.11 shows that the effect of joint shear stress is less pronounced at higher column axial loads. The high axial load applied to the joints increased the concrete stresses significantly resulting in fast deterioration of the concrete during reversal loadings. Therefore, even relatively low joint shear stresses caused significant damage to the joint area. More discussions regarding the effect of column axial load on the performance of beam-column joints are provided in the following sections.

5.4.2 Size of lateral beams

According to CSA/A23.3-14 (CSA 2014-a), lateral beams are considered to provide confinement to beam-column joints only if they cover at least 75% of the joint's face. However, Ghomi and El-Salakawy (2016) showed that even lateral beams covering lower percentage of the joint area (58%) can effectively improve the shear capacity of exterior beam-column joints. In order to extend the investigation of the effect of lateral beams size on the performance of edge beam-column joint, a series of FEMs were constructed to simulate edge connections with various lateral beam sizes and level of joint shear stress. Three level of joint shear stress, $1.2\sqrt{f'_c}$, $1.4\sqrt{f'_c}$ and $1.6\sqrt{f'_c}$, and four sets of dimensions for lateral beams were considered, resulting in a total of 12 combinations of joint shear stress and lateral beam size. Figure 5.12 shows dimensions of the lateral beams in each case. In all cases, the columns were 400 mm deep and 350 mm wide (same as the experimental specimen).

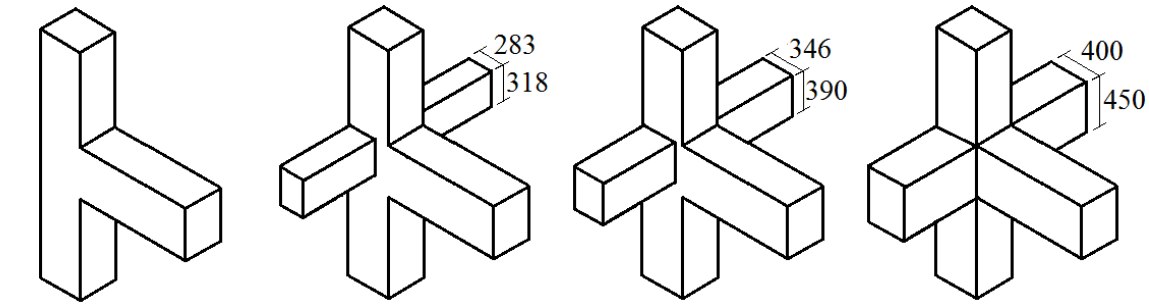

(a) 0% coverage (b) 50% coverage (c) 75% coverage (d) 100% coverage

Figure 5.12 - Dimensions of the lateral beams corresponding to each coverage percentage (dimensions in mm)

In this series of the modelled specimens, the last part in the specimens' identification indicates percentage of the joint area that is covered by lateral beams. Figure 5.13 shows the ratio of the maximum lateral load to the design capacity of the modelled specimens. As expected, increasing

the lateral beams size improves the performance of the joint. This is due to the better confinement that larger lateral beams provide to the joint.

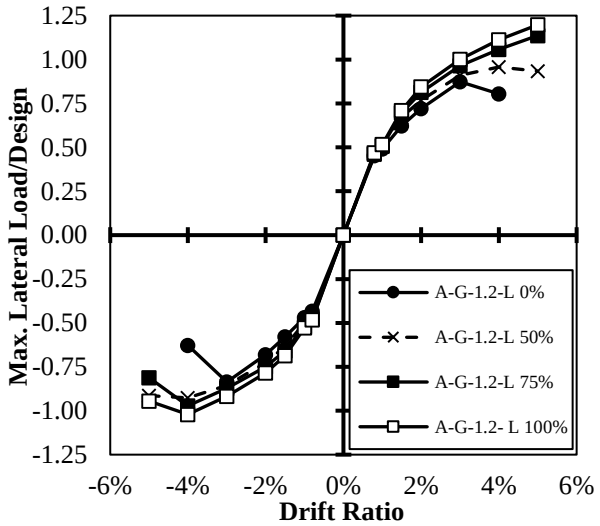

(a) Specimens with joint shear stress of $1.2\sqrt{f'_c}$

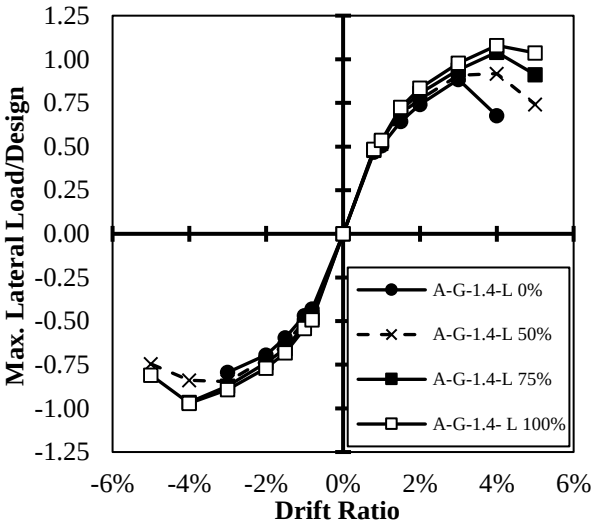

(b) Specimens with joint shear stress of $1.4\sqrt{f'_c}$

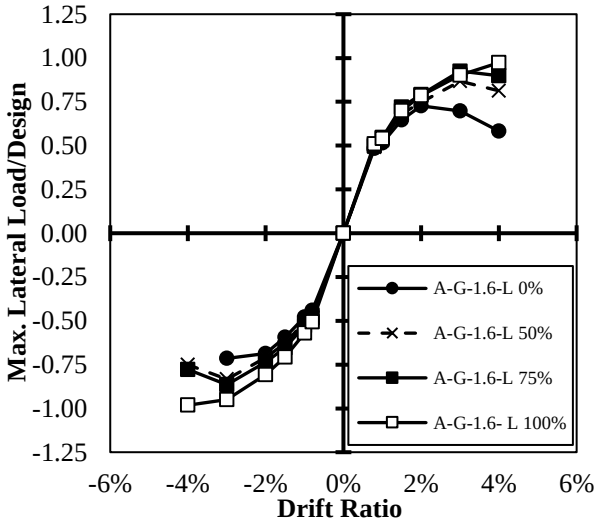

(c) Specimens with joint shear stress of $1.6\sqrt{f'_c}$

Figure 5.13 - Normalized lateral load-drift relationships for joints with various lateral beam sizes (15% nominal column capacity)

According to Figure 5.13, when lateral beams cover 75% of the joint surface, as required by CSA/A23.3-14 (CSA 2014-a), exterior beam-column joints can withstand joint shear stresses as

high as $1.4\sqrt{f'_c}$ in both negative and positive direction. However, the confinement provided by these lateral beams is not sufficient for the joint shear stress of $1.6\sqrt{f'_c}$.

Figure 5.14 compares the maximum strain in the joint stirrups of the modelled specimens with joint shear stress of $1.4\sqrt{f'_c}$. The dashed line indicates the strain limit set by the CSA/S806-12 (CSA 2012) for FRP reinforcement. The graphs indicate that increasing the size of lateral beams decreases the shear stress resisted by the joint stirrups (50% decrease from Specimen A-G-1.4-L-0% to Specimen A-G-1.4-L-100% at 3% drift ratio). Larger lateral beams provide more confinement to the joint area, thus less concrete damage occurs in the joint resulting in less shear stress transferring to the stirrups.

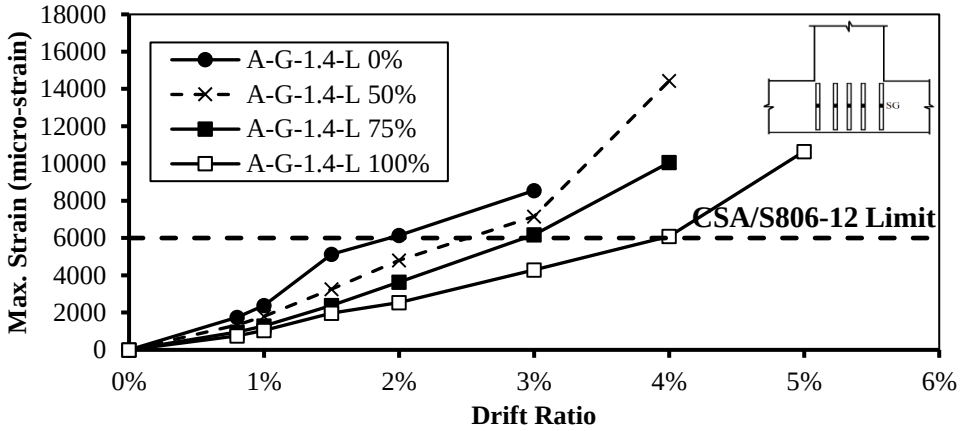

Figure 5.14 - Maximum joint stirrups strain in specimens with joint shear stress of $1.4\sqrt{f'_c}$

Furthermore, the computer models of the specimens presented in this section were also analyzed under a higher axial load representing 75% of the nominal column concentric capacity (indicated by "75%" in parentheses at the end of specimens' ID). Figure 5.15 shows the ratio of the maximum lateral load to the design capacity for these specimens. As shown in the graphs, none of the specimens with such high axial load achieved the design capacity, even with 100% lateral beam coverage. Moreover, the graphs indicate that the increase in column axial load significantly

reduces the deformability of the GFRP-RC beam-column joints. None of the specimens with 75% of the nominal column capacity were able to reach 5% lateral drift ratio.

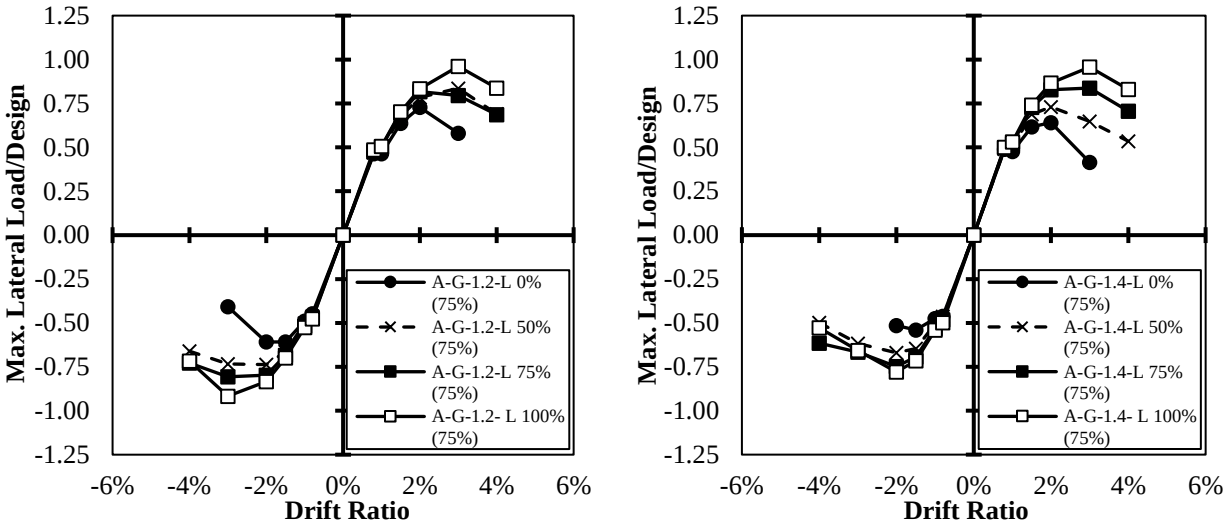

(a) Specimens with joint shear stress of $1.2\sqrt{f'_c}$ (b) Specimens with joint shear stress of $1.4\sqrt{f'_c}$

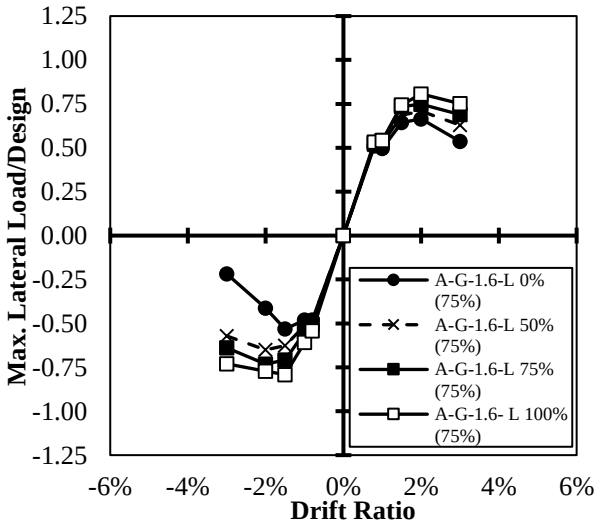

(c) Specimens with joint shear stress of $1.6\sqrt{f'_c}$

Figure 5.15 - Normalized lateral load-drift relationships for joints with various lateral beam sizes (75% nominal column capacity)

5.4.3 Effect of column axial load

As mentioned, the experimental specimens were tested while the column was under a constant axial load equal to approximately 15% of its maximum nominal axial capacity. The maximum axial load capacity of the GFRP-RC and steel-RC columns was calculated based on the requirements of the CSA/S806-12 (CSA 2012) and the CSA/A23.3-14 (CSA 2014-a), respectively. In this section, the effect of column axial load on the performance of GFRP-RC beam-column joints is studied through FEMs. In this series, the last part in the specimen identification indicates the columns axial load in terms of maximum axial capacity percentage. Five level of column axial load, 15%, 30%, 45%, 60% and 75%, were considered. Table 5.4 shows properties of the modelled specimens in this series.

Table 5.4 - Analytical test matrix for the effect of column axial load

Parameter under Study	Specimen ID	Joint Shear Stress × $\sqrt{f'_c}$	Lateral Beam Size*	Concrete Compressive Strength (MPa)	Column Axial Load**
Column axial load	A-G-1.0-C 15%	1.0	58%	48	15%
	A-G-1.0-C 30%				30%
	A-G-1.0-C 45%				45%
	A-G-1.0-C 60%				60%
	A-G-1.0-C 75%				75%

*Percentage of joints area

**Percentage of the maximum axial capacity of columns

Figure 5.16 - shows lateral load-drift envelope of the modelled GFRP-RC specimens. According to the graph, increasing column axial load degrades the performance of GFRP-RC beam-column connection. The GFRP-RC columns, tested and modelled in this program, are designed to fail by crushing of concrete under combined axial load and bending moment. Therefore, increasing the axial force resulted in reaching the concrete compressive strength at lower bending moments. Thus, the modelled specimens with higher axial load failed at lower drift ratios.

Figure 5.17 shows strain distribution (parallel to the column axis) in Specimen A-G-1.0-C 15% and A-G-1.0-C 75% at -4% drift ratio (Specimen A-G-1.0-C 75% was not able to achieve 5% drift ratio). The figure shows high compressive strains at the joint area in Specimen A-G-1.0-C 75%, which resulted in premature failure of the specimen due to concrete crushing. In Specimen A-G-1.0-C 15%, on the other hand, strains in the column remain below the concrete crushing level.

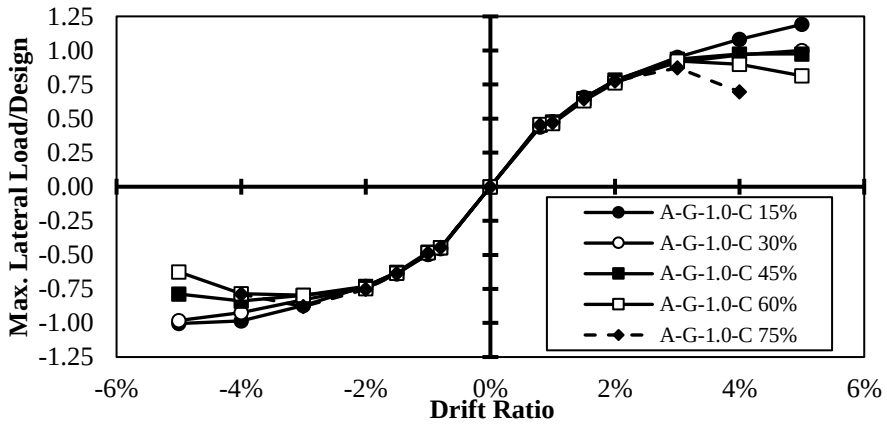

Figure 5.16 - Normalized lateral load-drift relationships for joints with various column axial loads

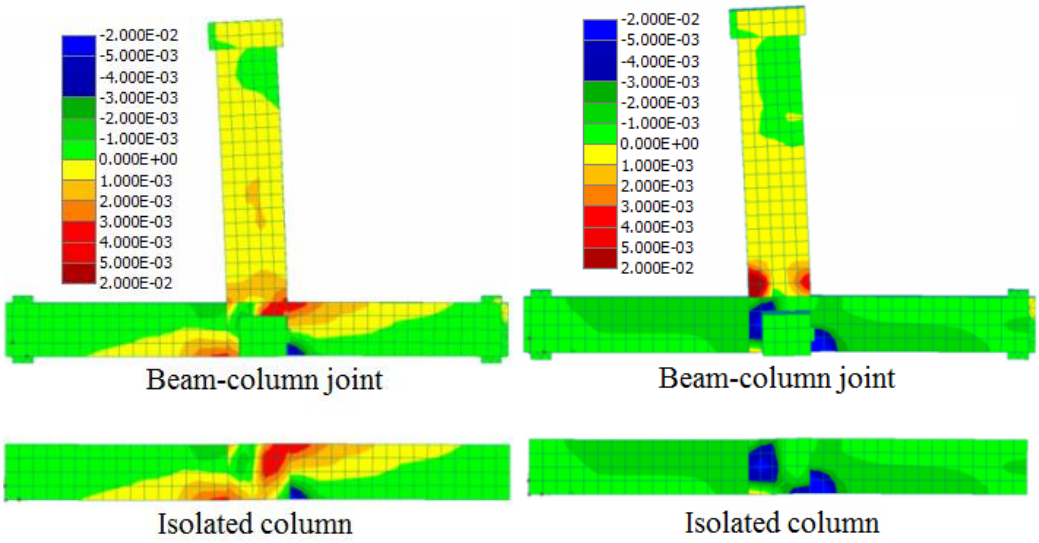

(a) Specimen A-G-1.0-C 15% (b) Specimen A-G-1.0-C 75%

Figure 5.17 - Strain distribution in the specimens with various column axial load

In order to investigate the effect of column axial load on the behaviour of steel-RC beam-column joints, FEM of Specimen E-S-1.0 was reconstructed with various column axial load levels (same ratios as the GFRP-RC specimen). The results indicated that, in contrary to the GFRP-RC specimen, increasing axial column load in the steel-RC specimen, did not show a significant impact on lateral load-drift envelop of the beam-column joints. This is because the steel-RC columns are designed to have tension failure (yielding of the reinforcement before crushing of concrete); therefore, increasing the axial force postpones the tension failure of the column reinforcement. Moreover, since moment capacity of the column was significantly higher than the beam (column-to-beam flexural strength ratio of 1.7) at none of the column axial load levels the column longitudinal reinforcement yielded in compression. Figure 5.18 compares lateral load-drift response of Specimen A-S-1.0-C 15% and Specimen A-S-1.0-C 75%. It can be seen that the behaviour did not show any significant change with increasing the column load.

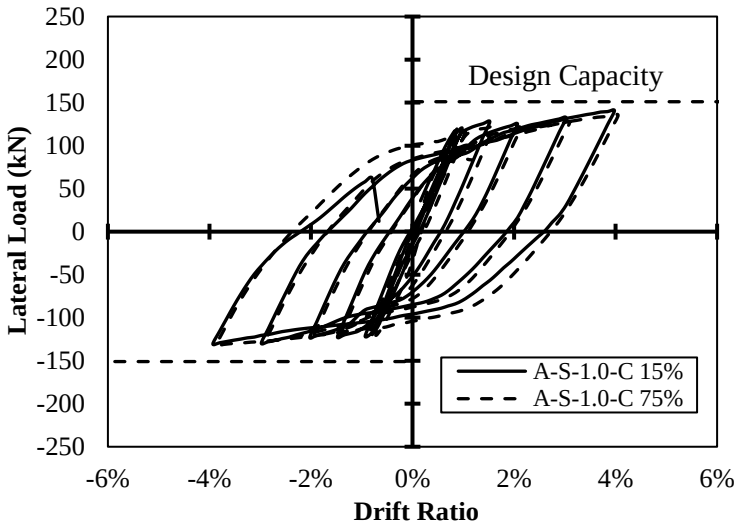

Figure 5.18 - Hysteresis diagram of steel-RC joints with different column axial loads

However, as mentioned earlier, the effect of secondary moments on the behaviour of columns is eliminated in this program by preventing relative displacement of the column ends. Therefore, the

results shown in Figure 5.14 and Figure 5.16 only represent the effect of column axial load due to change in the stress magnitude and distribution in the columns. It should be mentioned that by taking the effect of secondary moments into account, the increase in column axial load could result in premature failure of columns due to the increase in secondary moments.

5.4.4 Effect of reinforcement type

Due to its higher modulus of elasticity, carbon fiber-reinforced polymer (CFRP) reinforcement is commonly considered as a better option over GFRP bars and stirrups in terms of deflection and crack width under service load. However, as mentioned earlier, in the special case of seismic design "deformability" of FRP-RC structures is essential to prevent brittle failure. Even though CFRP reinforcement possesses higher modulus of elasticity, it fails at lower strain compared to GFRP reinforcement. This feature could make CFRP-RC structures susceptible to brittle failure at relatively low lateral deformations.

In order to evaluate the performance of CFRP-RC moment-resisting frames under seismic loading, a series of FEMs were constructed to simulate a CFRP-RC and a GFRP-RC beam-column joint with the same beam moment capacity. Table 5.5 shows properties of the specimens modelled in this series. Same as previous specimens, the second and the third terms in the specimens ID indicate reinforcement type and joint shear stress level, respectively. It should be mentioned that the bond-slip relationship introduced by Malvar and Cochran (2003) was used in modeling the CFRP-RC specimen. This was selected to eliminate the effect of other variables on the behaviour of the modeled specimens.

Table 5.5 - Analytical test matrix for the effect of reinforcement type

Parameter under Study	Specimen ID	Moment Capacity (kN.m)	Number of Beam Longitudinal Bars	Beam Reinforcement Area (mm^2)	Concrete Compressive Strength (MPa)
Reinforcement type	A-G-0.90	304	8	175	40
	A-C-0.85		4	120	

Figure 5.19 compares lateral load-drift response of the modelled specimens. As was expected, although Specimen A-C-1.0 was able to reach the design capacity and provide higher stiffness it was not able to reach lateral drift ratios more than 3%. Therefore, CFRP-RC frames do not provide satisfactory performance under seismic loading.

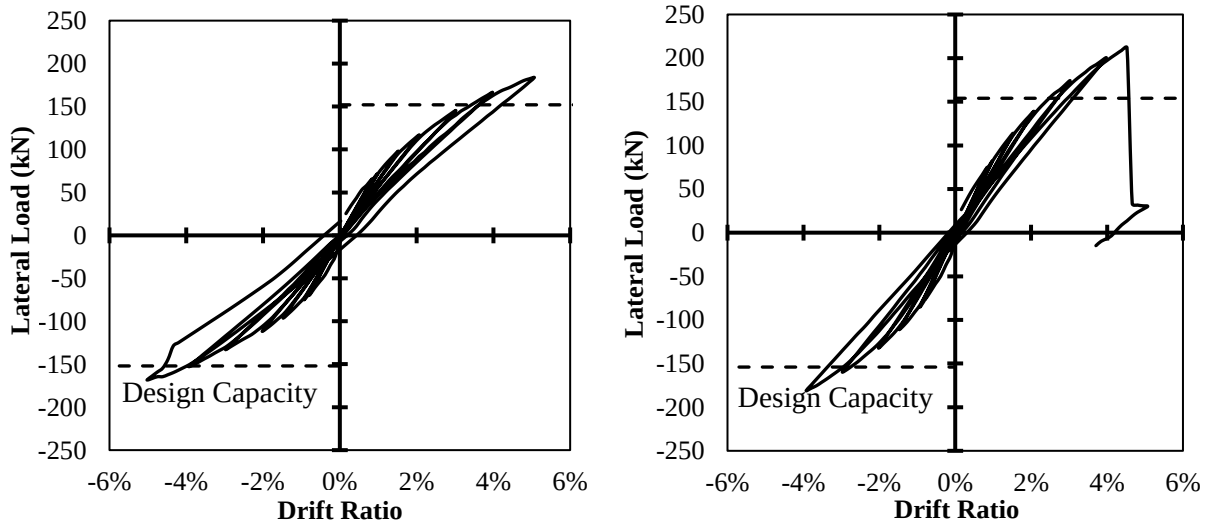

(a) Specimen A-G-0.90 (b) Specimen A-C-0.85

Figure 5.19 - Hysteresis diagrams of beam-column joints with various reinforcing materials

5.4.5 Effect of joint geometry

In order to investigate the effect of geometrical configurations, the seismic performance of corner, T-shaped and edge beam-column joints were studied. It should be mentioned that CSA/A23.3-14 (CSA 2014-a) does not consider the confinement provided by the lateral beams when they cover

only one side of beam-column joints (corner connections). However, to investigate the actual effectiveness of such confinements the seismic performance of three types of beam-column joints was compared. Figure 5.20 shows the configuration of the connections that were modelled. The columns measured 400 mm deep and 350 mm wide and the beams measured 450 mm deep and 350 mm wide. Three levels of joint shear stress, $0.85\sqrt{f'_c}$, $1.0\sqrt{f'_c}$ and $1.2\sqrt{f'_c}$, were studied for each configuration. Concrete with 40 MPa compressive strength and column axial load equal to 15% of the maximum concentric capacity was used to model the specimens.

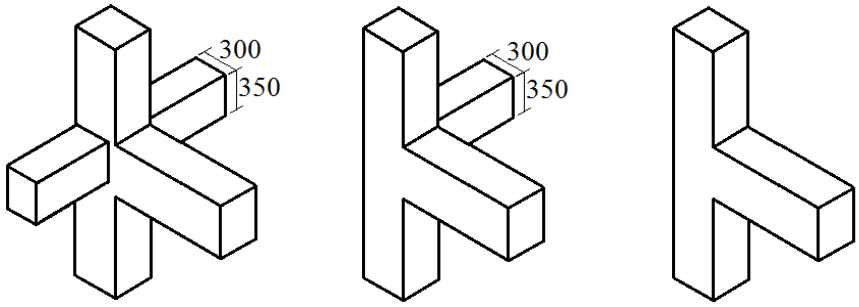

Figure 5.20 - Geometrical configurations for studied beam-column joints (dimensions in mm)

Figure 5.21 shows lateral load-drift envelope of the modelled specimens. According to the graph the effect of lateral beams on the seismic performance of the joints is more pronounced in the connections with higher joint shear stress. Low joint shear stress ($0.85\sqrt{f'_c}$), caused insignificant concrete expansion in the joint area. Therefore, additional confinement provided by lateral beams did not play significant role in improving the shear capacity of the joint. However, in connections with higher joint shear stress ($1.0\sqrt{f'_c}$ and $1.2\sqrt{f'_c}$) the confinement provided by lateral beams significantly improved the seismic performance by preventing joint's concrete expansion. Even though Specimen A-G-1.0-Corner was able to reach its design capacity in both directions, due to sufficient lateral confinement, Specimen A-G-1.2-Corner failed prior to reaching its design capacity.

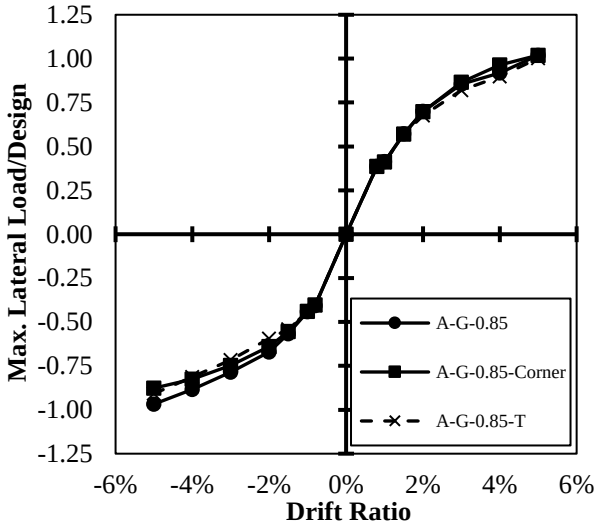

(a) Specimens with joint shear stress of $0.85\sqrt{f'_c}$

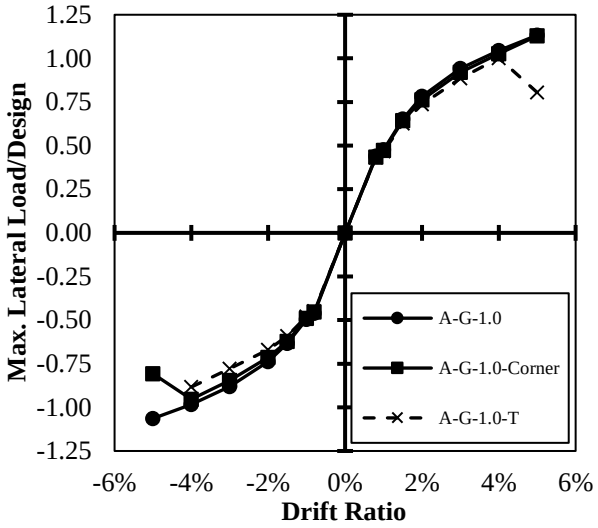

(b) Specimens with joint shear stress of $1.0\sqrt{f'_c}$

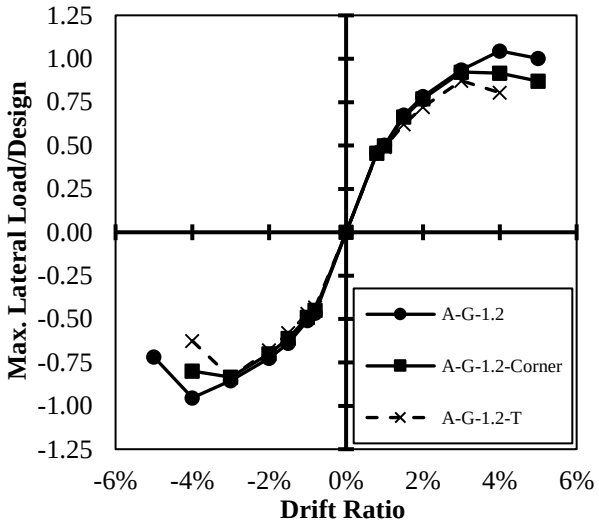

(c) Specimens with joint shear stress of $1.2\sqrt{f'_c}$

Figure 5.21 - Normalized lateral load-drift ratio relationships for joints with various geometrical configurations

5.5 Conclusions

Based on the results obtained from the experimentally tested and the simulated specimens by FEM, the following conclusions can be made:

- The GFRP-RC exterior beam-column joint confined with lateral beams covering 58% of the joint area and joint shear stress of $1.1\sqrt{f'_c}$ (Specimen E-G-1.1) was able to reach its design capacity without any significant damage in the joint area. However, increasing the joint shear stress to $1.4\ \sqrt{f'_c}$ in the same joint resulted in not achieving the design capacity in the pulling direction and failure prior to 5% drift ratio, due to excessive damage induced to the joint.
- Increasing the size of lateral beams improved the seismic performance of the GFRP-RC beam-column joints by providing more confinement to the joint area. Specimen A-G-1.4-L 75% with joint shear stress of $1.4\sqrt{f'_c}$ and lateral beams covering 75% of the joint area was able to reach its design capacity in both pushing and pulling directions. Moreover, increasing the size of lateral beams decreased the maximum shear stress resisted by the joint stirrups.
- Column axial load significantly influences the seismic performance of GFRP-RC beam-column joints. Increasing the column axial load degrades the performance of the joints due to premature concrete crushing. Specimen A-G-1.0-C 45% with joint shear stress of $1.0\sqrt{f'_c}$ and column axial load equal to 45% of its maximum capacity failed prematurely in the pulling direction prior to reaching the design capacity.
- Although CFRP reinforcement provides superior performance over GFRP reinforcement in terms of crack width and deflection, they lack deformable behaviour in seismic design. Specimen A-C-0.85 (reinforced with CFRP) with the same moment capacity as Specimen A-G-0.90 (reinforced with GFRP bars and stirrups) exhibited a brittle failure at 4% drift ratio, while Specimen A-G-0.9 successfully reached 5% lateral drift ratio.

- The effect of lateral beams on seismic performance of GFRP-RC beam-column joints is related to the level of joint shear stress. Due to low joint shear stress in Specimen A-G-0.85 (joint shear stress of $0.85\sqrt{f'_c}$), additional confinement provided by lateral beams did not play significant role in improving shear capacity of the joint. However, in the specimens with higher joint shear stress ($1.0\sqrt{f'_c}$ and $1.2\sqrt{f'_c}$) the confinement provided by lateral beams significantly improved the seismic performance of the joint.

6 SEISMIC BEHAVIOUR OF GFRP-REINFORCED CONCRETE INTERIOR BEAM-COLUMN-SLAB SUBASSEMBLIES

Shervin K. Ghomi and Ehab El-Salakawy

American Society of Civil Engineers (ASCE), Journal of Composites for Construction, 2019, Vol. 23, No. 6: 04019047, DOI: 10.1061/(ASCE)CC.1943-5614.0000980.

Abstract: Although the seismic behaviour of moment-resisting frames (MRF) reinforced with conventional steel has been extensively studied, the performance of MRFs that are reinforced with alternative materials, such as glass fibre reinforced polymers (GFRP) is not fully explored. The presence of floor slabs, integrally cast with beams, is one of the main factors that affects the seismic behaviour of GFRP-reinforced concrete (RC) MRFs, which is still uncovered. To fill this gap, three full-scale assemblies, one beam-column and two beam-column-slabs, were constructed and tested to failure under reversal quasi-static cyclic loading. The main test parameters were the presence of slabs and type of reinforcement (steel and GFRP). Moreover, a series of finite element models were developed and used to investigate the effect of slab width and lateral beam size on the contribution of slabs. Test results indicated that GFRP-RC slabs, when in tension, significantly contribute to the moment capacity of beams. It was also observed that the presence of slabs increases the initial lateral stiffness of GFRP-RC MRFs, which can reduce lateral deformations of the frames during earthquakes.

Keywords: GFRP-RC, Moment-resisting frames, Seismic performance, Cyclic loading, Beam-column connections, Beam-column-slab subassemblies, Lateral load-drift response.

6.1 Introduction

Reinforced concrete (RC) moment-resisting frames (MRF) are one of the main lateral load resisting systems that are commonly used in buildings in seismic regions. In such frames, rotational resistance of beam-column joints (B-CJs) is the main source of lateral stiffness of the frames. Therefore, investigating the seismic performance of individual beam-column connections is necessary to understand the behaviour of MRFs during an earthquake.

Many researchers have been exploring the effect of various parameters on seismic behaviour of RC beam-columns since 1960s (Hanson and Connor 1967; Pauly et al. 1978; Ehsani and Wight 1985-a; Kim and LaFave 2007; Le-Trung et al. 2013). However, the majority of available literature is focused on steel-RC B-CJs, while there is very few information available regarding the seismic performance of concrete B-CJs reinforced with alternative reinforcing materials such as fiber-reinforced polymers (FRP).

The FRP materials have been introduced to the construction industry as an alternative reinforcing material to provide superior performance, mainly in terms of corrosion resistance. Up to date, Carbon FRP (CFRP), Aramid FRP (AFRP), Glass FRP (GFRP), and recently Basalt FRP (BFRP) are the main FRP materials available for the construction industry.

In addition to its lower cost, GFRP, in particular, is considered the most suitable type of FRP for use in seismic regions due to its relatively high ultimate strain capacity. Previous studies (Ghomi and El-Salakawy 2016; Hasaballa and El-Salakawy 2016) indicated that GFRP-RC B-CJs are able to withstand significantly high lateral deformations (up to 9% lateral drift ratio) without exhibiting brittle failure.

Despite the promising results from the initial studies on the seismic performance of GFRP-RC B-CJs, the literature on this area is still scarce. Ghomi and El-Salakawy (2016) and Hasaballa and El-Salakawy (2016) studied a number of affecting parameters on the seismic behaviour of GFRP-RC B-CJs such as: reinforcement detailing, concrete strength and presence of lateral beams. However, there are still many parameters known to affect the seismic performance of GFRP-RC B-CJs. which are still not explored.

One of the main affecting parameters that has not been studied yet is the presence of slabs. The integral behaviour of concrete beams and slabs could significantly affect the lateral load capacity, lateral stiffness and energy dissipation of MRFs. Moreover, the increase in moment capacity of beams due to their interaction with slabs (T-beam action) can significantly change column-to-beam flexural strength ratio. According to current steel-RC building codes such as CSA/A23.3-14 (CSA 2014-a), the column-to-beam flexural strength ratio should be kept more than 1.0 to prevent the formation of weak column-strong beam condition in MRFs. This is to avoid formation of plastic hinges in columns prior to beams to maintain stability of the frames during earthquakes. These building codes require including the effect of slabs on moment capacity of beams in calculating column-to-beam flexural strength ratios.

The effect of floor slabs on seismic behaviour of steel-RC beam-columns has been studied extensively (Ehsani and Wight 1985-b; Pantazopoulou et al. 1988; Zerbe and Durrani 1990; Ning and Zhu 2014). Many parameters have been reported as influencing factors on the effective width of slabs, such as geometry of B-CJs, size and reinforcement detailing of lateral beams and beam-to-slab relative reinforcement ratio. Pantazopoulou et al. (1988) developed an analytical model to estimate the effective width of slabs in steel-RC frames. The researchers reported the effective slab width as a function of strains in longitudinal bars of beams. Based on their findings, prior to

yielding of the beam bars, the effective slab width (as an overhang on each side of the beam) in interior connections is equal to approximately 1.5 times the effective beam depth (*d*). However, as the strain in the beam bars increases beyond yielding, the effective slab width increases.

Current codes and guidelines for FRP-RC structures that contain seismic design provisions, such as CSA/S806-12 (CSA 2012), also require the column-to-beam flexural strength ratio of B-CJs to be more than 1.0. However, due to lack of research data, there is no guidelines regarding the effective width of floor slabs contributing to moment capacity of beams in FRP-RC frames. This lack of information could negatively affect the safety of FRP-RC frames since ignoring the effect of slabs on moment capacity of beams could result in over-estimation of columns-to-beams flexural ratios, which could result in unexpected formation of inelasticity centres in the columns during earthquakes.

Furthermore, ignoring the contribution of floor slabs in moment capacity of beams could result in underestimating lateral stiffness and load capacity of MRFs, which in turn results in over-estimation of lateral deformation of FRP-RC frames. This can affect the adequacy of buildings in the design stage as engineers must check the maximum expected lateral drift of the buildings against the maximum allowable lateral drift according to applicable building codes.

In addition, the contribution of floor slabs in compression could be more sensitive in FRP-RC beams compared to that of steel-RC ones. The FRP materials have linear elastic behaviour without any yielding plateau (in contrary to conventional steel). Therefore, FRP-RC beams are mainly designed as over-reinforced elements (CSA 2012) to ensure relatively deformable compressive mode of failure (concrete crushing) instead of sudden and brittle tensile mode of failure (FRP bar rupture). Contribution of floor slabs as an effective flange for an FRP-RC beam could change the section from an over-reinforced to an under-reinforced section; thus, resulting in the change of

mode of failure from concrete crushing to FRP bar rupture. This brittle mode of failure is not desirable, particularly in seismic design.

Steel-RC beams, on the other hand, are designed as under-reinforced sections (yielding of steel bars prior to concrete crushing); therefore, contribution of floor slabs as an effective flange does not change the mode of failure, as the sections remain under-reinforced. To fill this gap, in this program, one of the main objectives is to investigate the effect of slabs on the seismic performance of GFRP-RC B-CJs.

On the other hand, the linear elastic behaviour of GFRP materials could be beneficial since GFRP-RC B-CJs exhibit considerably less residual damage compared to their counterparts steel-RC ones (Ghomi and El-Salakawy 2016). Steel-RC frames are prone to significant residual damage after yielding of the reinforcement during an earthquake. In some cases, the residual damage, even after surviving an earthquake without complete collapse, is so significant that demolishing of the building is inevitable. In contrary, low residual damage in GFRP-RC frames increases the possibility of maintaining their serviceability after surviving an earthquake event. This can significantly reduce the post-disaster costs after a major earthquake.

However, to take advantage of this feature of GFRP-RC frames, it is necessary to determine the performance of such frames, after surviving an earthquake. Therefore, in this program, the seismic performance of GFRP-RC B-CJs was investigated through a two-phase loading scheme. During the first loading phase, the seismic performance of the specimens was evaluated under a loading scheme simulating a severe earthquake. In the second loading phase, the specimens of the first phase were immediately re-tested up to failure under similar seismic loading procedure to evaluate the performance of the GFRP-RC B-CJs after surviving seismic loading.

6.2 Experimental Program

6.2.1 Test specimens

A total of three full-scale interior beam-column assemblies were constructed and tested under reversal cyclic loading. In all specimens, the column measured 350-mm wide, 450-mm deep and 2,900-mm long and each of the main beams measured 450-mm deep, 350-mm wide and 2,300-mm long. The dimensions of the lateral beams (350 mm by 350 mm) were proportioned to cover 60% of the joint area. In two of the specimens, the beams were cast integrally with a 100-mm thick slab to form a beam-column-slab connection. Geometrical configuration and dimensions of the specimens with slab are shown in Figure 6.1. The specimens were designated with three letters, the first indicates the type of reinforcement ("G" for GFRP and "S" for steel) while, the second and third letters indicate whether or not there is a slab ("SL" for the specimens with slab and "XX" for the specimen without slab).

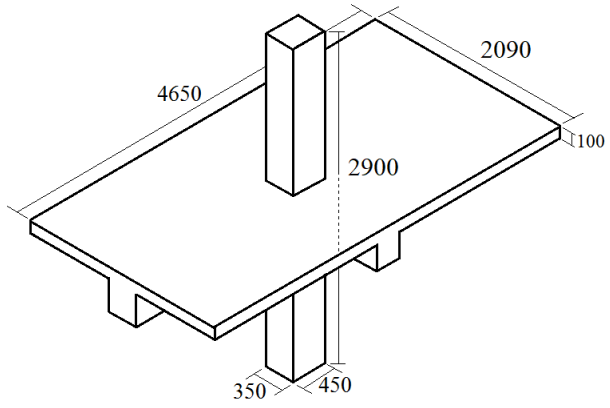

Figure 6.1 - Dimensions of specimens with slab (dimensions in mm)

The main beams in Specimen G-SL (reinforced with GFRP bars and stirrups) and Specimen S-SL (reinforced with steel bars and stirrups) were designed to have approximately the same bending moment capacity. The bending moment capacity of the beams in Specimen S-SL was calculated by assuming 25% increase in the yield stress of the longitudinal bars due to strain hardening (CSA

2014-a). Reinforcement detailing and properties of the test specimens are provided in Figure 6.2 and Table 6.1, respectively.

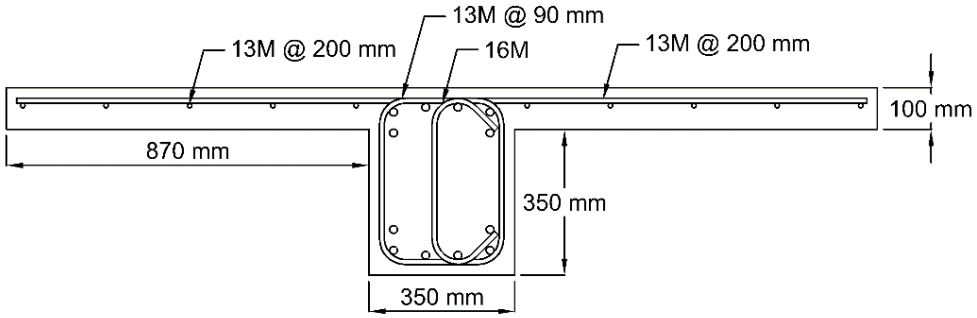

(a) Beam and slab of Specimen G-SL

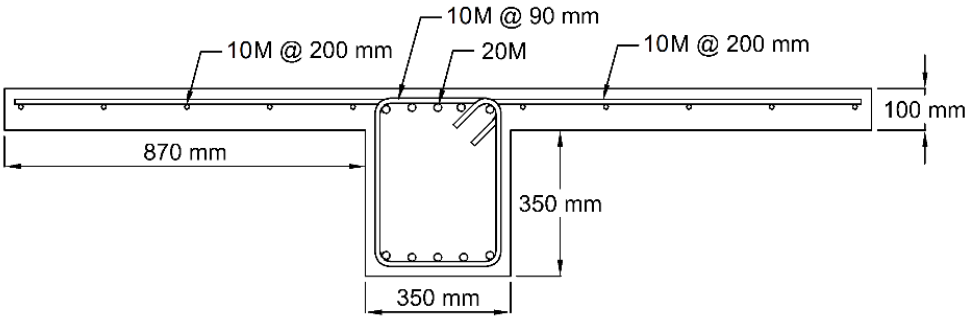

(b) Beam and slab of Specimen S-SL

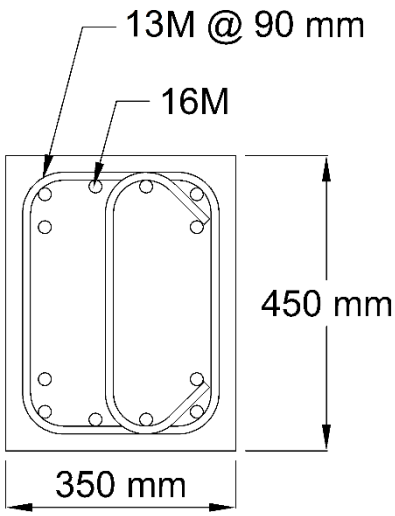

(c) Beam of Specimen G-XX

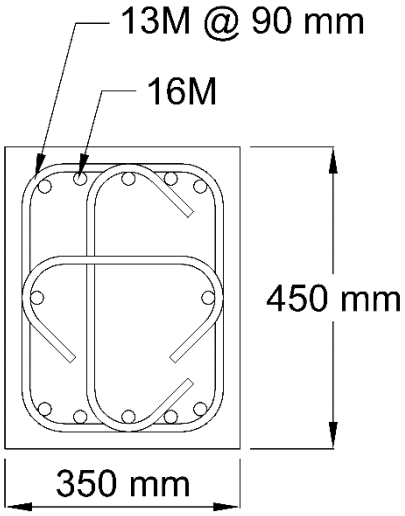

(d) Column of GFRP-RC Specimens

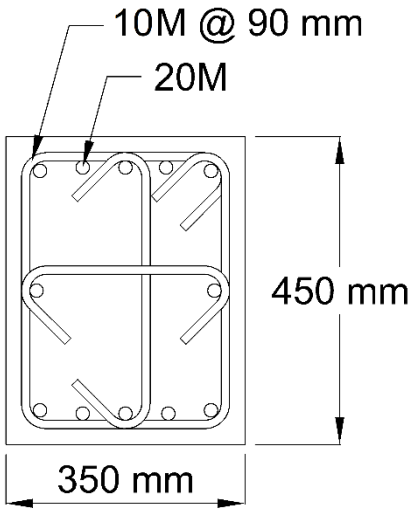

(e) Column of Steel-RC Specimen

Figure 6.2 - Reinforcement detailing of test specimens

Table 6.1 - Properties of test specimens

Specimen	Beam Flexural Capacity[(a)] (kN.m)	Column-to-Beam Flexural Ratio[(b)]	Joint Shear Stress ($\times \sqrt{f'_c}$)	Concrete Strength (MPa)
G-SL	333	0.99	1.49	50
S-SL	321[(c)]	1.30	1.29	55
G-XX	330	0.98	1.49	49

[(a)] Capacity without slab contribution
[(b)] Effect of column axial load is included in the flexural capacity of columns
[(c)] 25% increase in steel tensile strength due to strain hardening

Specimen G-XX was constructed by replicating Specimen G-SL except for eliminating the slab. The slab in Specimen G-SL contained minimum required reinforcement, according to CSA/S806-12 (CSA 2012) in both directions, leading to 13M (12.7-mm diameter) GFRP bars spaced at 200 mm. To be comparable with Specimen G-SL, the slab in Specimen S-SL was also reinforced with 10M (11.3-mm diameter) steel bars spaced at 200 mm.

6.2.2 Materials

Ready-mix concrete with target 28-day strength of 40 MPa was used to cast the specimens. The actual concrete strength was obtained on the day of testing using standard 100 mm × 200 mm concrete cylinder compressive tests and is reported in Table 6.1.

Sand-coated GFRP bars and stirrups were used in construction of the GFRP-RC specimens. The tensile strength and modulus of elasticity of the GFRP reinforcement are shown in Table 6.2 as reported by the manufacturer (Pultrall Inc. 2019).

Table 6.2 - Properties of reinforcement

Reinforcement	Nominal Cross-Sectional Area (mm^2)		GFRP Tensile Strength, Steel Yield Strength (MPa)	Modulus of Elasticity (GPa)
	Nominal [(a)]	Immersion test [(b)]		
16M GFRP Bars	198	263	1,184	62.6
13M GFRP Bars	127	158	1,312	65.6
13M GFRP Stirrups [(c)]	127	164	1,019	50.0
20M Steel Bars	300	N/A	458	192.9

[(a)] Nominal bar area used in all calculations.
[(b)] Experimentally tested in accordance with CSA/S806-12, Annex A (CSA 2012).
[(c)] Properties of straight portion of bent bars.

Deformed regular steel bars, CSA grade G400, were used for constructing the steel-RC beam-column-slab subassembly (S-SL). The tensile strength and modulus of elasticity of the steel reinforcement were measured from traction test and are reported in Table 6.2.

6.2.3 Test set-up

The test set-up, shown in Figure 6.3, was constructed to evaluate the seismic performance of the test specimens. The specimens were tested in their actual orientation in a MRF (vertical columns

and horizontal beams). A fully-dynamic actuator, fixed on a strong concrete wall, was used to apply horizontal reversal cyclic loading to the tip of the column.

Figure 6.3 - Test set-up

A hydraulic jack was used to apply a constant axial load to the column during the test. The hydraulic jack was mounted on a loading frame, which consisted of a stiffened I-beam and two hollow structural section (HSS) elements that were pinned at the bottom, thus rotating freely with the column while the actuator was applying reversal loading. It should be mentioned that rotation of the loading frame with the column eliminated the formation of secondary moments by maintaining coincidence of column axis and line of action of the axial load.

The column was sitting on a hinge that allowed rotation but restricted translational movement. Tips of the main beams were also attached to the strong floor by means of two double-hinged elements (links) allowing rotation and horizontal translation of the beam tips while restricting their vertical movement (roller boundary condition).

6.2.4 Loading scheme

Testing of the specimen started with the application of a constant axial load, approximately equal to 15% of the concentric axial capacity of the columns. This axial load was kept constant during the application of the lateral load. The reversal lateral loading protocol suggested by ACI 374.1-05 report on "Acceptance criteria for moment frames based on structural testing" (ACI Committee 374 2005) was adapted in the experimental program. The lateral load was applied in displacement-controlled mode and consisted of consecutive loading steps, each gradually increasing in the magnitude of lateral displacement. The lateral displacement was measured in terms of lateral drift ratio, defined as the ratio of the columns lateral displacement (stroke of the actuator) over the columns length. During each loading step, three identical loading cycles were applied to ensure stable crack propagation in the specimens.

The lateral loading of Specimen S-SL was scheduled to started with 0.8% drift ratio followed by 1%, 1.5%, 2%, 3%, 4%, 5%, 6%, 7% and 8%. This loading schedule was followed until failure of the specimen occurred.

As mentioned earlier, the GFRP-RC specimens (G-SL and G-XX) were tested under a two-phase cyclic loading. The same drift ratio sequence as that of Specimen S-SL was used in testing the GFRP-RC specimens except that the loading was stopped after 5% drift ratio and the specimens were immediately (without any repair) loaded under the same loading sequence starting over from 0.8% to 8%. As mentioned earlier, this two-phase loading was used to investigate the performance of GFRP-RC beam-columns after surviving a severe earthquake (simulated in the first loading phase).

To achieve the main purpose of the two-phase loading approach, it was necessary to reach the design capacity of the GFRP-RC specimens during the first loading phase. According to previous

experiments on seismic behaviour of GFRP-RC beam-columns (Ghomi and El-Salakawy 2016; Hasaballa and El-Salakawy 2016), such elements could deform up to 5% drift ratio before they reach their design capacity. Therefore, 5% drift ratio was set as the threshold for the first loading phase.

After 2% lateral drift ratio, a load-controlled cycle with the amplitude equal to the service load was applied after each loading step to measure the lateral stiffness reduction in the specimens, if any. The service load was calculated as the lateral load corresponding to 60% of the yield strain and 25% of the ultimate strain in beam reinforcement of the steel-RC and the GFRP-RC specimens, respectively. The loading protocol for the GFRP-RC specimens is shown in Figure 6.4.

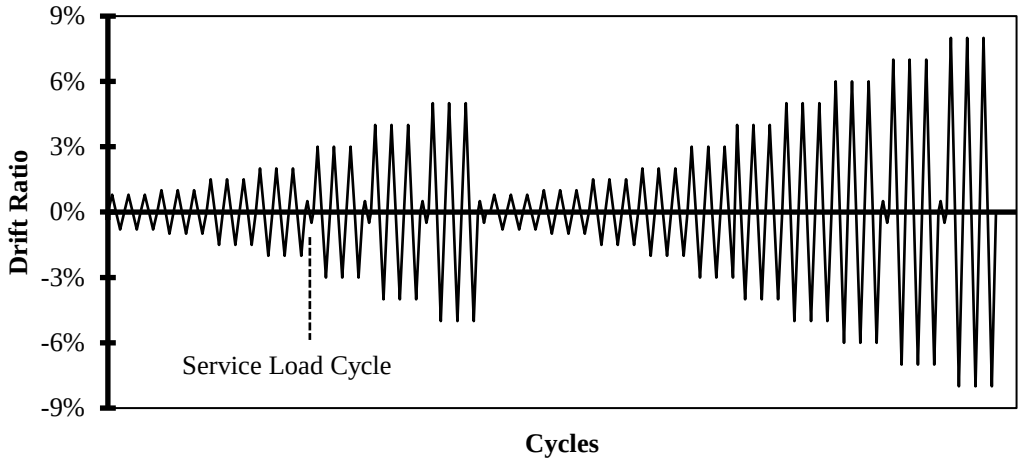

Figure 6.4 - Loading protocol of GFRP-RC specimens

6.3 Test Results and Discussions

6.3.1 Effect of reinforcement type

Figure 6.5 shows lateral load-displacement relationship (hysteresis diagrams) of the steel-RC specimen from 0% drift ratio until failure and the GFRP-RC specimens in the first loading phase (up to 5% drift ratio). As mentioned earlier, the steel-RC specimen was only tested under one loading phase. The dashed lines in the graphs show the lateral load corresponding to the design

bending moment capacity of the beams, without taking into account the effect of slabs (T-beams). It should be mentioned that the maximum bending moment capacity of the beam in Specimen S-SL was calculated by assuming 25% increase in the yield stress of the reinforcement due to strain hardening (CSA 2014-a).

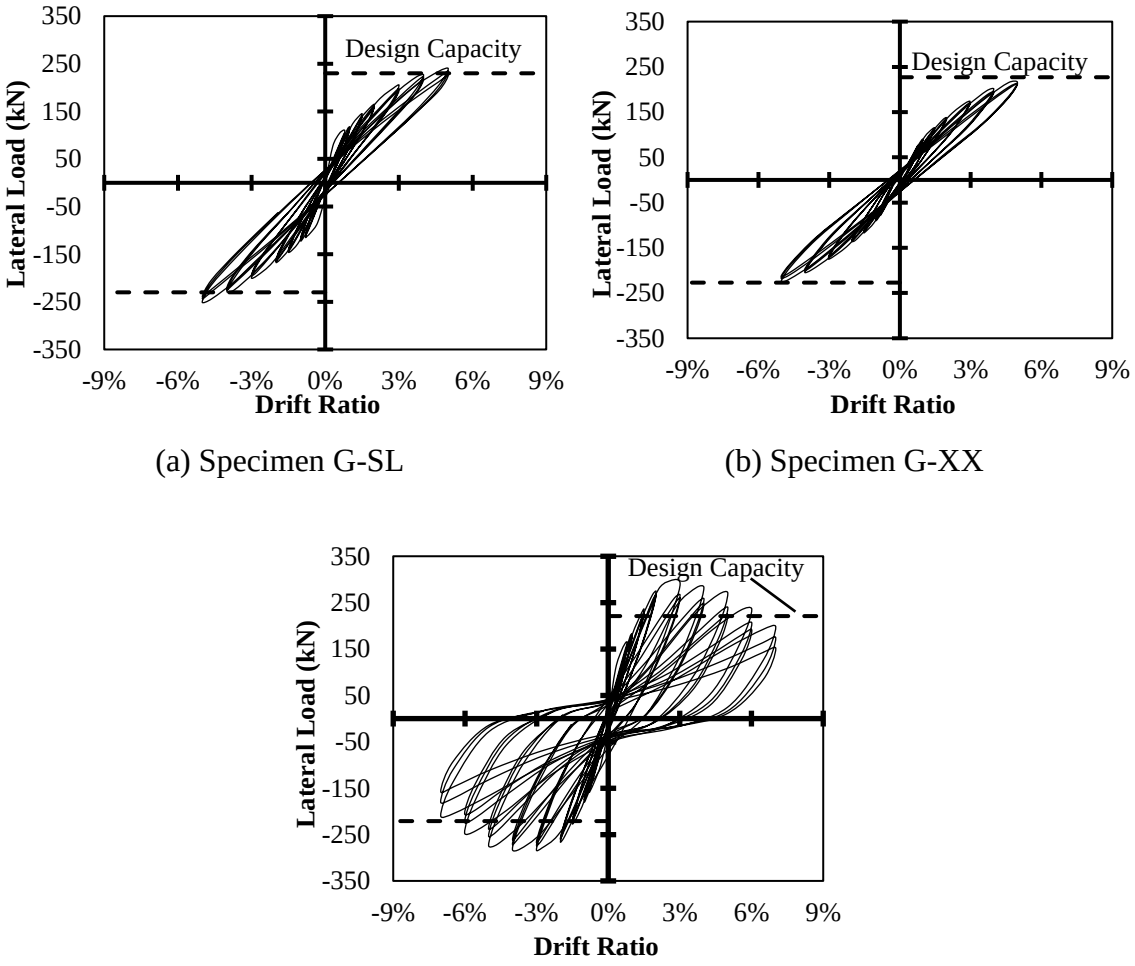

(a) Specimen G-SL

(b) Specimen G-XX

(c) Specimen S-SL

Figure 6.5 - Lateral load-drift response of test specimens

As Figure 6.5 shows, GFRP-RC specimens indicated significantly lower residual damage (pinching) compared to the steel-RC specimen. As mentioned earlier, this behaviour was expected from GFRP-RC elements due to the linear behaviour of GFRP reinforcement. Lack of ductile

behaviour of GFRP reinforcement also resulted in narrower loops in the hysteresis diagram of the GFRP-RC specimens compared to the steel-RC specimen.

Normalized maximum lateral load of the test specimens up to 5% drift ratio (the first loading phase of the GFRP-RC specimens), calculated as the ratio of the maximum lateral load over the maximum beam-only design capacity (without the effect of slabs), are compared in Figure 6.6. The lower modulus of elasticity of the GFRP reinforcement (62 GPa) compared to that of steel reinforcement (200 GPa) resulted in lower initial stiffness of the GFRP-RC specimens. Thus, specimens G-SL and G-XX reached their beam-only design capacity at 4% and 5% lateral drift ratio, respectively, while specimen S-SL achieved its beam-only design capacity at 1.5% drift ratio.

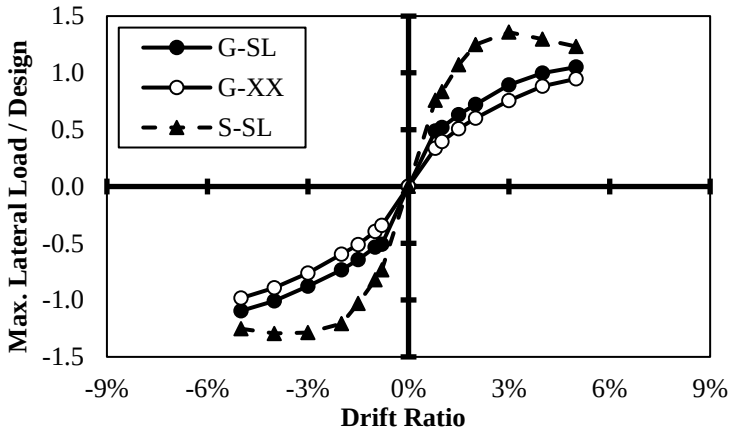

Figure 6.6 - Normalized maximum lateral load

As Figure 6.6 indicates, at equal drift ratios, Specimen G-SL showed higher lateral load resistance compared to Specimen G-XX, due to the effect of slabs on moment resistance of the beams (T-beam action). However, the effect of slabs on the lateral load increase was more pronounced in Specimen S-SL. The composite action of the slab with the beams in Specimen S-SL resulted in 36% increase in the lateral load carrying capacity with respect to the capacity of the beams alone, while this increase was only 10% in Specimen G-SL.

Figure 6.7 shows the condition of the specimens at the end of the loading step that their "beam-only" design capacity was reached during the first loading phase (4%, 5% and 1.5% drift ratio for Specimen G-SL, Specimen G-XX and Specimen S-SL, respectively). The thumbnail drawings at the lower corner of the figures indicate the part of the specimens that are shown in the pictures. The cracks were visually inspected and marked during the loading cycles. Even though both specimens were loaded to their maximum design capacity, insignificant concrete spalling was observed in the specimens. The majority of cracks completely closed after each loading step due to the elastic nature of GFRP reinforcement. This was also evident in Figure 6.5-a and Figure 6.5-b by the insignificant pinching in the hysteresis diagram of the specimens. Moreover, there were no signs of damage penetration into the joint area.

This indicates superior performance of GFRP-RC beam-columns compared to steel-RC ones in terms of residual damage. It should be mentioned that in steel-RC B-CJs, once the design capacity is reached (yielding of reinforcement), the joint is not able to restore its original condition since its reinforcement has already yielded (permanent deformation). Therefore, even if a steel-RC MRF survives an earthquake after yielding of its reinforcement without total collapse, it might fail to satisfy service limit conditions afterward. Thus, demolishing the building will be inevitable.

A GFRP-RC MRF, on the other hand, has the potential to maintain its original condition up to an acceptable degree even after reaching its maximum design capacity during a strong earthquake. Therefore, it might be possible to extend the service life of the structure after surviving a severe earthquake. This can significantly reduce post-disaster costs due to rehabilitation and reconstruction of damaged structures.

However, to take advantage of this superior behaviour, low energy dissipation and initial stiffness of GFRP-RC MRFs must be addressed. Hybrid lateral load-resisting systems (MRF combined with

shear walls) have been proposed as a possible approach to improve the seismic performance of GFRP-RC structures (Hasaballa and El-Salakawy 2016).

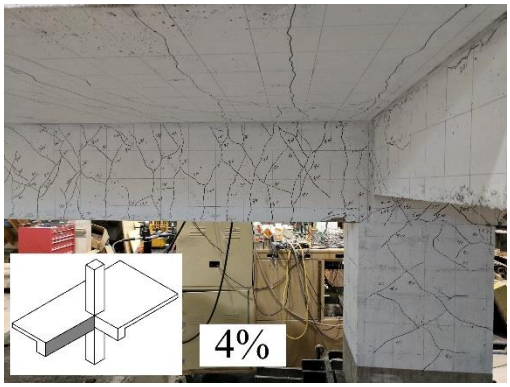

(a) Specimen G-SL after 4% drift ratio

(b) Specimen G-XX after 5% drift ratio

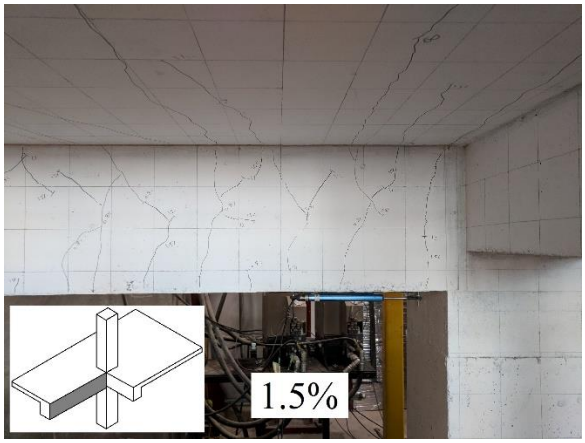

(c) Specimen S-SL after 1.5% drift ratio

Figure 6.7 - Condition of the specimens after reaching the design capacity

6.3.2 Behaviour of GFRP-RC specimens in the second loading phase

Figure 6.8 compares the lateral load envelope of the GFRP-RC specimens in the first and the second loading phases. Both specimens showed gradual decrease in lateral load after 6% drift ratio. The test was stopped at 8% drift ratio due to failure of the GFRP-RC specimens. According to ACI 374.1-05 report (ACI Committee 374 2005), the failure was defined when the lateral load resistance of a specimen decreases to lower than 75% of the maximum lateral load obtained during

the test. Specimens G-SL and G-X reached only 71% and 63% of their maximum lateral load during the third cycle of loading at 8% drift ratio.

This gradual mode of failure is very similar to what was observed from the steel-RC specimen. Specimen S-SL, also, showed gradual decrease in lateral load after 3% drift ratio. The test was stopped at 7% drift ratio due to significant decrease in lateral load carrying capacity of the specimen (decrease to 55% of the maximum lateral load). The failure of GFRP-RC beam-columns without any signs of sudden failure due to rupture of the longitudinal bars has been also observed in previous studies (Ghomi and El-Salakawy 2016).

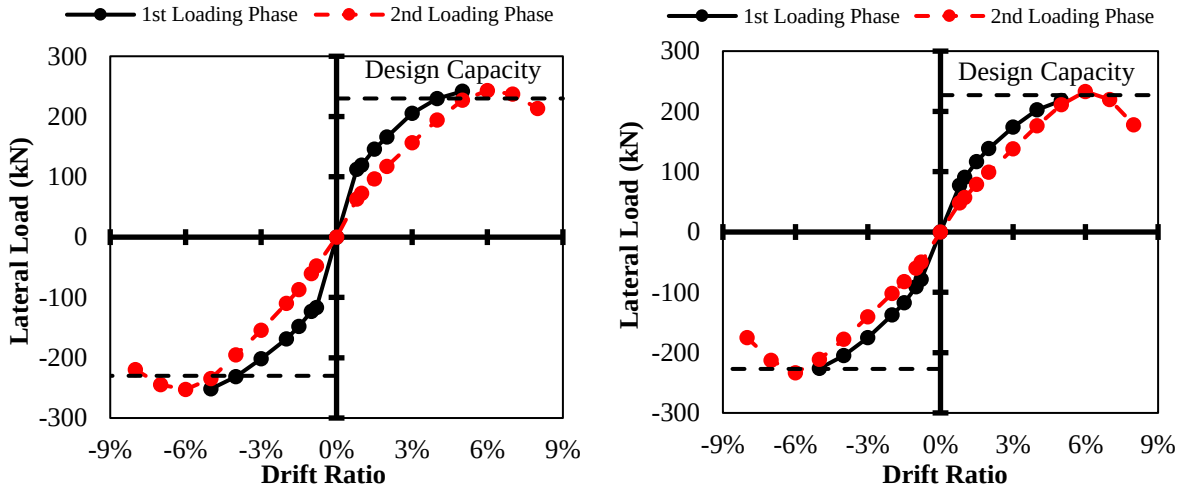

(a) Specimen G-SL (b) Specimen G-XX

Figure 6.8 - Lateral Load envelop of GFRP-RC specimens

Both GFRP-RC specimens were able to achieve their design capacity for the second time in the second loading phase. The GFRP-RC specimens behaved in a linear manner in the second loading phase up to 5% drift ratio. This is indicated by a straight-line connecting the origin to the maximum lateral load that was achieved by the specimens during the third load cycle at 5% drift ratio in the first loading phase.

6.3.3 Mode of failure

The condition of the specimens at the final stage (failure) is illustrated in Figure 6.9. Comparing the specimens indicates that Specimen G-SL exhibited more damage penetration into the joint area compared to Specimen G-XX. One of the main parameters affecting the location of the damage concentration in a beam-column assembly is the column-to-beam flexural strength ratio. As this ratio decreases (beams stronger than columns) the damage concentration moves toward the joint area. Interaction of the slabs with the beams (T-beam action) in Specimen G-SL increased the moment capacity of the beams and, consequently, decreased the column-to-beam flexural ratio in Specimen G-SL compared to Specimen G-XX, resulting in more concrete damage in the joint area.

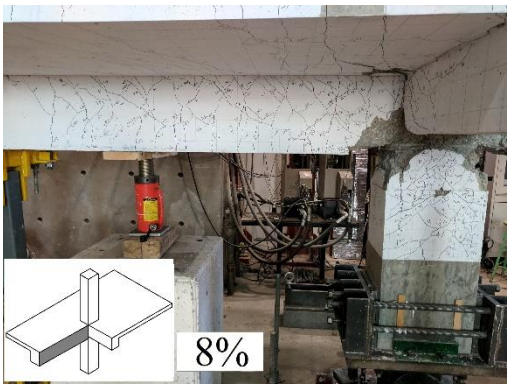

(a) Specimen G-SL

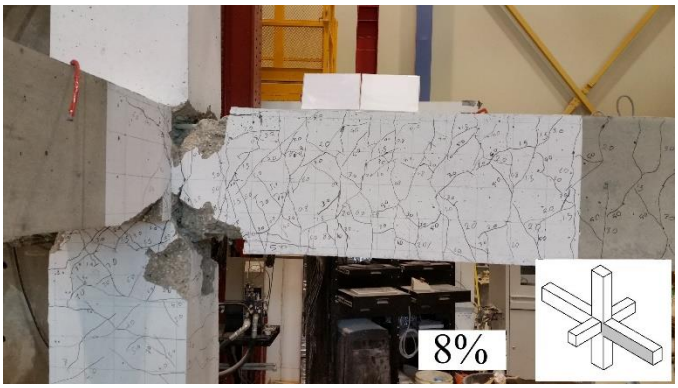

(b) Specimen G-XX

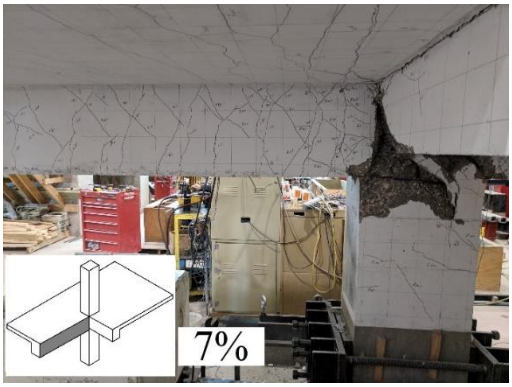

(c) Specimen S-SL

Figure 6.9 - Condition of the specimens at failure

This effect was more pronounced in Specimen S-SL (Figure 6.9-c). As mentioned earlier, Specimen S-SL exhibited more increase in the lateral load resistance compared to Specimen G-SL. Based on the maximum lateral load recorded during testing of Specimens S-SL and G-SL, the column-to-beam flexural strength ratio was recalculated as 0.96 and 0.90, respectively. By comparing these values with the initial ratios calculated based on beam-only capacity in Table 6.2, it is evident that the decrease in the flexural strength ratio for specimen S-SL was more pronounced compared to Specimen G-SL.

6.3.4 Effect of slabs on moment capacity of beams

An electrical strain gauge was installed on each of the slab longitudinal bars (parallel to the main beam) near the column face. The maximum stresses calculated based on strain gauge readings at the maximum lateral load (5% in G-SL and 3% in S-SL) are shown in Figure 6.10.

To estimate the effective slab width in tension, the average stress method, similar to the method suggested by Ning et al. (2014), is used:

$$b_{ef} = \frac{\sum_{i=1}^{n} \frac{1}{2}\left(\sigma_{sb(i)} + \sigma_{sb(i+1)}\right)s}{\sigma_{bb,max}} \qquad (6.1)$$

where, $\sigma_{bb,max}$ is the maximum stress in the beam longitudinal bars, σ_{sb} is the stress in the slab longitudinal bars, n is the total number of bars in the slab on each side of the beam and s is the spacing of longitudinal bars in the slab.

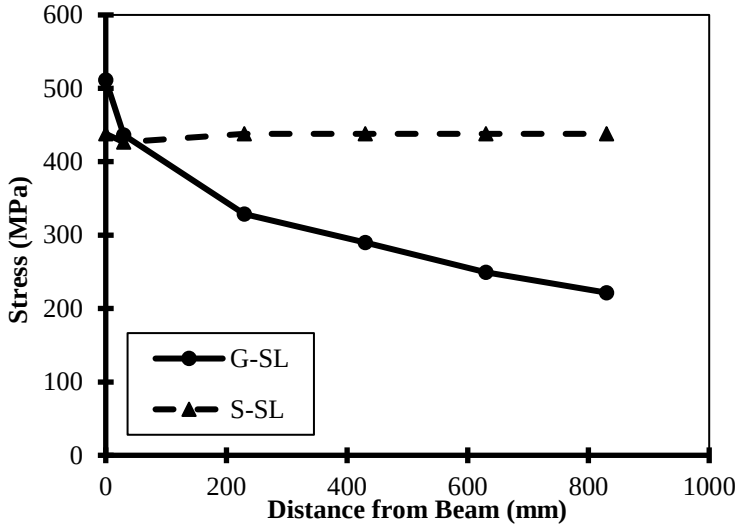

Figure 6.10 - Stress distribution in slabs

Based on the Equation 6.1, an effective slab width of 468 mm and 797 mm, as an overhang on each side of the beam, was calculated for Specimen G-SL and S-SL, respectively. This represents 1.2*d* and 2*d* (*d* is the effective beam depth) in the GFRP-RC and the steel-RC specimen, respectively.

The higher effective width in steel-RC slab versus the GFRP-RC slab could be due to the lower modulus of elasticity of GFRP reinforcement which resulted in more deflection of the slab in the transverse direction and hence less rigidity of the slab.

A PI-gauge was installed on the steel HSS links that connects tip of the main beams to the floor to measure reactions at the beam tips during the lateral loading. Figure 6.11 shows the maximum positive (slab-in-compression) and negative (slab-in-tension) moment at each drift ratio, calculated for the main beam of the specimens based on the reactions measured by the PI-gauges. The dashed lines in the figure represent the minimum and maximum theoretical bending moment capacity of the beam-slabs, including zero slab width (beam-only) and full slab width in the calculations, respectively.

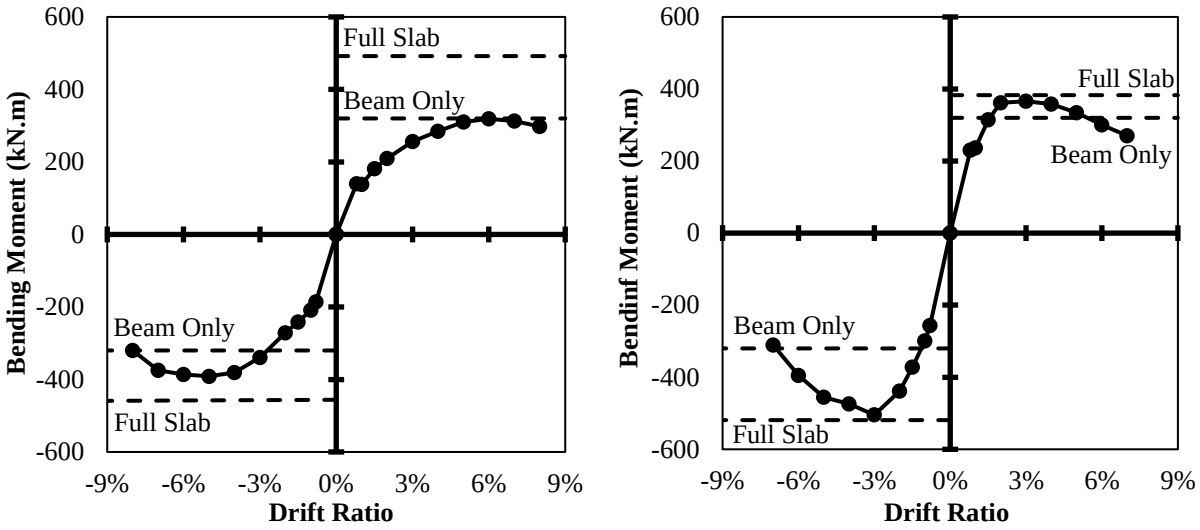

(a) Specimen G-SL (b) Specimen S-SL

Figure 6.11 - Bending moments in main beams

As indicated in the figure, the maximum measured negative moment achieved by the beam in Specimen G-SL was very close to the beam-only bending moment capacity (without including the effect of slab). This indicated that the floor slab did not contribute to the moment-resisting capacity of the GFRP-RC beam in compression.

It is worth mentioning that the theoretical positive moment capacity of GFRP-RC beam-slabs is more sensitive to the effective slab width compared to that of steel-RC beam-slabs. This can be observed in Figure 6.11 as the dashed lines, indicating the minimum and the maximum theoretical positive bending moments, are closer to each other for S-SL compared to that for G-SL. As mentioned earlier, this is attributed to the difference in theoretical mode of failure for Steel-RC and GFRP-RC beam-slabs.

However, despite the theoretical analysis, the test results indicated that the contribution of GFRP-RC slabs in positive bending moment capacity of beams is insignificant.

The maximum negative bending moment (slab-in-tension) recorded for Specimen G-SL; however, was more than the beam-only capacity but less than the capacity including full slab width. The

theoretical negative moment capacity, considering an effective slab width of 1.2*d* (468 mm) on each side of the beam, was calculated as 416 kN.m. This value is close to the maximum observed negative moment in the beams, 391 kN.m (Figure 6.11-a). Therefore, the maximum-recorded negative bending moment also confirms the effective slab width that was calculated previously from the strain readings of the slab longitudinal bars.

Specimen S-SL, on the other hand, showed higher values than beam-only capacity for both positive and negative moments. The maximum positive and negative moments measured for Specimen S-SL (Figure 6.11-b) were 366 kN.m and 504 kN.m, respectively. The maximum theoretical positive and negative moments, considering an effective slab width of 2*d* (797 mm) on each side of the beam, were calculated as 379 kN.m and 510 kN.m, respectively, which is in good agreement with the measured values during testing.

6.3.5 Effect of slabs on joint shear stress and column-to-beam flexural ratio

Ignoring the effect of slabs on moment-resisting capacity of beams can have adverse impact on the safety of buildings. One of the possible impacts is the excessive amount of shear stress exerted on the beam-column joint area due to the increase in negative bending moment capacity of beams. Figure 6.12 compares the maximum strain recorded from joint stirrups of Specimen G-XX and G-SL during the first loading phase. As expected, the composite action of the floor slabs with beams increased the maximum strains in the joint stirrups (44% increase at 5% drift ratio). However, despite the joint shear stress increase, the maximum strains recorded in the joint stirrups of Specimen G-SL remained lower than the maximum allowable limit of 5,000 micro-strain, specified by CSA/S806-12 (CSA 2012). This indicates that the requirements for transverse

reinforcement for columns in seismic regions suggested by CSA/S806-12 (CSA 2012) remains sufficient when the effect of slabs is included in the behaviour.

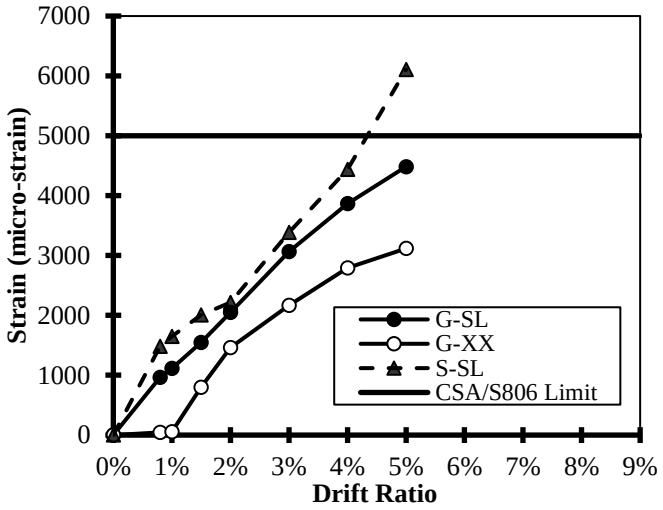

Figure 6.12 - Maximum strain in joint stirrups

Figure 6.12 also indicates that the joint stirrups in Specimen S-SL yielded at 2% drift ratio (strains larger than 2000 micro-strain), where the specimen reached the beam-only capacity. This is another indication that steel-RC frames are prone to permanent damage after strong earthquakes.

As mentioned earlier, the slab contribution to beams moment-capacity could result in an adverse alteration of the design from the desirable strong-column-weak-beam to the undesirable strong-beam-weak-column.

Even though the presence of the slab increased the moment-resisting capacity of the beams in specimen G-SL, observations during testing indicated that GFRP-RC B-CJs can exhibit stable satisfactory performance when column-to-beam flexural ratios less than unity. The maximum bending moment capacity of the column in G-XX was calculated as 325 kN.m, resulting in column-to-beam flexural strength ratio of 0.98. Moreover, as mentioned earlier, based on the maximum-recorded lateral load carrying capacity of Specimen G-SL, its moment strength ratio

decreased to 0.9. However, both specimens were able to reach their maximum lateral capacity (at 5% lateral drift ratio) with only minor concrete spalling in the concrete cover of the columns. This could be attributed to the confinement provided by the transverse reinforcement that increased the compressive strength of the concrete core and postponed the damage penetration into the column core.

Moreover, since the GFRP-RC columns were designed as over-reinforced elements, even after concrete cover crushing, the longitudinal reinforcement remains elastic with some reserved strain until rupture. Therefore, the columns can maintain their load carrying capacity to higher drift ratios after concrete cover loss. This is opposite to steel-RC elements that concrete crushing occurs after yielding of the reinforcement, which prevents load carrying increase of the columns.

The maximum strain measured in the columns longitudinal bars near the joint was 9,800 micro-strain in Specimen G-SL, which is significantly lower than the maximum tensile strain capacity of the GFRP bars (18,900 micro-strain).

6.3.6 Energy dissipation

Energy dissipation is one of the key influencing parameters in seismic performance of MRFs. Cumulative energy dissipation of the test specimens up to 5% drift ratio (first loading phase of GFRP-RC specimens) is calculated and compared in Figure 6.13. The magnitude of energy dissipation in each loading step is defined as the area enclosed by the hysteresis (load-displacement) loops in that step.

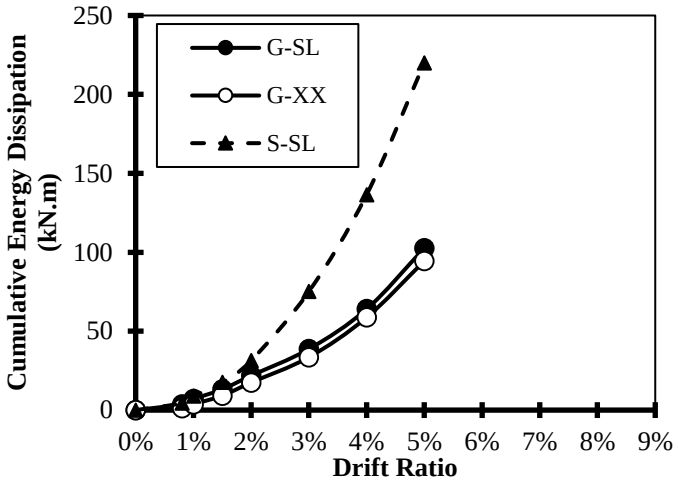

Figure 6.13 - Cumulative energy dissipation

Comparing the energy dissipation of Specimens G-XX and G-SL indicates that presence of floor slabs slightly increased the magnitude of energy dissipation. Specimen G-SL dissipated 15.5% and 8.7% more energy than Specimen G-XX at 3% and 5% lateral drift ratios, respectively.

The linear nature of GFRP material compared to ductile bilinear nature of conventional steel resulted in significantly lower energy dissipation in Specimen G-SL than the counterpart Specimen S-SL. Specimen S-SL showed 94% and 114% higher energy dissipation compared to that of G-SL at 3% and 5% drift ratio, respectively.

It should be mentioned that 5% drift ratio might be considered more than the response range expected from a typical building. For instance, the maximum allowable lateral drift ratio for buildings during seismic loading suggested by the National Building Code of Canada (NRCC 2015) is limited to 2.5%. Therefore, it seems more realistic to compare the energy dissipation of Specimens G-SL and S-SL at the lower drift ratio of 3% rather than 5%.

6.3.7 Lateral stiffness

Lateral stiffness of the test specimens up to 5% drift ratio is compared in Figure 6.14. The lateral stiffness is calculated as the maximum lateral load divided by the maximum displacement in each drift ratio. As expected, the steel-RC specimen showed a significantly higher lateral stiffness (approximately 45%) compared to its GFRP-RC counterpart. This was due to the higher modulus of elasticity of steel compared to GFRP (200 GPa versus 62 GPa).

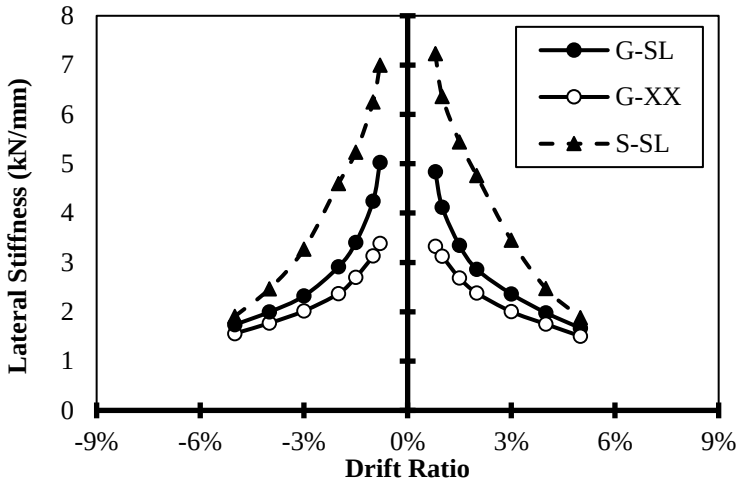

Figure 6.14 - Lateral stiffness

However, due to yielding of steel reinforcement, the rate of decrease in lateral stiffness was significantly higher in S-SL than that of G-SL, which means that by moving toward larger lateral displacements, the difference in the lateral stiffness between the two specimens decreased. The lateral stiffness calculated for Specimen S-SL was approximately 10% higher than the stiffness calculated for G-SL at 5% lateral drift ratio.

It is also evident form Figure 6.14 that floor slabs can significantly increase initial lateral stiffness of B-CJs. However, similar to the previous case, the effect of floor slabs on the stiffness decreased as the lateral displacement increases. The increase in the lateral stiffness of Specimen G-SL compared to Specimen G-XX decreased from 47% at 0.8% drift ratio to 11% at 5% drift ratio.

As mentioned earlier, the maximum allowable lateral drift ratio during an earthquake, according to the National Building Code of Canada (NRCC 2015), is 2.5%. Therefore, it is beneficial if MRFs mobilize their maximum lateral capacity within 2.5% drift ratio. However, previously tested GFRP-RC beam-column connections by Ghomi and El-Salakawy (2016), reached the design capacity at 4% or 5% lateral drift ratios. This low stiffness of GFRP-RC B-CJs could result in delaying the mobilization of full capacity of the connections beyond the reasonable response range of typical buildings. However, as shown in Figure 6.14, composite behaviour of slabs and beams could increase the initial stiffness of GFRP-RC MRFs, which enhances their performance by reducing their lateral deformation during earthquakes.

As indicated in Figure 6.8, the lateral load-drift response of GFRP-RC MRFs after surviving an earthquake can be simplified by a straight line connecting the origin to the point corresponding to the maximum lateral drift that was reached by the frame during the earthquake. Consequently, the lateral stiffness of the GFRP-RC specimens during the second loading phase up to 5% drift ratio was equal to the lateral stiffness corresponding to 5% drift ratio in the first loading phase, shown in Figure 6.14 (1.9 kN.mm and 1.5 kN.mm for G-SL and G-L, respectively).

Due to linear nature of GFRP reinforcement, it seems reasonable to assume the same type of behaviour for all GFRP-RC structural elements. This simplified approach might be used to estimate stiffness of each structural element to assess serviceability and ultimate performance of GFRP-RC frames after surviving an earthquake.

6.4 Analytical Investigation

To complement the experimental part of the program, several 3D finite element models (FEMs) were constructed to further investigate the effect of various factors on the performance of interior beam-column-slab assemblies. ATENA 3D (Cervenka et al. 2012) software package (version

5.3.5g) was used to analytically model the test specimens. ATENA 3D is a specialized FEM program suitable for modeling reinforced concrete structures by accounting for the nonlinear behaviour of concrete, effect of cracks and bond-slip behaviour of reinforcement.

The constructed analytical models were validated against the test results obtained from the experimental part of the program. Figure 6.15 compares the lateral load envelope and stress distribution of the slab bars obtained from the FEMs with those from the experiments, which showed good agreement. It should be mentioned that the lines representing the experimental and FEM results corresponding to Specimen S-SL coincide as both indicate yield stress in all longitudinal slab bars. The validated models were used to further investigate the effect of slab width and lateral beam size on the effective width of slabs.

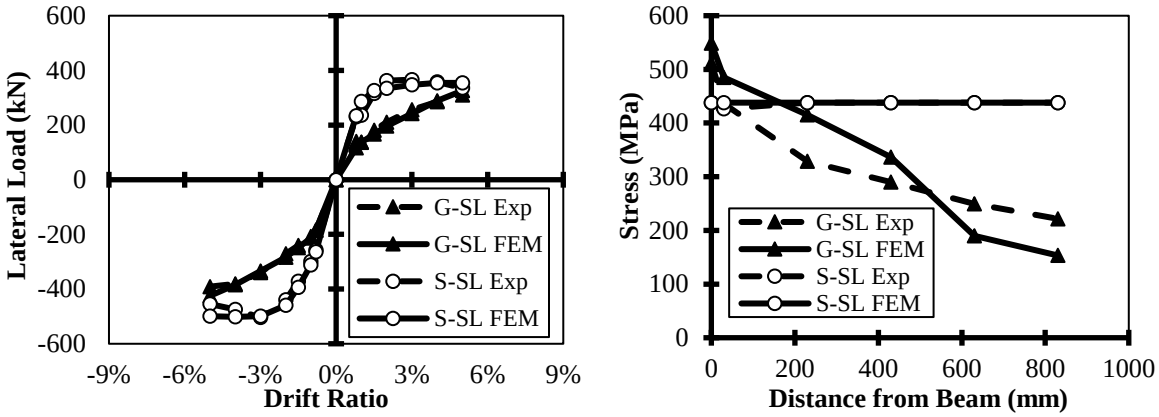

(a) Lateral load-drift (b) Stress distribution in slabs

Figure 6.15 - FEM validation

6.4.1 FEM model

The geometry of the constructed FEMs is shown in Figure 6.16-a. For time efficiency, in the analytical models the specimens were analyzed under one-directional pushover loadings only. It is believed that one directional pushover analysis can appropriately measure the effective slab

width in beam-column-slab assemblies through the stress distribution in the slab longitudinal bars. However, the pushover analysis may not be suitable to capture the energy dissipation characteristics and the level of residual damage in the test assemblies. For the purpose of comparison with the tested GFRP-RC specimens, the analytical models were loaded to the maximum of 5% drift ratio.

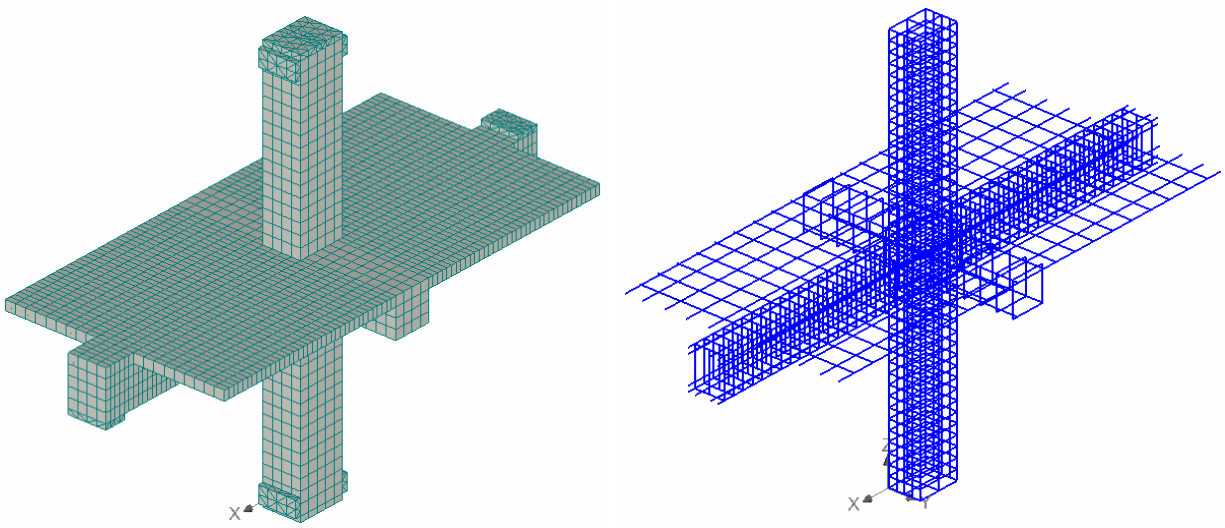

(a) FEM geometry (b) Discrete reinforcement

Figure 6.16 - Analytical model

6.4.2 Constitutive models

The built-in fracture-plastic constitutive model for cementitious materials in the software was used for concrete elements. This constitutive model combines a fracture model based on the Rankine failure criteria (for concrete in tension) with a hardening/softening plasticity model based on the Menetrey-Willam failure surface (for compression). The constitutive model is capable of accounting for the non-linear behaviour of concrete in compression, the effect of tension stiffening and the confinement provided by the internal reinforcement.

Longitudinal and transverse reinforcing bars were modeled as discrete reinforcement (Figure 6.16-b) with linear stress-strain relationship. The bond-slip model suggested by Tekle et al. (2016) for sand-coated GFRP bars was implemented in the analytical models.

More details regarding the constitutive models, implemented theories and FEMs of GFRP-RC elements under seismic loadings can be find in Cervenka et al. (2012) and Ghomi and El-Salakawy (2018-a).

6.4.3 Effect of slab width

As shown in Figure 6.1, width of the slab was identical for all test specimens (2090 mm). Observing the stress distribution among the longitudinal bars of Specimen G-SL (Figure 6.10) indicates that while the stress in the longitudinal bars decreases as the distance from the main beam increases, the tensile stress at the outermost bars remained significant. Moreover, all longitudinal bars in the slab of Specimen S-SL exhibited the yield stress at the maximum load carrying point, 3%. Therefore, the contribution of wider slab widths to the bending capacity of the main beams remains unassessed. To answer this question, the analytical models of Specimens G-SL and S-SL were re-generated with three additional slab widths, 2,890 mm, 3,290 mm and 4,090 mm.

Figure 6.17 compares the stress distribution among the longitudinal slab bars in the analytical models of Specimens G-SL and S-SL with various slab widths (at 3% in steel-RC specimens and at 5% in GFRP-RC specimens). In the graph legend, the numbers in brackets indicate the slab width. As expected, in the models with 4,090 mm slab width, as the slab width increases the stress in the outermost bar decreases to approximately zero.

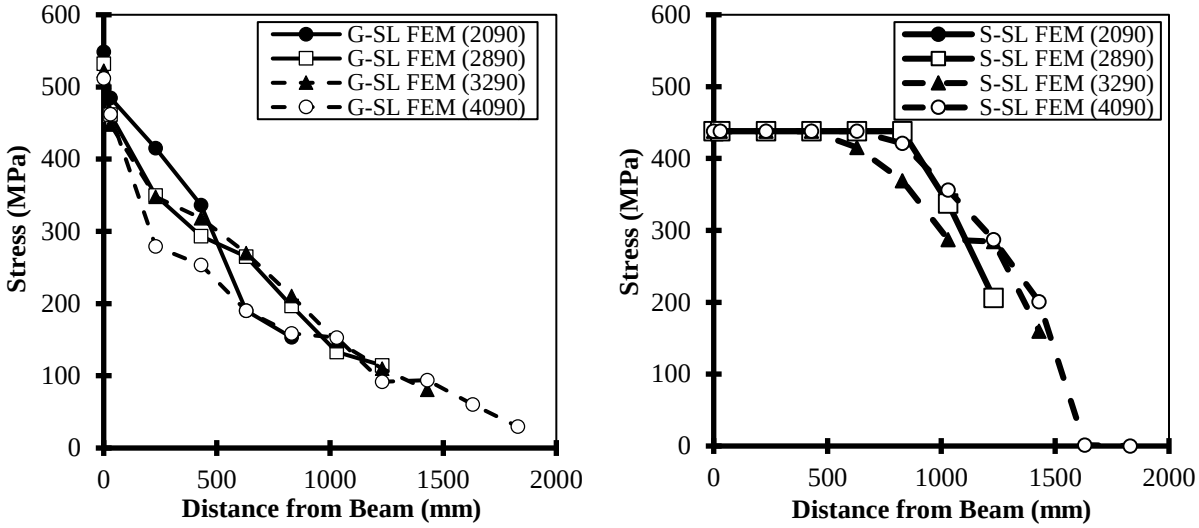

(a) Specimen G-SL (b) Specimen S-SL

Figure 6.17 - Effect of slab width on rebar stress distribution

The effective slab width corresponding to each analytical model is presented in Table 6.3. Widening the slabs resulted in 30% and 60% increase in the effective slab width in Specimen G-SL and S-SL, respectively. Moreover, the increase of slab width beyond 3,290 mm did not affect the effective slab width in Specimen G-SL, while the increase in the effective slab width continued with slab widening up to 4,090 mm in Specimen S-SL.

Table 6.3 - Effective slab width of FEMs with various width

Slab Width	Effective Slab Width /*d*	
	GFRP-RC	Steel-RC
2,090	1.2	2.0
2,890	1.5	2.8
3,290	1.7	2.9
4,090	1.7	3.2

6.4.4 Effect of lateral beam size

French and Boroojerdi (1989) studied the effect of lateral beam size on the performance of interior steel-RC beam-column-slabs and concluded that the effective slab width increases with the

increase in the torsional stiffness of lateral beams. Stiffer lateral beams improve the development of tensile stresses in the slab bars, which in turn increases the contribution of slabs.

To quantify the effect of lateral beam size on the performance of the test specimens, the FEMs of the beam-column-slabs with 4,090 mm slab width were re-generated with various lateral beam dimensions. In addition to the tested specimen, two sets of lateral beam dimensions were considered in the analytical study, one representing a beam-column-slab with no lateral beams and one representing an assembly with its lateral beams covering the entire joint area.

As shown in Figure 6.18, a similar trend was observed as the effective slab width increased with the increase in the lateral beams size for both GFRP-RC and steel-RC specimens. The effect of lateral beam size increase was more pronounced when the lateral beams cover smaller percentage of the joint area. Increasing the lateral beam cross-sectional area from 0% to 60% of the joint area resulted in 35% increase in the effective slab width in both G-SL and S-SL. However, only 13% increase in the effective slab width was observed when the lateral beams' area increased from 60% to 100% of the joint area.

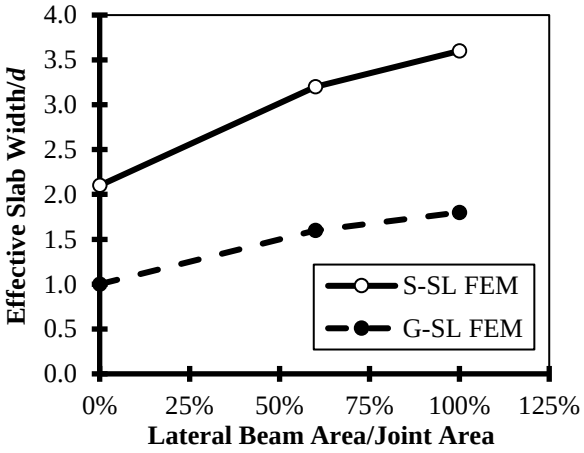

Figure 6.18 - Effect of lateral beam size on the effective slab width

6.5 Conclusions

Based on the test results and analysis, the following observations and conclusions were made:

- Both GFRP-RC specimens (beam-column and beam-column-slab connections) were able to reach their beam-only design capacity, with insignificant concrete loss. This indicates that GFRP-RC moment-resisting frames may survive a sever ground motion with minimum required repair.
- The GFRP-RC specimens were able to reach their beam-only design capacity for the second time during the second loading phase. This indicates that GFRP-RC moment-resisting frames may be capable of withstanding multiple severe ground motions. However, the reduction in lateral stiffness of these frames must be considered for the serviceability and ultimate state evaluation of the frames after surviving an earthquake.
- Based on the stress distribution among longitudinal bars in the slab of Specimen G-SL (GFRP-RC beam-column-slab), an effective overhang equal to 1.2 times the effective depth of the main beam on each side of the beam was obtained. The effective slab width in the GFRP-RC specimen was less than that of its counterpart steel-RC specimen with measured effective overhang of two times the effective beam depth. This was attributed to the lower stiffness of GFRP-RC slabs in the transverse direction compared to that of the steel-RC ones.
- Although the presence of floor slabs in the GFRP-RC interior beam-column connection (Specimen G-SL) increased the negative bending moment capacity of the main beams (slab-in-tension), it was observed that the contribution of the slab while in compression (positive moments) was insignificant. In contrary, significant contribution of the floor slab

to both positive and negative bending moment capacity of the main beams in the steel-RC beam-column connection was observed.

- The presence of slabs in GFR-RC specimens slightly increased the magnitude of energy dissipation. Specimen G-SL dissipated 15.5% and 8.7% more cumulative energy than Specimen G-XX (without slabs) at 3.0% and 5.0% lateral drift ratios, respectively. The steel-RC beam-column-slab connection (S-SL), however, exhibited significantly higher energy dissipation than the counterpart GFRP-RC beam-column-slab connection (G-SL) by 94% and 114.4% at 3.0% and 5.0% drift ratio, respectively.
- Specimen G-SL showed 47% higher lateral stiffness compared to Specimen G-XX during the first lateral drift ratio loading (0.8%). This indicates that integral behaviour of slabs and beams in a GFRP-RC MRF can reduce its lateral deformation during earthquakes. The increase in the lateral stiffness due to presence of slabs, however, becomes less significant as the frame undergoes larger deformations. Similar behaviour for the steel-RC Specimens S-SL was observed. Specimen S-SL showed 45% higher lateral stiffness during the first loading step (0.8%) compared to that of G-SL. However, this percentage decreased to only 10% at 5.0% drift ratio.
- Analytical modeling of the test specimens with various slab widths indicated that widening the slab to 3,290 mm (slab width-to-beam depth ratio of 7.3) and 4,090 mm (slab width-to-beam depth ratio of 9.1) in Specimens G-SL and S-SL, respectively, resulted in 30% and 60% increase in the effective slab width. Further widening of the slabs beyond these points; however, did not provide significant increase in the contribution of slabs.
- Increasing the cross-sectional area of the lateral beams resulted in improving the slab contribution to the negative bending moment capacity of the main beams due to the

improvement of the slab bars contribution. A beam-column-slab connection with lateral beams covering 100% of the joint area showed up to 80% wider effective slab width compared to a beam-column-slab connection with no lateral beams.

7 SEISMIC BEHAVIOUR OF GFRP-REINFORCED CONCRETE EXTERIOR BEAM-COLUMN-SLAB CONNECTIONS

Shervin K. Ghomi and Ehab El-Salakawy

Submitted to American Concrete Institute (ACI) Structural Journal, March 2019.

Abstract: The effect of various factors on the contribution of slabs to the seismic performance of beam-column joints in steel-reinforced concrete (RC) frames has been extensively investigated. However, no research data is available on the behaviour of beam-column-slabs reinforced with alternative materials such as glass fiber reinforced polymers (GFRP). To fill this gap, two full-scale GFRP-RC exterior beam-column-slabs were tested under reversal loading to investigate their seismic performance with a focus on the effect of lateral beams on the effective slab width. The results were compared with two previously tested beam-column specimens. Moreover, a series of finite element models were generated to determine the influence of lateral beams' size and slab thickness on the contribution of slabs. The results indicated that the contribution of cast-in situ slabs in the bending moment capacity of the main beams when the top fiber of the slab is in compression is insignificant.

Keywords: GFRP-RC, Moment-resisting frames, Seismic performance, Cyclic loading, Beam-column connections, Beam-column-slab subassemblies, Lateral load-drift response, Lateral beams, Exterior connections.

7.1 Introduction

Recently, fiber reinforced polymers (FRPs) have been introduced as an alternative for conventional steel reinforcement in concrete structures. Although the initial motive to replace steel reinforcement with FRPs has been the non-corrosive nature of these composites, recent studies aimed at expanding the implementation of these materials in the construction industry. One of the areas that implementation of FRP reinforcement in concrete structures has been sought recently is the seismic design. Pioneer investigations on the feasibility of using FRP reinforcement in seismic regions (Fukuyama et al. 1995; Said and Nehdi 2004; Mady et al. 2011) indicated that FRP-reinforced concrete (RC) structures can be designed to withstand the significant lateral deformations that are expected during a seismic event. However, to achieve a satisfactory deformability in FRP-RC structures, the lack of ductility of these composite materials due to their linear elastic nature must be addressed.

To achieve the desired deformability, the choice of FRP materials must have relatively large ultimate strain capacity, high tensile strength and low modulus of elasticity. Among various FRP materials commonly available to the construction industry, glass FRP (GFRP) has shown satisfactory performance (Ghomi and El-Salakawy 2016; Hasaballa and El-Salakawy 2016; Ghomi and El-Salakawy 2018-b) in terms of deformability. Previous experiments on GFRP-RC beam-column joints indicated that such elements can withstand lateral drift ratios as high as 9% without exhibiting brittle failure (Ghomi and El-Salakawy 2016). However, the linear nature and relatively low modulus of elasticity of GFRP compared to steel, typically 60 GPa vs. 200 GPa (8,700 ksi vs. 29,000 ksi), results in lack of energy dissipation and low lateral stiffness of GFRP-RC structures. These, in turn, could result in excessive deformation of relatively flexible lateral load resisting systems (LLRS), such as moment-resisting frames (MRFs), during an earthquake.

To compensate for this issue, researchers (Said and Nehdi 2004; Hasaballa and El-Salakawy 2016) suggest conjugating GFRP-RC MRFs with a more rigid LLRS, such as shear walls to control the lateral deformation of GFRP-RC structures during an earthquake. In addition, hybrid MRFs (replacing steel reinforcement only at exterior elements of an MRF to provide corrosion-resistance to the structure from harsh environmental condition) also has been introduced as a possible solution (Hasaballa and El-Salakawy 2016).

However, in both approaches, there is still a need to fully understand the behaviour of GFRP-RC MRFs. To achieve this goal, a solid understanding of the seismic behaviour of beam-column connections, as the key elements in the seismic performance of MRFs, is essential. Although some aspects of the seismic behaviour of GFRP-RC beam-column connections have been recently investigated (Mady et al. 2011; Ghomi and El-Salakawy 2016; Hasaballa and El-Salakawy 2016; Ghomi and El-Salakawy 2018-b), the studies in this area are still in early stages and the effect of many parameters on the seismic behaviour of GFRP-RC beam-columns are still unrevealed.

One of the main affecting parameters, that has not been investigated yet, is the presence of cast-in situ slabs. The significance of cast-in situ slabs in steel-RC MRFs has been fully stablished (Ehsani and Wight 1985-b; Durrani and Zerbe 1987; Pantazopoulou et al. 1988; French and Boroojerdi 1989; Ammerman and French 1989; Zerbe and Durrani 1990; Qi and Pantazopoulou 1991; Shahrooz and Pantazopoulou 1992; Pantazopoulou and French 2001; Ning et al. 2014). By an analogy, the composite behaviour of slabs and beam-column assemblies is also expected to significantly affect energy dissipation, lateral stiffness, beam-to-column flexural strength ratio and mode of failure of GFRP-RC MRFs. This program aims at investigating the effect of cast-in situ slabs on the seismic behaviour of GFRP-RC exterior beam-column connections.

7.2 Research Significance

The current program addresses the lack of research data in the area of seismic performance of FRP-RC beam-column-slab assemblies. The contribution of cast-in situ slabs to the positive and negative bending moment capacity of beams in exterior GFRP-RC beam-column connections was determined. A two-phase loading approach was implemented to investigate the effect of initial damage due to a severe seismic event on the performance of GFRP-RC moment frames. Moreover, the effect of size of lateral beams and thickness of slabs on the effective slab width was studied through analytical modeling.

7.3 Description of Specimens and Test Program

Two full-scale beam-column-slab subassemblies were constructed and tested in this program. The results obtained from testing the specimens were compared with two corresponding beam-column specimens available in the literature (Ghomi and El-Salakawy 2016; Hasaballa and El-Salakawy 2016). The corresponding beam-column specimens were identical to the test specimens except for presence of slabs. The main parameters under investigation were presence of cast-in situ slab and lateral beams.

7.3.1 Test specimens

The test specimens represented two beam-column-slab connections, one with and one without lateral beams, designated as BCS-L and BCS-X, respectively. A beam-column specimen with lateral beams (designated as BCS-L), previously tested by Ghomi and El-Salakawy (2016), was used as the base for Specimen BCS-L. Specimen BCS-L was constructed identical to Specimen BCX-L with the addition of cast-in situ slab. Similarly, a beam-column specimen without lateral beams (designated as BCX-X), previously studies by Hasaballa and El-Salakawy (2016), was used

as the base for constructing Specimen BCS-X. Figure 7.1 shows the dimensions and reinforcement detailing of the test specimens. The specimens were isolated from assumed points of contra-flexure in an MRF at mid-height of the columns and mid-span of the beams. Properties of the specimens are summarized in Table 7.1.

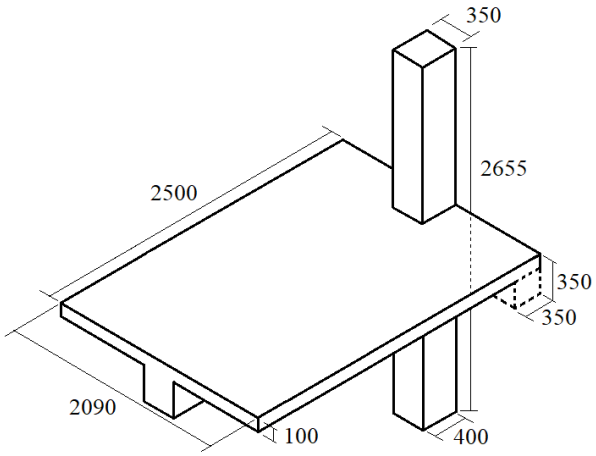

(a) dimensions of test specimens

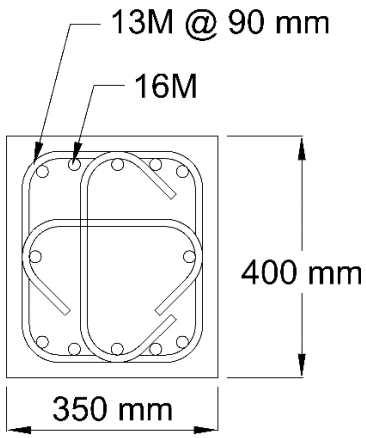

(b) column of test specimens

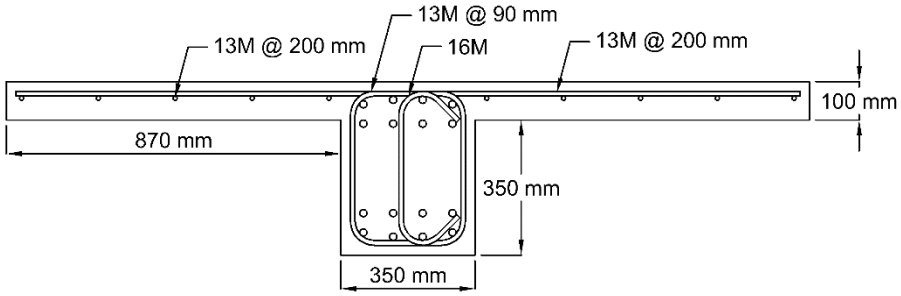

(c) beam of Specimen BCS-L

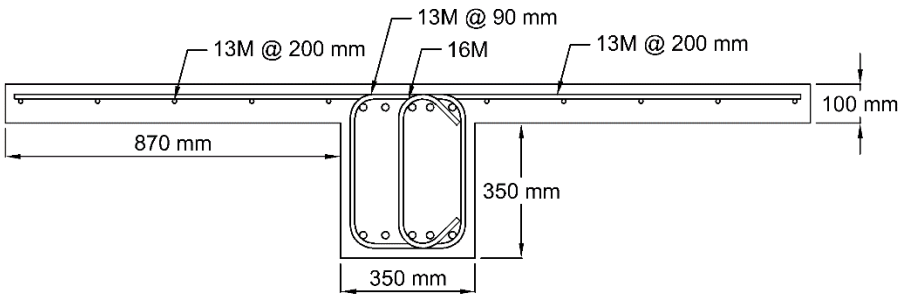

(d) beam of Specimen BCS-X

Figure 7.1 - Dimensions and reinforcement detailing of test specimens.

Table 7.1 - Properties of test specimens

Specimen	Beam Flexural Capacity* kN.m (kip.ft)	Column-to-Beam Flexural Ratio**	Concrete Strength MPa (psi)
BCS-L	363 (267.7)	1.47	51 (7,397)
BCS-X	327 (241.2)	1.60	49 (7,107)
BCX-L	350 (258.1)	1.47	48 (6,962)
BCX-X	332 (244.9)	1.64	53 (7,687)

*Capacity without slab contribution
**Effect of column axial load is included in the flexural capacity of columns

7.3.2 Test set-up and load history

Test specimens in the current program (BCS-L and BCS-X) were tested under reversal cyclic loading to simulate the effect of a seismic event. Figure 7.2 shows the test set-up with Specimen BCS-L, ready for testing.

Figure 7.2 - Test set-up.

The reversal cyclic loading was applied to the upper tip of the columns by means of a hydraulic actuator mounted on a strong wall. The columns were sitting on a hinge to simulate a pin connection. Tip of the main beams were attached to the strong floor by means of a double hinged hollow structural section (HSS), to simulate a roller boundary condition. The columns were under constant axial load during testing, applied by a hydraulic jack attached to a stiff reaction beam on

top of the specimens. The reaction beam was also attached to the strong floor by two double-hinged HSSs. This configuration allowed free rotation of the reaction beam during the reversal loading of the columns. Free rotation of the reaction beam maintained the axes of column load and the column centerline to eliminate formation of secondary moments during loading.

The cyclic loading procedure was in displacement-controlled mode, including several loading steps gradually increasing in the magnitude of displacement applied to the column. The magnitude of displacement was measured in terms of lateral drift ratio, defined as the ratio of column tip displacement (actuator stroke) to the column length. During each loading step, three identical cycles were applied to ensure stable crack propagation in the specimen.

Ghomi and El-Salakawy (2018-b) proposed a two-phase loading method for testing GFRP-RC beam-column joints under reversal cyclic loading to investigate the performance of GFRP-RC MRFs under simulated seismic loading. The same approach was adopted in the current study. Therefore, Specimens BCS-L and BCS-X were tested under two back-to-back loading phases. During the first phase, the specimens were loaded from 0% to 5% lateral drift ratio. Immediately after completion of the first loading phase, the specimens were loaded from 0% drift ratio to failure. The reason for the second loading phase was to evaluate the performance of GFRP-RC frames after surviving a strong earthquake. Details of the loading procedure is explained in Ghomi and El-Salakawy (2018-b). The loading scheme is shown in Figure 7.3.

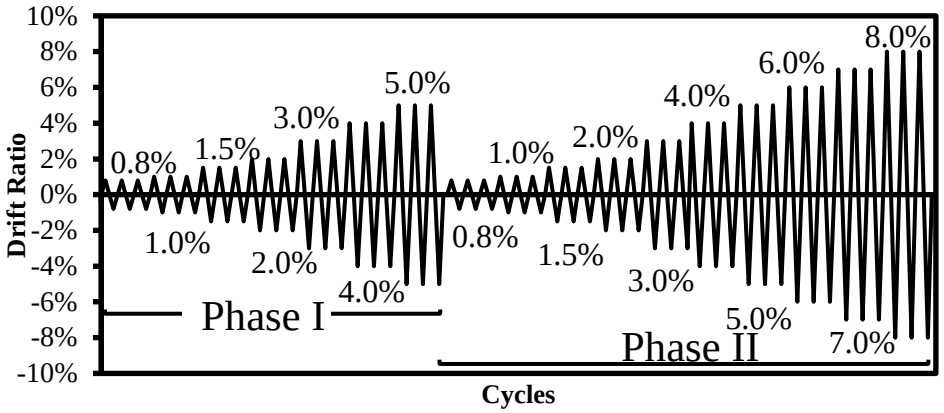

Figure 7.3 - Loading schedule

7.3.3 Materials

Ready mix concrete with a target 28-day strength of 40 MPa was used to cast the specimens. The actual compressive strength of concrete on the day of testing was obtained by standard concrete cylinder testing as reported in Table 7.1.

Sand-coated GFRP bars and stirrups were used to construct the reinforcement cage of the specimens. Headed-end bars were used to anchor the longitudinal bars of the main beams in the joint area and the longitudinal bars of the slab at the column-side of the slab. Mechanical properties of the reinforcement, as provided by the manufacturer (Pultrall Inc. 2019), are reported in Table 7.2. Moreover, the mechanical properties of the reinforcement of Specimens BCX-L and BCX-X are also included in Table 7.2 for comparison purposes.

Table 7.2 - Properties of GFRP reinforcement

Specimen	Reinforcement	Cross-Sectional Area mm^2 (in^2)	Modulus of Elasticity GPa (ksi)	Tensile Strength MPa (ksi)
BCS-L BCS-X	Beam and Column Longitudinal	198 (0.31)	62 (9,079)	1184 (172)
	Slab Longitudinal	127 (0.20)	65 (9,514)	1312 (190)
	Stirrups and Ties*	127 (0.20)	50 (7,251)	1019 (148)
BCX-L BCX-X	Beam and Column Longitudinal	201 (0.31)	60 (8,702)	1100 (160)
	Stirrups and Ties*	113 (0.18)	50 (7,251)	1000 (145)

*Properties of straight portion

7.4 Analysis of Test Specimens

In the specimens with slabs, the bending moment capacity of the main beams depends on the effective width of the slab acting as a flange for the beams. The extent of this contribution; however, is expected to vary between the negative and positive bending moment capacity, where the slab is in tension or compression, respectively. The lower bound of the flexural capacity of the main beams (positive and negative) is when the beam is assumed to act independent of the slab (zero effective slab width), named as "beam-only" condition in the current study. On the other hand, the upper bound of the bending moment capacity is when the full width of the slab is assumed to effectively interact with the main beam as a flange, named as "full-width" condition in the present study.

The positive and negative bending moment capacity of the main beam in Specimens BCS-L and BCS-X with respect to the effective slab width, up to full width of the slab, is shown in Figure 7.4. However, there is a certain effective width of the slab that contributes to the bending moment capacity of the main beam. Previous studies on the behaviour of steel-RC beam-column-slab connections reported various factors influencing the effective width of slabs, including geometrical

configurations (Ammerman and French 1989), size (torsional stiffness) of lateral beams (French and Boroojerdi 1989), load history (French and Boroojerdi 1989), and story drift (Ning et al. 2014).

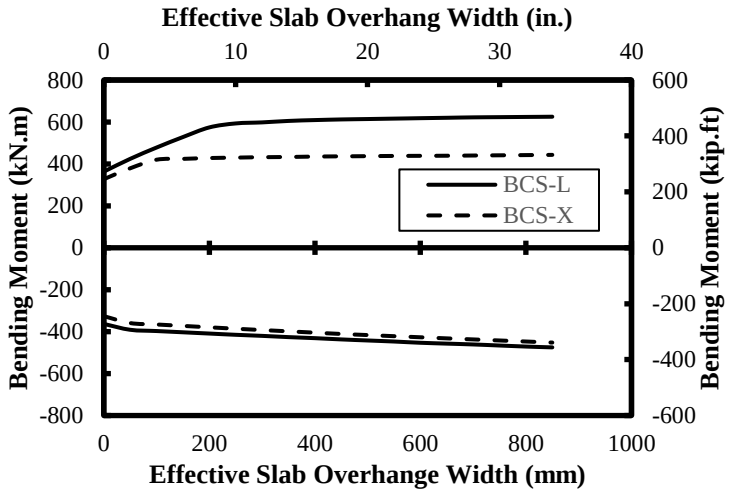

Figure 7.4 - Bending moment-effective slab width relationship

Previous studies on steel-RC structures (French and Boroojerdi 1989) indicated that presence of lateral beams results in an increase in the effective width of slabs. However, due to lack of research data, the extent of this increase in the effective slab width due to lateral beams in GFRP-RC structures is still uncovered.

Therefore, current codes and design guidelines for FRP-RC structures, such as CSA-S806 (CSA 2012) and ACI 440.1R-15 (ACI Committee 440 2015), do not include any information on the effective width of cast-in situ slabs on the bending capacity of beams. Ignoring the contribution of slabs could adversely affect FRP-RC structures in seismic regions. For example, ignoring the slab contribution could result in an unrealistic low estimation of initial lateral stiffness of LLRS, which results in underestimating the performance of such structure. Moreover, the increase in bending moment capacity of beams due to contribution of slabs could reduce the column-to-beam flexural

strength ratio, creating weak-column-strong-beam connections with plastic hinges in the columns, which in turn could threaten the stability of structures during seismic events.

FRP-RC structures, in particular, are prone to the change of mode of failure due to composite behaviour of monolithically cast beams and slabs. Unlike steel-RC elements that are generally designed as tension-controlled sections (CSA 2014-a), FRP-RC structures are designed as compression-controlled sections (CSA 2012), where failure of flexural elements are initiated by concrete crushing in compression zones. However, contribution of slabs as compression flanges for beams could significantly reduce the reinforcement ratio of FRP-RC sections and result in the change of mode of failure from desirable compression-controlled to the undesirable tension-controlled failure. This change in mode of failure is evident in Figure 7.4 by the sudden change of slope in the lines corresponding to positive bending moments at 200 mm (7.87 in.) and 100 mm (3.93 in.) effective width in Specimen BCS-L and BCS-X, respectively.

7.5 Test Results and Discussions

7.5.1 Flexural strength and effective slab width

The beam bending moment envelope, calculated as the product of the maximum beam tip load and the beam length, during the first loading phase is shown in Figure 7.5. The response obtained from testing of Specimens BCX-L (Ghomi and El-Salakawy 2016) and BCX-X (Hasaballa and El-Salakawy 2016), up to 5% drift ratio, is also included in the graphs of Figure 7.5 for comparison. Moreover, the upper and lower bounds of the bending moment capacity ("full-slab" and "beam-only", respectively) are also indicated in the graphs.

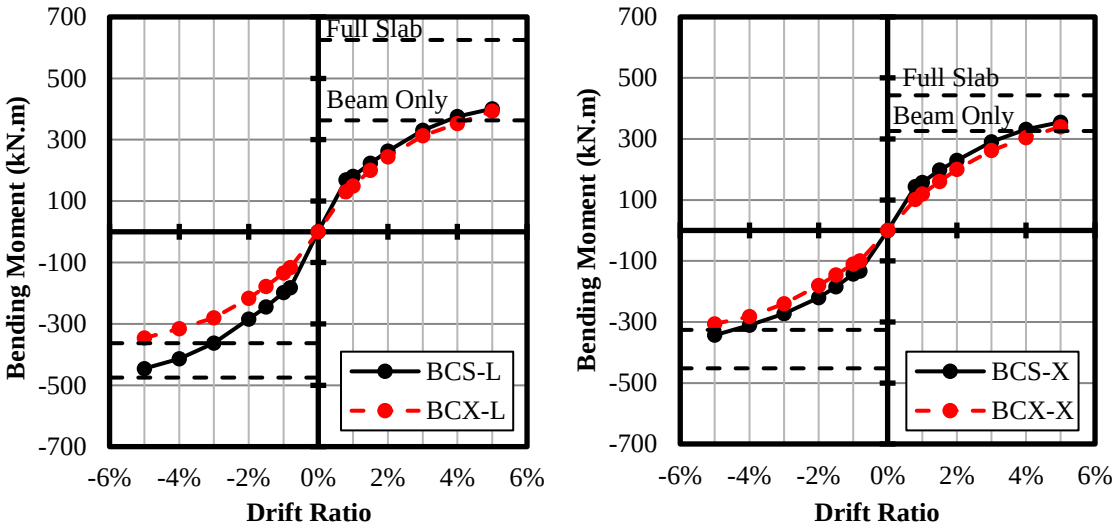

(a) Specimens with lateral beams (b) Specimens without lateral beams

Figure 7.5 - Maximum beam bending moment-drift ratio.

Comparing the performance of Specimens BCS-L and BCX-L indicates that the contribution of slab, when in compression (positive moments), is insignificant. This observation contradicts the main concerns regarding the change of mode of failure due to contribution of cast-in situ slabs in FRP-RC structures. However, the contribution of slab to the negative moment (slab in tension) capacity of Specimen BCS-L is noticeable. The maximum negative bending moment calculated at 5% drift ratio was 346 kN.m (255.3 kip.ft) and 446 kN.m (329.1 kip.ft) in Specimen BCX-L and BCS-L, respectively, indicating 30%. It should be mentioned that the effect of the slight difference in concrete compressive strength of BCS-L and BCX-L (Table 7.1) is ignored in the analysis.

Figure 7.6 shows the maximum strain measured in the longitudinal bars of slabs at the face of the column. To calculate the effective slab width, the procedure suggested by Pantazopoulou et al. (1988), as shown in Equation 7.1, is adopted.

$$b_e = \frac{\sum_{i=1}^{n} \frac{1}{2}\left(\varepsilon_{s(i)} + \varepsilon_{s(i+1)}\right)s}{\varepsilon_{b,max}} \qquad (7.1)$$

where $\varepsilon_{s(i)}$ is the strain at the i^{th} longitudinal bar of the slab (counted from the beam), s is the slab longitudinal bars spacing, n is the number of longitudinal bars in the slab on each side of the main beam, and $\varepsilon_{b,max}$ is the maximum strain measured in the beam longitudinal bars at face of the column.

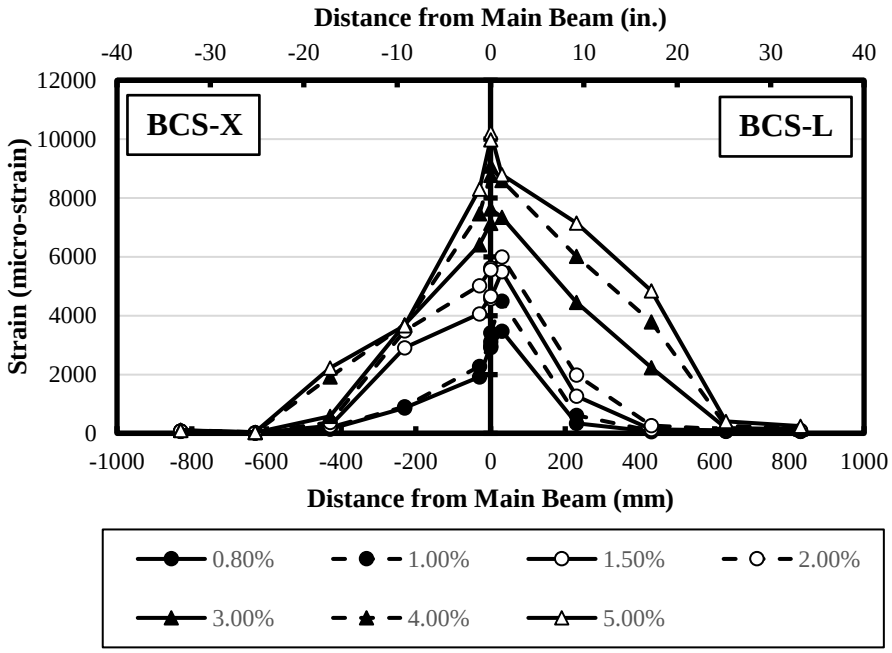

Figure 7.6 - Maximum strain in slabs longitudinal bars.

It should be mentioned that the first sign of concrete crushing in the beams cover of Specimen BCS-L (indicating the onset of theoretical bending capacity as calculated in Figure 7.4) was observed at 4% drift ratio. Therefore, by implementing Equation 7.1, the effective slab width, on each side of the beam (overhang), in Specimen BCS-L at 4% drift ratio is calculated as 318 mm (12.52 in.). It is common to measure the effective width of slabs as a ratio of the effective depth of beams, *d*. Thus, the effective overhang width of Specimen BCS-L is equal to 0.85*d*.

The contribution of slab in Specimen BCS-X was significantly less pronounced compared to Specimen BCS-L. Comparing the behaviour of Specimens BCX-X and BCS-X in Figure 7.5

indicates 4% and 12% increase in the positive and negative bending moment capacity, respectively, due to the contribution of slab. The first sign of concrete crushing in the main beam cover was observed at 5% drift ratio in Specimen BCS-X. Therefore, by applying Equation 7.1 to the strains measured at 5% drift ratio, 203 mm (7.99 in.) of effective slab width was calculated for Specimen BCS-X on each side of the main beam. This value is equivalent to 0.5*d*.

7.5.2 General behaviour and mode of failure

Figure 7.7 shows hysteresis diagrams (beam tip load vs. lateral drift ratio) of the specimens up to 5% drift ratio (end of the first loading phase for Specimens BCS-L and BCS-X). Both specimens without slabs (BCX-L and BCX-X) showed very similar behaviour, exhibiting narrow hysteresis loops with approximately linear behaviour up to 5% drift ratio with insignificant residual damage at zero load condition (pinching effect). Presence of slabs in Specimens BCS-L and BCS-X; however, resulted in slightly wider hysteresis loops compared to the specimens without slabs. This can be attributed to propagation of cracks and concrete damage in the slabs, which resulted in additional energy dissipation and residual damage in the specimens. This effect is also evident as wider pinching occurred in the specimens with slabs.

Comparing the behaviour of the specimens with slabs, indicates more residual displacements at zero load condition in the negative drift ratios (slab in tension) than those on the positive side (slab in compression). Considering the residual displacement as an indicator of the magnitude of damage, this observation concludes higher magnitude of damage induced to the specimens when the slabs are in tension compared to the slab-in-compression case.

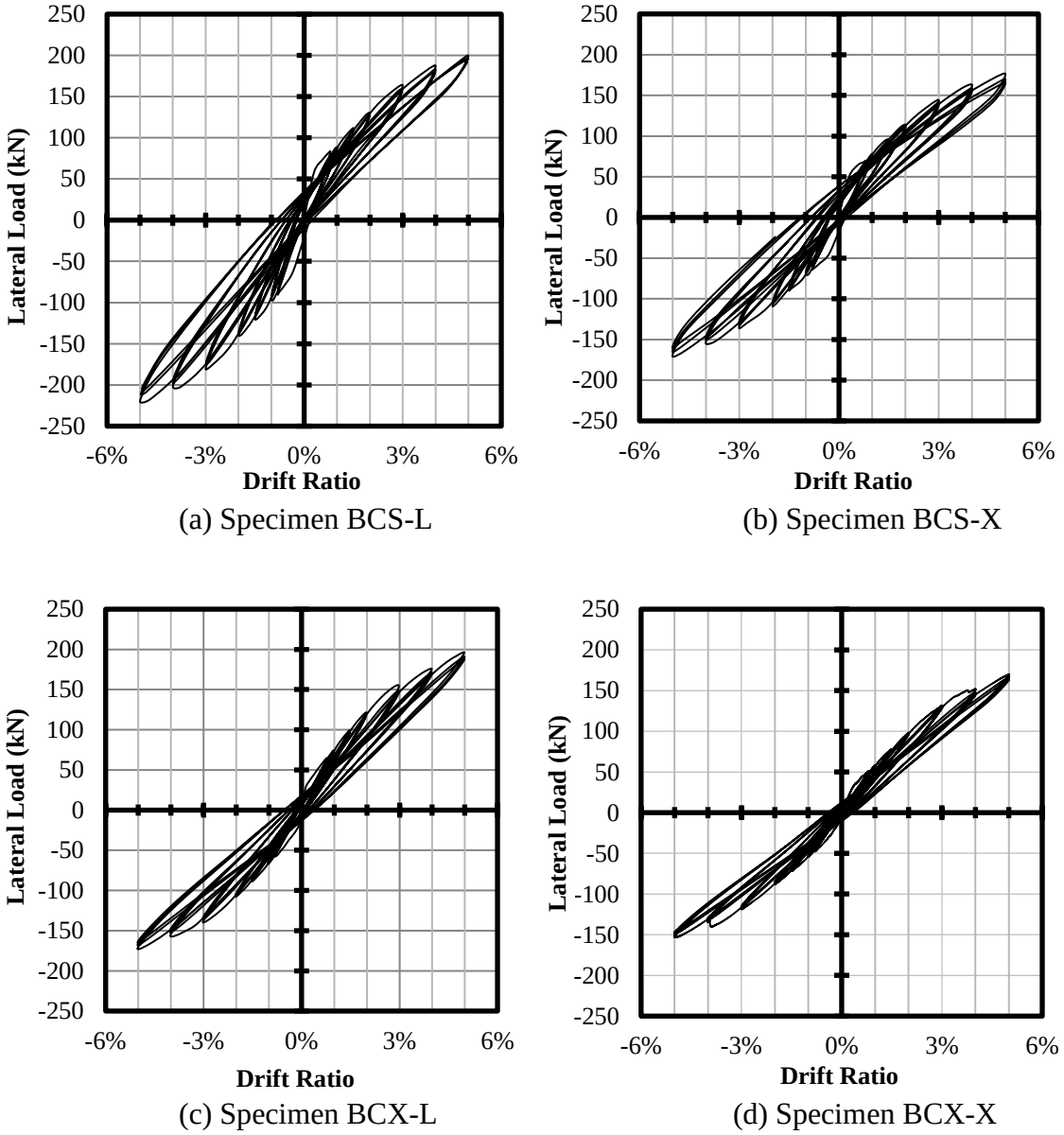

(a) Specimen BCS-L (b) Specimen BCS-X

(c) Specimen BCX-L (d) Specimen BCX-X

Figure 7.7 - Lateral load-drift ratio response of test specimens.

Figure 7.8 shows the condition of the beam-column-slab specimens at the end of the first loading phase (5%). In Specimen BCS-L, concrete crushing was observed at the bottom face of the main beam at the beam-column intersection, while no significant damage was found at the top face of the beam (intersection with bottom side of the slab). This could be attributed to the contribution of the longitudinal bars in the slab to the negative flexural capacity, which resulted in increase in the

compressive stress in the concrete at the bottom of the main beam. Hence, the earlier concrete crushing at the bottom of the beam compared to the top face. Figure 7.8-a shows the back view of Specimen BCS-L, indicating clear torsional cracks in the lateral beams due to tension forces from the longitudinal bars of the slab. Moreover, a concrete loss on the backside of the slab at the location of reinforcement head was observed. This resulted in partial exposure of the headed-end in one of the main reinforcements in the slab and minor damage to the head.

In contrary to BCS-L, damage concentration in BCS-X was not at the bottom face of the main beam, but mainly at the intersection of the slab and column at the top and backside of the specimens. Due to the absence of lateral beams, the tension forces in the slab bars transferred to the column, which caused a significant concrete damage in the column and top of the slab.

Figure 7.9 compares the lateral load envelope (actuator's load) of BCS-L and BCS-X during the first and the second loading phases. As expected, both specimens showed lower lateral stiffness during the second loading phase, due to the damage induced during the first loading phase. The behaviour of the specimens during the second loading phase up to 5% drift ratio can be approximated by a straight line connecting the origin (zero load and zero displacement) to the point corresponding to the peak load during the third cycle of 5% drift ratio step in the first loading phase.

(a) Specimen BCS-L

(b) Specimen BCS-X

Figure 7.8 - Condition of specimens at the end of the first loading phase.

Following the loading procedure beyond 5% drift ratio, both specimens exhibited slight increase in the lateral load until the failure occurred at 6% and 7% drift ration in Specimen BCS-X and BCS-L, respectively. Both specimens exhibited brittle failure due to rupture of the longitudinal bars in the main beams. In Specimen BCS-L the rupture occurred in the bottom reinforcement (corresponding to slab-in-compression), while in Specimen BCS-X the rupture occurred in the top reinforcement (corresponding to slab-in-tension).

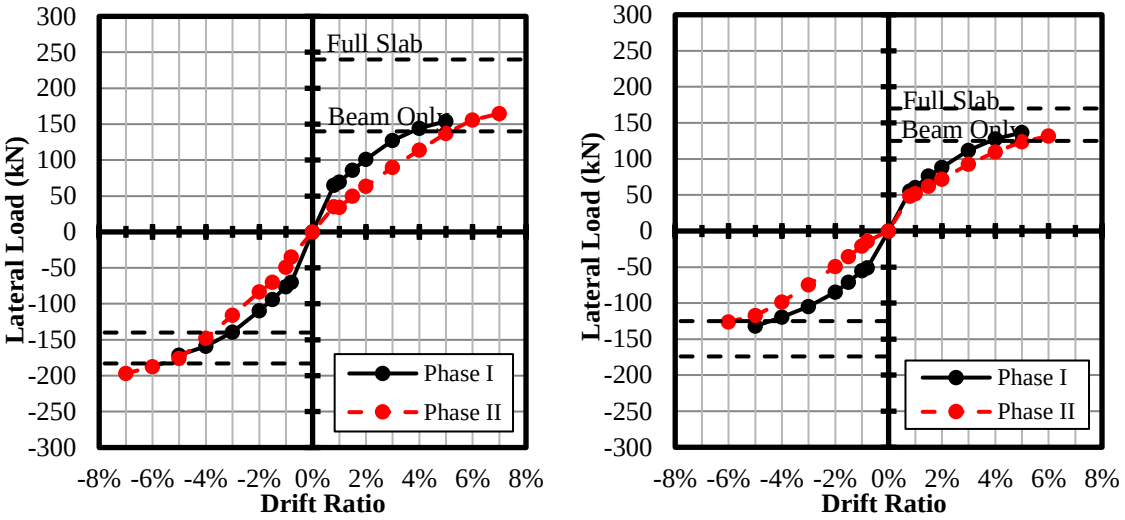

(a) Specimen BCS-L (b) Specimen BCS-X

Figure 7.9 - Maximum lateral load envelope.

Figure 7.10 shows condition of the specimens after failure. In both specimens, significant dislocation of some of the reinforcement heads was observed, indicating slippage of the longitudinal bars in the main beams and slabs. Slippage of the bars could result in increase in the tensile stress of the bars that did not slip (redistribution of stresses), which could, in turn, result in rupture of the bars.

Significant damage penetration in to the joint area was observed in Specimen BCS-X, compared to Specimen BCS-L, due to the lack of confinement provided by lateral beams. Clear tension cracks were observed in the joint area of BCS-X, joining wide splitting cracks along the outer longitudinal bars of the column, below the main beam. This type of crack was also observed in beam-column joints without lateral beams tested by Ghomi and El-Salakawy (2016) and Hakuto et al. (2000) which could be attributed to the insufficient support provided to the concrete compression strut in the joint area, which resulted in concrete push-off on the backside of the column.

(a) Specimen BCS-L

(b) Specimen BCS-X

Figure 7.10 - Condition of specimens at failure.

7.5.3 Energy dissipation

Energy dissipation is one of the key characteristics of LLRSs in seismic regions. Due to linear elastic properties of FRP materials (no yielding), FRP-RC elements are expected to exhibit low ductility and energy dissipation. In this case, the main source of energy dissipation would be crack propagation, bar slippage and concrete damage. Thus, the increase in the concrete volume could potentially increase the energy dissipation of FRP-RC elements. Therefore, presence of slabs is expected to result in increase in the energy dissipation of beam-column connections.

The magnitude of energy dissipation in each loading step is calculated as the area enclosed by the corresponding hysteresis loops in the lateral load-displacement graphs of the specimens. The cumulative energy dissipation of the specimens up to 5% drift ratio (end of the first loading phase for Specimens BCS-L and BCS-X) is shown in Figure 7.11.

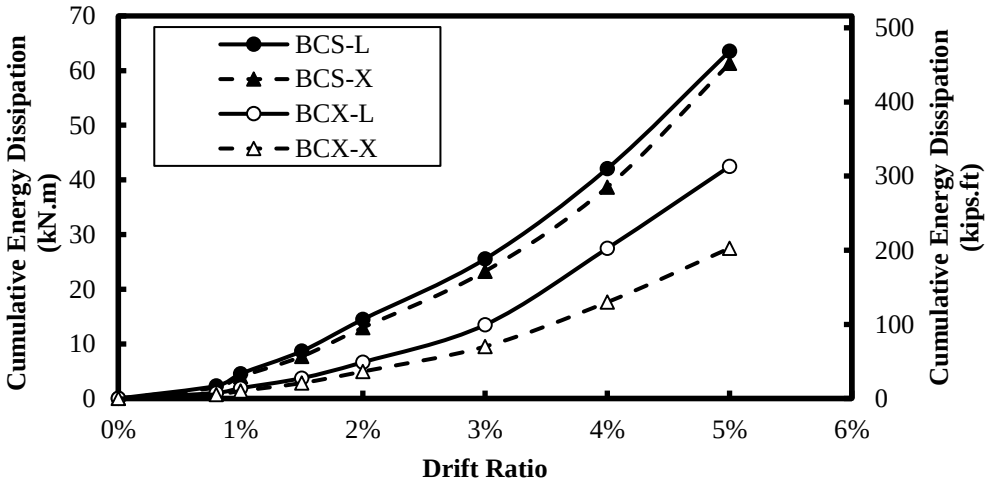

Figure 7.11 - Cumulative energy dissipation.

For both BCS-L and BCS-X, the amount of energy dissipation with respect to BCX-L and BCX-X, increased with increase in the lateral drift ratio. At 5% drift ratio, Specimens BCS-L and BCS-X exhibited 49% and 122% more energy dissipation compared to Specimens BCX-L and BCX-X, respectively. However, 5% drift ratio might be beyond the maximum drift ratio expected from a typical MRF during an earthquake. For instance, the maximum allowable lateral drift ratio set by National Building Code of Canada (NRCC 2015) is 2.5%. Therefore, to obtain a more realistic comparison, the cumulative energy dissipation of the specimens was also compared at 3% drift ratio as well (closest to the 2.5% limit). At 3% drift ratio, BCS-L and BCS-X showed 89% and 145% more energy dissipation compared to BCX-L and BCX-X, respectively. Therefore, the effect of slabs on energy dissipation is more pronounced at lower drift ratios.

7.5.4 Lateral stiffness

Although linear elastic feature of GFRP rebars could result in lack of energy dissipation and ductility, it can significantly reduce the level of residual damage in LLRSs. This could lower the cost and time required to repair structures after a strong lateral loading event (earthquake). However, to benefit from this feature, the performance of the structure after surviving such strong lateral loading must be investigated. One of the key properties of beam-columns that could be significantly influenced by the damage induced to the structure is the lateral stiffness. The lateral stiffness of BCS-L and BCS-X during both loading phases are shown in Figure 7.12. The lateral stiffness is calculated as the slop of the straight line connecting the origin to the maximum positive or negative lateral loads at each drift ratio in Figure 7.9.

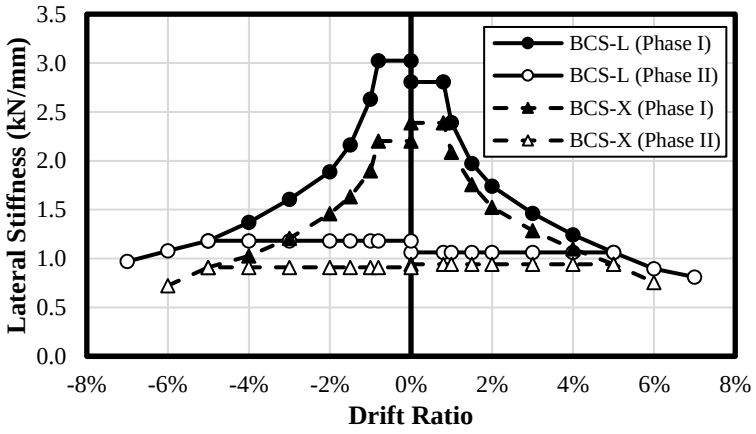

Figure 7.12 - Lateral stiffness.

The higher lateral stiffness of BCS-L compared to BCS-X was expected due to higher number of longitudinal bars in the main beams. However, the difference between the stiffness of BCS-L and BCS-X is more pronounced in the negative direction (slab-in-tension) due to significantly higher contribution of the slab in BCS-L.

Comparing the initial lateral stiffness (up to 0.8%) of BCS-L and BCS-X with their lateral stiffness at 5% drift ratio (end of the first loading phase) indicates approximately 60% reduction in both

negative and positive directions, in both specimens. This significant reduction in the lateral stiffness could result in unsatisfactory performance of GFRP-RC MRFs after surviving an earthquake. Therefore, to prevent significant reductions in the lateral stiffness of structures, the maximum lateral displacement of the frames during a seismic event should be limited to a lower drift ratio. As mentioned earlier, 3% lateral drift limit, based on the requirements of National Building Code of Canada (NRCC 2015), seems to be a reasonable estimation. Comparing the lateral stiffness of the specimens at 3% drift ratio with their initial stiffness indicates approximately 47% reduction.

7.6 Analytical Program

To further investigate the effect of lateral beam size and slab thickness on the effective slab width, several 3D finite element models (FEMs) were constructed to simulate the performance of test specimens, using a commercial program, ATENA 3D, version 5.3.5g (Cervenka et al. 2012). ATENA 3D is a specialized program in modeling reinforced concrete structures with the ability to include the nonlinear behaviour of concrete, effect of cracks and bond-slip model between reinforcement and concrete.

7.6.1 FEM model

Figure 7.13 shows geometry of the analytical model for Specimen BCS-L. For simplicity and reducing the processing time, the beam-column-slabs connections in the FEMs were loaded in one direction only (pushover).

Since the main objective of the analytical program is to investigate the effective slab width, the one-direction loading can be considered sufficient as the relative strain distribution in the

longitudinal reinforcement of the beams and slabs can be captured within an acceptable degree of error without considering the effect of reversal loadings. However, it is understood that the one-direction loading approach is not capable of capturing the effect of reversal loadings on the lateral load-carrying capacity, residual displacements and energy dissipations as the unloading behaviour of the specimens is not considered (Mander et al. 1988). For comparison purposes, the analytical models were loaded up to 5% drift ratio, the threshold at the first loading phase.

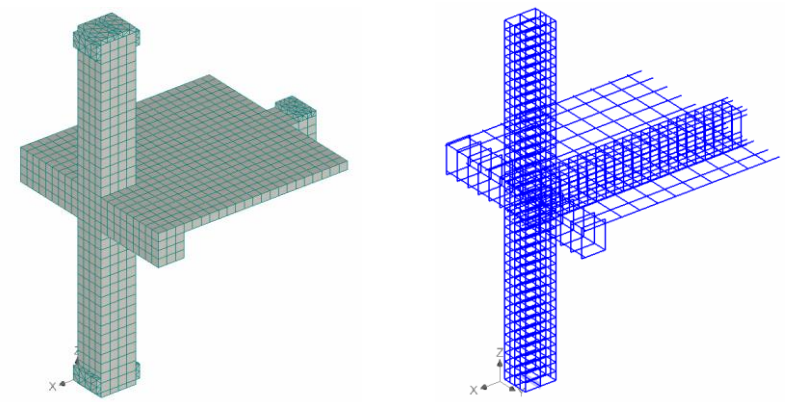

(a) Concrete meshing (b) Discrete reinforcement

Figure 7.13 - Geometry of finite element model for Specimen BCS-L.

7.6.2 Constitutive models

The 8-node brick elements were used to model concrete material using the built-in 3D nonlinear constitutive model in the software. This constitutive model is capable of including the effect of nonlinear stress-strain relationship of concrete, confinement provided by internal reinforcement and tension stiffening. More details on the concrete constitutive model can be found in Cervenka et al. (2012).

Discrete reinforcement model (Figure 7.13-b) with linear stress-strain relationship (as shown in Table 7.2) was used in the FEMs. A user defined bond-slip model was used to simulate the bond characteristics between the embedded reinforcement and surrounding concrete. The bond-slip model suggested by Tekle et al. (2016) for sand coated GFRP bars was adopted in the FEMs. However, to simulate the effect of anchorage provided by the headed ends of the GFRP bars, the slippage at the headed end of the longitudinal bars was eliminated in the model (fixed nodes). More details on analytical modeling of GFRP-RC beam-column connections can be found in Ghomi and El-Salakawy (2018-a).

7.6.3 Validation

Figure 7.14-a compares the strain distribution in the longitudinal reinforcement of slabs obtained from the experimental tests (BCS-L and BCS-X) and the analytical modeling at 4% and 5% drift ratios, confirming a good agreement between the results. For further comparison, Figure 7.14-b compares the negative beam moment (slab-in-tension) envelope obtained from the experimental and the analytical part of the program. Similarly, the results are considered in good agreement with a maximum error of 10%.

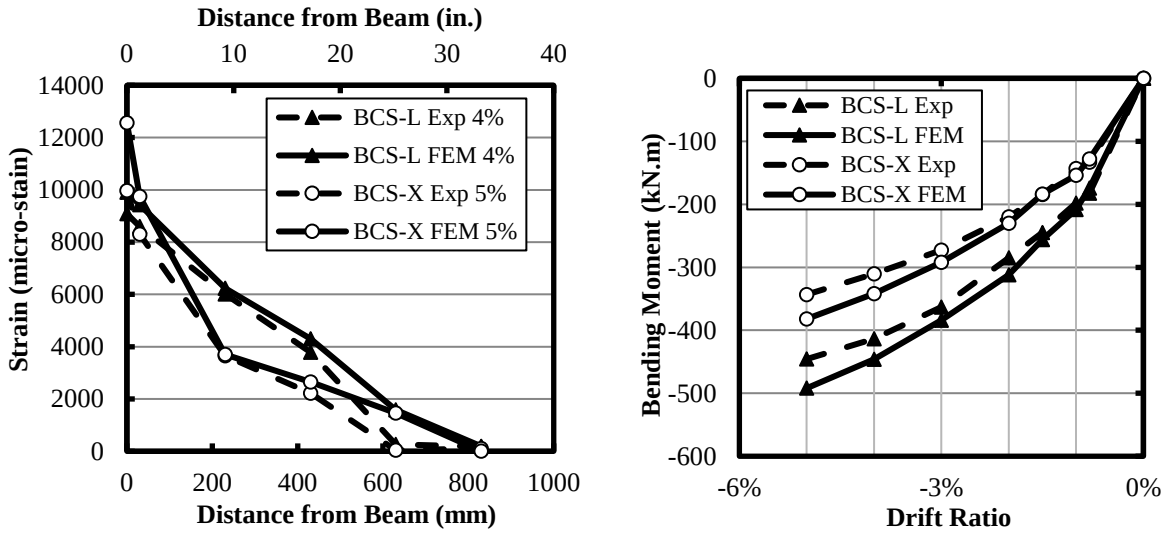

(a) Strain in slab longitudinal bars (b) Negative bending moment-drift response

Figure 7.14 - FEM validation.

7.6.4 Effect of lateral beam size

Following the validation of the FEMs, the model constructed for Specimen BCS-L was regenerated with three sets of additional lateral beam dimensions. In total, three beam-column-slab subassemblies with lateral beam dimensions of 400 mm × 450 mm (15.7 in. × 17.7 in.), 300 mm × 350 mm (11.8 in. × 13.8 in.) and 200 mm×250 mm (7.9 in. × 9.8 in.) and one beam-column-slab subassembly with no lateral beams were considered.

Strain distribution through the slab reinforcement was measured in each model and Equation 7.1 was used to calculate the effective slab width as a ratio of the effective beam depth, *d*. The relationship between the effective slab width (at 4% drift ratio) and the torsional constant of the lateral beams is shown in Figure 7.15 (the numbers in the brackets indicate the lateral beam dimensions in mm). It should be mentioned that only the torsional constant of the lateral beams

was considered in the calculations, thus the torsional constant corresponding to the specimen without lateral beams was set to zero.

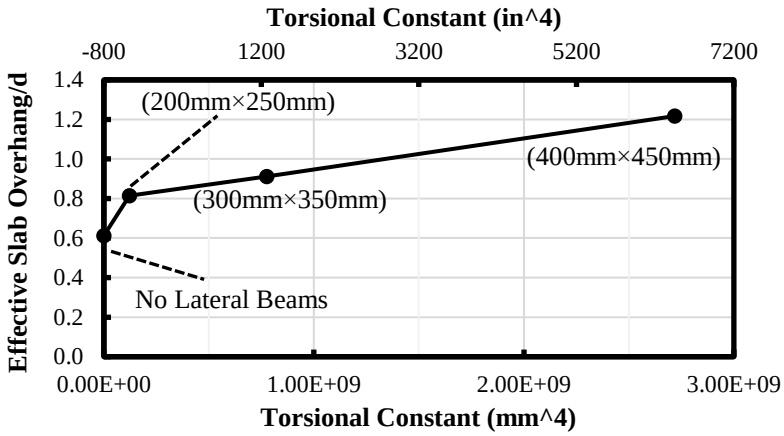

Figure 7.15 - Torsional constant-effective slab overhang relationship.

As expected, increasing the torsional stiffness of the lateral beams increased the effective overhang width. From Figure 7.15, it is evident that the presence of lateral beams, even with relatively low torsional constant, can significantly increase the effective slab width, indicated by the sharp increase in the effective overhang width of the FEM with the 200 mm × 250 mm (7.9 in. × 9.8 in.) lateral beams compared to the one without lateral beams. Moreover, the further increase in the lateral beams' dimensions, from 200 mm × 250 mm (7.9 in. × 9.8 in.) to 400 mm × 450 mm (15.7 in. × 17.7 in.), resulted in a linear increase in the effective overhang width by 50%.

7.6.5 Effect of slab thickness

To evaluate the influence of slab thickness on the effective overhang width, the analytical model of Specimens BCS-L was re-generated with a 200 mm (7.8 in.) deep slab and two layers of reinforcement in each direction. The reinforcement size and spacing in each layer was kept identical to the original reinforcement in the test specimens.

Figure 7.16 compares the beam moment-drift ratio response of Specimen BCS-L to its analytical models with a 100 mm (3.9 in.) and 200 mm (7.8 in.) slab thickness. The FEM with 200 mm (7.8 in.) slab thickness exhibited 5% and 8% (at 4% drift ratio) higher bending moment capacity compared to the FEM with 100 mm (3.9 in.) slab thickness in the negative and positive direction, respectively. An overhang width of 454 mm (17.9 in.) and 342 mm (13.5 in.) was calculated for the analytical models with the 200 mm (7.8 in.) and 100 mm (3.9 in.) slab, respectively. Comparing the positive bending moments corresponding to the effective overhang width of 454 mm (17.9 in.) and 342 mm (13.5 in.) from Figure 7.4 also indicates an insignificant increase in the bending moment capacity.

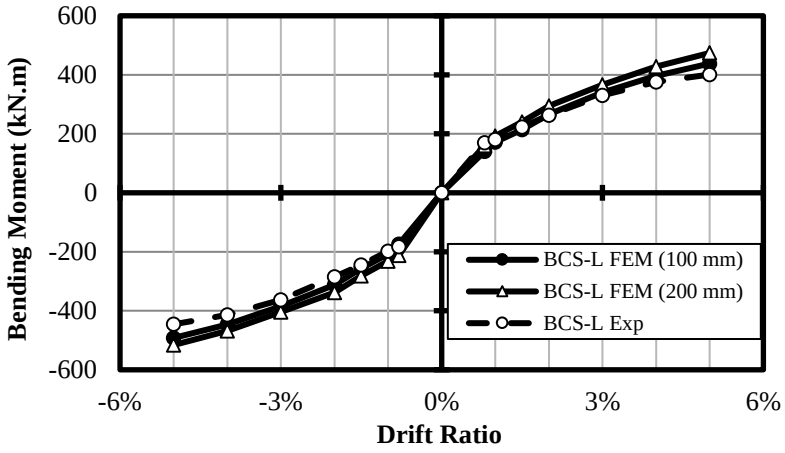

Figure 7.16 - Effect of slab thickness on bending moment capacity.

The observation of insignificant contribution of the slab when the top fiber was in compression obtained from the FEMs agrees with the conclusions from the experimental part. The crack propagation and stress distribution on the top surface of the slab and the main beam of the FEMs at 4% drift ratio are shown in Figure 7.17. It should be mentioned that only cracks wider than 0.1 mm (0.004 in.) are indicated in the figure. It is evident that the compressive concrete stress (near the column) is significantly higher in the main beam compared to the adjacent concrete in the slab,

confirming the insignificant sab contribution in the positive direction. The reason for this behaviour could be explained by the development of longitudinal cracks parallel to the main beam at the beam-slab interface (Figure 7.17), which reduced the composite action of the slab and the beam in compression. It should be mentioned that the development of these parallel cracks was also observed during the experimental tests.

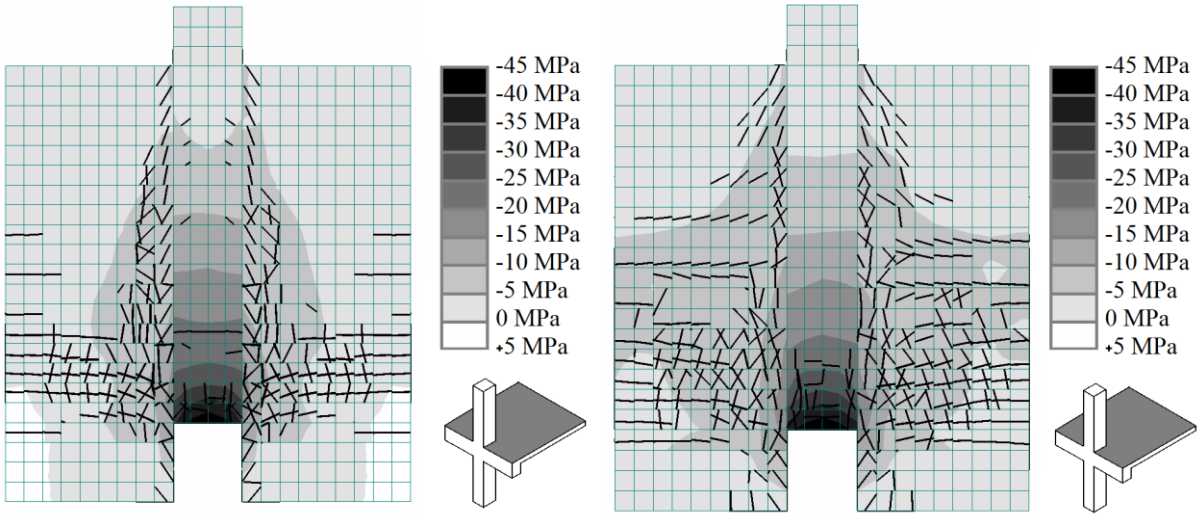

(a) 100 mm (3.9 in.) slab thickness (b) 200 mm (7.9 in.) slab thickness

Figure 7.17 - Crack propagation and stress distribution in slabs.

7.7 Conclusions

Based on the results obtained from the experimental and analytical studies as well as the comparison with test results from the literature on GFR-RC MRFs, the following conclusions can be made:

- The presence of slabs did not show any significant increase in the bending moment capacity of the main beams when in compression. The contribution of slab in the negative bending moment capacity of the beams (slab-in-tension), on the other hand, was noticeable. The

FRP-RC MRFs could benefit from the lack of slab contribution in compression, as it prevents the possibility of changing the mode of failure from the desirable compression-failure to the undesirable tension-failure one.

- The presence of lateral beams significantly increased the width of effective slab, in tension. A 70% increase in the overhang width, from 0.85*d* in Specimen BCS-L (beam-column-slab with lateral beams) to 0.5*d* in Specimen BCS-X (beam-column-slab without lateral beams), was observed.
- Both beam-column-slab specimens failed due to rupture of longitudinal bars in the main beam. Failure occurred during the second loading phase at 6% and 7% drift ratio in BCS-X and BCS-L, respectively. During the first loading phase (up to 5% drift ratio); however, both specimens showed stable behaviour with minor sings of concrete crushing in the main beam cover at the higher drift ratios (4 and 5%).
- The presence of slabs significantly increased energy dissipation of beam-column connections. Specimens BCS-L and BCS-X showed 49% and 122% higher cumulative energy dissipation compared to their corresponding specimens without slabs at 5% drift ratio. The increase in energy dissipation was even higher at the lower drift ratio limit of 3% (89% and 145%, respectively).
- Comparing the lateral stiffness of the test specimens at the beginning and end of the first loading phase indicated approximately 60% reduction in the stiffness of the specimens. To reduce the loss of lateral stiffness in GFRP-RC MRFs, it is suggested to limit the allowable lateral drift ratio of the frames to lower drift ratios.
- Increasing the cross-sectional area of lateral beams improved the contribution of slabs to the negative moment capacity of the beams (slab-in-tension). The FEM of the beam-

column-slab assembly with lateral beams covering the entire area of the joint exhibited 100% increase in the effective overhang width compared to the corresponding FEM without lateral beams.

- Cracks parallel to the main beam at the beam-slab interface was observed in both experimental tests and analytical models. The development of such cracks reduced the composite action of beam and slabs and prevented the contribution of slabs to positive moments (slab-in-compression).

8 SEISMIC PERFORMANCE IMPROVEMENT OF GFRP-REINFORCED CONCRETE MOMENT FRAMES

Shervin K. Ghomi and Ehab El-Salakawy

Canadian Journal of Civil Engineering, 2019, DOI: 10.1139/cjce-2019-0274.

Abstract: Although concrete structures reinforced with Fiber Reinforced Polymers (FRPs) have shown promising performance under gravity loads, their performance under cyclic loading is still one of the main concerns. Although the linear nature of FRP reinforcement could be advantageous in terms of limiting the residual damage after an earthquake event, it lowers the energy dissipation of the structure, which can compromise its seismic performance. In this research, adding steel plates at selected locations in moment-resisting frames is proposed as a solution to improve seismic performance of FRP-RC structures. Three full-scale cantilever beams, one steel-RC, one FRP-RC and one FRP-RC with proposed steel plates were constructed and tested under reversal-cyclic loading. The results indicated that the proposed mechanism effectively improves the seismic performance of FRP-RC beams through increasing their initial stiffness and energy dissipation. Moreover, a computer simulation, using moment-curvature determination process, was conducted to calculate bending moment capacity of FRP-RC beams with steel plates.

Keywords: Bolted steel side plates, GFRP-RC structures, FRP-RC moment-resisting frames, Seismic behaviour.

8.1 Introduction

Superior behaviour of Fiber Reinforced Polymer (FRP) in terms of corrosion resistance, electrical and magnetic non-conductivity, and high strength-to-weight ratio introduced this material as a promising alternative for steel reinforcement in reinforced concrete (RC) structures. Up to date, many researchers have been involved in investigating the behaviour of various FRP-RC elements ranging from individual members such as beams and slabs to structural assemblies where two or more structural elements interact with each other, such as beam-column joints and slab-column connections.

Although performance of FRP-RC structures under monotonic loading has shown promising results toward replacing steel reinforcement with FRP, the performance of such structures under earthquake-induced loads is still a major concern. One of the main reasons is the linear behaviour of FRP reinforcement, which results in lack of ductile behaviour of concrete structures under seismic loading. Therefore, without any special consideration, this linear behaviour could increase the probability of brittle failure and collapse of FRP-RC structures exposed to large deformations, such as moment-resisting frames in seismic regions.

Up to date, only few studies have been involved in investigating the seismic performance of FRP-RC frames (Ghomi and El-Salakawy 2016; Hasaballa and El-Salakawy 2016; Mady et al. 2011; Said and Nehdi 2004; Fukuyama et al. 1995). To evaluate the seismic performance of FRP-RC frames, the majority of the researchers in this field focused on the behaviour of beam-column connections, as key elements in stability of moment-resisting frames and determining their performance under reversal lateral loading. Previous work by the authors (Ghomi and El-Salakawy 2016; Hasaballa and El-Salakawy 2016; Mady et al. 2011) investigated the feasibility of using

FRP-RC moment-resisting frames in seismic regions and the effect of various parameters on the seismic performance of beam-column connections.

Results of these studies showed that beam-column assemblies reinforced with Glass Fibre Reinforced Polymers (GFRP) can be proportioned such that they are able to withstand high lateral drift ratios (9%) without exhibiting brittle failure due to rupture of the reinforcement. This observation was against what is generally expected from FRP-RC elements. This particular behaviour was observed in GFRP-RC members due to the relatively low modulus of GFRP (60 GPa) combined with relatively high tensile strength (1,100 MPa), which makes these materials capable of withstanding high strains compared to the other main FRP alternatives, carbon FRP and aramid FRP.

Moreover, the test results indicated that GFRP-RC beam-column joints can maintain their elastic properties up to drift ratios as high as 5% with minimum residual damage. Due to this linear behaviour, replacing steel with GFRP materials might be an effective solution to eliminate the drastic damage caused by plastic deformation of steel-RC elements during an earthquake event. Damage to steel-RC structures after an earthquake can cause costly rehabilitation or even, in some cases, result in the demolition of the whole structure. Therefore, using GFRP-RC frames in seismic regions can be a new approach toward earthquake-resistant structures since the frame could be capable of withstanding several severe ground shakings without significant residual damage.

However, despite the satisfactory performance of GFRP-RC moment-resisting frames in terms of residual damage, these structures still show lack of energy dissipation which is one of the main philosophies for designing earthquake-resistant structures. Moreover, low modulus of elasticity of GFRP reinforcement decreases initial stiffness of RC moment-resisting frames which increases

the lateral deformation of the frames during earthquakes. Large lateral deformation of the frames results in excessive secondary moments especially at the lower grades due to significant movement of the centre of gravity of the building from its original location. This effect is known as P-Δ effect. Moreover, large lateral deformation increases the pounding probability of adjacent buildings. Therefore, the advantage of FRP's linear behaviour cannot be utilized in eliminating the residual damage after an earthquake unless these two issues are addressed.

In this research, improving the seismic performance of GFRP-RC moment-resisting frames is sought. In previous studies (Ghomi and El-Salakawy 2016; Hasaballa and El-Salakawy 2016), to compensate for low energy dissipation, researchers suggested to use conjugated lateral load resisting systems in FRP-RC frames. For example, using steel-RC shear walls or hybrid system frames (using FRP-RC elements only in surrounding parts of the frame that have direct contact with harsh environment while the core of the frame is reinforced with steel). However, these solutions are suggested based on the assumption that the main goal of using FRP reinforcement is to protect the structure against corrosion and not improving its seismic performance. Therefore, these solutions necessarily include using steel-RC elements in some parts of the frame, which again increases the probability of permanent deformation after an earthquake.

Up to date, no solution has been introduced to improve energy dissipation and low initial stiffness of GFRP-RC elements, which seems to be the only reason for holding back GFRP-RC moment-resisting frames from being eligible for resisting lateral seismic loads by themselves.

The focus of this research is on conjugating GFRP-RC frames with simple and easy-to-install mechanical devices to improve their seismic performance. The approach is to improve the overall performance of GFRP-RC frames by installing the device on specific locations in the frame. In

this approach, the energy dissipation and stiffness of FRP-RC frames will be improved while still possible to take advantage of their linear behaviour nature.

8.2 Proposed Solution

8.2.1 Background

The conventional approach to design an earthquake-resistant RC structure is based on members' plastic deformation mainly due to yielding of reinforcing steel. Ductility of steel-RC structures provides significant energy dissipation due to inelastic deformation of members. This plastic deformation; however, comes with the cost of severe damage to the elements after an intense earthquake. In some cases, the damage is so drastic that the structure may need to be demolished.

On the other hand, lack of plastic deformation in GFRP-RC structures, despite of eliminating costly repairs after earthquakes, significantly decreases the amount of seismic energy dissipated by the structure. In this case, using an energy dissipation-improvement technique such as using additional damping mechanism may be effective to improve the dynamic response of GFRP-RC moment-resisting frames. There are many damping mechanisms available for the construction industry; however, the focus of this research is to introduce an easy-to-build damping system with relatively low cost.

8.2.2 Steel plates

In this research, attaching side steel plates to GFRP-RC beams is proposed as an effective solution to improve dynamic performance of GFRP-RC frames. In this approach, plastic behaviour of steel is used to dissipate energy and high modulus of elasticity of steel is used to increase stiffness of the frames. In the proposed method, the concrete section is reinforced with GFRP bars and is

designed based on GFRP material characteristics. A metal member (steel plates), then, will be added to the section in order to dissipate energy through plastic deformations while the member undergoes large deformations. The metallic element is attached to the structure externally. Assuming perfect linear and bi-linear stress-strain relationship for GFRP-RC beams and steel plates, respectively, schematic behaviour of a GFRP-RC beam with a steel plate is shown in Figure 8.1.

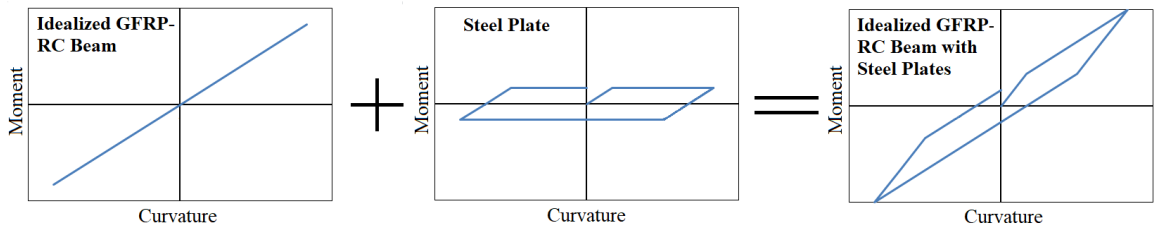

Figure 8.1 - Idealized behaviour of GFRP-RC beams with steel plates

Figure 8.2 shows a schematic drawing of a GFRP-RC cantilever beam with the proposed metallic plates. As shown, one steel plate is attached on each vertical side of the main beam. The plates are tied to the concrete beam by several structural bolts (or cast-in anchors) embedded in the concrete core to ensure that the plates deflect with the same curvature as the concrete beam under bending moments. The steel plates are predominately-flexural members and their yielding moment can be calculated using analytical methods. Therefore, the steel plates can be proportioned to yield at relatively low deformations to dissipate seismic energy by plastic deformation during seismic loading. The damaged and deformed plates following an earthquake will be replaced with new plates. As mentioned before, since GFRP-RC frames can undergo large deformations while maintaining their linear nature and original condition (to an acceptable degree), by replacing damaged steel plates with new ones the original condition of the structure will be restored with minimal additional repairing. This feature is one of the key advantages of the proposed structure

over a conventional steel-RC structure. In an internally steel-RC frame, since there is no access to the embedded reinforcement, the original condition can never be stored once yielding of the reinforcement has occurred.

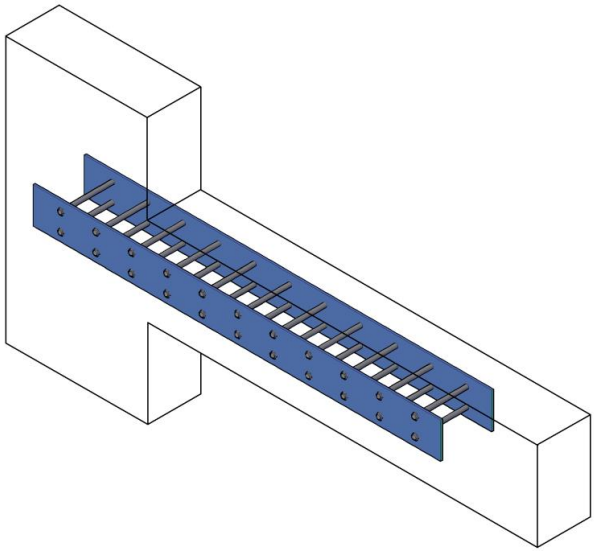

Figure 8.2 - Proposed mechanism for seismic performance enhancement of GFRP-RC elements

In RC moment-resisting frames, the maximum bending moment in beams, hence the maximum curvature, during lateral loading (earthquakes) is expected to occur at beam ends near columns (see Figure 8.3), known as locations of plastic hinges (locations of inelasticity concentration). Therefore, attaching the proposed steel plates to GFRP-RC beams near beam-column joints is expected to maximize the effectiveness of steel plates in dissipating energy. However, it is important to sufficiently anchor the plates at beams support (columns in moment-resisting frames) to ensure development of yielding stresses in steel plates.

It should be mentioned that, in this research, the focus is on the linear behaviour of GFRP-RC members and their ability to withstand large deformations and not on their corrosion resistance, which may be the conventional motivation for replacing steel reinforcement with GFRP material.

The goal is to achieve a new type of structure with improved seismic performance compared to the structures that are solely reinforced with steel or GFRP.

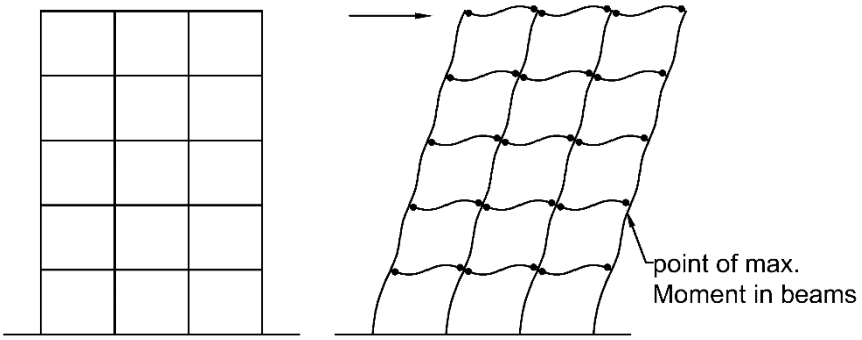

Figure 8.3 - Point of maximum bending moments in beams during lateral loading

Therefore, using corrodible steel plates in a GFRP-RC frame will not interfere with this goal since the focus is not on introducing a corrosion-resistant structure. However, the proposed frame structure does have superior behaviour in terms of controlling corrosion of steel components compared to conventional steel-RC structures. Since the main metallic components of the proposed structure are visually and physically accessible, corrosion assessment and prevention are more convenient compared to the structures that are internally reinforced with steel. Moreover, stainless or galvanized steel can be used to prevent corrosion of exposed plates.

It should be mentioned that in buildings, the presence of slabs on top of beams could impose limitations on the depth of steel side plates. In such cases, as shown in Figure 8.2, depth of the steel side plates should be selected such that not to interfere with the concrete slabs on top of the beams in real structures.

It worth mentioning that using steel plates as a strengthening method for steel-RC beams has been introduced previously and has been studied extensively by researchers. However, in majority of previous studies the main objective was to improve flexural and shear resistance and stiffness of

steel-RC beams, mainly under monotonic loading, while in this research the use of steel plates is proposed to improve the seismic performance of GFRP-RC beams, which has not been studied before. Moreover, the proposed method is not a strengthening technique, but is a new composite structure with superior dynamic performance compared to moment-resisting frames solely reinforced with either steel or FRP. However, some of the concepts used by previous researchers to utilize steel side plates to improved flexural and shear capacity of steel-RC beams under monotonic loading can be used in the proposed method in this research as well.

In general, there are two methods in attaching steel plates to the base RC beam: 1) by adhesive materials and 2) by fasteners (bolts). In the current study, bolt connections were used to facilitate steel plate replacement after damage, which is a key feature of the proposed composite structures.

Su et al. (2010) investigated the effect of bolt-plate arrangements on ductility of strengthened beams. The authors investigated the performance of bolted side-plated beams considering various relative strength of bolts and steel plates. The authors reported that strong bolt-weak plate arrangement results in sufficient strength and ductility enhancement of RC beams, while strong bolt-strong plate arrangement results in brittle failure. Therefore, it was concluded that the amount of steel side plates should be limited while strong bolts should be provided to ensure desirable ductile behaviour of RC beams.

However, it should be mentioned that the study conducted by Su et al. (2010) was considering beams predominantly subjected to gravity loads. Therefore, steel side plates were only provided in the tension zone of the test beams. However, since the current study investigates seismic performance of GFRP-RC beams, the test elements should be designed for reversal loading. Thus, it is necessary to proportion dimensions of steel plates to be active under both negative and positive

bending moments. Therefore, relatively deeper side steel plates were selected for the beam in the current study.

Previous studies on utilizing steel plates for strengthening RC beams indicated that attaching plates to beam soffits could result in significant decrease in ductility of RC beams, while attaching the plates to vertical sides of RC beams could maintain satisfactory ductility (Subedi and Baglin 1998; Foley and Buckhouse 1999). Since one of the focuses of steel side plates in the proposed method is to enhance ductility of GFRP-RC beams, steel plates are attached to the vertical sides of the beams. Moreover, as mentioned earlier, since the steel plates need to be active in both positive and negative direction, attaching steel plates to the bottom side of beams should be accompanied with attaching counterpart plates to the top side of the beams, which may not be practical due to the presence of stabs.

Lo et al. (2014) studied partial interaction between bolted side plates and RC beams. The authors reported partial interaction in longitudinal and transverse direction as one of the key parameters affecting the performance of RC beams with bolted side plates. Therefore, adequate fasteners should be provided to eliminate the longitudinal and transverse bolt slip. Su et al. (2014) and Oehlers et al. (1997) provided a relationship between the number of fasteners and the degree of longitudinal and partial interaction. These relationships were used in the current study to calculate adequate number of fasteners to minimize bolt slip.

It is worth mentioning that several researchers have studied the seismic behaviour of hybrid concrete elements (mainly beams and columns), internally reinforced with both FRP and steel bars (Aiello and Ombres 2002; Kara et al. 2015; Ibrahim et al. 2016; Qin et al. 2017). Although this approach could result in enhancement of the seismic response of FRP-RC moment-resisting frames

in terms of ductility and energy dissipation, it still leaves the issue of repairability unresolved. Since steel rebars are embedded inside concrete elements, it won't be feasible to replace yielded steel reinforcement after severe earthquakes. Hence, the proposed method in this program (concrete elements internally reinforced with FRP bars and external side plates) aims to resolve this drawback.

8.3 Experimental Program

To evaluate the effectiveness of the proposed solution on the seismic performance enhancement of GFRP-RC moment-resisting frames, three full-scale cantilever beams (one steel-RC, one GFRP-RC and one GFRP-RC with steel plates) were constructed and tested under reversal-cyclic loading. These three specimens were tested as a pilot study to investigate the feasibility of implementing the proposed method and its effectiveness. As explained earlier, the steel plates are predominately flexural members and are suggested to be attached to the main beams at the points of high bending moments (due to lateral loading), therefore, cantilever beams were selected as test elements to focus on the composite performance of the proposed structures in predominately flexural loading.

Results of this pilot study will be used to design the second phase of experimental tests, studying the performance of the proposed structures in more complicated structural elements (beam-column assemblies).

8.3.1 Specimens

The test specimens were identical (dimensions in Figure 8.4) except for the type of reinforcement in the beam (GFRP or steel) and presence of the steel plates. The beams' reinforcement was

anchored in a 350 × 500 × 1400-mm concrete block which simulated a fixed support. Two of the beams were used as control specimens with no steel plates, one representing a GFRP-RC beam and one representing a conventional steel-RC beam. The control beams were designed to have the same flexural capacity. Figure 8.5 shows reinforcement detailing of the specimens. Deformed (ribbed) steel and GFRP bars and stirrups were used to provide sufficient bond between the reinforcement and the concrete. The longitudinal bars were anchored into the concrete supports with a 90-degree standard bend. Test results of the control specimens were used to investigate the differences between the seismic behaviour of GFRP-RC structures and steel-RC ones. Moreover, the results drew guidelines to assess the effectiveness of the proposed method on improving the seismic response of the GFRP-RC beam.

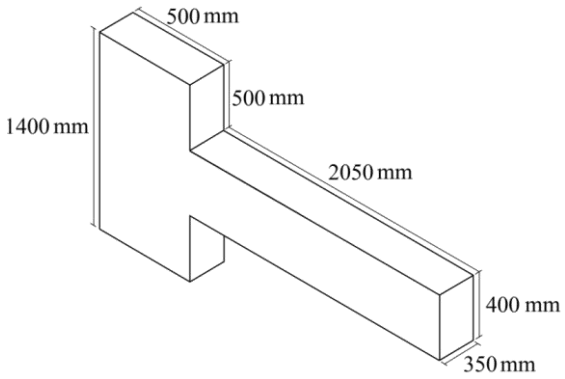

Figure 8.4 - Dimensions of test specimens (dimensions in mm)

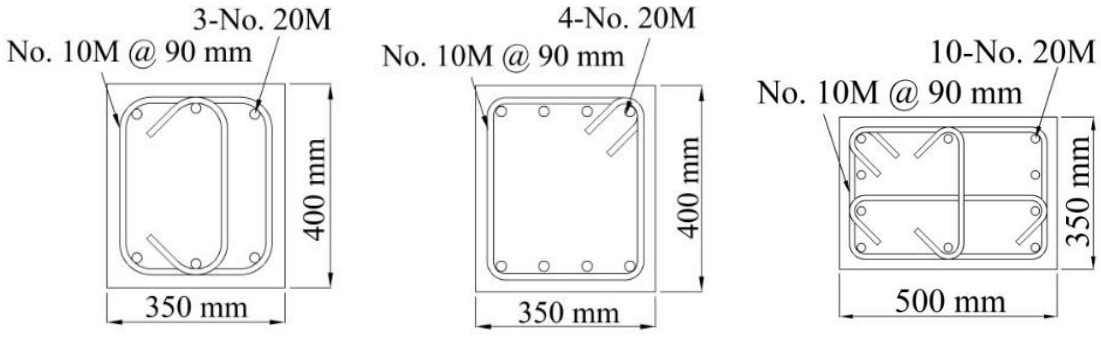

(a) GFRP-RC Beam (b) Steel-RC Beam (c) Support

Figure 8.5 - Cross-sections of test specimens

The third specimen was constructed by replicating the control GFRP-RC beam with addition of the plates. Figure 8.6 shows detailed drawing and pictures of the specimen. Two 1600 × 300 × 5-mm steel plates were attached, one on each side of the beam, by means of fourteen 8-200 mm-long 25M bolts.

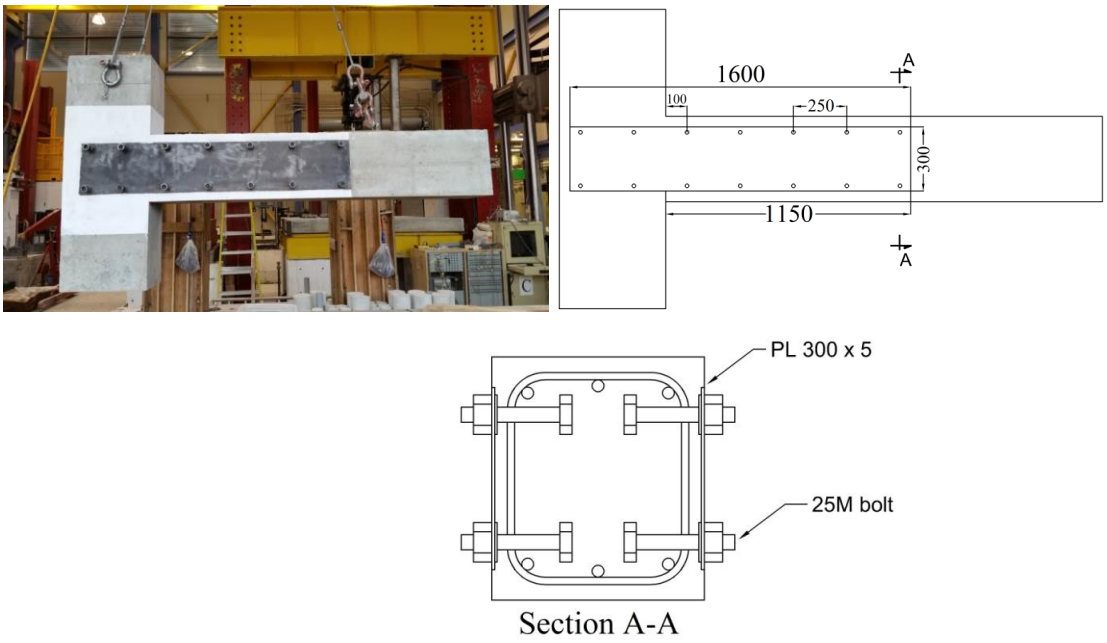

Figure 8.6 - Specimen G-M

The test specimens were designated with two letters. The first letter indicates reinforcing material ("G" for GFRP and "S" for steel). The second letter indicates whether the steel plates are attached to the specimens ("N" for the specimens with no plates, "M" for the specimen with the metallic plates). Table 8.1 shows properties of test specimens.

Table 8.1 - Properties of control specimens

Specimen ID	Beam Reinforcement (Top and Bottom)	Beam Flexural Capacity (kN.m)	Support Flexural Capacity (kN.m)	Concrete Strength (MPa)
G-N	3-No. 20M	231	420	47
S-N	4-No. 20M	214	420	47
G-M	3-No. 20M	336	420	49

8.3.2 Materials

The specimens were cast with ready-mix concrete with a target 28-day strength of 40-MPa, normal weight and maximum aggregate size of 20-mm. The actual concrete compressive strength of the specimens was obtained based on standard 150 × 300-mm cylinder test on the day of testing, as reported in Table 8.1.

Deformed CSA grade G400 regular steel bars were used in the steel-RC specimen. The average yield and tensile strengths of the longitudinal bars, 440 and 620 MPa, respectively, were obtained in the laboratory according to CSA/A23.1-14 (2014-a). Deformed GFRP bars and stirrups (Schoeck Canada Inc. 2019) were used in the GFRP-RC specimens. The mechanical characteristics and dimensions of used GFRP reinforcement, as provided by the manufacturer, are listed in Table 8.2.

Table 8.2 - Mechanical properties of used GFRP reinforcement

Type	Bar size	Diameter (mm)	Area (mm^2)		Tensile strength Straight portion (MPa)	Elastic Modulus (GPa)	Ultimate strain (micro-strain)
			Nominal	Annex A[a]			
Bent bar	20M	20	314	392	850	50	17,000
Stirrups	10M	12	113	166	1,000	50	20,000

[a] CSA/S806-12

8.3.3 Test set-up

Figure 8.7 shows pictures of the test set-up with a specimen ready for testing. A 5,000-kN-capacity actuator on a "*Material Testing Systems*" (MTS) loading frame was used to apply reversal-cyclic displacements to the tip of the beam to simulate seismic loading. The support of the cantilever beam was under constant axial load during the test, by means of a hydraulic jack. A strong frame was used to provide sufficient support for the jack (Figure 8.7-a). Top and bottom of the concrete

support was clamped to the frame to prevent any lateral movement. The actuator was attached to the tip of the beam by means of a swivel head to prevent any moment application. Moreover, a set of rollers were put between the concrete beam and loading plates to prevent the actuator from applying unwanted axial loads to the beam during the reversal vertical loading.

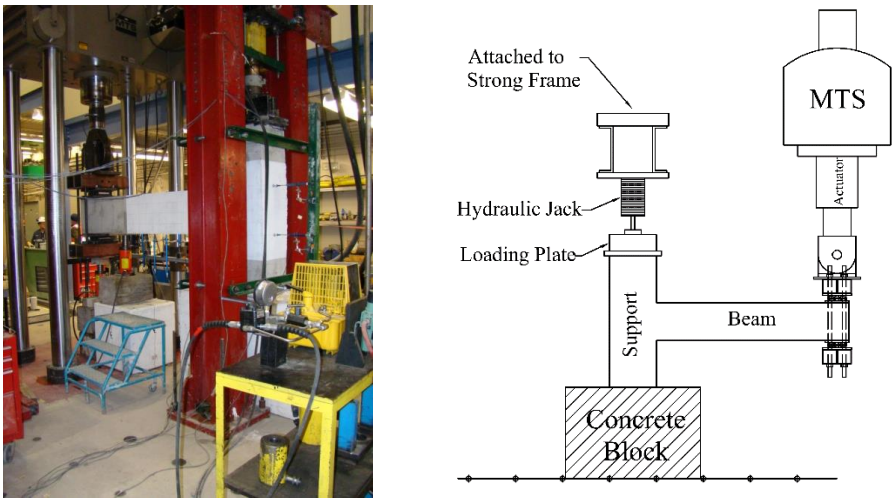

(a) Constructed test set-up (b) Schematic side view

Figure 8.7 - Test set-up

8.3.4 Loading procedure

The loading procedure was started by applying axial compressive load to the support portion. The magnitude of the load was equal to 15% of maximum concentric capacity of the support. This load remained constant during the testing procedure.

Following the support loading, the reversal-cyclic loading of the beam started. The loading was in a displacement-controlled mode. Figure 8.8 shows the cyclic loading scheme used in the testing procedure. A series of loading stages progressively increasing in drift ratio were applied to the specimens. The drift ratio is defined as the relative displacement of beam tip to its length.

Moreover, three identical loading cycles for each drift ratio was applied to achieve stable crack propagation in the specimens.

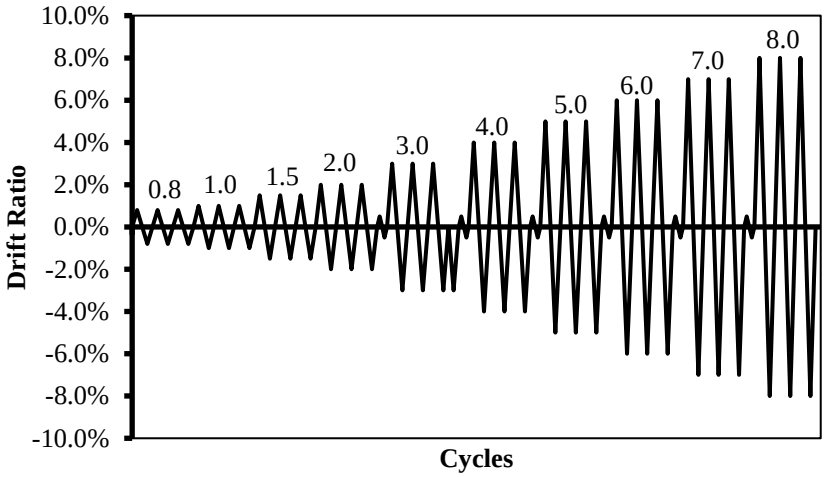

Figure 8.8 - Seismic loading scheme

As mentioned earlier, one of the main objectives of this program was to evaluate the ability of GFRP-RC elements to maintain their original condition after being loaded to high drift ratios. Therefore, the GFRP-RC specimens were tested under two series of cyclic loading. In the first series, they were loaded under the above specified loading procedure up to 4% drift ratio. In the second series, the loading scheme was repeated from 0% drift ratio and was continued until failure of the specimens. It should be mentioned that according to ACI 374.1-05 (ACI Committee 374 2005), failure is defined when at least 25% decrease in load-carrying capacity of the specimens compared to the maximum observed capacity is occurred.

This two-phase loading procedure was to investigate the performance of the GFRP-RC beams after undergoing a severe seismic loading and to measure possible stiffness reduction. The reasons for choosing the 4% drift ratio as the limit for the first loading step are as follows:

1. Previous studies on the seismic behaviour of GFRP-RC beam-column assemblies (Ghomi and El-Salakawy 2016) indicated that the specimens generally achieve their design capacity at 4% drift ratio. Therefore, to evaluate the seismic performance of the GFRP-RC test beams after being loaded to their maximum design capacity, 4% drift ratio was selected.

2. Moreover, any drift ratios higher than 4% is considered to be beyond the actual response of a regular moment-resisting frame. The National Building Code of Canada (NRCC 2015) limits the maximum allowable lateral drift of each story to 2.5%. Moreover, the maximum expected lateral drift ratio of a story in CSA/S806-12 (CSA 2012) for FRP-RC building structures is 4%.

It should be mentioned that although the limiting drift ratios suggested by codes and guidelines are based on lateral drift ratios of columns it can be shown, through structural analysis, that applying the same drift ratios at beams' points of contra-flexure (mid-span) while maintain the axis of columns produces the same effect in beam-column assemblies in quasi-static testing. Many researches (Ghomi and El-Salakawy 2016; Hasaballa and El-Salakawy 2016; Ehsani and Wight 1985-a) have adopted this method to facilitate the testing procedure. The same rational was used as the ground base for applying drift ratios to the tip of the test beams in this program.

8.4 Test Results

8.4.1 Overall behaviour and hysteresis diagram

Figure 8.9 shows pictures of Specimen G-N after the first loading phase and its beam tip load-drift response (hysteresis diagram). The dashed lines in the hysteresis diagram show the design capacity

of the specimen. It should be mentioned that to prevent line congestions, only results of the first cycle in each loading stage is presented in the hysteresis diagrams.

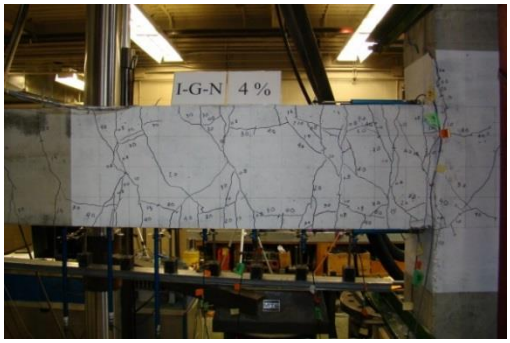

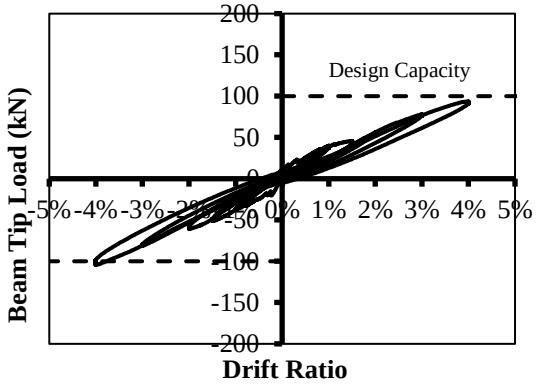

(a) Picture of Specimen G-N after 4% drift ratio (b) Hysteresis diagram of Specimen G-N

Figure 8.9 - Specimen G-N after the first loading phase

As shown in Figure 8.9-b, Specimen G-N (reinforced with GFRP without steel plates) showed linear behaviour until 4% drift ratio with insignificant residual displacement. This agrees with picture of the specimen in Figure 8.9-a that shows no concrete spalling or crushing. Moreover, there was no sign of damage penetration into the support. This low magnitude of concrete damage is also indicated by narrow loops in the specimen's hysteresis diagram, which also confirms low energy dissipation of the GFRP-RC beam. These observations indicate that GFRP-RC structures can undergo large deformations while maintaining their linear nature and original condition to an acceptable degree.

Followed by the first loading phase, the specimen was loaded under the second loading series from 0% drift ratio until failure. Picture of the specimen at failure and its hysteresis diagram in the second loading phase are shown in Figure 8.10. The failure occurred at 6% drift ratio due to rupture of the longitudinal reinforcement. It should be mentioned again that 6% drift ratio is considered

beyond the response range of a regular structure, since significant secondary moments can be generated in the structural elements due to P-Δ effect.

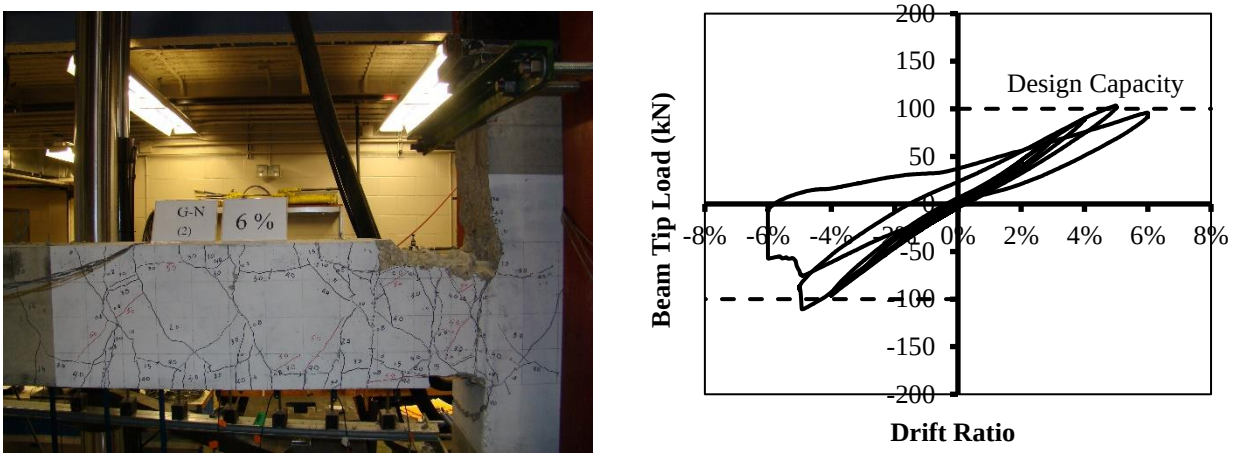

(a) Picture of Specimen G-N at failure (b) Hysteresis diagram of Specimen G-N

Figure 8.10 - Specimen G-N after the second loading phase

Figure 8.11 shows hysteresis diagram of Specimen S-N and its pictures after 4% drift ratio and failure. According to the specimen's hysteresis diagram, the longitudinal reinforcement yielded at 1.5% drift ratio which resulted in ductile behaviour of the specimen indicated by wide hysteresis loops. However, at the same time this yielding increased the residual displacement (pinching) at zero load condition, therefore severe concrete damage was observed in the beam at the vicinity of support while reaching 4% drift ratio.

Due to yielding of steel reinforcement, it was not possible to restore the original condition of Specimen S-N after the first loading phase, thus the logic of two-phase loading procedure that was used for the GFRP-RC specimens, did not apply for the steel-RC specimen. Therefore, after 4% drift ratio the loading procedure was continued according to Figure 8.8 until failure of the specimen. The specimen failed at 6% drift ratio by exhibiting significant decrease in load-carrying capacity (30% decrease from the maximum load).

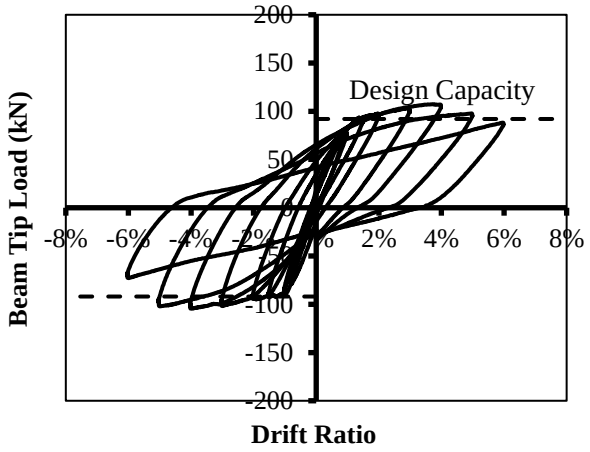

(a) Hysteresis diagram of Specimen S-N

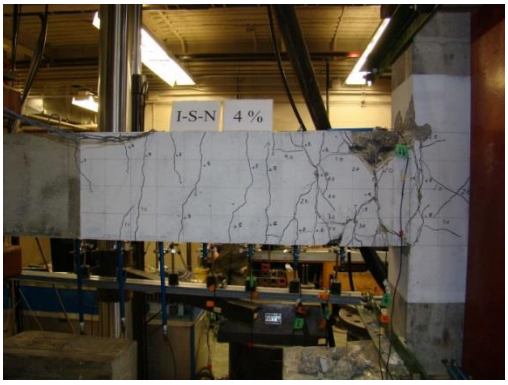

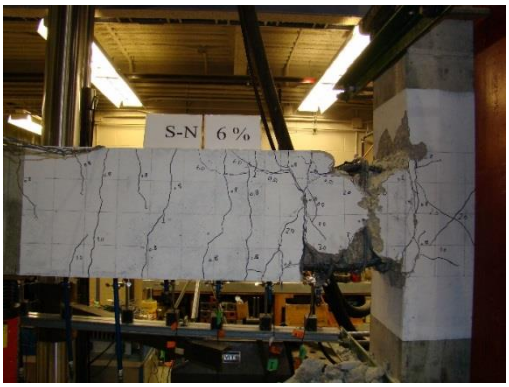

(b) Picture of Specimen S-N after 4% drift ratio (c) Picture of Specimen S-N at failure

Figure 8.11 - Performance of Specimen S-N

Figure 8.12 shows beam tip load-drift respond of Specimen G-M in the first loading phase and its condition at 4% drift ratio. Specimen G-M combined linearity of GFRP-RC structures with ductility of steel-RC structures. Yielding of the steel plates was observed at 1.5% drift ratio where the specimen started to exhibit non-linear load-drift response and wider hysteresis loops. Although the steel plates were severely deformed and damaged (Figure 8.12-b), the concrete beam maintained its integrity and original condition (to an acceptable degree) after 4% drift ratio. Figure 8.13 shows picture of the beam after removing the steel plates. It was observed that steel plates

also improved the performance of the specimen by reducing the number of cracks in the concrete beam compared to Specimen G-N (GFRP-RC without steel plates).

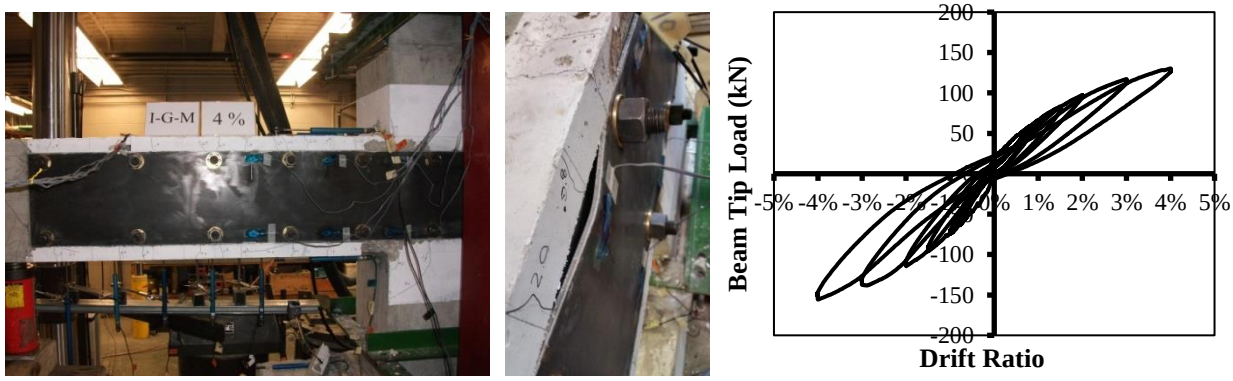

(a) Specimen G-M after 4% (b) Yielding of steel plates (c) Hysteresis diagram

Figure 8.12 - Specimen G-M after the first loading phase

Figure 8.13 - Crack propagation in Specimen G-M after the first loading phase

Figure 8.14 compares envelops of load-drift response of the specimens in the first loading phase. As expected, the steel plates improved the seismic performance of the GFRP-RC beam by increasing its initial stiffness up to approximately the initial stiffness of Specimen S-N. However, unlike specimen S-N, Specimen G-M did not reach any plateau and continued on carrying increasing load after 1.5% drift ratio.

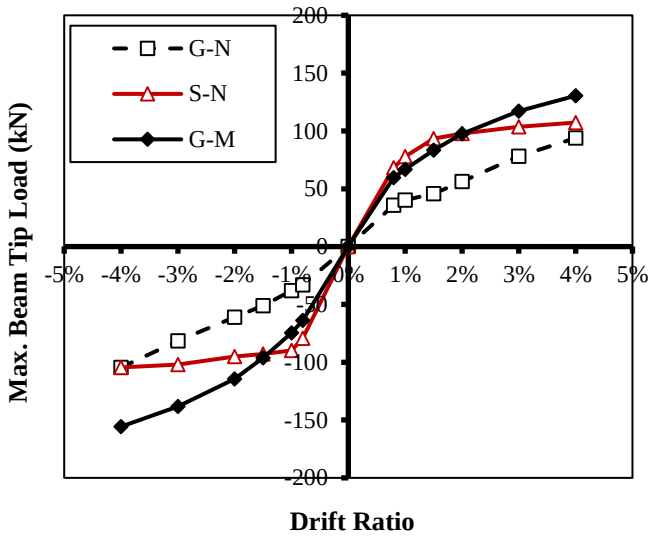

Figure 8.14 - Load-drift envelop of specimens in the first loading phase

The damaged steel plates in Specimen G-M were replaced with new plates and the specimen was re-tested under the second series of cyclic loading (from 0% till failure). Figure 8.15 shows a picture of the specimen at failure and its hysteresis diagram in the second loading phase. The failure occurred due to rupture of the longitudinal bars at 7% drift ratio.

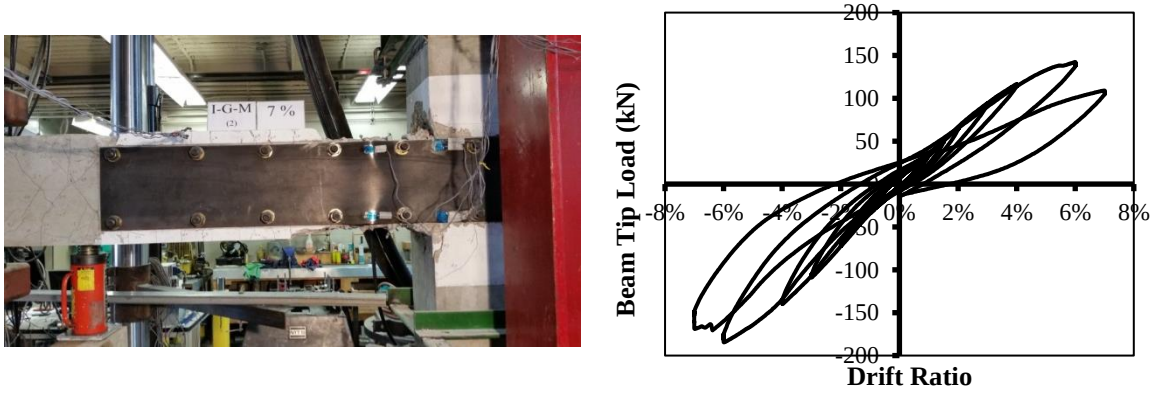

(a) Picture of Specimen G-M at failure (b) Hysteresis diagram of Specimen G-M

Figure 8.15 - Specimen G-M after the second loading phase

Figure 8.16 compares load-drift envelop of the specimens in the second loading phase. As the graph shows, although replacing the damaged steel plates with the new ones increased the initial stiffness of Specimen G-M compared to Specimen G-N in the second loading phase, the initial

stiffness was not as high as Specimen S-N. The authors believe one of the reasons for lower initial stiffness of Specimen G-M in the second loading phase may be due to the gap between the bolts and steel plates (in the second loading phase) which delayed loading of the steel plates. It should be mentioned that due to the construction process, the first set of steel plates were left inside the formwork while the beam was cast with concrete. Therefore, all gaps between the bolts and the plates were filled with concrete, thus the plates performed satisfactory. The authors believe that the issue of the gap between the bolts and the new steel plates could be simply resolved by injecting grout into the gaps and sealing it with washers and nuts. As mentioned earlier, the reported experimental program was designed as a pilot study for feasibility investigations and proof of concept. Further experimental investigations are required to determine the performance of the proposed structure in more realistic simulation of moment-resisting frames, taking into account important factors such as the effect of columns' rotation and anchorage method of the steel plates into the joint area on the effectiveness of the steel plates.

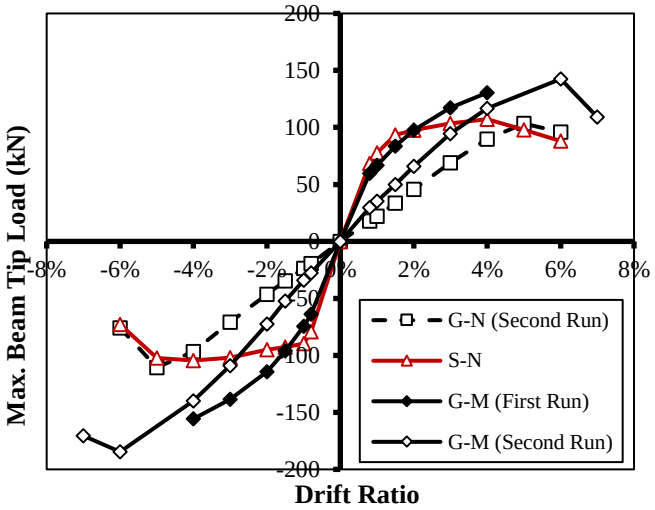

Figure 8.16 - Load-drift envelop of specimens

8.4.2 Energy dissipation

Figure 8.17 compares the cumulative amount of energy dissipated by the specimens at the first cycle of each drift ratio in the first loading phase. The dissipated energy is calculated as the area enclosed by the hysteresis loops in beam tip load-displacement response of the specimens.

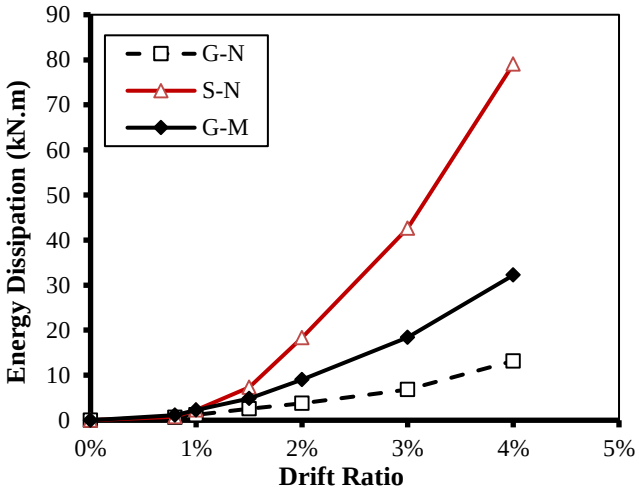

Figure 8.17 - Cumulative energy dissipation in the first loading phase

As expected, steel plates increased the amount of energy dissipated by the GFRP-RC beam. The improvement was 160% at 2.5% drift ratio and 145% at 4% drift ratio compared to Specimen G-N. It should be mentioned that the dissipated energy by Specimen S-N was 475% and 500% higher compared to Specimen G-N at 2.5% and 4% drift ratio, respectively.

8.4.3 Strain-drift relationship

Figure 8.18-a shows the maximum strain captured in the stirrups located in the joint area during the first loading phase. As shown in the graph, adding steel plates resulted in increasing the maximum strain in the joint area in the GFRP-RC specimens at drift ratios higher than 2%. This is attributed to the higher bending moment capacity of Specimen G-M compared to Specimen G-N, which resulted in transferring higher shear stresses to the joint area. This effect must be taken

into account when implementing the proposed method in moment-resisting frames to prevent failure of beam-column joints during lateral movement of frames due to earthquakes. Moreover, the effect of steel plates on increasing the flexural capacity of the beams must be considered in calculating column-to-beam flexural strength ratios in beam-column connections of moment-resisting frames to ensure that strong column-weak beam concept is fulfilled.

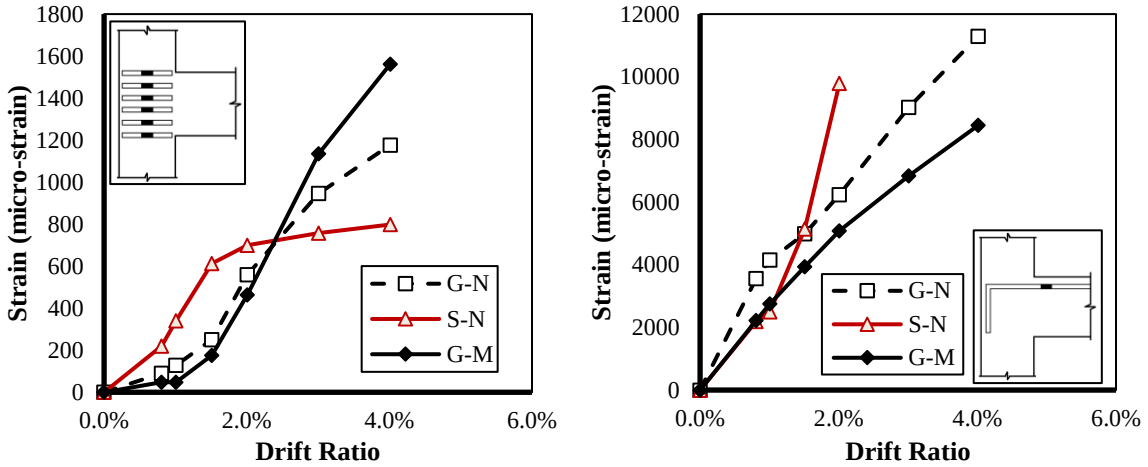

(a) Maximum strain in joint stirrups (b) Maximum strain in longitudinal bars

Figure 8.18 - Strain-drift relationship

In Specimen S-N, yielding of beam longitudinal reinforcement resulted in a plateau in the maximum strain of joint stirrups since the maximum stress in the longitudinal bars anchored in the joint area remained approximately constant after yielding.

Figure 8.18-b shows the maximum strain captured in the longitudinal bars adjacent to the support during the first loading phase. As shown in the graph, presence of side plates reduced the maximum strain in the longitudinal bars of the GFRP-RC specimens. This agrees with the observation of less damage induced to the concrete beam in Specimen G-M compared to Specimen G-N.

8.5 Design Procedure

A numerical method based on moment-curvature determination was used to investigate the maximum bending moment capacity of the GFRP-RC specimens (G-N and G-M). The modified moment-curvature analysis introduced by Lo et al. (2014) was adopted in this study and the moment-curvature diagrams were generated by a computer program using the commercial software "Matlab". The modified moment-curvature method measures the degree of partial interaction between the side plates and the RC beam by two factors, one corresponding to longitudinal partial interaction and one corresponding to transverse partial interaction. However, as mentioned earlier, adequate number of bolts were selected for Specimen G-M to prevent bolt slip; therefore, both factors were set as unity (full interaction) in this study.

To determine the moment-curvature relationship of the GFRP-RC beams, the cross-section was divided into several horizontal strips with identical depths (as shown in Figure 8.19 for Specimen G-M). The calculation process is shown in Figure 8.20. The moment-curvature determination process consisted of incrementally increasing the curvature in the cross-section and calculating the corresponding bending moment.

The constitutive relationship proposed by Blakeley and Park (1973) for concrete was adopted in the calculation process. The tensile strength of concrete was ignored. Linear and bi-linear with strain-hardening stress-strain relationship was used for GFRP and steel, respectively. Yield stress, elastic modulus and plastic modulus of the steel plates were selected as 375 MPa, 200 GPa and 2 GPa, respectively.

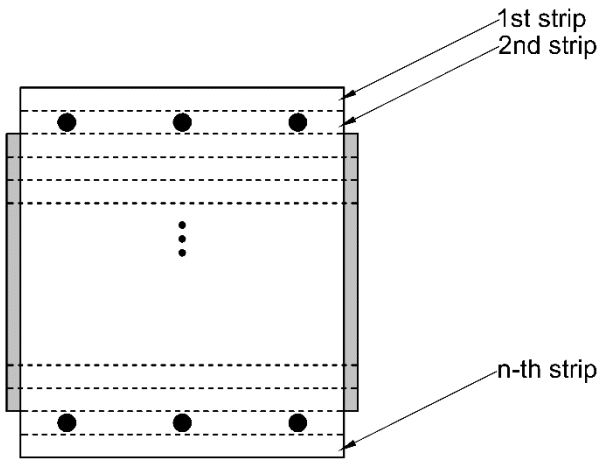

Figure 8.19 - Layered cross-section of beam in Specimen G-M

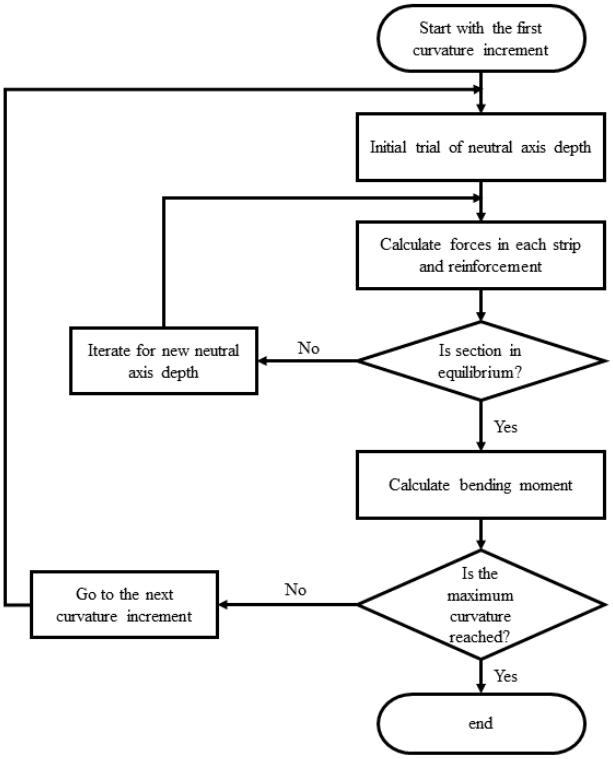

Figure 8.20 - Moment-curvature determination process

The process of calculating bending moments corresponding to a specific curvature started by assuming a neutral axis depth and calculating strains in each cross-sectional strip (in concrete and

steel plates) and longitudinal reinforcement accordingly. Based on the calculated strain and the stress-strain relationship adopted for each material, stress in each strip of concrete, steel plates and longitudinal bars was calculated. The cross-sectional forces then were checked for equilibrium. The assumed neutral axis depth was adjusted accordingly, and the process was repeated until equilibrium was reached. The process then was repeated for the next increment of cross-sectional curvature until full moment-curvature graph was determined.

Figure 8.21 shows the moment-curvature graph determined for the test specimens. As shown in Figure 8.18-b, the maximum strain recorded in the longitudinal reinforcement of the beam in Specimen G-M, during the first loading phase (4% drift ratio) was 8,450 micro-strain. According to the calculations conducted in moment-curvature determination process, the bending moment corresponding to 8,450 micro strain in the reinforcement is 297 kN.m, which is very close to the maximum bending moment observed in the first loading phase (310 kN.m). Therefore, it can be concluded that the theoretical moment-curvature determination process can accurately predict the behaviour of GFRP-RC beams with steel plates up to drift ratios as high as 4%. It worth repeating that drift ratios higher than 4% are considered beyond the response range of normal buildings.

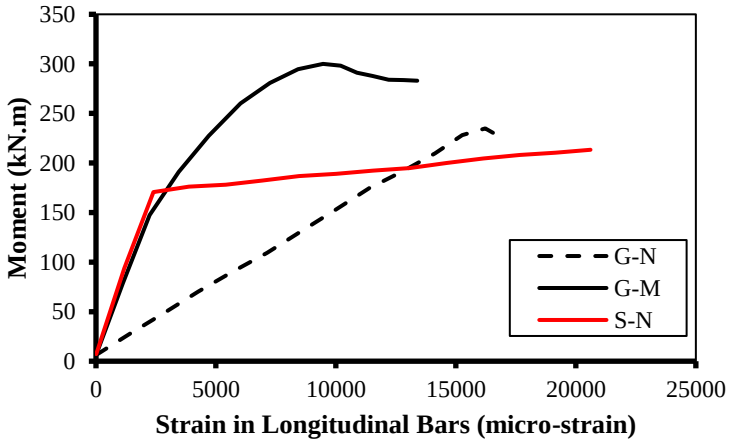

Figure 8.21 - Moment-curvature relationships of specimens

8.6 Conclusions

According to the results obtained from the test specimens and the analytical study, the following conclusions can be made:

- The proposed combination of steel plates and concrete beams improved the seismic performance of the tested GFRP-RC beam by increasing its initial stiffness and cumulative energy dissipation. The steel plates increased the energy dissipation of the GFRP-RC beam by 160% at 2.5% drift ratio (the maximum allowable drift ratio by *NRCC* 2015). Moreover, the plates increased the initial stiffness of the GFRP-RC beam to be similar to that of the steel-RC counterpart with the same moment capacity. In addition, at 4% drift ratio, the magnitude of concrete damage in the GFRP-RC beam with steel plates was lower than its counterpart without steel plates.

- Replacing damaged steel plates with new ones could restore the initial properties of the beam; however, special care must be taken in filling the gaps between the bolts embedded in the concrete and the plates.

- Attaching steel side plates to GFRP-RC beams results in increase in shear stress exerted to beam-column joints due to increase in bending moment capacity. This should be taken into account in designing moment-resisting buildings to prevent shear failure of beam-column joints during extreme lateral loading.

- The contribution of steel side plates to the bending resistance of the GFRP-RC beam resulted in reduction of tensile strains in the longitudinal GFRP bars. The level of strains in the longitudinal bars can be interpreted as an indicator of crack widths (damage) in the concrete beams. Therefore, it is concluded that attachment of side plates improves the

performance of base GFRP-RC elements by reducing the magnitude of damage during a seismic event.

- The moment-curvature determination process adopted in the analytical study accurately predicted the bending moment capacity of the GFRP-RC beam with steel plates (G-M). It can be concluded that this process can be used to calculate the maximum bending moment capacity of proposed structures up to drift ratios as high as 4%.

9 SUMMARY, CONCLUSIONS AND RECOMMENDATIONS

9.1 Summary

This research program aimed to provide comprehensive experimental and analytical studies to improve the understanding of the seismic behaviour of GFRP-RC framed structures. An extensive experimental program was conducted by constructing and testing 12 full-scale RC beam-column connections under reversed-cyclic loads. The experimental studies were accompanied with a comprehensive analytical program to further investigate the influencing parameters on the seismic performance of GFRP-RC structures and to simulate their response under dynamic loads.

The seismic performance of GFRP-RC interior beam-column connections has been studied experimentally by testing four full-scale beam-column subassemblies. The main test parameters were type of reinforcement (GFRP and steel) and the magnitude of joint shear stress. The GFRP-RC specimens were tested under multiple reversal loading protocols to investigate the effect of concrete damage on their performance at service and ultimate states.

Moreover, a full-scale exterior beam-column joint was constructed and tested to investigate the effect of joint geometry (interior and exterior) on the performance of GFRP-RC beam-columns. In addition, a modified damage index was proposed to quantify the magnitude of damage in GFRP-RC beam-column joints under dynamic loadings. Additionally, the results obtained from this program were compared with a study previously conducted by the authors on the seismic performance of GFRP-RC exterior beam-columns to complement the previous findings about the joint shear capacity of GFRP-RC exterior joints.

A comprehensive analytical study was carried out using a specialized FEM program, ATENA 3D (Cervenka et al. 2012), by taking into account the nonlinear behaviour of concrete, effect of cracks, bond-slip relationship of reinforcement and concrete confinement. The behaviour of exterior beam-column joints was simulated and the effect of various parameters such as joint shear stress, size of lateral beams, reinforcement material, column axial load and geometrical configuration was studied.

Two full-scale interior beam-column-slab connections, one fully reinforced with GFRP bars and stirrups, and one fully reinforced with steel, were tested. The contribution of the slab in the lateral load capacity of GFRP-RC specimen and its effect on energy dissipation and mode of failure of the subassembly was investigated and compared to the control steel-RC specimen. Also, a nonlinear FEM was constructed to further investigate the effect of slab width and lateral beam size on the contribution of slabs to the moment capacity of beams.

Moreover, the seismic performance of exterior beam-column-slab connections fully reinforced with GFRP reinforcement has been investigated. Two full-scale GFRP-RC exterior beam-column-slab connections were constructed and tested under reversed-cyclic loads to study the effect of cast-in situ slabs on energy dissipation, ultimate capacity and stiffness of the connections with and without lateral beams. An effective slab width was calculated. Furthermore, a nonlinear FEM was used to investigate the effect of lateral beam size and slab thickness on the performance of the connections.

One of the main objectives of this research program was to explore a solution to improve the seismic performance of GFRP-RC structures. Attaching bolted steel side-plates to GFRP-RC beams was proposed as an effective approach to improve the energy dissipation feature of GFRP-

RC elements and to increase their initial stiffness. The effectiveness of the proposed method was evaluated experimentally through testing of three full-scale cantilever beams. A computer simulation using the commercial software MATLAB, was conducted to calculate the bending moment capacity of GFRP-RC beams with steel side-plates through moment-curvature determination process.

9.2 Conclusions

Based on the results obtained from the experimental and analytical studies conducted in this program, the following conclusion are drawn:

9.2.1 Seismic performance of GFRP-RC interior beam-column joints

- All tested specimens were able to achieve their design capacity. This indicates that interior GFRP-RC beam-column joints with lateral beams covering 60% of the joint area are able to withstand the maximum joint shear stress ratio considered in this program, $1.8\sqrt{f'_c}$.
- All specimens exhibited a gradual failure without any sign of reinforcement rupture. The lateral load carrying capacity gradually decrease and ultimately the test was stopped at 7% or 8% drift ratio. This indicates that GFRP-RC beam-column joint can be designed in a manner that allows them to reach significantly high lateral drift ratios without exhibiting brittle failure.
- The maximum strain measured in the joint stirrups remained lower than the limit suggested by the CSA/S806-12 (CSA 2012) up to 5% drift. This observation along with insignificant concrete damage in the joint area up to 5% drift ratio indicated that the requirements of the CSA/S806-12 (CSA 2012) for confinement of columns in seismic regions are adequate.

- Including the effect of secondary moments due to P-delta effect resulted in reaching the design capacity of the columns prior to design capacity of the beams. This behaviour does not agree with the strong-column-weak-beam concept suggested by CSA/S806-12 (CSA 2012). Therefore, a value of 1.2 for the minimum column-to-beam flexural strength ratio is suggested.
- The linear nature of GFRP reinforcement resulted in lower energy dissipation of the GFRP-RC test specimen compared to its steel-RC counterpart with the same magnitude of joint shear stress. The steel-RC specimen showed 1.44- and 3.06-times higher energy dissipation than a GFRP-RC specimen with an identical joint shear stress at 2% and 5% drift ratio, respectively. Moreover, test results indicated that the increase in the joint shear stress increases the magnitude of energy dissipation in GFRP-RC beam-column joints.
- Investigating the tri-relationship between joint shear stress ratio, longitudinal reinforcement ratio and concrete compressive strength in the joints indicated that the joint shear stress ratio in GFRP-RC beam-column joints are less sensitive to the reinforcement ratio and concrete compressive strength compared to their steel-RC counterparts.

9.2.2 Effect of joint geometry on the performance of GFRP-RC beam-column joints

- The GFRP-RC exterior beam-column joint with joint shear stress of $1.3\sqrt{f'_c}$ was able to reach its maximum design capacity. Therefore, it is concluded that exterior GFRP-RC beam-column joints with lateral beams can withstand joint shear stress ratios of 1.3.

- Both interior and exterior GFRP-RC specimens with joint shear stress of $1.3\sqrt{f'_c}$ were able to reach their design capacity during the first loading phase (up to 5% drift ratio) without exhibiting significant concrete damage. Therefore, it is concluded that GFRP-

RC moment-resisting frames can withstand significant lateral deformations and still maintain their original condition up to an acceptable level. This characteristic can significantly reduce the repair costs of moment-resisting frames after an earthquake event.

- At failure, significant damage was observed in the joint area of the exterior specimen, while the concrete damage in the interior specimen was concentrated in the beam area in the vicinity of the joint. This was attributed to the better confinement provided to the joint area in the interior specimen by the main beams which increased the shear capacity of the joint.

- The confinement provided by the longitudinal reinforcement in the main beams to the concrete core, can significantly improve the performance of beam-column assemblies by limiting the magnitude of damage in the main beam.

- Test results showed that the longitudinal reinforcement ratio of the main beams had a significant effect on the maximum strain observed in the longitudinal bars during an earthquake. This should be taken into account to prevent rupture of the longitudinal bars by providing sufficient margin between the maximum expected strain in the bars and their tensile strain capacity.

- Measured cumulative energy dissipation of the test specimens indicated that interior beam-column joints dissipate more energy than their exterior beam-column counterparts with equal magnitude of joint shear stress. This is attributed to the fact that, compared to exterior ones, interior beam-column joints have more concrete which increases the

area of damage concrete (cracked or crushed) that represents the main source of energy dissipation in GFRP-RC beam-column joints.

- Investigating the performance of the test specimens under service loading condition indicated that the reinforcement ratio of the main beams have significant effect on the performance of the specimens in terms of deformations under service loads. Higher reinforcement ratios resulted in less deformation increase under service loads after undertaking seismic loading cycles.

9.2.3 Analytical study on the seismic behaviour of GFRP-RC exterior beam-column joints

- Although the GFRP-RC exterior beam-column joint with joint shear stress of $1.1\sqrt{f'_c}$ was able to reach its design capacity without any significant damage in the joint area, increasing the joint shear stress to $1.4\sqrt{f'_c}$ in the same joint resulted in premature failure of the specimen (prior to 5% drift ratio) due to excessive damage induced to the joint.
- Increasing the size of lateral beams improves the seismic performance of GFRP-RC beam-column joints by providing more confinement to the joint area. Moreover, increasing the size of lateral beams decreases the shear stress demand of the joint stirrups.
- Column axial load significantly influences the seismic performance of GFRP-RC beam-column joints. Increasing the column axial load degrades the performance of the joints due to premature concrete crushing.
- Although CFRP reinforcement provides superior performance over GFRP reinforcement in terms of crack width and deflection, they lack deformable behaviour in seismic design. The modeled CFRP-RC beam-column joint exhibited a brittle failure at 4% drift ratio,

while its GFRP-RC counterpart (with the same beam moment capacity) successfully reached 5% lateral drift ratio.

- The effect of lateral beams on seismic performance of GFRP-RC beam-column joints is related to the level of joint shear stress. In beam-column joints with low joint shear stress additional confinement provided by lateral beams did not play a significant role in improving the shear capacity of the joint. However, in the joints with higher joint shear stress the confinement provided by lateral beams significantly improved the seismic performance.

9.2.4 Seismic performance of GFRP-RC interior beam-column-slab subassemblies

- Based on the stress distribution among longitudinal bars in the slab of the GFRP-RC beam-column, an effective overhang equal to 1.2 times the effective depth of the main beam on each side of the beam was calculated. The effective slab width in the GFRP-RC specimen was less than that of its counterpart steel-RC specimen with measured effective overhang of two times the effective beam depth. This was attributed to the lower stiffness of GFRP-RC slabs in the transverse direction compared to that of the steel-RC ones.
- Although the presence of floor slabs in the GFRP-RC interior beam-column connection increased the negative bending moment capacity of the main beams (slab-in-tension), it was observed that the contribution of the slab while in compression (positive moments) was insignificant. In contrary, significant contribution of the floor slab to both positive and negative bending moment capacity of the main beams in the steel-RC beam-column connection was observed.

- The presence of slabs in the GFRP-RC specimen slightly increased the magnitude of energy dissipation. The GFRP-RC beam-column-slab dissipated 15.5% and 8.7% more cumulative energy than its counter part GFRP-RC beam-column specimen (without slabs) at 3.0% and 5.0% lateral drift ratios, respectively.
- The GFRP-RC beam-column-slab specimen exhibited 47% higher lateral stiffness compared to its GFRP-RC counterpart specimen without slab during the first lateral drift ratio loading (0.8%). This indicates that integral behaviour of slabs and beams in a GFRP-RC moment-resisting frame can reduce its lateral deformation during earthquakes. The increase in the lateral stiffness due to presence of slabs; however, becomes less significant as the frame undergoes larger deformations. Similar behaviour as observed for the steel-RC Specimens.
- Analytical modeling of the test specimens with various slab widths indicated that widening the slab to 3,290 mm (slab width-to-beam depth ratio of 7.3) and 4,090 mm (slab width-to-beam depth ratio of 9.1) in the GFRP-RC and steel-RC beam-column-slab subassemblies, respectively, resulted in 30% and 60% increase in the effective slab width. Further widening of the slabs beyond these points; however, did not provide significant increase in the contribution of slabs.
- Increasing the cross-sectional area of the lateral beams resulted in improving the slab contribution to the negative bending moment capacity of the main beams due to the improvement of the slab bars contribution. A beam-column-slab connection with lateral beams covering 100% of the joint area showed up to 80% wider effective slab width compared to a beam-column-slab connection with no lateral beams.

9.2.5 Seismic performance of GFRP-RC exterior beam-column-slab subassemblies

- The presence of slabs did not show any significant increase in the bending moment capacity of the main beams when in compression. The contribution of slab in the negative bending moment capacity of the beams (slab-in-tension), on the other hand, was noticeable. The FRP-RC MRFs could benefit from the lack of slab contribution in compression, as it prevents the possibility of changing the mode of failure from the desirable compression-failure to the undesirable tension-failure one.
- The presence of lateral beams significantly increased the width of effective slab, in tension. A 70% increase in the overhang width from 0.85*d* in the GFRP-RC beam-column-slab specimen with lateral beams to 0.5*d* in the GFRP-RC beam-column-slab without lateral beams was observed.
- Both GFRP-RC beam-column-slab specimens (one with and one without lateral beams) failed due to rupture of longitudinal bars in the main beam. Failure occurred during the second loading phase at 6% and 7% drift ratio in the specimen without and with lateral beams, respectively. During the first loading phase (up to 5% drift ratio); however, both specimens showed stable behaviour with minor sings of concrete crushing in the main beam cover at the higher drift ratios (4 and 5%).
- The presence of slabs significantly increased energy dissipation of beam-column connections. Specimens BCS-L (GFRP-RC beam-column-slab with lateral beams) and BCS-X (GFRP-RC beam-column-slab without lateral beams) showed 49% and 122% higher cumulative energy dissipation compared to their corresponding specimens without slabs at 5% drift ratio. The increase in energy dissipation was even higher at the lower drift ratio limit of 3% (89% and 145%, respectively).

- Comparing the lateral stiffness of the test specimens at the beginning and end of the first loading phase indicated approximately 60% reduction in the stiffness of the specimens. To reduce the loss of lateral stiffness in GFRP-RC MRFs, it is suggested to limit the allowable lateral drift ratio of the frames to lower drift ratios.
- Increasing the cross-sectional area of lateral beams improved the contribution of slabs to the negative moment capacity of the beams (slab-in-tension). The FEM of the beam-column-slab assembly with lateral beams covering the entire area of the joint exhibited 100% increase in the effective overhang width compared to the corresponding FEM without lateral beams.
- Cracks parallel to the main beam at the beam-slab interface was observed in both experimental tests and analytical models. The development of such cracks reduced the composite action of beam and slabs and prevented the contribution of slabs to positive moments (slab-in-compression).

9.2.6 Seismic performance improvement of GFRP-RC frames

- The proposed combination of steel plates and concrete beams improved the seismic performance of the tested GFRP-RC beam by increasing its initial stiffness and cumulative energy dissipation. The steel plates increased the energy dissipation of the GFRP-RC beam by 160% at 2.5% drift ratio (the maximum allowable drift ratio by NRCC 2015). Moreover, the plates increased the initial stiffness of the GFRP-RC beam to be similar to that of the steel-RC counterpart with the same moment capacity. In addition, at 4% drift ratio, the magnitude of concrete damage in the GFRP-RC beam with steel plates was lower than its counterpart without steel plates.

- Replacing damaged steel plates with new ones could restore the initial properties of the beam; however, special care must be taken in filling the gaps between the bolts embedded in the concrete and the plates.

- Attaching steel side plates to GFRP-RC beams results in increase in shear stress exerted to beam-column joints due to increase in bending moment capacity. This should be taken into account in designing moment-resisting buildings to prevent shear failure of beam-column joints during extreme lateral loading.

- The contribution of steel side plates to the bending resistance of the GFRP-RC beam resulted in reduction of tensile strains in the longitudinal GFRP bars. The level of strains in the longitudinal bars can be interpreted as an indicator of crack widths (damage) in the concrete beams. Therefore, it is concluded that attachment of side plates improves the performance of base GFRP-RC elements by reducing the magnitude of damage during a seismic event.

- The moment-curvature determination process adopted in the analytical study accurately predicted the bending moment capacity of the GFRP-RC beam with steel side plates. It can be concluded that this process can be used to calculate the maximum bending moment capacity of proposed structures up to drift ratios as high as 4%.

9.3 Recommendations for Future Work

Based on the results obtained from the presented experimental and analytical investigations, the followings are recommended for future work:

- One of the main objectives of this program was to introduce a design philosophy that takes advantage of the linear nature of GFRP-RC elements to maintain the serviceability of GFRP-RC structures after withstanding a severe lateral loading. The two-phase loading method proposed in this program along with the proposed modified damage index could be used as a baseline to further investigate this design philosophy. More in-depth studies on the effect of concrete damage on the performance of GFRP-RC frames by taking into account the magnitude of damage, reinforcement detailing, and concrete properties could shed more light on this path.
- The experimental and analytical studies of this program indicated that the interaction between structural elements such as slabs and beams can significantly affect the performance of structures. Despite the comprehensive testing procedure and complexity of the test specimens and laboratory apparatuses, some simplifying assumptions in the structural behaviour of the test elements was inevitable. To gain a more comprehensive understanding of the seismic behaviour of GFRP-RC moment frames as an integral system, performing dynamic testes on scaled multi-story and multi-bay GFRP-RC moment frames could be of significant value.
- Through out this research program, some of the seismic design methods suggested by the Canadian code for design of FRP-RC structures (CSA 2012) has been used in the design of the test specimens with the primary goal of evaluating its sufficiency. However, studies on the efficiency of code provisions remains necessary. More investigations on the reinforcement detailing such as stirrup spacing in the beams and columns are recommended.

- This program was designed as a pilot study to investigate the feasibility of using steel side-plates to improve the seismic performance of GFRP-RC moment-resisting frames. Further investigations are required to study the effectiveness of the proposed method in more realistic simulation of the behaviour of moment-resisting frames under seismic loading. The effect of important parameters such as rotation of columns and anchorage method of steel plates in the joint area must be addressed.

REFERENCES

ACI Committee 318 (2008). "Building Code Requirements for Structural Concrete and Commentary" ACI 318-08, American Concrete Institute, Farmington Hills, Detroit, MI, 471p.

ACI-ASCE Committee 352 (2002). "Recommendation for Design of Beam-Column Connections in Monolithic Reinforced Concrete Structures." ACI 352-02, American Concrete Institute, Farmington Hills, Detroit, MI, 37p.

ACI Committee 374. (2005). "Acceptance Criteria for Moment Frames Based on Structural Testing and Commentary." ACI 374.1-05, American Concrete Institute, Farmington Hills, MI, 88p.

ACI Committee 440. (2015). "Guide for Design and Construction of Concrete Reinforced with FRP Bars," ACI 440.1R-15, American Concrete Institute, Farmington Hills, MI, 88p.

Aiello, M.A., and Ombres, L. (2002). "Structural performances of concrete beams with hybrid (fiber-reinforced polymer-steel) reinforcements." Journal of Composite for Construction, 6(2):133-140.

Al-Dulaijan, S. U., Nanni, A., Al-Zaheani, M. M. and Bakis, C. E. (1996). "Bond Evaluation of Environmentally Conditioned GFRP/Concrete System." Proceedings of the Second International Conference on Advanced Composite Materials in Bridges and Structures (ACMBS-2), Canadian Society for Civil Engineering, Montreal, QC, Canada, pp. 845-852.

Alsayed, S., Al-Salloum, Y., Qlmusallam, T. and Amjad, M. (1999). "Concrete Columns Reinforced by Glass Fibre Reinforced Polymer Rods." ACI special publication, SP-188: 103-112.

Ammerman, O. V. and French, C. W. (1989). "R/C Beam-Column-Slab Sub-assemblages Subjected to Lateral Loads." Journal of Structural Engineering, ASCE, 115(6): 1289-1308.

Bakis, C. E., Freimanis, A. J., Gremel, D. and Nanni, A. (1998). "Effect of Resin Material on Bond and Tensile Properties of Unconditioned and Conditioned FRP Reinforcement Rods." Proceedings of the First International Conference on Durability of Composites for Construction, Sherbrooke, QC, Canada, pp. 525-535.

Bank, L. C., Puterman, M. and Katz, A. (1998). "The Effect of Material Degradation on Bond Properties of FRP Reinforcing Bars in Concrete." ACI Material Journal, 93(3): 232-243.

Benmokrane, B., Tighiouart, B. and Chaallal, O. (1996). "Bond Strength and Load Distribution of Composite GFRP Reinforcing Bars in Concrete." ACI Material Journal, 93(3): 246-252.

Blakeley, R. and Park, R. (1973). "Prestressed Concrete Sections with Cyclic Flexure." ASCE Journal of Structural Division, 99(ST8): 1717-1742.

Bonacci, J. and Pantazopoulou, S. (1993). "Parametric Investigation of Joint Mechanics." ACI Structural Journal, 90(1): 61-71.

Brown, V. and Bartholomew, C. (1993). "FRP Reinforcing Bars in Reinforced Concrete Members." ACI Materials Journal, 90(1): 34-39.

Choo, C. C., Harik, I. E. and Gensund, H. (2006). "Strength of Rectangular Concrete Columns Reinforced with Fiber-Reinforced Polymer Bars." ACI Structural Journal, 103(3): 452-459.

Cervenka, V., Jendele, L. and Cervenka, J. (2012). "ATENA Program Documentation Part 1: Theory." Cervenka Consulting Ltd., Prague, Czech Republic.

Cosenza, E., Manfredi, G. and Realfonzo, R. (1997). "Behavior and Modeling of Bond of FRP Rebars to Concrete." ASCE Journal of Composite for Construction, 1(2): 40-51.

CSA. (2012). "Design and Construction of Building Structures with Fibre Reinforced Polymers." CAN/CSA-S806-12, Canadian Standards Association, Toronto, ON, Canada, 206 p.

CSA. (2014-a). "Design of Concrete Structures." CAN/CSA A23.3, Canadian Standard Association, ON, Canada, 297 p.

CSA. (2014-b). "Canadian Highway Bridge Design Code." CAN/CSA-S6-14, Canadian Standards Association, ON, Canada, 894 p.

Debaiky, A.S., Nkurunziza, G., Benmokrane, B. and Cousins, P. (2006). "Residual Tensile Properties of GFRP Reinforcing Bars after Loading in Severe Environments." ASCE Journal of Composites for Construction, 10(5): 1-11.

Duggal, S. (2013). "Earthquake Resistant Design of Structures (2nd Edition)." Oxford University Press, 528 p.

Dulude, C., Hassan, M., Ahmed, E. A. and Benmokrane, B. (2013). "Punching Shear Behavior of Flat Slabs Reinforced with Glass Fiber-Reinforced Polymer Bars." ACI Structural Journal, 110(5): 723-734.

Durrani, A. J. and Zerbe, H. E. (1987). "Seismic Resistance of R/C Exterior Connections with Floor Slabs." Journal of Structural Engineering, ASCE, 113(8): 1850-1864.

Ehsani, M.R. and Wight, J.K. (1985-a). "Effect of Transverse Beams and Slabs on Behaviour of Reinforced Concrete Beam-to-Column Connections." ACI Journal Proceedings, 82(4): 188-195.

Ehsani, M. and Wight, J. (1985-b). "Exterior Reinforced Concrete Beam-to-Column Connections Subjected to Earthquake." ACI Journal Proceedings, 82(4): 492-499.

El-Gendy, M.G. and El-Salakawy, E. (2016). "Effect of Shear Studs and High Moments on Punching Behavior of GFRP-RC Slab-Column Edge Connections." Journal of Composites for Construction, 20(4), doi: 10.1061/(ASCE)CC.1943-5614.0000668.

El-Sayed, A., El-Salakawy, E. and Benmokrane, B. (2007). "Mechanical and Structural Characterization of New Carbon FRP Stirrups for Concrete Members." Journal of Composites for Construction, ASCE, 11(4): 352-362.

Foley, C.M. and Buckhouse, E.R. (1999). "Method to Increase Capacity and Stiffness of Reinforced Concrete Beams." Practice Periodical on Structural Design and Construction, 4(1), doi:10.1061/(ASCE)1084-0680(1999)4:1(36).

French, C. W. and Boroojerdi, A. (1989). "Contribution of R/C Floor Slabs in Resisting Lateral Loads." Journal of Structural Engineering, ASCE, 115(1): 1-18.

Fukuyama, H., Masuda, Y., Sonobe, Y. and Tanigaki, M. (1995). "Structural performances of concrete frame reinforced with FRP reinforcement." Non-Metallic (FRP) Reinforcement for Concrete Structures, Proc., 2nd Int. RILEM Symp. (FRPRCS-2), E & FN Spon, London, 275-286.

Ghomi, S.K. and El-Salakawy, E. (2016). "Seismic Performance of GFRP-RC Exterior Beam-Column Joints with Lateral Beams." Journal of Composites for Construction, 20(1), doi:10.1061/(ASCE)CC.1943-5614.0000582.

Ghomi, S.K. and El-Salakawy, E. (2018-a). "Seismic Behaviour of Exterior GFRP-RC Beam-Column Connections: Analytical Study." Journal of Composites for Construction, 22(4), doi:10.1061/(ASCE)CC.1943-5614.0000858.

Ghomi, S. K. and El-Salakawy, E. (2018-b) "Seismic Performance of Interior GFRP-RC Beam-Column Joints." ACI Special Publication, SP-327: 10.1-10.18.

Hakuto, S., Park, R. and Tanaka, H. (2000) "Seismic Load Tests on Interior and Exterior Beam-Column Joints with Substandard Reinforcing Details." ACI Structural Journal, 97(1): 11-25.

Hanson, N. and Conner, H. (1967). "Seismic Resistance of Reinforced Concrete Beam-Column Joints." Journal of the Structural Division, Proceeding of the ASCE, 93(ST5): 533-560.

Hasaballa, M., El-Ragaby, A. and El-Salakawy, E. (2011). "Seismic Performance of Exterior Beam-Column Joints Reinforced with Glass Fibre Reinforced Polymer Bars and Stirrups." Canadian Journal of Civil Engineering, 38(10): 1092-1102.

Hasaballa, M. and El-Salakawy, E. (2016). "Shear Capacity of Type-2 Exterior Beam-Column Joints Reinforced with GFRP Bars and Stirrups." Journal of Composites for Construction, 20(2), doi:10.1061/(ASCE)CC.1943-5614.0000609.

Hassan, M., Ahmed E. A. and Benmokrane, B. (2015). "Punching Shear Behavior of Two-Way Slabs Reinforced with FRP Shear Reinforcement." Journal of Composites for Construction, 19(1), doi: 10.1061/(ASCE)CC.1943-5614.0000493.

Hassan, M., Fam, A., Benmokrane, B and Ferrier, E. (2017). "Effect of Column Size and Reinforcement Ratio on Shear Strength of Glass Fiber-Reinforced Polymer Reinforced Concrete Two-Way Slabs." ACI Structural Journal, 114(4): 937-950.

Ibrahim, A.M.A., Fahmy, A.F. and Wu, Z. (2016). "3D finite element modeling of bond-controlled behavior of steel and basalt FRP-reinforced concrete square bridge columns under lateral loading." Composite Structures, 143: 33-52.

ISIS Canada. (2007). "Reinforcing Concrete Structures with Fibre Reinforced Polymers." Design Manual No.3., ISIS Canada Corporation, University of Manitoba, Winnipeg, MB, Canada, 103 p.

Kara, I.F., Ashour, M.F.M. and Körog˘lu, M.A. (2015). "Flexural Behavior of Hybrid FRP/Steel Reinforced Concrete Beams." Composite Structures, 129: 111-121.

Kim, J. and LaFave, J. (2007). "Key Influence Parameters for The Joint Shear Behaviour of Reinforced Concrete (RC) Beam-Column Connections." Engineering Structures. 29(10): 2523-2539.

Le-Trung, K., Lee, K., Shin, M. and Lee, J. (2013). "Seismic Performance Evaluation of RC Beam-Column Connections in Special and Intermediate Moment Frames." Journal of Earthquake Engineering, 17(2): 187-208.

Lo, S.H., Li, L. and Su, R.K.L. (2014). "Optimization of partial interaction in bolted side-plated reinforced concrete beams." Computers and Structures, 131: 70-80.

Mady, M., El-Ragaby, A. and El-Salakawy, E. (2011), "Seismic Behavior of Beam-Column Joints Reinforced with GFRP Bars and Stirrups." ASCE Journal of Composite Construction, 15(6): 875-886.

Mallick, P.K. (1988). "Fiber Reinforced Composites, Materials, Manufacturing, and Design." Marcell Dekker Inc., New York, 496p.

Malvar, L. J. and Cochran, K. B. (2003). "Bond between Carbon Fiber Reinforced Polymer Bars and Concrete: Experimental Study." Journal of Composites for Construction, 7(2): 154-163.

Mander, J. B., Priestley, M. J. N. and Park, R. (1988). "Theoretical Stress-Strain Model for Confined Concrete." Journal of Structural Engineering, 114(8): 1804-1826.

Maranan, G. A., Manalo, A. and Benmokrane, B. (2017). "Effect of Axial Load Ratio in the Seismic Behavior of GFRP-Reinforce Shear Wall." Proceedings of the 5th International Conference on Durability and Sustainability of Fibre Reinforced Polymer (FRP) Composites for Construction and Rehabilitation of Structures (CDCC-2017), Sherbrooke, Quebec, Canada, July 19-21, 8 p.

Mohammed, M. G., Farghaly, A. and Benmokrane, B. (2015). "Simulated Seismic Behavior of GFRP-Reinforced Concrete Columns." Proceedings of the 11th Canadian Conference on Earthquake Engineering (CCEE-11), Victoria, Canada, July 21-24, 10p.

Nanni, A. and Nenninger, J. (1997). "Experimental Bond Behavior of Hybrid Rods for Concrete Reinforcement." Structural Engineering and Mechanics, 5(4): 339-335.

Naqvi, S. and El-Salakawy, E. (2017). "Lap Splice in GFRP-RC Rectangular Columns Subjected to Cyclic-Reversed Loads." Journal of Composites for Construction, 21(4), doi:10.1061/(ASCE)CC.1943-5614.0000777.

Ning, N., Qu, W. and Zhu, P. (2014). "Role of Cast-in Situ Slabs in RC Frames under Low Frequency Cyclic Load." Engineering Structures, 36(1): 28-38.

NRCC. (2015). "National Building Code of Canada." National Research Council of Canada, Ottawa, ON, Canada, 1404 p.

Oehlers, D.J., Nquyen, N.T., Ahmed, M. and Bradford, M.A. (1977). "Transverse and Longitudinal Partial Interaction in Composite Bolted Side-Plated Reinforced-Concrete Beams." Structural Engineering and Mechanics, 5(5): 553-563.

Ospina, C. E. and Alexander, S. D. B. (1998). "Transmission of Interior Concrete Column Loads Through Floors." Journal of Structural Engineering, 124(6): 602-610.

Pantazopoulou, S.J., Moehle, J.P. and Shahrooz, B.M. (1988). "Simple Analytical Model for T-Beams in Flexure." Journal of Structural Engineering, 114(7): 1507-1523.

Pantazopoulou, S. J. and French, C. W. (2001). "Slab Participation in Practical Earthquake Design of Reinforced Concrete Frames." ACI Structural Journal, 98(4): 479-489.

Paramanatham, N. (1993). "Investigation of the Behaviour of Concrete Columns Reinforced with Fiber Reinforced Plastic Rebars." Master of Science thesis, Lamar University, Beaumont, Texas, 75 p.

Park, R. and Ang, A.H.S. (1985). "Reinforced Concrete Beam-Column Joints under Seismic Actions." ACI Journal Proceedings, 75(11): 585-593.

Paulay, T., Park, R. and Priestley, M.J. (1978). "Reinforced Concrete Beam-Column Joints under Seismic Actions." ACI Journal Proceedings, 75(11): 585-593.

Paulay, T. and Park, R. (1984). "Joints in reinforced concrete frames designed for earthquake resistance." University of Canterbury, Christchurch, New Zeeland, 71p.

Porter, M. L. and Barnes. B. A. (1998). "Accelerated Aging Degradation of Glass Fiber Composites." Second International Conference on Composites in Infrastructure, Tucson, AZ: 446-459.

Pultrall Inc. (2019). GFRP Specification Guide, Available at http://www.vrodcanada.com/product-data/gfrp-specification-guide, visited on May 17.

Qi, X. and Pantazopoulou, S. J. (1991). "Response of RC Frames under Lateral Loads." Journal of Structural Engineering, 117(4): 1167-1188.

Qin, R., Zhou, A. and Lau, D. (2017). "Effect of reinforcement ratio on the flexural performance of hybrid FRP reinforced concrete beams." Composites Part B, 108: 200-209.

Robert, M., Cousin, P. and Benmokrane, B., (2009). "Durability of GFRP Reinforcing Bars Embedded in Moist Concrete." Journal of Composite for Construction, 13(2): 66-73.

Saatcioglu, M. and Razvi, R. (1992). "Strength and Ductility of Confined Concrete." Journal of Structural Engineering, 118(6):1590-1607.

Said, A. M. and Nehdi, M. L. (2004), "Use of FRP for RC Frames in Seismic Zones: Part II. Performance of Steel-Free GFRP-Reinforced Beam-Column Joints." Applied Composite Materials, V.11: 227-245.

Schoeck Canada Inc. (21019). technical information sheet, Available at https://www.schoeck.com/en/download/eyJjYXRlZ29yeSI6eyI3Ijo3fX0, visited on May 17.

Shahrooz, B. M. and Pantazopoulou, S. J. (1992). "Modeling Slab Contribution in Frame Modeling." Journal of Structural Engineering, 118(9): 2475-2495.

Sharbatdar, M. (2003). "Concrete columns and beams reinforced with FRP bars and grids under monotonic and reversed cyclic loading." Ph.D. Thesis, Univ. of Ottawa, Ottawa, ON, Canada.

Sharbatdar, M. K. and Saatcioglu, M. (2009). "Seismic Design of FRP Reinforced Concrete Structures." Asian Journal of Applied Sciences, 2(3): 211-222.

Sharbatdar, M. K., Saatcioglu, M. and Benmokrane, B. (2011). "Seismic Flexural Behavior of Concrete Connections Reinforced with CFRP Bars and Grids." Composite Structures, 93(10): 2439-2449.

Shehata, E., Morphy, R. and Rizkalla, S. (2000). "Fibre Reinforced Polymer Shear Reinforcement for Concrete Members: Behaviour and Design Guideline." Canadian Journal of Civil Engineering, 27(5): 859-872.

Soric, Z., Kisicek, T. and Galic, J. (2002). "Deflections of Concrete Beams Reinforced with FRP Bars." ACI Structural Journal, 99(3): 308-316.

Su, R.K.L., Li, L.Z. and Lo, S.H. (2014). "Longitudinal Partial Interaction in Bolted Side-Plated Reinforced Concrete Beams." Advances in Structural Engineering, 17(7): 921-936.

Su, R.K.L., Siu, W.H. and Smith, S. T. (2010). "Effects of bolt-plate arrangements on steel plate strengthened reinforced concrete beams." Engineering Structures, 32(6): 1769-1778.

Subedi, N. K. and Baglin, P.S. (1998). "External Plate Reinforcement for Concrete Beams." Journal of Structural Engineering, 124(12), doi: 10.1061/(ASCE)0733-9445(1998)124:12(1490).

Tavassoli, A., Liu, J. and Sheikh, S. (2015). "Glass fiber-reinforced polymer-reinforced circular columns under simulated seismic loads." ACI Structural Journal, 112(1): 103-114.

Tekle, B. H., Khennane, A. and Kayali, O. (2016). "Bond Properties of Sand-Coated GFRP Bars with Fly Ash-Based Geopolymer Concrete." Journal of Composites for Construction, 20(4), doi: 10.1061/(ASCE)CC.1943-5614.0000685.

Tobbi, H., Farghaly, A.S. and Benmokraine, B. (2012). "Concrete Columns Reinforced Longitudinally and Transversally with Glass Fibre-Reinforced Polymer Bars." ACI Structural Journal 109(4): 551-558.

Tobbi, H., Farghaly, A. S. and Benmokrane, B. (2014). "Strength Model for Concrete Columns Reinforced with Fiber-Reinforced Polymer Bars and Ties." ACI Structural Journal, 111(4): 789-798.

Vijay, P.V. and GangaRao, H.V.S. (2010). "Bending Behavior and Deformability of Glass Fiber-Reinforced Polymer Reinforced Concrete Members." Materials and Structures, 43: 73-90.

Wu, W. P. (1990). "Thermomechanical Properties of Fiber Reinforced Plastic (FRP) Bars." PhD dissertation, West Virginia University, Morgantown, WV, 292p.

Yost, J.R. and Gross, S.P. (2002). "Flexural Design Methodology for Concrete Beams Reinforced with Fibre-Reinforced Polymers." ACI Structural Journal, 99(3): 308-316.

Yu, J., Shang, X. and Lu, Z. (2016). "Efficiency of Externally Bonded L-Shaped FRP Laminates in Strengthening Reinforced-Concrete Interior Beam-Column Joints." Journal of Composites for Construction, ASCE, 20(3), 10 p, DOI: 10.1061/(ASCE)CC.1943-5614.0000622.

Zerbe, H.E. and Durrani, A.J. (1990). "Seismic Response of Connections in Two-Bay Reinforced Concrete Frame Subassemblies with a Floor Slab." ACI Structural Journal, 87(4): 406-415.

APPENDICES

APPENDIX A

DESIGN CALCULATIONS OF GFRP-RC BEAM-COLUMN-SLAB SPECIMEN

Reinforcement Properties

Straight bars

Cross-sectional area of 16M bars (#5), A_{16M}: 200 mm^2

Modulus of elasticity of 16M bars (#5), $E_{F,16}$: 62.6 GPa

Tensile strength of 16M bars (#5), $T_{F,16}$: 1184 MPa

Max. tensile strain of 16M bars (#5), $\varepsilon_{F,16}$: 1.89% (0.0189)

Cross-sectional area of 13M bars (#4), A_{13M}: 127 mm^2

Modulus of elasticity of 13M bars (#4), $E_{F,13}$: 65.6 GPa

Tensile strength of 13M bars (#4), $T_{F,13}$: 1312 MPa

Max. tensile strain of 13M bars (#4), $\varepsilon_{F,13}$: 2.00% (0.0200)

Stirrups and ties (bent bars)

Cross-sectional area of 13M bars (#4), A_{13M}: 127 mm^2

Modulus of elasticity of 13M bars (#4), $E_{F,b}$: 50.0 GPa

Tensile strength of 13M bars (#4), straight portion, $T_{F,bs}$: 1019 MPa

Max. tensile strain of 13M bars (#4), $\varepsilon_{F,b}$: 2.04% (0.0204)

Min. tensile strength of 13M bars (#4), bent portion, $T_{F,bb}$: 459 MPa

Concrete Properties

Compressive strength at the day of testing, f'_c: 50 MPa

Compressive strain at failure, ε_{cu}: 0.0035

$\alpha_1 = 0.85 - 0.0015 \times 50 = 0.78 > 0.67$

$\beta_1 = 0.97 - 0.0025 \times 50 = 0.85 > 0.67$

Flexural Capacity of Beam (without Slab)

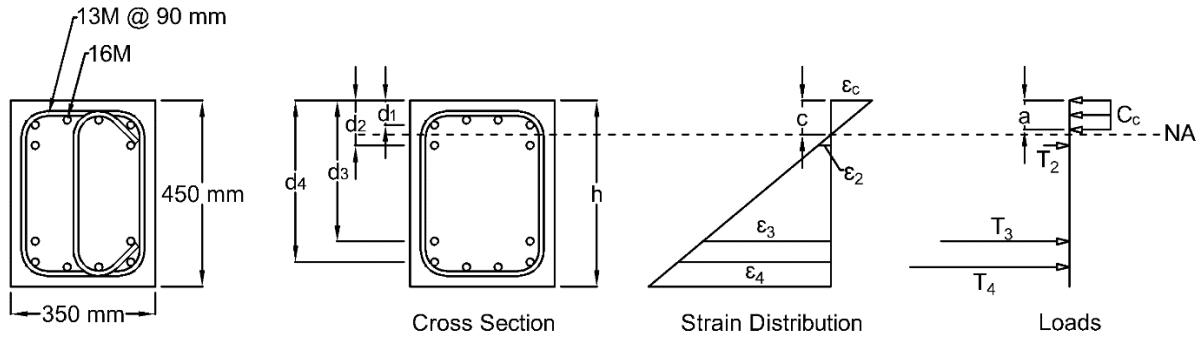

Figure A.1 – Cross-sectional properties and compatibility of strains for beam in GFRP-RC specimen

$d_1 = 50\ mm, d_2 = 100\ mm,\ d_3 = 350\ mm,\ d_4 = 400\ mm$

Assume $c = 83\ mm$

$$d_1 = 50\ mm < c = 83\ mm \rightarrow C_1 = 0\ kN\ (in\ compression)$$

$$\varepsilon_{r2} = 0.0035 \times \frac{c - d_2}{c} = 0.0035 \times \frac{83 - 100}{83} = -0.0007 > -0.0189$$

$$\varepsilon_{r3} = 0.0035 \times \frac{c - d_3}{c} = 0.0035 \times \frac{83 - 350}{83} = -0.0113 > -0.0189$$

$$\varepsilon_{r4} = 0.0035 \times \frac{c - d_4}{c} = 0.0035 \times \frac{83 - 400}{83} = -0.0133 > -0.0189$$

Concrete block compression:

$$C_c = \alpha_1 \times f'_c \times \beta_1 \times b \times c = {}^{0.78 \times 50 \times 0.85 \times 350 \times 83}/_{10^3} = 963\ kN$$

where b is the effective beam width.

Reinforcement tension:

$$T_2 = A_2 \times E_{F,16} \times \varepsilon_2 = {-2 \times 200 \times 62600 \times 0.0007}/{10^3} = -18\ kN$$

$$T_3 = A_3 \times E_{F,16} \times \varepsilon_3 = {-2 \times 200 \times 62600 \times 0.0113}/{10^3} = -283\ kN$$

$$T_4 = A_4 \times E_{F,16} \times \varepsilon_4 = {-4 \times 200 \times 62600 \times 0.0133}/{10^3} = -666\ kN$$

Equilibrium check:

$$|C_c| = 963\ kN \cong\ |T_2 + T_3 + T_4| = |-18 - 283 - 666| = 967\ kN$$

Moment resistance:

$$a = \beta_1 \times c = 0.85 \times 83 = 71\ mm$$

Moment about the centre of compression block:

$$\begin{aligned} M_{beam} &= T_2 \times \left(\frac{a}{2} - d_2\right) + T_3 \times \left(\frac{a}{2} - d_3\right) + T_4 \times \left(\frac{a}{2} - d_4\right) \\ &= {-18 \times \left(\frac{71}{2} - 100\right) - 283 \times \left(\frac{71}{2} - 350\right) - 666 \times \left(\frac{71}{2} - 400\right)}\Big/{10^3} \\ &= 333\ kN.m \end{aligned}$$

Joint shear stress

Joint area:

$$A_{joint} = 450 \times 350 = 157\,500\ mm^2$$

Shear load applied from the column to the joint:

$$V_{col} = \frac{M}{L_{col}} = \frac{2 \times 333}{2.9} = 230\ kN$$

Shear load applied to the joint:

$$V_{joint} = |T_3| + |T_4| + |C_c| - |T_2| - |V_{col}| = 283 + 666 + 963 - 18 - 230 = 1664\ kN$$

Shear stress applied to the joint:

$$\frac{V_{joint}}{A_{joint}} = \frac{1664 \times 10^3}{157500} = 10.57$$

Joint shear stress ratio (as a multiplier of $\sqrt{f'_c}$):

$$\frac{10.57}{\sqrt{50}} = 1.49$$

Converting beam moments to the actuator load:

$$\frac{2 \times M}{L_{col}} = \frac{2 \times 333}{2.9} = 230\ kN$$

Flexural Capacity of Beam (Full Slab Contribution)

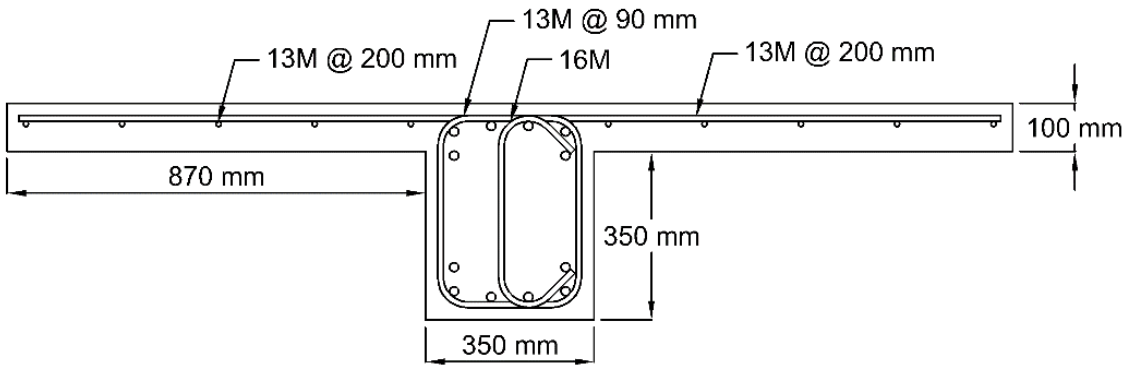

Figure A.2 – Reinforcement detailing of beams in GFRP-RC beam-column-slab specimen

Slab in tension

Assume $c = 116\ mm$

$$d_1 = 50\ mm < c = 116\ mm \rightarrow C_1 = 0\ kN\ (in\ compression)$$

$$d_2 = 100\ mm < c = 116\ mm \rightarrow C_2 = 0\ kN\ (in\ compression)$$

$$\varepsilon_{r3} = 0.0035 \times \frac{c - d_3}{c} = 0.0035 \times \frac{116 - 350}{116} = -0.0071 > -0.0189$$

$$\varepsilon_{r4} = 0.0035 \times \frac{c - d_4}{c} = 0.0035 \times \frac{116 - 400}{116} = -0.0086 > -0.0189$$

$$\varepsilon_{slab} = 0.0035 \times \frac{c - d_{slab}}{c} = 0.0035 \times \frac{116 - 400}{116} = -0.0086 > -0.0200$$

Concrete block compression:

$$C_c = \alpha_1 \times f'_c \times \beta_1 \times b \times c = {0.78 \times 50 \times 0.85 \times 350 \times 116}/{10^3} = 1346\ kN$$

Reinforcement tension:

$$T_3 = A_3 \times E_{F,16} \times \varepsilon_3 = {-2 \times 200 \times 62600 \times 0.0071}/{10^3} = -178\ kN$$

$$T_4 = A_4 \times E_{F,16} \times \varepsilon_4 = {-4 \times 200 \times 62600 \times 0.0086}/{10^3} = -431\ kN$$

All the longitudinal bars in the slab are considered effective in the bending moment capacity of the specimen. Therefor:

$$T_{slab} = A_{slab} \times E_{F,13} \times \varepsilon_{slab} = {-10 \times 127 \times 65600 \times 0.0086}/{10^3} = -716\ kN$$

Equilibrium check:

$$|C_c| = 1346\ kN \cong |T_3 + T_4 + T_{slab}| = |-178 - 431 - 716| = 1325\ kN$$

Moment resistance:

$$a = \beta_1 \times c = 0.85 \times 116 = 99\ mm$$

Moment about the centre of compression block:

$$\begin{aligned} M_{beam} &= T_3 \times \left(\frac{a}{2} - d_3\right) + T_4 \times \left(\frac{a}{2} - d_4\right) + T_{slab} \times \left(\frac{a}{2} - d_{slab}\right) \\ &= {-178 \times \left(\frac{99}{2} - 350\right) - 431 \times \left(\frac{99}{2} - 400\right) - 716 \times \left(\frac{99}{2} - 400\right)}\Big/{10^3} \\ &= 456\ kN.m \end{aligned}$$

<u>Slab in compression</u>

Failure due to bar rupture.

Assume $c = 32\ mm$

$$\varepsilon_c = 0.0189 \times \frac{32}{400 - 32} = 0.0016 < 0.0035$$

To calculate the equivalent concrete block stress, values of α and β are obtained from the design manual for "Reinforcing Concrete Structures with Fibre Reinforced Polymers" by ISIS Canada (ISIS Canada 2007):

$$\alpha = 0.70$$

$$\beta = 0.68$$

By assuming the full width of slab ($b = 2090\ mm$) effective in compression, the concrete block compression is calculated as:

$$C_c = \alpha \times f'_c \times \beta \times b \times c = {0.70 \times 50 \times 0.68 \times 2090 \times 32}/{10^3} = 1592\ kN$$

Moreover, the corresponding strain in the reinforcing bars are calculated as:

$$\varepsilon_{r1} = 0.0016 \times \frac{c - d_1}{c} = 0.0016 \times \frac{32 - 50}{32} = -0.0009 > -0.0189$$

$$\varepsilon_{r2} = 0.0016 \times \frac{c - d_2}{c} = 0.0016 \times \frac{32 - 100}{32} = -0.0035 > -0.0189$$

$$\varepsilon_{r3} = 0.0016 \times \frac{c - d_3}{c} = 0.0016 \times \frac{32 - 350}{32} = -0.0163 > -0.0189$$

$$\varepsilon_{r4} = -0.0189$$

$$\varepsilon_{slab} = 0.0016 \times \frac{c - d_{slab}}{c} = 0.0016 \times \frac{32 - 50}{32} = -0.0009 > -0.0200$$

Tension in reinforcement:

$$T_1 = A_1 \times E_{F,16} \times \varepsilon_1 = {-4 \times 200 \times 62600 \times 0.0009}/{10^3} = -46\ kN$$

$$T_2 = A_2 \times E_{F,16} \times \varepsilon_2 = {-2 \times 200 \times 62600 \times 0.0035}/{10^3} = -88\ kN$$

$$T_3 = A_3 \times E_{F,16} \times \varepsilon_3 = {-2 \times 200 \times 62600 \times 0.0163}/{10^3} = -409\ kN$$

$$T_4 = A_4 \times T_{F,16} = {-4 \times 200 \times 1184}/{10^3} = -947\ kN$$

$$T_{slab} = A_{slab} \times E_{F,13} \times \varepsilon_{slab} = {-10 \times 127 \times 65600 \times 0.0009}/{10^3} = -77\ kN$$

Equilibrium check:

$$|C_c| = 1592\ kN \cong\ |T_1 + T_2 + T_3 + T_4 + T_{slab}| = |-46 - 88 - 409 - 947 - 77| = 1567\ kN$$

Moment about the centre of compression block:

$$a = \beta \times c = 0.68 \times 32 = 22\ mm$$

Moment about the centre of compression block:

$$M_{beam} = T_1 \times \left(\frac{a}{2} - d_1\right) + T_2 \times \left(\frac{a}{2} - d_2\right) + T_3 \times \left(\frac{a}{2} - d_3\right) + T_4 \times \left(\frac{a}{2} - d_4\right) + T_{slab} \times \left(\frac{a}{2} - d_{slab}\right) = -46 \times \left(\frac{22}{2} - 50\right) - 88 \times \left(\frac{22}{2} - 100\right) - 409 \times \left(\frac{22}{2} - 350\right) - 947 \times \left(\frac{22}{2} - 400\right) - 716 \times \left(\frac{22}{2} - 50\right) / 10^3 = 517\ kN.m$$

Shear Capacity of Beam

Three branches of 13M bars are used as transverse reinforcement. Therefore, the cross-sectional area of shear reinforcement:

$$A_{F,v} = 3 \times 127 = 381\ mm^2$$

The contribution of concrete to the shear capacity, according to Clause 8.4.4.5 of CSA S806-12 (CSA 2012), for members with an effective depth not more than 300 mm, is calculated as:

$$V_c = 0.05 \times \lambda \times K_m \times K_r \times \left(f'_c\right)^{1/3} \times b \times d_v$$

where:

$$d = \frac{2 \times d_3 + 4 \times d_4}{6} = \frac{2 \times 350 + 4 \times 400}{6} = 383\ mm$$

$$d_v = \max(0.9d, 0.72h) = \max(345,324) = 345$$

$$K_m = \sqrt{\frac{V_f d}{M_f}} \leq 1.0$$

$$K_r = 1 + \left(E_{F,16} \times \rho_{fW}\right)^{\frac{1}{3}}$$

where:

$$\rho_{fW} = \frac{6 \times 200}{350 \times 383} = 0.0090$$

According to the previous calculations:

$$M_r = 333\ kN.m$$

Therefore:

$$V_f = \frac{M_r}{l_b} = \frac{230}{2.225} = 150\ kN$$

where l_b is the distance between the point of loading at the beam tip and the centre of the column.

By substituting these values into the equations:

$$K_m = \sqrt{\frac{V_f d}{M_f}} = \sqrt{\frac{150 \times 0.383}{333}} = 0.173 \leq 1.0$$

$$K_r = 1 + \left(E_{F,16} \times \rho_{fW}\right)^{\frac{1}{3}} = 1 + (62600 \times 0.0090)^{\frac{1}{3}} = 9.24$$

$$V_c = {0.05 \times 0.173 \times 9.24 \times (50)^{1/3} \times 350 \times 345}\Big/{10^3} = 36\ kN$$

However:

$$0.11 \times \lambda \times \sqrt{f'_c} \times b \times d_v < V_c < 0.22 \times \lambda \times \sqrt{f'_c} \times b \times d_v$$

$${0.11 \times \sqrt{50} \times 350 \times 345}\Big/{10^3} < V_c < {0.22 \times \sqrt{50} \times 350 \times 345}\Big/{10^3}$$

$$94\ kN < V_c < 188\ kN \rightarrow USE\ V_c = 94\ kN$$

Therefore, the shear demand for GFRP stirrups is calculated as:

$$V_{SF} = 150 - 94 = 56\ kN$$

According to Clause 8.4.4.8 of CSA S806-12 (CSA 2012), the shear adjustment factor for members with an effective depth more than 300 mm can be set to unity if at least the minimum shear reinforcement suggested by Clause 8.4.5.2 of CSA S806-12 (CSA 2012) is provided to the section:

$$A_{v,min} = 0.07 \times \sqrt{f'_c} \times \frac{b \times s}{0.4 \times f_{FU}}$$

where f_{FU} can be taken as the minimum of:

- $0.005 \times E_{F,b} = 0.005 \times 50000 = 250$ MPa
- $T_{F,bs} = 1019$ MPa
- The stress corresponding to failure of corners, $T_{F,bb} = 459$ MPa
- 1200 MPa

Clause 8.4.4.9 of CSA S806-12 (CSA 2012) requires limiting the value of f_{FU} to $0.005 \times E_{F,b}$. However, this limitation leads to a very conservative design, which could affect the

constructability of the beam due to close spacing of the stirrups. Therefore, to achieve a more practical design, the minimum guaranteed f_{FU} provided by the manufacturer for the bent portion of the stirrups (459 MPa) is used as f_{FU} (Pultrall Inc. 2019). As a result, by assuming three branches of 13M bars as shear reinforcement:

$$\frac{A_{v,min} \times 0.4 \times f_{FU}}{0.07 \times \sqrt{f'_c} \times b} = s_{max}$$

$$s_{max} = \frac{3 \times 127 \times 0.4 \times 459}{0.07 \times \sqrt{50} \times 350} = 403\ mm$$

From CSA S806-12 (CSA 2012), Clause 8.4.4.9:

$$V_{SF} = \frac{0.4 \times f_{FU} \times d_v \times A_{F,v}}{s} \times cot\theta$$

$$\varepsilon_l = \frac{\frac{M_f}{d_v} + (V_f)}{2 \times (E_{F,16} \times A_F)}$$

where A_F is the area of FRP tension reinforcement.

$$\varepsilon_l = \frac{\frac{333 \times 10^6}{345} + (150 \times 10^3)}{2 \times (62600 \times 6 \times 200)} = 0.0074$$

$$\theta = 30° + 7000 \times \varepsilon_l = 30 + 7000 \times 0.0074 = 82° > 60° \rightarrow USE\ \theta = 60°$$

Therefore:

$$s = \frac{0.4 \times 456 \times 345 \times 3 \times 127}{56 \times 10^3} \times \cot(60°) = 247\ mm$$

Since there is no provision in CSA S806-12 (CSA 2012) for the minimum spacing of stirrups in flexural elements, Clause 21.3.3.2 of CSA A23.3-14 (CSA 2014-a) has been used to calculate the minimum spacing of stirrups. According to CSA A23.3-14 (CSA 2014-a), the spacing between stirrups should be the least of:

- $\frac{d}{4} = \frac{383}{4} = 96\ mm$
- Eight times the diameter of the smallest longitudinal bars, $8 \times 16 = 128\ mm$
- 24 times the diameter of the hoop bars, $24 \times 13 = 312\ mm$
- 300 mm

Therefore:

USE 3 branches of 13M @ 90 mm

Flexural Capacity of Column

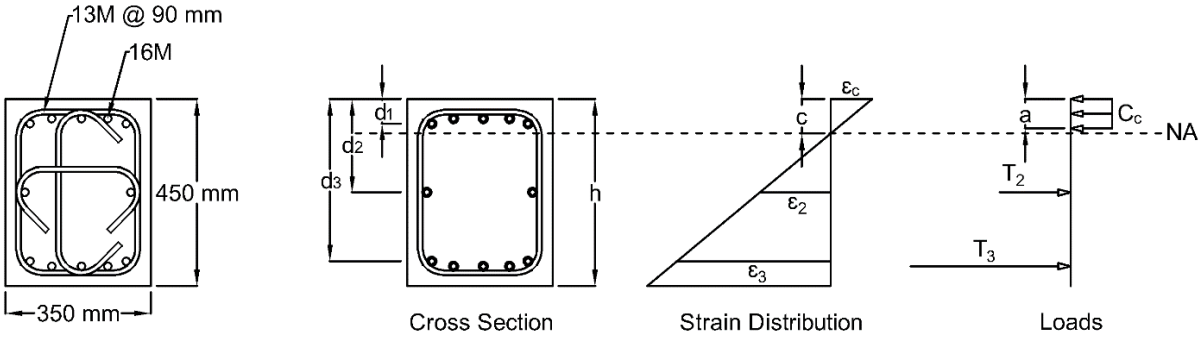

Figure A.3 – Cross-sectional properties and compatibility of strains for column in GFRP-RC specimen

$d_1 = 50\ mm, d_2 = 225\ mm,\ d_3 = 400\ mm$

Required reinforcement to avoid brittle tension failure (balanced reinforcement) is calculated follows. The depth of concrete compressive block corresponding to the balanced failure (c_b) is calculated as:

$$\frac{\varepsilon_{cu}}{c_b} = \frac{\varepsilon_{F,16} + \varepsilon_{cu}}{d_3}$$

$$c_b = \frac{\varepsilon_{cu}}{\varepsilon_{cu} + \varepsilon_{F,16}} \times d_3$$

$$\varepsilon_{Fu} = \frac{T_{F,16}}{E_{F,16}} = \frac{1184}{62600} = 0.0189$$

$$c_b = \frac{0.0035}{0.0035 + 0.0189} \times 400 = 63\ mm$$

$$C_c = \alpha_1 \times f'_c \times b \times \beta_1 \times c = {0.78 \times 50 \times 350 \times 0.85 \times 63}/{10^3} = 731\ kN$$

Assume 2-16M bars at d_2:

$$\varepsilon_2 = \varepsilon_{cu} \times \frac{c_b - d_2}{c_b} = 0.0035 \times \frac{63 - 225}{63} = -0.0090$$

$$T_2 = \varepsilon_2 \times E_{F,16} \times A_2 = {-0.0090 \times 62600 \times 2 \times 200}/{10^3} = -225\ kN$$

$$C_c + T_2 = 731 - 225 = 506\ kN$$

Required number of bars:

$$n = \frac{F}{T_{F,16} \times A_{16M}} = \frac{506 \times 10^3}{1184 \times 200} = 2.13$$

Provided number of bars:

$$5 > 2.13 \rightarrow OK$$

Axial load-moment interaction diagram

- Point One (pure axial load)

According to Clause 8.4.3.7 of CSA-S806-12 (CSA 2012):

$$P_o = \alpha_1 \times f'_c \times (A_g - A_F) = {0.78 \times 50 \times (450 \times 350 - 12 \times 200)}/{10^3} = 6049\ kN$$

$$P_r = 0.8 \times P_o = 4839\ kN$$

- Point Two ($c = 400\ mm$)

$$T_1 = T_2 = T_3 = 0$$

$$C_c = {0.78 \times 50 \times 350 \times 0.85 \times 400}/{10^3} = 4641\ kN$$

Moment about centre line of the cross-section:

$$M = {4641 \times \left(\frac{450}{2} - \frac{0.85 \times 400}{2}\right)}\Big/{10^3} = 255\ kN.m$$

Therefore, an external load equal to C_c is applied at the centre of the section to satisfy the equilibrium.

$$(c = 400\ mm, \qquad P_e = 4641\ kN, \qquad M = 255\ kN.m)$$

❖ Point Three ($c = 350\ mm$)

$$T_1 = T_2 = 0$$

$$C_c = {0.78 \times 50 \times 350 \times 0.85 \times 350}/{10^3} = 4061\ kN$$

$$\varepsilon_3 = 0.0035 \times \frac{350 - 400}{350} = -0.0005$$

$$T_3 = {\varepsilon_3 \times E_{F,16} \times A_3 = -0.0005 \times 62600 \times 5 \times 200}/{10^3} = -31\ kN$$

$$P_e = C_c + T_3 = 4061 - 31 = 4030\ kN$$

Moment about centre line of the cross-section:

$$M = {4061\ \times \left(\frac{450}{2} - \frac{0.85 \times 350}{2}\right) - 31 \times \left(\frac{450}{2} - 400\right)}\Big/{10^3} = 315\ kN.m$$

$$(c = 350\ mm, \qquad P_e = 4030\ kN, \qquad M = 315\ kN.m)$$

❖ Point Four ($c = 300\ mm$)

$$T_1 = T_2 = 0$$

$$C_c = {0.78 \times 50 \times 350 \times 0.85 \times 300}/{10^3} = 3481\ kN$$

$$\varepsilon_3 = 0.0035 \times \frac{300 - 400}{300} = -0.0012$$

$$T_3 = {\varepsilon_3 \times E_{F,16} \times A_3 = -0.0012 \times 62600 \times 5 \times 200}/{10^3} = -75\ kN$$

$$P_e = C_c + T_3 = 3481 - 75 = 3406\ kN$$

$$M = {3481\ \times \left(\frac{450}{2} - \frac{0.85 \times 300}{2}\right) - 75 \times \left(\frac{450}{2} - 400\right)}\Big/{10^3} = 353\ kN.m$$

$$(c = 300\ mm, \qquad P_e = 3406\ kN, \qquad M = 353\ kN.m)$$

❖ Point Five ($c = 250\ mm$)

$$T_1 = T_2 = 0$$

$$C_c = {0.78 \times 50 \times 350 \times 0.85 \times 250}/{10^3} = 2901\ kN$$

$$\varepsilon_3 = 0.0035 \times \frac{250 - 400}{250} = 0.0021$$

$$T_3 = {\varepsilon_3 \times E_{F,16} \times A_3 = -0.0021 \times 62600 \times 5 \times 200}/{10^3} = -131\ kN$$

$$P_e = C_c + T_3 = 2901 - 131 = 2770\ kN$$

$$M = {2901\ \times \left(\frac{450}{2} - \frac{0.85 \times 250}{2}\right) - 131 \times \left(\frac{450}{2} - 400\right)}\Big/{10^3} = 367\ kN.m$$

$$(c = 250\ mm, \qquad P_e = 2770\ kN, \qquad M = 367\ kN.m)$$

❖ Point Six ($c = 200\ mm$)

$$T_1 = 0$$

$$C_c = {0.78 \times 50 \times 350 \times 0.85 \times 200}/{10^3} = 2321\ kN$$

$$\varepsilon_2 = 0.0035 \times \frac{200 - 225}{200} = -0.0004$$

$$\varepsilon_3 = 0.0035 \times \frac{200 - 400}{200} = -0.0035$$

$$T_2 = {\varepsilon_2 \times E_{F,16} \times A_2 = -0.0004 \times 62600 \times 2 \times 200}/{10^3} = -10\ kN$$

$$T_3 = {\varepsilon_3 \times E_{F,16} \times A_3 = -0.0035 \times 62600 \times 5 \times 200}/{10^3} = -219\ kN$$

$$P_e = C_c + T_3 + T_2 = 2321 - 10 - 219 = 2092\ kN$$

$$M = {2321\ \times \left(\frac{450}{2} - \frac{0.85 \times 200}{2}\right) - 219 \times \left(\frac{450}{2} - 400\right)}\Big/{10^3} = 363\ kN.m$$

$$(c = 200\ mm, \qquad P_e = 2092\ kN, \qquad M = 363\ kN.m)$$

❖ Point Seven ($c = 150\ mm$)

$$T_1 = 0$$

$$C_c = {0.78 \times 50 \times 350 \times 0.85 \times 150}/{10^3} = 1740\ kN$$

$$\varepsilon_2 = 0.0035 \times \frac{150 - 225}{150} = -0.0018$$

$$\varepsilon_3 = 0.0035 \times \frac{150 - 400}{150} = -0.0058$$

$$T_2 = {\varepsilon_2 \times E_{F,16} \times A_2 = -0.0018 \times 62600 \times 2 \times 200}/{10^3} = -45\ kN$$

$$T_3 = {\varepsilon_3 \times E_{F,16} \times A_3 = -0.0058 \times 62600 \times 5 \times 200}/{10^3} = -363\ kN$$

$$P_e = C_c + T_3 + T_2 = 1740 - 45 - 363 = 1332\ kN$$

$$M = {1740\ \times \left(\frac{450}{2} - \frac{0.85 \times 150}{2}\right) - 363 \times \left(\frac{450}{2} - 400\right)}\Big/{10^3} = 344\ kN.m$$

$$(c = 150\ mm, \quad P_e = 1332\ kN, \quad M = 344\ kN.m)$$

❖ Point Eight ($c = 100\ mm$)

$$T_1 = 0$$

$$C_c = {0.78 \times 50 \times 350 \times 0.85 \times 100}/{10^3} = 1160\ kN$$

$$\varepsilon_2 = 0.0035 \times \frac{100 - 225}{100} = -0.0044$$

$$\varepsilon_3 = 0.0035 \times \frac{100 - 400}{100} = -0.0105$$

$$T_2 = {\varepsilon_2 \times E_{F,16} \times A_2 = 0.0044 \times 62600 \times 2 \times 200}/{10^3} = -110\ kN$$

$$T_3 = {\varepsilon_3 \times E_{F,16} \times A_3 = 0.0105 \times 62600 \times 5 \times 200}/{10^3} = -657\ kN$$

$$P_e = C_c + T_3 + T_2 = 1160 - 110 - 657 = 393\ kN$$

$$M = {1160\ \times \left(\frac{450}{2} - \frac{0.85 \times 100}{2}\right) - 657 \times \left(\frac{450}{2} - 400\right)}\Big/{10^3} = 327\ kN.m$$

$$(c = 100\ mm, \quad P_e = 393\ kN, \quad M = 327\ kN.m)$$

❖ Point Nine (*pure bending*)

$$\varepsilon_2 = \varepsilon_{cu} \times \frac{c - d_2}{c} = 0.0035 \times \frac{c - 225}{c}$$

$$\varepsilon_3 = \varepsilon_{cu} \times \frac{c - d_3}{c} = 0.0035 \times \frac{c - 400}{c}$$

$$f_2 = \varepsilon_2 \times E_{F,16} = 0.0035 \times 62600 \times \frac{c - 225}{c} = 219.1 \times \frac{c - 225}{c}$$

$$f_3 = \varepsilon_3 \times E_{F,16} = 0.0035 \times 62600 \times \frac{c - 400}{c} = 219.1 \times \frac{c - 400}{c}$$

$$T_2 = f_2 \times A_2 = 2 \times 200 \times 219.1 \times \frac{c - 225}{c} = 87640 \times \frac{c - 225}{c}$$

$$T_3 = f_3 \times A_3 = 5 \times 200 \times 219.1 \times \frac{c - 400}{c} = 219100 \times \frac{c - 400}{c}$$

$$C_c = \alpha_1 \times f'_c \times b \times \beta_1 \times c = 0.78 \times 50 \times 350 \times 0.85 \times c = 11602.5 \times c$$

Assuming $c > 50\ mm$, from force equilibrium:

$$C_c = T_2 + T_3$$

Solving equation above for "c":

c = 84 mm ($> 50\ mm$)

$$a = 0.85 \times 84 = 70\ mm$$

$$C_c = {}^{11602.5 \times 84}/_{10^3} = 975\ kN$$

$$T_2 = {}^{87640 \times \frac{84 - 225}{84}}\Big/_{10^3} = -147\ kN$$

$$T_3 = {}^{175280 \times \frac{84 - 400}{84}}\Big/_{10^3} = -824\ kN$$

$$M = {}^{975\ \times \left(\frac{450}{2} - \frac{70}{2}\right) - 824 \times \left(\frac{450}{2} - 400\right)}\Big/_{10^3} = 329\ kN.m$$

$$(c = 84\ mm, \quad P_e = 0\ kN, \quad M = 329\ kN.m)$$

- Point Ten ($c = 113\ mm$)

A constant axial load of 650 kN was applied to the column during the test:

$$\frac{650}{4839} = 13.4\%$$

Assuming $c = 113\ mm$

$$T_1 = 0$$

$$\varepsilon_2 = 0.0035 \times \frac{113 - 225}{113} = 0.0035$$

$$\varepsilon_3 = 0.0035 \times \frac{113 - 400}{113} = 0.0089$$

$$T_2 = {\varepsilon_2 \times E_{F,16} \times A_2 = -0.0035 \times 62600 \times 2 \times 200}/{10^3} = -87\ kN$$

$$T_3 = {\varepsilon_2 \times E_{F,16} \times A_2 = -0.0089 \times 62600 \times 5 \times 200}/{10^3} = -557\ kN$$

$$C_c = {0.78 \times 50 \times 350 \times 0.85 \times 113}/{10^3} = 1311\ kN$$

$$P_e = C_c + T_3 + T_2 = 1311 - 557 - 87 = 667\ kN$$

Moment about centre line of the cross-section:

$$M = {1311\ \times \left(\frac{450}{2} - \frac{0.85 \times 113}{2}\right) - 557 \times \left(\frac{450}{2} - 400\right)}\Big/{10^3} = 329\ kN.m$$

$$(c = 113\ mm, \qquad P_e = 667\ kN, \qquad M = 329\ kN.m)$$

Column-to-beam flexural strength ratio:

$$\frac{2 \times M_{col}}{2 \times M_{beam}} = \frac{2 \times 329}{2 \times\ 333} = 0.99$$

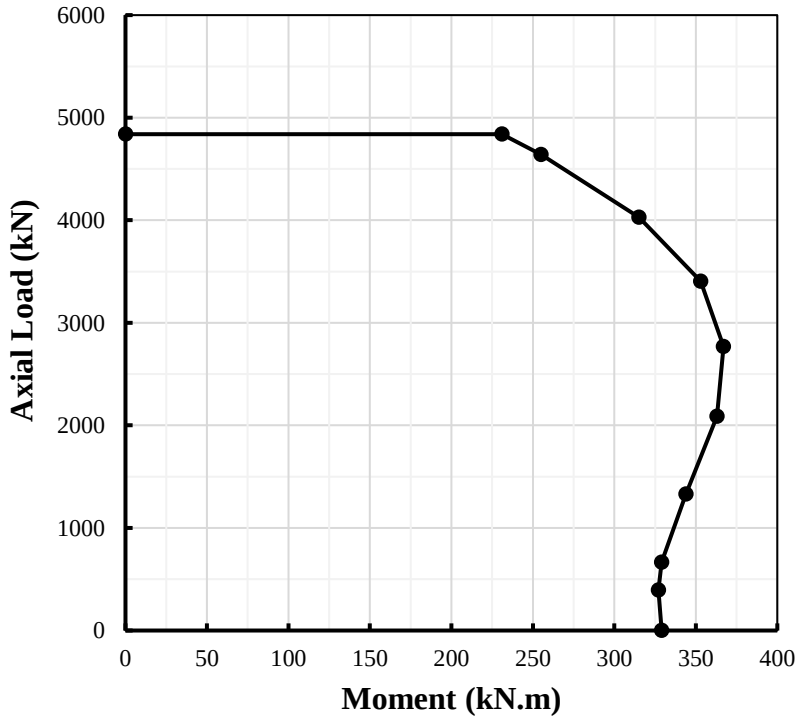

Figure A.4 – Axial load-bending moment interaction diagram for GFRP-RC column

Shear Capacity of Column

Three branches of 13M bars are used as transverse reinforcement. Therefore, the cross-sectional area of shear reinforcement:

$$A_{F,v} = 3 \times 127 = 381\ mm^2$$

According to the previous calculations, at c = 113 mm:

$$M_f = 329\ kN.m$$

$$N_f = 650\ kN$$

According to Clause 8.4.4.5 of CSA S806-12 (CSA 2012), concrete shear resistance is calculated as:

$$V_c = 0.05 \times \lambda \times K_m \times K_r \times \left(f'_c\right)^{1/3} \times b \times d_v$$

$$K_m = \sqrt{\frac{V_f d}{M_f}} \leq 1.0$$

$$K_r = 1 + \left(E_{F,16} \times \rho_{fW}\right)^{\frac{1}{3}}$$

Moreover:

$$d = \frac{2 \times d_2 + 5 \times d_3}{7} = \frac{2 \times 225 + 5 \times 400}{7} = 350\ mm$$

$$d_v = \max(0.9d, 0.72h) = \max(315,324) = 324$$

$$\rho_{fW} = \frac{7 \times 200}{350 \times 350} = 0.0114$$

$$V_f = \frac{M_{r,col}}{h_c} = \frac{2 \times 329}{2.9} = 227\ kN$$

where $M_{r,col}$ is the moment resistance of the column under the applied axial load during testing and h_c is the height of the column.

Therefore:

$$K_m = \sqrt{\frac{V_f d}{M_f}} = \sqrt{\frac{227 \times 0.35}{329}} = 0.49 \leq 1.0$$

$$K_r = 1 + \left(E_{F,16} \times \rho_{fW}\right)^{\frac{1}{3}} = 1 + (62600 \times 0.0114)^{\frac{1}{3}} = 9.94$$

$$V_c = {0.05 \times 0.49 \times 9.94 \times (50)^{1/3} \times 350 \times 324}/{10^3} = 102\ kN$$

However:

$$0.11 \times \lambda \times \sqrt{f'_c} \times b \times d_v < V_c < 0.22 \times \lambda \times \sqrt{f'_c} \times b \times d_v$$

$${0.11 \times \sqrt{50} \times 350 \times 324}/{10^3} < V_c < {0.22 \times \sqrt{50} \times 350 \times 324}/{10^3}$$

$$88 < 102 < 176 \rightarrow OK$$

Minimum reinforcement is calculated according to Clause 8.4.5.2 of CSA S806-12 (CSA 2012):

$$A_{v,min} = 0.07 \times \sqrt{f'_c} \times \frac{b \times s}{0.4 \times f_{FU}}$$

f_{fu} can be taken as the minimum of:

- $0.005 \times E_{F,b} = 0.005 \times 50000 = 250$ MPa
- $T_{F,bs} = 1019$ MPa
- The stress corresponding to failure of corners, $T_{F,bb} = 459$ MPa
- 1200 MPa

Similar to the shear design of the beam, the minimum guaranteed f_{FU} provided by the manufacturer for the bent portion of the stirrups (459 MPa) is used as f_{FU} (Pultrall Inc. 2019). Therefore, by assuming three branches of 13M bars as shear reinforcement:

$$\frac{A_{v,min} \times 0.4 \times f_{FU}}{0.07 \times \sqrt{f'_c} \times b} = s_{max}$$

$$s_{max} = \frac{3 \times 127 \times 0.4 \times 456}{0.07 \times \sqrt{50} \times 350} = 401\ mm$$

Shear demand for GFRP stirrups:

$$V_{SF} = 227 - 102 = 125\ kN$$

From CSA S806-12 (CSA 2012) Clause 8.4.4.9:

$$V_{SF} = \frac{0.4 \times f_{FU} \times d_v \times A_{F,v}}{s} \times cot\theta$$

$$\varepsilon_l = \frac{\frac{M_f}{d_v} + (V_f) + 0.5 \times N_f}{2(E_{F,16} \times A_F)} = \frac{\frac{329 \times 10^6}{324} + (227 + 0.5 \times 650) \times 10^3}{2(62600 \times 7 \times 127)} = 0.01408$$

where A_F is the area of FRP tension reinforcement.

$$\theta = 30° + 7000 \times \varepsilon_l = 30° + 7000 \times 0.01408 = 129° > 60° \rightarrow USE\ \theta = 60°$$

Moreover, F_u shall not be taken greater than $0.005 \times E_{F,b} = 250$ MPa, therefore:

$$s = \frac{0.4 \times 1 \times 456 \times 324 \times 3 \times 127}{125 \times 10^3 \times tan\,(60)} = 104\ mm$$

According to Clause 8.4.6.1 CSA S806-12 (CSA 2012), maximum spacing of the stirrups should be limited to the minimum of:

- $0.6 \times d_v \times \mathrm{Cot}\theta = 120$ mm
- 400 mm

Also, according to Clause 12.7.4.4 (CSA 2012) spacing between stirrups should not exceed the least of:

- $\frac{d}{4} = \frac{350}{4} = 88\ mm$;
- Eight times the diameter of the smallest longitudinal bars$= 8 \times 16 = 128\ mm$;
- 24 times the diameter of the hoop bars$= 24 \times 13 = 312\ mm$; or
- 300 mm.

Therefore:

USE 3 branches of 13M @ 90 mm

Confinement of Column

Clause 12.7.5.2 of CSA S806-12 (CSA 2012) refers to Clause 12.7.3.3 and 12.7.3.4 to check for confinement of the columns reinforced with FRP longitudinal and transverse reinforcement. According to Clause 12.7.3.4, transverse reinforcement shall be spaced at distances not exceeding the least of the following:

a) one-quarter of the minimum member dimension; $\frac{350}{4} = 88 \approx 90$ mm
b) 150 mm;
c) 6 times the diameter of the smallest longitudinal bar; $6 \times 16 = 96\ mm$

Moreover, Clause 12.7.3.3 of CSA S-806-12 (CSA 2012) defined the required confinement reinforcement for columns in seismic regions as:

$$A_{FH} = 14 \times s \times h_c \times \frac{f'_c}{f_{fh}} \times \left(\frac{A_g}{A_c} - 1\right) \times \frac{\delta}{\sqrt{k_c}} \times \frac{P}{P_o}$$

where:

h_c is dimension of the concrete core of rectangular section measured perpendicular to the direction of the confinement bars to outside of peripheral hoop.

f_{fh} is the least of:

a) $0.006 \times E_{F,b} = 0.006 \times 50000 = 300$ MPa
b) $T_{F,bs} = 1019$ MPa.

A_g is the gross area of the section, $350 \times 450 = 157500$ mm^2.

A_c is the cross-sectional area of core (to outside of the stirrups). Centre-to-centre width and height of the stirrups is measured 275 mm and 375 mm, respectively. Therefore, $A_c = (275 + 13) \times (375 + 13) = 111744$ mm^2.

δ is design lateral drift ratio, which should not be taken less than 0.04.

k_c is equal to $0.15 \times \sqrt{\frac{h_c^{\,2}}{s \times s_l}}$.

s_l is spacing of tie legs in the cross-sectional plane of the column.

s is stirrup spacing.

P is applied axial load to the member.

P_o is axial load resistance of the member.

Therefore:

$$\left(\frac{A_g}{A_c} - 1\right) = \frac{157500}{111744} - 1 = 0.41 \ > 0.3$$

$$\frac{P_f}{P_{ro}} = 0.123 \ < 0.2 \rightarrow USE\ 0.2$$

For the shorter dimension:

$$h_c: 275 + 13 = 288\ mm$$

$$s_l = \frac{275 + 13}{2} = 144\ mm$$

Substituting these values in the equation of Clause 12.7.3.3 (CSA 2012):

$$3 \times 127 = 14 \times s \times 288 \times \frac{50}{300} \times (0.41) \times \frac{0.04}{\sqrt{\frac{288^2}{144 \times s}}} \times 0.2$$

Solving equation above for "s":

$$\rightarrow s = 260\ mm\ > 90\ mm$$

USE 3 branches of 13M @ 90 mm

For the longer dimension:

$$h_c: 375 + 13 = 388\ mm$$

$$s_l = \frac{375 + 13}{2} = 194\ mm$$

APPENDIX B

DESIGN CALCULATIONS OF STEEL-RC BEAM-COLUMN-SLAB SPECIMEN

Reinforcement Properties

Cross-sectional area of 10M bars, A_{10M}: 100 mm^2

Cross-sectional area of 20M bars, A_{20M}: 300 mm^2

Modulus of elasticity, E_s: 192.8 GPa

Tensile strength for longitudinal bars, $f_{y,s}$: 458 MPa

Tensile strength for transverse reinforcement, $f_{y,b}$: 400 MPa

Strain hardening factor: 1.25

Yield strain for longitudinal bars, $\varepsilon_{y,s}$: 0.24% (0.0024)

Concrete properties

Compressive strength at the day of testing, f'_c: 55 MPa

Compressive strain at failure, ε_{cu}: 0.0035

$\alpha_1 = 0.85 - 0.0015 \times 55 = 0.77 > 0.67$

$\beta_1 = 0.97 - 0.0025 \times 55 = 0.83 > 0.67$

Flexural Capacity of Beam (without Slab)

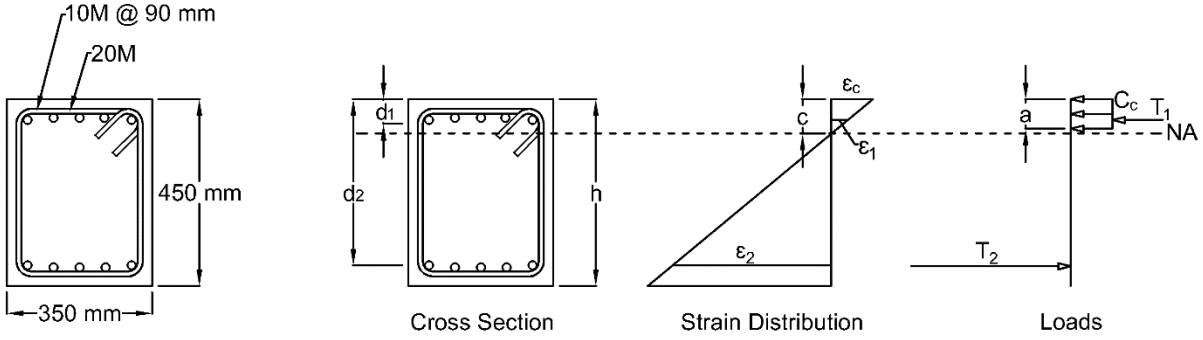

Figure B.1 – Cross-sectional properties and compatibility of strains for beam in steel-RC specimen

$d_1 = 50\ mm, d_2 = 400\ mm$

Assume $c = 58\ mm$

$$\varepsilon_{r1} = 0.0035 \times \frac{c - d_1}{c} = 0.0035 \times \frac{58 - 50}{58} = 0.0005 < 0.0024$$

$$\varepsilon_{r2} = 0.0035 \times \frac{c - d_2}{c} = 0.0035 \times \frac{58 - 400}{58} = -0.0206 < 0.0024 \rightarrow yielded$$

Concrete block compression:

$$C_c = \alpha_1 \times f'_c \times \beta_1 \times b \times c = {}^{0.77 \times 55 \times 0.83 \times 350 \times 58}/_{10^3} = 714\ kN$$

where b is the effective beam width.

According to Clause 21.5.1.2 of CSA A23.3-14 (CSA 2014-a), 25% increase in the yield stress of the steel reinforcement is considered due to the strain hardening effect. Therefore, the tensile force in the reinforcement is calculated as:

$$C_1 = A_1 \times E_s \times \varepsilon_{r1} = {}^{5 \times 300 \times 192.8 \times 0.0005}/_{10^3} = 140\ kN$$

$$T_2 = A_2 \times f_{y,s} \times K_{sh} = {}^{-5 \times 300 \times 458 \times 1.25}/_{10^3} = -855\ kN$$

where K_{sh} is the factor to include the strain hardening effect.

Equilibrium check:

$$|C_c| = 714\ kN \cong\ |C_1 + T_2| = |-140 + 855| = 715\ kN$$

Moment resistance:

$$a = \beta_1 \times c = 0.83 \times 58 = 48\ mm$$

Moment about the centre of compression block:

$$M_{beam} = C_1 \times \left(\frac{a}{2} - d_1\right) + T_2 \times \left(\frac{a}{2} - d_2\right) = {140 \times \left(\frac{48}{2} - 50\right) - 855 \times \left(\frac{48}{2} - 400\right)}\Big/_{10^3}$$
$$= 321\ kN.m$$

Joint shear stress

Joint area:

$$A_{joint} = 450 \times 350 = 157\,500\ mm^2$$

Shear load applied from the column to the joint:

$$V_{col} = \frac{M}{L_{col}} = \frac{2 \times 321}{2.9} = 221\ kN$$

Shear load applied to the joint:

$$V_{joint} = |T_2| + |C_c| - |T_1| - |V_{col}| = 859 + 726 + 133 - 221 = 1497\ kN$$

Shear stress applied to the joint:

$$\frac{V_{joint}}{A_{joint}} = \frac{1497 \times 10^3}{157500} = 9.5$$

Joint shear stress ratio (as a multiplier of $\sqrt{f'_c}$):

$$\frac{9.5}{\sqrt{55}} = 1.29$$

Converting beam moments to the actuator load:

$$\frac{2 \times M}{L_{col}} = \frac{2 \times 321}{2.9} = 221\ kN$$

Flexural Capacity of Beam (Full Slab Contribution)

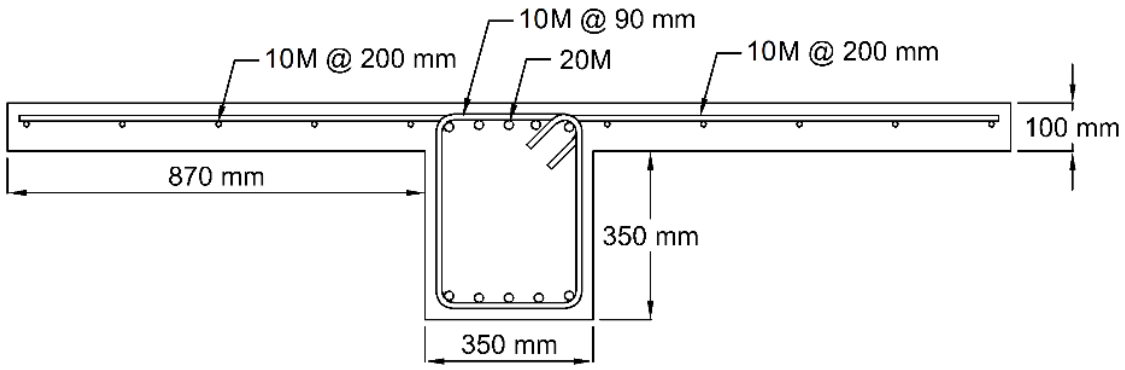

Figure B.2 – Reinforcement detailing of beams in steel-RC beam-column-slab specimen

Slab in tension

Assume $c = 84\ mm$

$$\varepsilon_{r1} = 0.0035 \times \frac{c - d_1}{c} = 0.0035 \times \frac{84 - 50}{84} = 0.0014 < 0.0024$$

$$\varepsilon_{r2} = 0.0035 \times \frac{c - d_2}{c} = 0.0035 \times \frac{84 - 400}{84} = -0.0132 < -0.0024 \rightarrow yielded$$

$$\varepsilon_{slab} = 0.0035 \times \frac{c - d_{slab}}{c} = 0.0035 \times \frac{84 - 400}{84} = -0.0132 < -0.0024 \rightarrow yielded$$

Concrete block compression:

$$C_c = \alpha_1 \times f'_c \times \beta_1 \times b \times c = {}^{0.77 \times 55 \times 0.83 \times 350 \times 84}/_{10^3} = 1033\ kN$$

Reinforcement tension:

$$C_1 = A_1 \times E_s \times \varepsilon_1 = {}^{5 \times 300 \times 192800 \times 0.0014}/_{10^3} = 410\ kN$$

$$T_2 = A_2 \times f_{y,s} \times K_{sh} = {}^{-5 \times 300 \times 458 \times 1.25}/_{10^3} = -855\ kN$$

All the longitudinal bars in the slab are considered effective in the bending moment capacity of the specimen. Therefor:

$$T_{slab} = A_{slab} \times f_{y,s} \times K_{sh} = {}^{-10 \times 100 \times 458 \times 1.25}/_{10^3} = -570\ kN$$

Equilibrium check:

$$|C_c| = 1033\ kN \cong\ |C_1 + T_2 + T_{slab}| = |410 - 855 - 570| = 1015\ kN$$

Moment resistance:

$$a = \beta_1 \times c = 0.83 \times 84 = 70\ mm$$

Moment about the centre of compression block:

$$\begin{aligned} M_{beam} &= C_1 \times \left(\frac{a}{2} - d_1\right) + T_2 \times \left(\frac{a}{2} - d_2\right) + T_{slab} \times \left(\frac{a}{2} - d_{slab}\right) \\ &= 410 \times \left(\frac{70}{2} - 50\right) - 855 \times \left(\frac{70}{2} - 400\right) - 570 \times \left(\frac{70}{2} - 400\right) \Big/ 10^3 \\ &= 510\ kN.m \end{aligned}$$

Slab in compression

Assume $c = 27\ mm$

$$\varepsilon_{r1} = 0.0035 \times \frac{c - d_1}{c} = 0.0035 \times \frac{27 - 50}{27} = -0.0030 < -0.0024 \rightarrow yielded$$

$$\varepsilon_{r2} = 0.0035 \times \frac{c - d_2}{c} = 0.0035 \times \frac{27 - 400}{27} = -0.0484 < -0.0024 \rightarrow yielded$$

$$\varepsilon_{slab} = 0.0035 \times \frac{c - d_{slab}}{c} = 0.0035 \times \frac{27 - 50}{27} = -0.0030 < -0.0024 \rightarrow yielded$$

Concrete block compression by assuming the full width of slab ($b = 2090\ mm$) effective in compression:

$$C_c = \alpha_1 \times f'_c \times \beta_1 \times b \times c = 0.77 \times 55 \times 0.83 \times 2090 \times 27 \Big/ 10^3 = 1983\ kN$$

Reinforcement tension:

$$T_1 = A_1 \times E_s \times \varepsilon_1 = -5 \times 300 \times 458 \Big/ 10^3 = -687\ kN$$

$$T_2 = A_2 \times f_{y,s} \times K_{sh} = -5 \times 300 \times 458 \times 1.25 \Big/ 10^3 = -855\ kN$$

$$T_{slab} = A_{slab} \times f_{y,s} = -10 \times 100 \times 458 \Big/ 10^3 = -458\ kN$$

Equilibrium check:

$$|C_c| = 1983\ kN \cong\ |T_1 + T_2 + T_{slab}| = |-687 - 855 - 458| = 2000\ kN$$

Moment resistance:

$$a = \beta_1 \times c = 0.83 \times 27 = 22\ mm$$

Moment about the centre of compression block:

$$\begin{aligned} M_{beam} &= T_1 \times \left(\frac{a}{2} - d_1\right) + T_2 \times \left(\frac{a}{2} - d_2\right) + T_{slab} \times \left(\frac{a}{2} - d_{slab}\right) \\ &= {-687 \times \left(\frac{22}{2} - 50\right) - 458 \times \left(\frac{22}{2} - 50\right) - 855 \times \left(\frac{22}{2} - 400\right)}\Big/{10^3} \\ &= 379\ kN.m \end{aligned}$$

Shear Capacity of Beam

Two branches of 10M bars are used as transverse reinforcement. Therefore, the cross-sectional area of shear reinforcement:

$$A_v = 2 \times 100 = 200\ mm^2$$

According to the previous calculations:

$$M_r = 321\ kN.m$$

$$V_f = \frac{M_r}{l_b} = \frac{321}{2.225} = 144\ kN$$

where l_b is the distance between the point of loading at the beam tip and the centre of the column.

Moreover:

$$d = 400\ mm$$

$$d_v = \max(0.9d, 0.72h) = \max(360,324) = 360$$

Due to large deformations at the plastic hinge, the contribution of concrete to the shear capacity is ignored. Therefore, all shear demands must be resisted by the transverse reinforcement. According to Clause 11.2.8.2 of CSA A23.3-14 (CSA 2014-a):

$$A_{v,min} = 0.06 \times \sqrt{f'_c} \times \frac{b \times s}{f_{y,b}}$$

by assuming two branches of 10M bars as shear reinforcement:

$$\frac{A_{v,min} \times f_{y,b}}{0.06 \times \sqrt{f'_c} \times b} = s_{max}$$

$$s_{max} = \frac{2 \times 100 \times 400}{0.06 \times \sqrt{55} \times 350} = 514\ mm$$

Shear demand for steel stirrups:

$$V_S = 144\ kN$$

From CSA A23.3-14 (CSA 2014-a) Clause 11.3.5:

$$V_S = \frac{f_{y,b} \times d_v \times A_v}{s} \times cot\theta$$

However, according to Clause 21.3.4.2 (CSA 2014-a):

$$\theta = 45°$$

Therefore:

$$s = \frac{400 \times 360 \times 2 \times 100}{144 \times 10^3} \times cot\theta = 200\ mm$$

Clause 21.3.3.2 of CSA A23.3-14 (CSA 2014-a) is used to calculate the minimum spacing of stirrups. The spacing between stirrups should be the least of:

- $\frac{d}{4} = \frac{400}{4} = 100\ mm$
- Eight times the diameter of the smallest longitudinal bars, $8 \times 20 = 160\ mm$
- 24 times the diameter of the hoop bars, $24 \times 10 = 240\ mm$
- 300 mm

Therefore:

USE 2 branches of 10M @ 90 mm

Flexural Capacity of Column

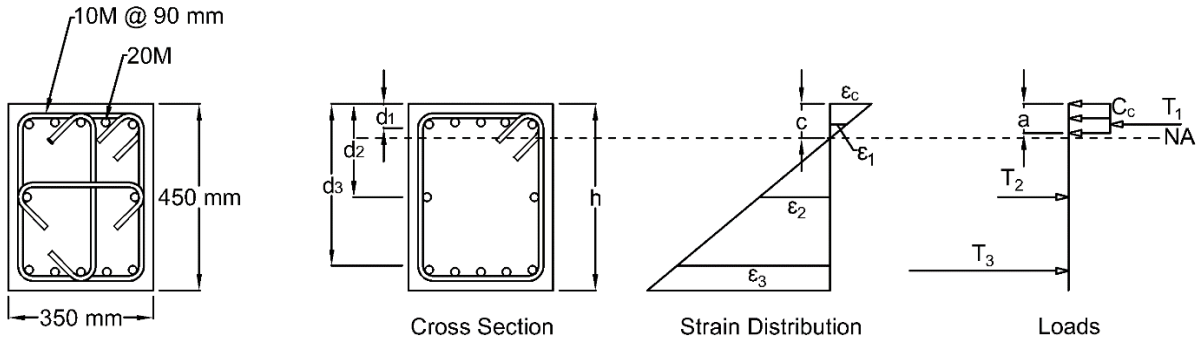

Figure B.3 – Cross-sectional properties and compatibility of strains for column in steel-RC specimen

$d_1 = 50\ mm, d_2 = 225\ mm,\ d_3 = 400\ mm$

According to Clause 10.9.1 of CSA A23.3-14 (CSA 2014-a), the area of longitudinal bars for compression members shall not be less than 0.01 times the gross area:

$$\frac{12 \times 200}{350 \times 450} = 0.0152 > 0.0100 \ \rightarrow OK$$

Axial load-moment interaction diagram

- Point One (pure axial load)

According to Clause 10.10.4 of CSA A23.3-14 (CSA 2014-a):

$$P_o = \alpha_1 \times f'_c \times (A_g - A_s) + f_{y,s} \times A_s$$
$$= {0.77 \times 55 \times (450 \times 350 - 12 \times 200) + 458 \times 12 \times 200}/{10^3} = 7667\ kN$$

$$P_r = 0.8 \times P_o = 6134\ kN$$

- Point Two (pure bending)

Assuming $c = 62\ mm$:

$$a = \beta_1 \times c = 0.83 \times 65 = 54\ mm$$

$$\frac{a}{2} = \frac{54}{2} = 27\ mm$$

$$\varepsilon_1 = \varepsilon_{cu} \times \frac{c - d_1}{c} = 0.0035 \times \frac{62 - 50}{62} = -0.0007 > -0.0024$$

$$\varepsilon_2 = \varepsilon_{cu} \times \frac{c - d_2}{c} = 0.0035 \times \frac{225 - 62}{62} = 0.0092 > 0.0024 \rightarrow yielded$$

$$\varepsilon_3 = \varepsilon_{cu} \times \frac{c - d_3}{c} = 0.0035 \times \frac{400 - 62}{62} = 0.0191 > 0.0024 \rightarrow yielded$$

The effect of strain hardening (25% increase in the tensile strength of steel) is not considered in the calculations for the flexural capacity of the column:

$$C_1 = A_{s1} \times E_s \times \varepsilon_1 = {1500 \times 192800 \times 0.0007}/{10^3} = 196\ kN$$

$$T_2 = A_2 \times f_{y,s} = {600 \times 458}/{10^3} = 275\ kN$$

$$T_3 = A_3 \times f_{y,s} = {1500 \times 458}/{10^3} = 687\ kN$$

$$C_c = \alpha_1 \times f'_c \times b \times \beta_1 \times c = {0.77 \times 55 \times 350 \times 0.83 \times 62}/{10^3} = 763\ kN$$

Equilibrium check:

$$C_c = 763\ kN \cong\ C_1 + T_2 + T_{slab} = -196 + 275 + 687 = 766\ kN$$

Bending moment capacity:

$$M = {763 \times (225 - 27) + 196 \times (225 - 50) + 687 \times (400 - 225)}/{10^3} = 307\ kN.m$$

$$(c = 62\ mm, \quad P_e = 0\ kN, \quad M = 307\ kN.m)$$

- Point Three ($c = 400\ mm$)

$$a = \beta_1 \times c = 0.83 \times 400 = 332\ mm$$

$$\frac{a}{2} = \frac{332}{2} = 166\ mm$$

$$\varepsilon_1 = \varepsilon_{cu} \times \frac{c - d_1}{c} = 0.0035 \times \frac{400 - 50}{400} = 0.0031 > 0.0024 \rightarrow yielded$$

$$\varepsilon_2 = \varepsilon_{cu} \times \frac{c - d_2}{c} = 0.0035 \times \frac{400 - 225}{400} = 0.0015$$

$$\varepsilon_3 = \varepsilon_{cu} \times \frac{c - d_3}{c} = 0.0035 \times \frac{400 - 400}{400} = 0$$

$$C_1 = A_1 \times f_{y,s} = {1500 \times 458}/{10^3} = 687\ kN$$

$$C_2 = A_2 \times E_s \times \varepsilon_2 = {600 \times 192800 \times 0.0015}/{10^3} = 177\ kN$$

$$T_3 = 0\ kN$$

$$C_c = \alpha_1 \times f'_c \times b \times \beta_1 \times c = {0.77 \times 55 \times 350 \times 0.83 \times 400}/{10^3} = 4921\ kN$$

Therefore, an external load equal to P_e is applied at the centre of the section to satisfy the equilibrium.

$$P_e = C_c + C_1 + C_2 = 4921 + 177 + 687 = 5785\ kN$$

Moment about centre line of the cross-section:

$$M = {4921 \times \left(\frac{450}{2} - 166\right) + 687 \times \left(\frac{450}{2} - 50\right)}/{10^3} = 410\ kN.m$$

$$(c = 400\ mm, \quad P_e = 5785\ kN, \quad M = 410\ kN.m)$$

❖ Point Four ($c = 350\ mm$)

$$a = \beta_1 \times c = 0.83 \times 350 = 291\ mm$$

$$\frac{a}{2} = \frac{291}{2} = 146\ mm$$

$$\varepsilon_1 = \varepsilon_{cu} \times \frac{c - d_1}{c} = 0.0035 \times \frac{350 - 50}{350} = 0.0030 > 0.0024 \rightarrow yielded$$

$$\varepsilon_2 = \varepsilon_{cu} \times \frac{c - d_2}{c} = 0.0035 \times \frac{350 - 225}{350} = 0.0013$$

$$\varepsilon_3 = \varepsilon_{cu} \times \frac{c - d_3}{c} = 0.0035 \times \frac{350 - 400}{350} = -0.0005$$

$$C_1 = A_1 \times f_{y,s} = {1500 \times 458}/{10^3} = 687\ kN$$

$$C_2 = A_2 \times E_s \times \varepsilon_2 = {600 \times 192800 \times 0.0013}/{10^3} = 145\ kN$$

$$T_3 = A_3 \times E_s \times \varepsilon_3 = {-1500 \times 192800 \times 0.0005}/{10^3} = -145\ kN$$

$$C_c = \alpha_1 \times f'_c \times b \times \beta_1 \times c = {0.77 \times 55 \times 350 \times 0.83 \times 350}/{10^3} = 4305\ kN$$

$$P_e = C_c + C_1 + C_2 + T_3 = 4305 + 687 + 145 - 145 = 4992\ kN$$

Moment about centre line of the cross-section:

$$M = {4305 \times \left(\frac{450}{2} - 146\right) + 687 \times \left(\frac{450}{2} - 50\right) - 145 \times \left(\frac{450}{2} - 400\right)}/{10^3} = 487\ kN.m$$

$$(c = 350\ mm, \quad P_e = 4992\ kN, \quad M = 487\ kN.m)$$

❖ Point Five ($c = 300\ mm$)

$$a = \beta_1 \times c = 0.83 \times 300 = 249\ mm$$

$$\frac{a}{2} = \frac{249}{2} = 125\ mm$$

$$\varepsilon_1 = \varepsilon_{cu} \times \frac{c - d_1}{c} = 0.0035 \times \frac{300 - 50}{300} = 0.0029 > 0.0024 \rightarrow yielded$$

$$\varepsilon_2 = \varepsilon_{cu} \times \frac{c - d_2}{c} = 0.0035 \times \frac{300 - 225}{300} = 0.0009$$

$$\varepsilon_3 = \varepsilon_{cu} \times \frac{c - d_3}{c} = 0.0035 \times \frac{300 - 400}{300} = -0.0012$$

$$C_1 = A_1 \times f_{y,s} = {1500 \times 458}/{10^3} = 687\ kN$$

$$C_2 = A_2 \times E_s \times \varepsilon_2 = {600 \times 192800 \times 0.0009}/{10^3} = 101\ kN$$

$$T_3 = A_3 \times E_s \times \varepsilon_3 = {-1500 \times 192800 \times 0.0012}/{10^3} = -337\ kN$$

$$C_c = \alpha_1 \times f'_c \times b \times \beta_1 \times c = {0.77 \times 55 \times 350 \times 0.83 \times 300}/{10^3} = 3690\ kN$$

$$P_e = C_c + C_1 + C_2 + T_3 = 3690 + 687 + 101 - 337 = 4141\ kN$$

Moment about centre line of the cross-section:

$$M = {3690 \times \left(\frac{450}{2} - 125\right) + 687 \times \left(\frac{450}{2} - 50\right) - 337 \times \left(\frac{450}{2} - 400\right)}/{10^3} = 549\ kN.m$$

$$(c = 300\ mm, \qquad P_e = 4141\ kN, \qquad M = 549\ kN.m)$$

- Point Six ($c = 250\ mm$)

$$a = \beta_1 \times c = 0.83 \times 250 = 208\ mm$$

$$\frac{a}{2} = \frac{208}{2} = 104\ mm$$

$$\varepsilon_1 = \varepsilon_{cu} \times \frac{c - d_1}{c} = 0.0035 \times \frac{250 - 50}{250} = 0.0028 > 0.0024 \rightarrow yielded$$

$$\varepsilon_2 = \varepsilon_{cu} \times \frac{c - d_2}{c} = 0.0035 \times \frac{250 - 225}{250} = 0.0004$$

$$\varepsilon_3 = \varepsilon_{cu} \times \frac{c - d_3}{c} = 0.0035 \times \frac{250 - 400}{250} = -0.0021$$

$$C_1 = A_1 \times f_{y,s} = {1500 \times 458}/{10^3} = 687\ kN$$

$$C_2 = A_2 \times E_s \times \varepsilon_2 = {600 \times 192800 \times 0.0004}/{10^3} = 40\ kN$$

$$T_3 = A_3 \times E_s \times \varepsilon_3 = {-1500 \times 192800 \times 0.0021}/{10^3} = -607\ kN$$

$$C_c = \alpha_1 \times f'_c \times b \times \beta_1 \times c = {0.77 \times 55 \times 350 \times 0.83 \times 250}/{10^3} = 3075\ kN$$

$$P_e = C_c + C_1 + C_2 + T_3 = 3075 + 687 + 40 - 607 = 3195\ kN$$

Moment about centre line of the cross-section:

$$M = {3075 \times \left(\frac{450}{2} - 104\right) + 687 \times \left(\frac{450}{2} - 50\right) - 607 \times \left(\frac{450}{2} - 400\right)}/{10^3} = 599\ kN.m$$

$$(c = 250\ mm, \qquad P_e = 3195\ kN, \qquad M = 599\ kN.m)$$

- Point Seven ($c = 200\ mm$)

$$a = \beta_1 \times c = 0.83 \times 200 = 166\ mm$$

$$\frac{a}{2} = \frac{166}{2} = 83\ mm$$

$$\varepsilon_1 = \varepsilon_{cu} \times \frac{c - d_1}{c} = 0.0035 \times \frac{200 - 50}{200} = 0.0026 > 0.0024 \rightarrow yielded$$

$$\varepsilon_2 = \varepsilon_{cu} \times \frac{c - d_2}{c} = 0.0035 \times \frac{200 - 225}{200} = -0.0004$$

$$\varepsilon_3 = \varepsilon_{cu} \times \frac{c - d_3}{c} = 0.0035 \times \frac{200 - 400}{200} = -0.0035 < -0.0024 \rightarrow yielded$$

$$C_1 = A_1 \times f_{y,s} = {1500 \times 458}/{10^3} = 687\ kN$$

$$T_2 = A_2 \times E_s \times \varepsilon_2 = {-600 \times 192800 \times 0.0004}/{10^3} = -51\ kN$$

$$T_3 = A_3 \times f_y = {-1500 \times 458}/{10^3} = -687\ kN$$

$$C_c = \alpha_1 \times f'_c \times b \times \beta_1 \times c = {0.77 \times 55 \times 350 \times 0.83 \times 200}/{10^3} = 2460\ kN$$

$$P_e = C_c + C_1 + T_2 + T_3 = 2460 + 687 - 51 - 687 = 2409\ kN$$

Moment about centre line of the cross-section:

$$M = {2460 \times \left(\frac{450}{2} - 83\right) + 687 \times \left(\frac{450}{2} - 50\right) - 687 \times \left(\frac{450}{2} - 400\right)}/{10^3} = 590\ kN.m$$

$$(c = 200\ mm, \qquad P_e = 2409\ kN, \qquad M = 590\ kN.m)$$

- Point Eight ($c = 150\ mm$)

$$a = \beta_1 \times c = 0.83 \times 150 = 125\ mm$$

$$\frac{a}{2} = \frac{125}{2} = 63\ mm$$

$$\varepsilon_1 = \varepsilon_{cu} \times \frac{c - d_1}{c} = 0.0035 \times \frac{150 - 50}{150} = 0.0023$$

$$\varepsilon_2 = \varepsilon_{cu} \times \frac{c - d_2}{c} = 0.0035 \times \frac{150 - 225}{150} = -0.0018$$

$$\varepsilon_3 = \varepsilon_{cu} \times \frac{c - d_3}{c} = 0.0035 \times \frac{150 - 400}{150} = -0.0058 < -0.0024 \rightarrow yielded$$

$$C_1 = A_1 \times E_1 \times \varepsilon_1 = {}^{1500 \times 192800 \times 0.0023}/_{10^3} = 674\ kN$$

$$T_2 = A_2 \times E_s \times \varepsilon_2 = {}^{-600 \times 192800 \times 0.0004}/_{10^3} = -202\ kN$$

$$T_3 = A_3 \times f_{y,s} = {}^{-1500 \times 458}/_{10^3} = -687\ kN$$

$$C_c = \alpha_1 \times f'_c \times b \times \beta_1 \times c = {}^{0.77 \times 55 \times 350 \times 0.83 \times 150}/_{10^3} = 1845\ kN$$

$$P_e = C_c + C_1 + T_2 + T_3 = 1845 + 674 - 202 - 687 = 1630\ kN$$

Moment about centre line of the cross-section:

$$M = {}^{1845 \times \left(\frac{450}{2} - 63\right) + 674 \times \left(\frac{450}{2} - 50\right) - 687 \times \left(\frac{450}{2} - 400\right)}\Big/_{10^3} = 537\ kN.m$$

$$(c = 150\ mm, \quad P_e = 1845\ kN, \quad M = 537\ kN.m)$$

- Point Nine ($c = 100\ mm$)

$$a = \beta_1 \times c = 0.83 \times 100 = 83\ mm$$

$$\frac{a}{2} = \frac{83}{2} = 42\ mm$$

$$\varepsilon_1 = \varepsilon_{cu} \times \frac{c - d_1}{c} = 0.0035 \times \frac{100 - 50}{100} = 0.0018$$

$$\varepsilon_2 = \varepsilon_{cu} \times \frac{c - d_2}{c} = 0.0035 \times \frac{100 - 225}{100} = -0.0044 < -0.0024 \rightarrow yielded$$

$$\varepsilon_3 = \varepsilon_{cu} \times \frac{c - d_3}{c} = 0.0035 \times \frac{100 - 400}{100} = -0.0105 < -0.0024 \rightarrow yielded$$

$$C_1 = A_1 \times E_1 \times \varepsilon_1 = {}^{1500 \times 192800 \times 0.0018}/_{10^3} = 506\ kN$$

$$T_2 = A_2 \times f_{y,s} = {}^{-600 \times 458}/_{10^3} = -275\ kN$$

$$T_3 = A_3 \times f_{y,s} = {-1500 \times 458}/{10^3} = -687\ kN$$

$$C_c = \alpha_1 \times f'_c \times b \times \beta_1 \times c = {0.77 \times 55 \times 350 \times 0.83 \times 100}/{10^3} = 1230\ kN$$

$$P_e = C_c + C_1 + T_2 + T_3 = 1230 + 506 - 275 - 687 = 774\ kN$$

Moment about centre line of the cross-section:

$$M = {1230 \times \left(\frac{450}{2} - 42\right) + 506 \times \left(\frac{450}{2} - 50\right) - 687 \times \left(\frac{450}{2} - 400\right)}\Big/{10^3} = 434\ kN.m$$

$$(c = 100\ mm, \qquad P_e = 774\ kN, \qquad M = 434\ kN.m)$$

- Point Ten ($c = 93\ mm$)

A constant axial load of 650 kN was applied to the column during the test:

$$\frac{650}{6134} = 10.6\%$$

Assuming $c = 93\ mm$

$$a = \beta_1 \times c = 0.83 \times 93 = 77\ mm$$

$$\frac{a}{2} = \frac{77}{2} = 39\ mm$$

$$\varepsilon_1 = \varepsilon_{cu} \times \frac{c - d_1}{c} = 0.0035 \times \frac{93 - 50}{93} = 0.0016$$

$$\varepsilon_2 = \varepsilon_{cu} \times \frac{c - d_2}{c} = 0.0035 \times \frac{93 - 225}{93} = -0.0050 < -0.0024 \rightarrow yielded$$

$$\varepsilon_3 = \varepsilon_{cu} \times \frac{c - d_3}{c} = 0.0035 \times \frac{93 - 400}{93} = -0.0116 < -0.0024 \rightarrow yielded$$

$$C_1 = A_1 \times E_1 \times \varepsilon_1 = {1500 \times 192800 \times 0.0016}/{10^3} = 463\ kN$$

$$T_2 = A_2 \times f_{y,s} = {-600 \times 458}/{10^3} = -275\ kN$$

$$T_3 = A_3 \times f_{y,s} = {-1500 \times 458}/{10^3} = -687\ kN$$

$$C_c = \alpha_1 \times f'_c \times b \times \beta_1 \times c = {0.77 \times 55 \times 350 \times 0.83 \times 93}/{10^3} = 1144\ kN$$

$$P_e = C_c + C_1 + T_2 + T_3 = 1144 + 463 - 275 - 687 = 645\ kN$$

Moment about centre line of the cross-section:

$$M = {1144 \times \left(\frac{450}{2} - 39\right) + 463 \times \left(\frac{450}{2} - 50\right) - 687 \times \left(\frac{450}{2} - 400\right)}\Big/_{10^3} = 414\ kN.m$$

$$(c = 930\ mm, \qquad P_e = 645\ kN, \qquad M = 414\ kN.m)$$

Column-to-beam flexural strength ratio:

$$\frac{2 \times M_{col}}{2 \times M_{beam}} = \frac{2 \times 414}{2 \times\ 321} = 1.29$$

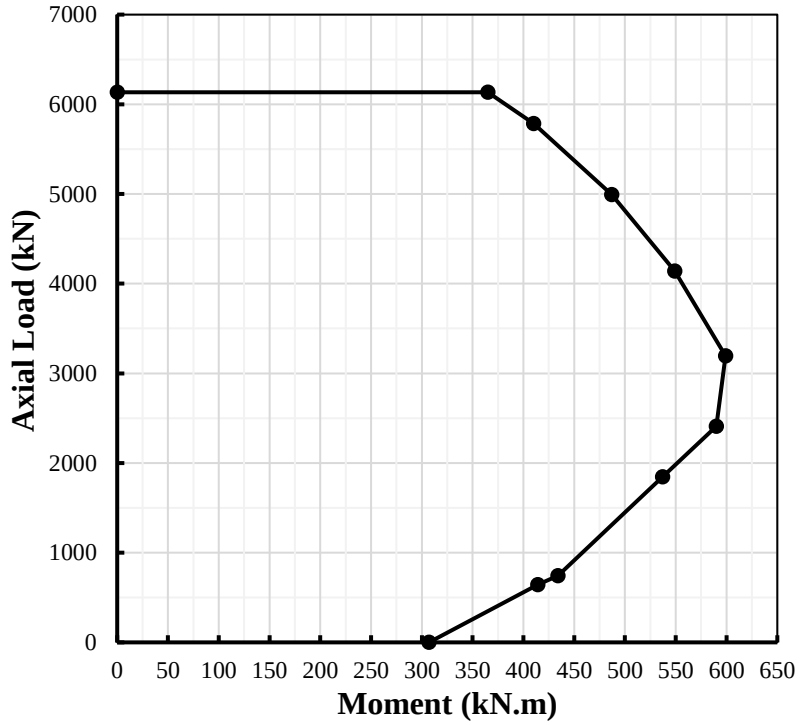

Figure B.4 – Axial load-bending moment interaction diagram for steel-RC column

Shear Capacity of Column

Three branches of 10M bars are used as transverse reinforcement. Therefore, the cross-sectional area of shear reinforcement:

$$A_v = 3 \times 100 = 300\ mm^2$$

According to the previous calculations, at c = 93 mm:

$$M_f = 414\ kN.m$$

$$N_f = 650\ kN$$

Applied shear force:

$$V_f = \frac{M_{r,col}}{h_c} = \frac{2 \times 414}{2.9} = 286\ kN$$

where $M_{r,col}$ is the moment resistance of the column under the applied axial load during testing and h_c is the height of the column.

Moreover:

$$d = \frac{2 \times d_1 + 5 \times d_2}{7} = \frac{2 \times 225 + 5 \times 400}{7} = 350\ mm$$

$$d_v = \max(0.9d, 0.72h) = \max(315{,}324) = 324$$

According to Clause 11.3.3 of CSA A23.3-14 (CSA 2014-a):

$$V_{r,Max} = 0.25 \times f'_c \times b \times d_v$$

Therefore:

$$(0.25 \times 55 \times 350 \times 324)/_{10^3} = 1559\ kN\ > 286\ kN\ \rightarrow OK$$

Total shear resistance of the section is calculated as the sum of concrete and steel resistance:

$$V_r = V_c + V_s$$

where:

$$V_c = \lambda \times \beta \times \sqrt{f'_c} \times b \times d_v$$

From Clause 21.4.5.2 (CSA 2014-a):

$$\beta \leq 0.1 \quad , \quad \theta \geq 45°$$

According to Clause 11.3.6.4 (CSA 2014-a):

$$\varepsilon_x = \frac{\left(\frac{M_f}{d_v} + V_f + 0.5 \times N_f\right)}{2 \times E_s \times A_s}$$

As a result:

$$\varepsilon_x = \frac{\left(\frac{414 \times 10^6}{324} + 286 \times 10^3 - 0.5 \times 650 \times 10^3\right)}{2 \times 192800 \times 7 \times 300} = 0.0015$$

From Clause 11.3.6.4 (CSA 2014-a):

$$\beta = \frac{0.4}{(1 + 1500 \times \varepsilon_x)} \times \frac{1300}{(1000 + S_{ze})}$$

Since $A_v > A_{v,Min}$, $S_{ze} = 300$ mm

$$\beta = \frac{0.4}{(1 + 1500 \times 0.0015)} \times \frac{1300}{(1000 + 300)} = 0.12 > 0.1 \rightarrow USE\ 0.1$$

From Clause 11.3.6.4 (CSA 2014-a):

$$\theta = 29 + 7000 \times \varepsilon_x$$

$$\theta = 29 + 7000 \times 0.0015 = 40° \rightarrow USE\ 45°$$

Therefore:

$$V_c = {0.1 \times \sqrt{55} \times 350 \times 324}/{10^3} = 84\ kN$$

$$V_S = V_r - V_c = 286 - 84 = 202\ kN$$

According to Clause 11.3.5.1 (CSA 2014-a):

$$s = \frac{A_v \times f_{y,b} \times d_v \times cot\theta}{V_S}$$

Therefore, by using three branches of 10M bars as shear reinforcement:

$$s = \frac{3 \times 100 \times 400 \times 324}{202 \times 10^3} = 192\ mm$$

Minimum required shear reinforcement is calculated based on Clause 11.2.8.2 (CSA 2014-a):

$$A_{v,min} = 0.06 \times \sqrt{f'_c} \times \frac{b \times s}{f_{y,b}}$$

By rearranging:

$$\frac{A_v \times f_y}{0.06 \times \sqrt{f'_c} \times b} = s_{max}$$

$$s_{max} = \frac{3 \times 100 \times 400}{0.06 \times \sqrt{55} \times 350} = 771\ mm$$

Checking for minimum spacing according to Clause 11.3.8.1 and 11.3.8.3 of CSA A23.3-14 (CSA 2014-a):

$$0.125 \times \lambda \times f'_c \times b \times d_v = {0.125 \times 55 \times 350 \times 324}/{10^3} = 780\ kN > V_r = 286\ kN$$

Therefore, the maximum spacing between the stirrups should not exceed:

- $0.7d_v = 0.7 \times 324 = 227$ mm
- 600 mm

Also, from Clause 21.4.4.3 (CSA 2014-a), s_{max} is equal to the least of:

- One-quarter of the minimum member dimension, $\frac{350}{4} = 87.5 \approx 90\ mm$
- Six times the diameter of the smallest longitudinal bar, $6 \times 20 = 120\ mm$
- $S_x = 100 + \left(\frac{350 - h_x}{3}\right) = 100 + \left(\frac{350-190}{3}\right) = 153$ mm

where h_x is maximum horizontal center-to-center spacing between longitudinal bars on all faces of the column that are laterally supported by seismic hoops or crosstie legs. Therefore, we use:

USE 3 branches of 10M @ 90 mm

Confinement of Column

CSA A23.3-14 (CSA 2014-a) in Clause 21.4.4.2 defines the required reinforcement in columns in ductile frames as:

$$A_{sh} = Max\left(0.2 \times k_n \times K_p \times \frac{A_g}{A_{ch}} \times \frac{f'_c}{f_{y,b}} \times S \times h_c\ , 0.09 \times \frac{f'_c}{f_{y,b}} \times S \times h_c\right)$$

where:

$$K_n = \frac{n_l}{(n_l - 2)}$$

$$k_p = \frac{P_f}{P_0}$$

The parameters in the equation are defined as:

n_l: Total number of longitudinal bars in the column cross-section that are laterally supported by the corner of hoops or hooks or seismic crossties, 8

A_g: Gross area of the section, $350 \times 450 = 157500$ mm^2

P_f: Maximum axial load, 650 kN

h_c: Dimension of concrete core of rectangular section measured perpendicular to the direction of the confinement bars to outside of peripheral hoop

A_{ch}: Cross-sectional area of core (to outside of the stirrups): $(350 - 2 \times 50 + 19.5 + 2 \times 11.3) \times (450 - 2 \times 50 + 19.5 + 2 \times 11.3) = 114327$ mm^2

P_f: Applied axial load to the member

P_0: Axial resistance of the member

Therefore:

$$k_n = \frac{8}{(8-2)} = 1.33$$

$$k_p = \frac{650}{6134} = 0.106$$

For the longer dimension:

$$h_c = (450 - 2 \times 50 + 19.5 + 2 \times 11.3) = 392\ mm$$

$$S = \frac{A_{sh} \times A_{ch} \times f_{y,b}{}_y}{0.2 \times k_n \times K_p \times A_g \times f'_c \times h_c} = \frac{3 \times 300 \times 114327 \times 400}{0.2 \times 1.33 \times 0.106 \times 157500 \times 55 \times 393} = 429\ mm$$

$$S = \frac{A_{sh} \times f_{y,b}}{0.09 \times f'_c \times h_c} = \frac{3 \times 100 \times 400}{0.09 \times 55 \times 393} = 62\ mm$$

$$Max(370\ mm, 62\ mm) = 370\ mm$$

For the smaller direction:

$$h_c = (350 - 2 \times 50 + 19.5 + 2 \times 11.3) = 292\ mm$$

$$S = \frac{A_{sh} \times A_{ch} \times f_{y,b}}{0.2 \times k_n \times K_p \times A_g \times f'_c \times h_c} = \frac{3 \times 100 \times 114327 \times 400}{0.2 \times 1.33 \times 0.106 \times 157500 \times 55 \times 293} = 192\ mm$$

$$S = \frac{A_{sh} \times f_{y,b}}{0.09 \times f'_c \times h_c} = \frac{3 \times 100 \times 400}{0.09 \times 55 \times 293} = 83\ mm$$

$$Max(165\ mm, 83\ mm) = 165\ \text{mm}$$

According to Clause 7.6.5.5 of CSA-A23-14 (CSA 2014-a), ties in compressive members shall be arranged so that every corner and alternate longitudinal bar shall have lateral support provided by the corner of a tie having an included angle of not more than 135°, and no bar shall be farther than 150 mm clear on either side from such a laterally supported bar. These requirements are fulfilled in the cross-section of the column.

Therefore:

USE 3 branches of 10M @ 90 mm

APPENDIX C

LATERAL LOAD-DRIFT RESPONSE AND PROPERTIES OF TEST SPECIMENS

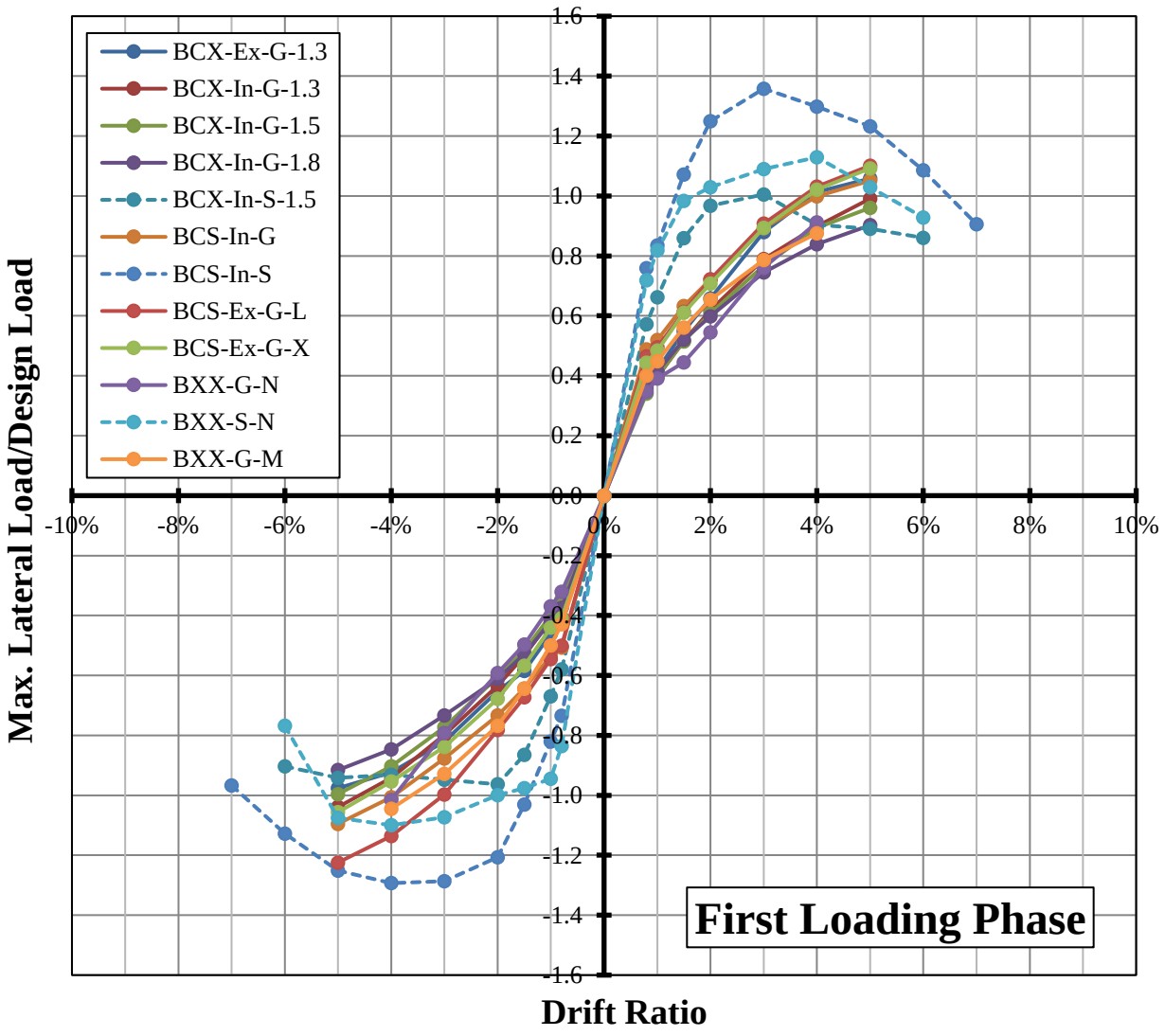

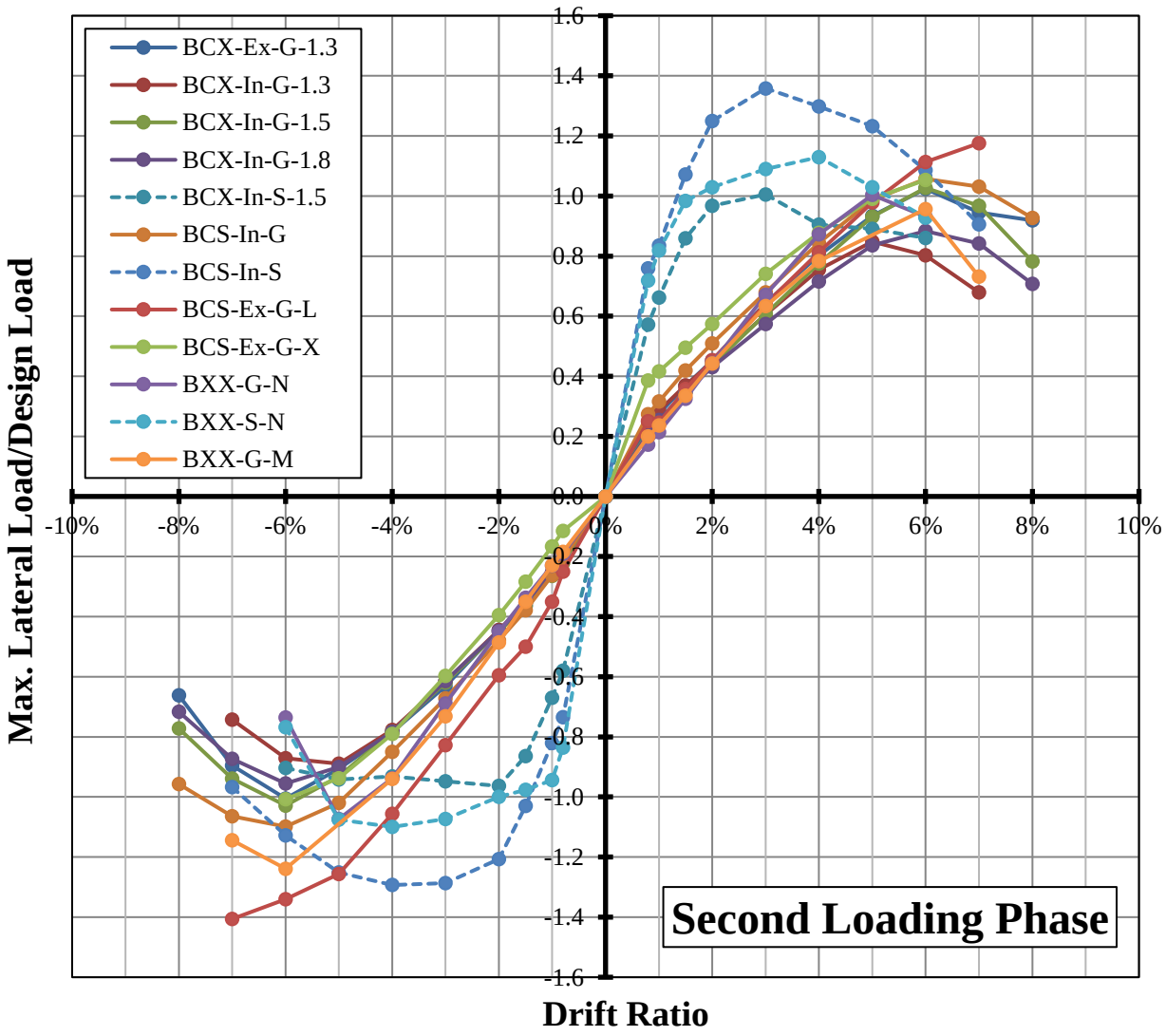

Note:

Specimen BCX-Ex-G-1.3: GFRP-RC exterior beam-column with joint shear stress of $1.3\sqrt{f'_c}$

Specimen BCX-In-G-1.3: GFRP-RC interior beam-column with joint shear stress of $1.3\sqrt{f'_c}$

Specimen BCX-In-G-1.5: GFRP-RC interior beam-column with joint shear stress of $1.5\sqrt{f'_c}$

Specimen BCX-In-G-1.8: GFRP-RC interior beam-column with joint shear stress of $1.8\sqrt{f'_c}$

Specimen BCX-In-S-1.5: Steel-RC interior beam-column with joint shear stress of $1.5\sqrt{f'_c}$

Specimen BCS-In-G: GFRP-RC interior beam-column-slab with lateral beams

Specimen BCS-In-S: Steel-RC interior beam-column-slab with lateral beams

Specimen BCS-Ex-L: GFRP-RC exterior beam-column-slab with lateral beams

Specimen BCS-Ex-X: GFRP-RC exterior beam-column-slab without lateral beams

Specimen BXX-G-N: GFRP-RC cantilever beam without steel side plates

Specimen BXX-S-N: Steel-RC cantilever beam without steel side plates

Specimen BXX-G-M: GFRP-RC cantilever beam with steel side plates

Test Matrix

Specimen	Beam Reinforcement (Top and Bottom)	Beam Flexural Capacity (kN.m)	Joint Shear Ratio	Column-to-Beam Flexural Ratio	Concrete Strength (MPa)
BCX-Ex-G-1.3	8-25M	452	1.29	1.15	49
BCX-In-G-1.3	4-16M	264	1.30	1.06	38
BCX-In-G-1.5	6-16M	330	1.49	0.98	49
BCX-In-G-1.8	10-16M	422	1.85	0.83	58
BCX-In-S-1.5	6-20M	361[(a)]	1.56	1.16	56
BCS-In-G	6-16M	333[(b)]	1.49[(b)]	0.99[(b)]	50
BCS-In-S	5-20M	321[(a)(b)]	1.29[(b)]	1.30[(b)]	55
BCS-Ex-G-L	8-16M	363[(b)]	0.95[(b)]	1.47[(b)]	51
BCS-Ex-G-X	5-16M	327[(b)]	0.79[(b)]	1.60[(b)]	49
BXX-G-N	3-20M	231	-	3.64	47
BXX-S-N	4-20M	214[(a)]	-	3.93	47
BXX-G-X	3-20M	336	-	2.50	49

[(a)] 25% increase in steel tensile strength due to strain hardening
[(b)] Without slab contribution